THE ELECTRONIC PROPERTIES OF PURE AND TRANSITION METAL DOPED AMORPHOUS SILICON-DIOXIDE FILMS.

Thesis submitted by

JOAQUIM JOAO De LIMA

for the degree of

DOCTOR OF PHILOSOPHY

Faculty of Science

University of Edinburgh

February 1987

DECLARATION

Testimony is hereby given that this thesis is the original composition of the author and that the work described herein, except where stated otherwise, has been undertaken.

To my parents and sisters for their unfailing support, understanding and encouragement.

CONTENTS

ACKNOWLEDGEMENTS

I would like to thank my supervisor, Professor A. E. Owen for his support and interest in this work. I wish to also offer my thanks to Dr. K. V. Krishna for his expert help with the rf sputtering system.

Special thanks are due to Dr. Dearnaley and his group at AERE Harwell for their help with the Rutherford backscattering measurements and to Dr. C. Baker of the BP Research Centre, Sunbury, on-Thames, for his help with the Auger electron spectroscopy measurements.

The co-operation of Dr. S. Henderson of the Department of Chemistry in making available his infrared machine is greatly appreciated as is the help of Dr. M. Schröder also of the Department of Chemistry, for the use of his ESR machine.

The financial assistance of the SERC is gratefully acknowledged as is the CASE award with Hughes Microelectronics Ltd. In particular, I wish to acknowledge the helpful discussions with my industrial supervisor, Jim West and also Dr. A. Hawryliw.

I am indebted to Dr. A. P. Firth for his advise on some of the experimental work and also acknowledge the help of the technical staff of the Department of Electrical Engineering.

Finally, I wish to thank my friends and colleagues and in particular, Wee Kiong Choi, Ian Flanagan and Keith Sylvan, who have been continual sources of confidence, kindness and trust.

LIST OF SYMBOLS

A - Area of contact.

B_e - Electronic Bohr magneton.

E_c - Bottom of the conduction band in semiconductor.

E_f - Fermi energy.

E_t - Trap energy level above the edge of the valence band.

E_v - Energy of the top of the valence band.

F - Electric-field strength.

g - Degeneracy factor.

$<g>$ - Lande factor.

h - Planck's constant.

H - Magnetic field.

I - Current.

J - Current density.

k - Boltzmann's constant.

L - Sample thickness.

m - Free-electron mass.

m_s - Spin magnetic moment.

n_o - Density of free carriers.

N_t - Trap density.

q - Magnitude of electronic charge.

T - Absolute temperature.

V - Voltage.

ϵ_o - Permittivity of free space.

ϵ_r - Relative permittivity.

ϕ_b - Height of schottky barrier (measured from fermi level of metal).

ϕ_i - Insulator work-function.

ϕ_m - Work function of metal.

ϕ_s - Semiconductor work-function.

$\Delta\phi_b$ - Lowering of potential barrier due to image force and field.

$\Delta\phi_{pf}$ - Barrier lowering due to Poole-Frenkel effect.

β_{pf} - Poole-Frenkel constant.

σ -Conductivity.

$\psi(x)$ - Electrostatic potential.

μ - Mobility of electrons.

ABSTRACT

This study has concentrated on the electrical and optical properties of pure and vanadium doped amorphous silicon dioxide films prepared by the rf sputtering of a silicon dioxide target in an argon atmosphere.

Detailed d.c. measurements of well annealed pure and vanadium co-sputtered films have been undertaken in the temperature range, 273-500K, with electric fields of up to $8\times10^{5}Vcm^{-1}$. Although these films exhibit low- and high- conducting states similar to previous reports on amorphous silicon dioxide, there are also very significant differences. The low- and high- conducting states have been characterised and it is shown that both these states are stable bulk phenomena.

Despite the increased conductivity, lower activation energies and reduced trap densities associated with the presence of vanadium, both types of films display bulk conduction via the process of single-carrier space-charge-limited current.

The composition and impurity profile of the doped oxides has been probed using Rutherford Backscattering (RBS) and Auger Electron Spectroscopy (AES) and there is no evidence for any segregation or clustering of the metallic impurity. Measurements using X-ray Photoelectron Spectroscopy (XPS) have indicated that the vanadium is present in the oxide as V_2O_5. The possibility of lower states of vanadium being present have been explored using infrared measurements and indications are that some of the impurity is reduced to V^{4+}.

Finally, device related experiments indicate that the vanadium doped oxides have significant advantageous effects on the device characteristics, sufficient to make them potentially important in device applications where very thin films of undoped amorphous silicon dioxide are commonly used.

CHAPTER 1

INTRODUCTION.

1.1 INTRODUCTION

Silicon-dioxide is perhaps the wide bandgap insulator with the best characterised electrical properties yet the depth of understanding does not approach that of common crystalline semiconductors, such as silicon.

The most common use of silicon dioxide in solid state devices is in the form of metal-oxide-silicon (MOS) structures as a gate dielectric and for purposes of isolation in integrated circuits. As a result of its importance in silicon technology a great deal of experimental work has been done on the Si-SiO_2 system yet many aspects of the MOS structure where great benefit would be achieved with a better understanding of the main factors which determine the electronic properties of amorphous insulators, in particular factors such as charge storage and transport, still remain unresolved

There is at present a serious gap in the understanding of the influence which impurities or *dopants* have on the electronic transport and charge storage. Although considerable attention has been directed at ionic impurities such as protons and sodium ions in silicon dioxide, practically nothing is known about the effects of specific electronically-active dopants and it is this aspect of amorphous silicon dioxide which forms the subject matter of this thesis.

Controllable and specific electronic effects are thought more likely to occur by the incorporation of transition-metals (incomplete d-shell atoms) into the oxide. In this work, the emphasis is on amorphous silicon dioxide doped with vanadium. Transition metals are interesting for this purpose because

(i) *they are known to form specific electronic states in vitreous SiO_2, and related silicate glasses, at energies within the band-gap [1].*

(ii) *the electronic states depend on the charge states of the transition-metal atoms, which in turn depend on how the ions are bound in the host network [1] and*

(iii) *transition metals are known to have a significant effect on the electrical properties of oxide glasses such as electronic conductivity, carrier mobility and dielectric absorption [2].*

Vanadium(V) has been incorporated into amorphous silicon dioxide at concentrations in the range 1-9 atomic percent. Samples were prepared in the form of metal-insulator(a-SiO_2)-silicon(MIS) structures, by rf sputtering from a target of fused silica. The rf sputtered oxides were uniformly doped with vanadium either by co-sputtering of the metal, or they were ion-implanted.

Undoped (pure) rf sputtered a-SiO_2 thin films ranging in thickness from 0.1-2.2μm have also been studied as a check and reference to previous work on the electrical properties of SiO_2. All samples were annealed carefully before measurement, usually at 900^{0}C in nitrogen for 30 minutes and were subsequently characterised by optical techniques in an attempt to ensure that they were essentially the same as good quality oxides, thermally grown on silicon.

A range of electrical and optical measurements have been carried out on the pure and V-doped a-SiO_2 films. Current-Voltage(I-V) characteristics as a function of field and temperature; capacitance-voltage; optical spectra in the infra-red, electron spin resonance(ESR), Auger electron spectroscopy(AES) and Rutherford Back Scattering(RBS).

This study commences with high field conduction processes in thin films and is immediatedly followed by a discussion of the methods of film preparation and the role of silicon-dioxide in solid state devices. A detailed review of transport properties in both pure and 'doped' silicon dioxide is given. The experimental techniques employed in this study are then reviewed and used in examining and characterising the pure and vanadium co-sputtered films.

Finally, the possibility of modulating the electrical properties of silicon dioxide in a controlled fashion by the incorporation of an electronically-active dopant such as vanadium shows, via preliminary measurements, that the presence of vanadium in relatively thick silicon dioxide films, does possibly avoid the types of problems commonly encountered with devices which use very thin ($\leq$10nm) insulating layers to pass current, such as the metal— silicon-nitride— silicon-dioxide— silicon (MNOS) and the floating-gate— avalanche— injection— type MOS (FAMOS), memory devices.

1.2 REFERENCES

(1) J. Wong and C.A. Angell, "Spectroscopy of Glasses", (Marcel Dekker),New York (1976).

(2) N.F. Mott and I.G. Austin, Adv. in Phys., 18, 41 (1969).

CHAPTER 2

ELECTRODE EFFECTS AND HIGH FIELD CONDUCTION IN INSULATORS.

2.1 INTRODUCTION

High field effects ($>10^4 Vcm^{-1}$) have been the subject of extensive theoretical and experimental research since the 1950s [1-5]. The effects of high electric fields on the current-voltage(I-V) characteristics are thought to arise as a result of a change in the distribution of traps and mobility of carriers, or by a change in the rate of carrier injection, or both. The main features to emerge from these studies particularly in the case of solids of high resistivity(or low mobility), such as insulators, is that the high field effects may be divided into three categories, namely

(1) ELECTRODE EFFECTS: *High field effects arise as a result of a field dependent rate of carrier injection or emission from electrodes through either Schottky-type thermionic emission or tunnelling through a potential barrier at the contact.*

(2) BULK EFFECTS: *The high field effects are caused by a field dependent carrier mobility due to scattering phonons and impurity centers; by field dependent carrier density due to field dependent trapping probabilities, detrapping processes, and tunnelling of trapped carriers; and by the field dependent thermal effect arising from the Joule heating of the specimen.*

(3) BOTH ELECTRODE AND BULK EFFECTS: *As the applied field is increased, the high field effects may change from bulk-limited to electrode-limited or from electrode-limited to bulk-limited processes.*

In the sections which follow some of the high field effects mentioned above are considered in more detail. In particular, attention is drawn to the Schottky and Poole-Frenkel effects, the change from contact to bulk controlled processes, tunnelling and space charge limited conduction. In all the discussions an electron current is considered, ie. an n-type semiconductor or insulator. The same considerations would apply to a hole current (p-type material) with appropriate changes of sign.

2.2 CONTACTS

2.2.1 Thermionic Emission

The current which flows through an insulator at high temperatures or when the potential barrier is too thick to permit tunnelling is strongly dependent on the rate at which electrons can be excited from the contact, over the potential barrier into the insulator conduction band. This type of barrier prevents the easy injection of electrons from the

metal into the insulator, leading to electrode-limited conduction in which the current voltage characteristic is given by [3,4].

$$I = A^{*}T^{2} \exp\left(\frac{-\phi_b}{kT}\right) \tag{2.1}$$

where A^{*}, the Richardson constant, is

$$A^{*} = \frac{4\pi q k^2 m}{h^3}$$

for thermionic emission into vacuum. For thermionic emission into an insulator however, the value of A^{*} is quite different from its value in vacuum [6].

In the following two sections the factors which affect the lowering of the barriers for both neutral and ohmic contacts are examined in more detail.

2.2.2 Neutral Contacts

A neutral contact is one in which the regions adjacent to the contact on both sides are electrically neutral. This condition is commonly referred to as the flat band condition and arises when the metal work function (ϕ_m) is equal to the insulator work function (ϕ_i).

The lowering of the potential barrier as a result of the combination of an applied electric field and an image force is termed the *Schottky effect*. Taking these into consideration the resultant potential barrier is as shown in Fig.(2.1) and may be expressed as

$$\psi(x) = \phi_m - \chi - \left(\frac{q^2}{16\pi\epsilon x}\right) - qFx \tag{2.2}$$

While the total lowering of the potential barrier is given by

$$\Delta\phi_b = (\phi_m - \chi) - \phi_b \tag{2.3}$$

$$= \left(\frac{q^3 F}{4\pi\epsilon}\right)^{1/2} = \beta_{sc} F^{1/2} \tag{2.4}$$

with $\beta_{sc} = \left(\frac{q^3}{4\pi\epsilon}\right)^{1/2}$

This results in an effective potential barrier height of the form

$$\phi_b = (\phi_m - \chi) - \left(\frac{q^3}{4\pi\epsilon}\right)^{1/2} F^{1/2} \tag{2.5}$$

which is field dependent.

Substituting $\phi_b=(\phi_m-\chi)-\Delta\phi_b$ for ϕ_b in eqn.(2.1) gives.

$$I=A^*T^2\left[\frac{(\phi_m-\chi)}{kT}\right]\exp\left(\frac{\beta_{sc}F^{1/2}}{kT}\right) \tag{2.6}$$

This represents the Richardson-Schottky equation and according to Simmons [7,8], it is only valid for insulators if the electron mean free path is of the same order as the insulator thickness.

The first observation of the Richardson-Schottky effect at a neutral contact in an insulator was made by Emptage and Tantraporn [9] in 1962 and since then there have been several other similar reports.

2.2.3 Ohmic Contacts

An ohmic contact between a metal and a semiconductor or insulator, is defined as one which has a negligible impedance compared to the impedance of the bulk of the specimen. Under these conditions the free carrier density at and in the neighbourhood of the contact is much greater than in the bulk. The term *ohmic* however, is inappropriate in so far as describing the current-voltage relationship. In general, the conduction is ohmic at low fields if the metal does not inject more carriers than are generated thermally in the bulk but becomes non-linear or non-ohmic when carrier injection from the metal dominates.

There are two principle methods by which ohmic contacts may be formed:

(1) *Using metals of low work-function such that $\phi_m<\phi_s$ for electron injection or*

(2) *By heavily doping the material surface near the contact, in order to make the potential barrier thin enough for quantum mechanical tunnelling to prevail.*

Figure(2.2a) depicts the energy level diagram for an ohmic contact between a metal and an intrinsic semiconductor in the absence of surface states and for $\phi_m<\phi_s$. Although the semiconductor may be intrinsic, when an ohmic contact injects free carriers into the semiconductor which overwhelm those that are generated thermally, the conduction in the intrinsic semiconductor becomes extrinsic and space charge limited in nature. Even in the case of an insulator, the ohmic contact always tends to inject electrons into it when $\phi_m<\phi_i$ in order to align at the same level the Fermi energies in both the metal and the insulator.

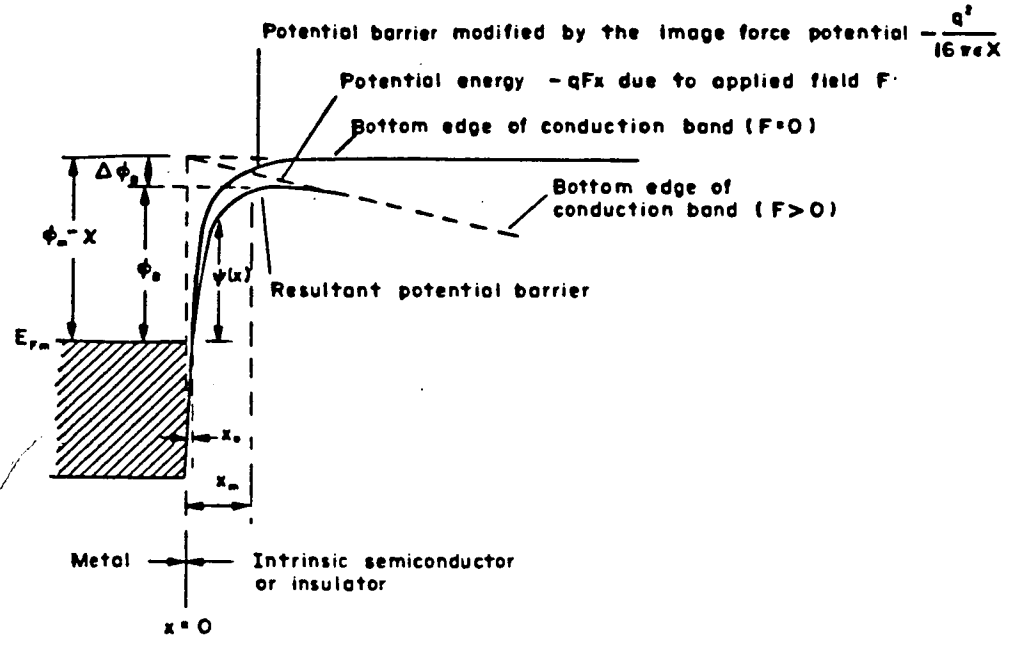

Fig 2.1 Energy level diagram showing the lowering of potential barrier due to the combination of image force and applied field, for a neutral contact [6].

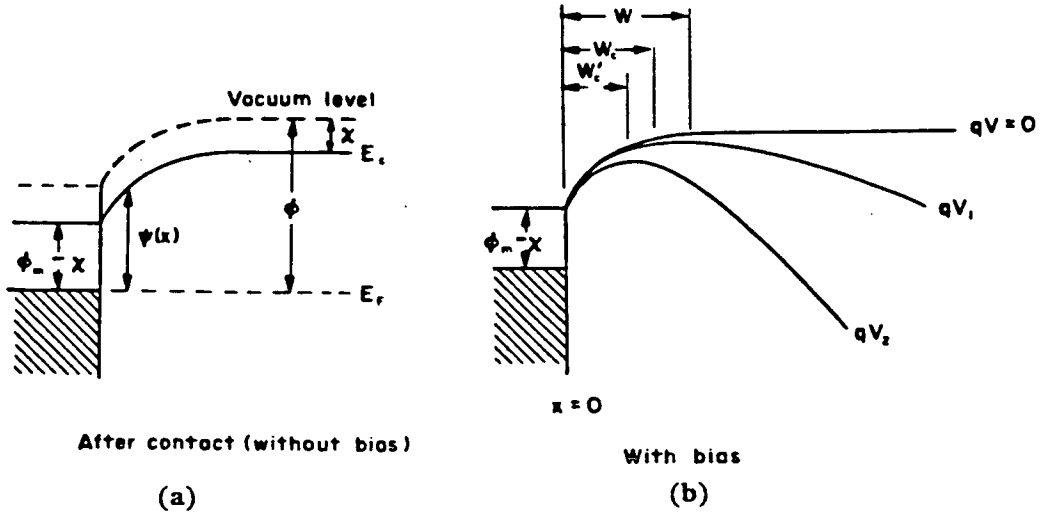

Fig 2.2 Energy level diagrams for an ohmic contact between a metal and an intrinsic semiconductor or insulator, $\phi_m < \phi$ and applied voltage $V_2 > V_1 > 0$ [6].

The internal field created by this accumulated space charge decreases with increasing distance into the specimen since the injected space charge density decreases and reaches a final value equal to that thermally generated in the insulator at some finite distance X where X= W in Fig.(2.2b).

On the application of an electric field, E_1 (E_1= V_1/Thickness) the energy bands begin to tilt and the well known potential energy maximum at X= W_c appears, as shown in Fig.(2.2b). The electric field at this point is equal and opposite to the internal field in a manner such that the product of the diffusion field and the charge carrier density is equal to the product of the applied field and the charge carrier density in the bulk of the sample [6]. This point, (where dV/dX = 0) is also referred to as the *virtual cathode* and under equilibrium conditions the negative potential gradient at $X<W_c$ tends to repel back to the contact all electrons which represent the excess space charge limited current. At this virtual cathode therefore, the electrons are released with zero velocity and since the ohmic contact acts as a reservoir of free charge electric conduction is controlled by the impedance of the insulator and is therefore bulk limited. When the applied field is increased to a higher value, E_2 (E_2= V_2/Thickness) for instance, this field balances a higher internal field at X= W_c' which implies that the electron density at X= W_c' is higher than at X= W_c -the higher the applied field, the closer is the virtual cathode to the contact [6]. By adjustment of the position of the virtual cathode, an ohmic contact is therefore able to provide a plentiful supply of carriers to participate in conduction as and when required.

When the field is so high that the virtual cathode coincides with the contact at X=0, the effect of space charge ceases and the conduction becomes ohmic. Any further increase in the field causes the conduction to change from being bulk limited to electrode limited since conduction is then governed by the rate of electron injection from the contact. If however, (ϕ_m-χ) is large and the applied field is high but not high enough to cause breakdown, the potential barrier can become so thin that quantum mechanical tunnelling may dominate. The tunnelling process through such a barrier is discussed in more detail in section (2.3).

2.2.4 Electrode to Bulk Limited Conduction

The aim of this section is to provide a brief descriptive overview of the principal features surrounding the transition from electrode to bulk limited conduction.

Consider a metal-insulator interface in the absence of surface states in which the insulator contains shallow donors as well as deep traps. If the assumption is made that the metal work function is greater than the insulator work function then a blocking contact with a narrow depletion region results as shown in Fig.(2.3). Since both the donor and trap level lie above the fermi level they are empty, which means that a positive charge density exists in this region [6,19].

At low fields the contact resistance is much greater than that of the bulk and the current-voltage (I-V) characteristic is due mainly to field emission from the electrode into the conduction band of the insulator, c.f.eqn.(2.1). This process is characterised by a steep increase in the current with voltage which in turn gives rise to a rapid decrease in the contact resistance. The I-V characteristic in this region is practically independent of sample thickness since a greater portion of the applied voltage appears across the contact. If the applied voltage is increased further both the bulk and contact resistance tend to decrease but the rate of decrease for the latter is more rapid [6]. Eventually, at some critical voltage V_c, the contact and bulk resistance coincide and the applied voltage is shared equally between them. Any voltage in excess of V_c then falls predominantly across the bulk and the remainder across the contact. This is reflected in the I-V characteristic with the current increasing less rapidly while the conduction becomes thickness dependent and bulk controlled through processes such as the Poole-Frenkel effect or space charge conduction. These effects are considered in some detail in the sections which follow.

In a comprehensive study of metal-insulator-metal structures, Simmons [19] has shown that in the presence of donors and traps of the order of $10^{17}cm^{-3}$ or higher, a transition from electrode to bulk limited conduction occurs. In a detailed treatment of this phenomenon his results show that at low voltages the I-V characteristic is extremely steep and independent of thickness but the high voltage characteristic is thickness dependent and of the form $I \propto \exp(\beta V^{1/2})$.

Hartman et al [20] have also published similar data on SiO_x films and typical results demonstrating such a transition are shown in the results of Stuart [21] on Al-SiO-Al structures, in Fig.(2.4).

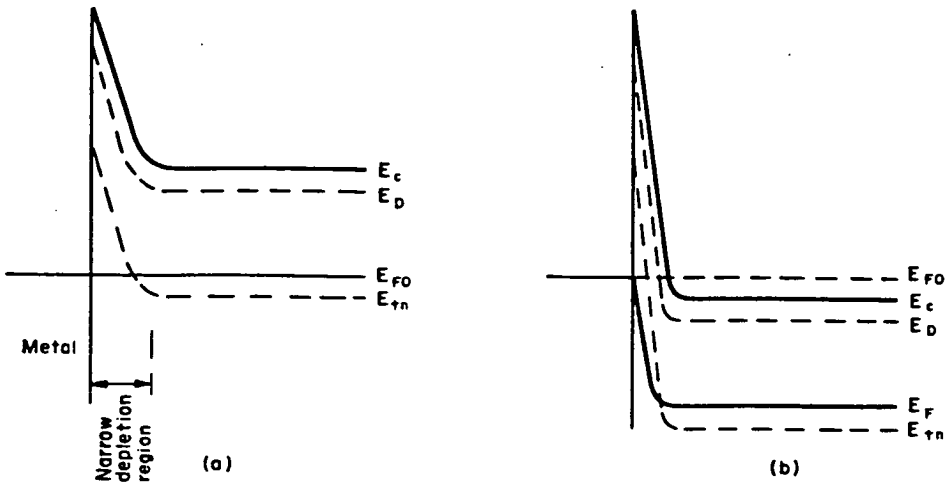

Fig 2.3 Schematic diagrams showing the energy levels for electron tunnelling field emission from a blocking contact into an insulator with deep traps of trapping level E_{tn} (a) without bias in thermal equilibrium, and (b) under a bias for tunnelling injection. This illustrates the possible transition from electrode-limited to bulk-limited conduction by an increase in the applied field [6].

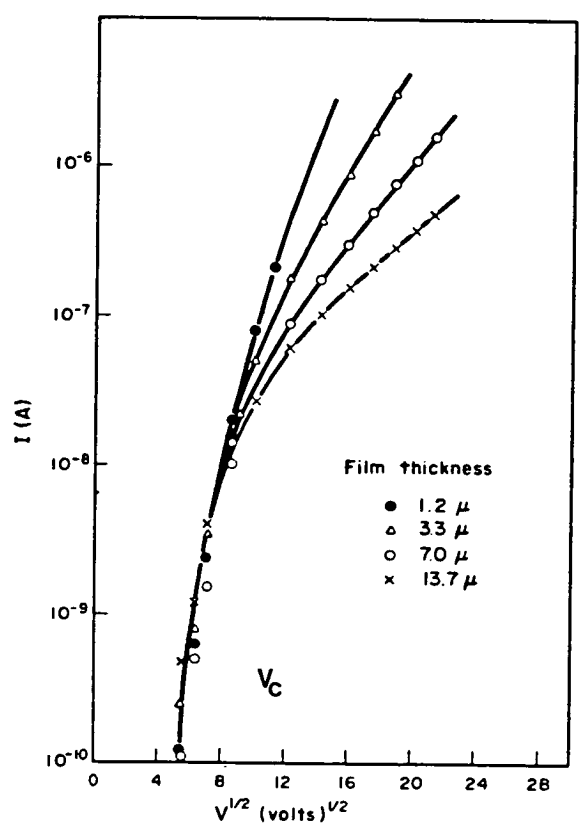

Fig 2.4 Transition from the electrode-limited to the bulk-limited electric conduction in Al-SiO-Al films. Electrode area: 0.1cm^2 [21].

2.3 TUNNELLING

Since 1930, when Frenkel [10] first considered the problem of electron tunnelling in thin insulating films, several workers [11-15] have made significant extensions to the subject.

There are essentially two aspects of tunnelling, one due to field emission which occurs when the field is large enough to assist electrons to tunnel through part of the insulator, and the other, when the insulator thickness is less than about 50Å when the process of quantum mechanical tunnelling occurs between the contacts.

Field assisted tunnelling is important for thick insulators at very high fields and at low temperatures [6]. For thin insulators(10-50Å), there exists a finite probability for an electron to pass through the dielectric by quantum mechanical tunnelling and this problem has received examination in great detail by, Stratton [11], Simmons [13-15] and McColl and Mead [16].

The equations for both processes however are identical, indicating that the basic tunnelling process in field emission and that in tunnelling through a thin film are the same [6].

The tunnelling characteristics are strong functions of the interfaces between the insulating film and the electrodes as well as the properties of the insulator and the work-functions of the metal electrodes [13-15].

Several studies of tunnelling phenomena in metal-insulator-semiconductor (MIS) systems, have been reported with particular attention to the use of these phenomena as a spectroscopic tool for the investigation of the electronic band structure of the semiconductor surface [17,18], and for purposes of device applications in the form of MIS tunnel diodes.

2.4 POOLE-FRENKEL EMISSION

The Poole-Frenkel(P-F) effect is associated with the high ($>10^4 Vcm^{-1}$) electric field modification of the potential barrier of a trap, making it easier for the trapped carrier to be liberated.

In order to experience the P-F effect a trap must be neutral when filled and charged when empty. Traps which are neutral when empty and charged when filled will not manifest this effect for lack of coulombic interaction. The effect of a lowered coulombic potential barrier when it interacts with an electric field is shown in Fig.(2.5)

which closely resembles the Schottky effect in thermionic emission, Fig.(2.1). Both effects are due to the coulombic interaction between an escaping electron and a positive charge yet differ in that the positive charge is fixed for the P-F trapping barrier but is a mobile image for the Schottky barrier. The resulting barrier lowering due to the P-F effect is therefore twice that due to the Schottky effect. The amount of barrier lowering due to the P-F effect may be written as

$$\Delta\phi_{pf}=\left[\frac{e^3F}{\pi\epsilon_o\epsilon_r}\right]^{1/2}=\beta_{pf}F^{1/2} \tag{2.7}$$

where β_{pf} is termed the P-F constant and is given by

$$\beta_{pf}=\left[\frac{e^3}{\pi\epsilon_o\epsilon_r}\right]^{1/2}$$

This one dimensional treatment was first employed by Frenkel in 1938 [22]. He maintained that in the presence of a uniform field the ionisation potential of the atoms in a solid are lowered by an amount given by eqn.(2.7) making the conductivity field dependent and of the form

$$\sigma=\sigma_o\exp\left[\frac{\beta_{pf}F^{1/2}}{kT}\right] \tag{2.8}$$

where σ_o is the low-field conductivity.

There exist a large number of insulating materials in which the current at high fields increases exponentially with the square root of the applied voltage [23-27]. Although this type of I-V characteristic has generally been ascribed to P-F or Schottky emission it is not easy to distinguish between the P-F effect which is observed when the conduction is bulk limited and the Schottky effect which is electrode limited since, they both follow the same field dependence, namely $\ln\sigma\propto F^{1/2}$.

In order to distinguish between the two it is necessary to compare both experimental and theoretical values of β_{pf} and β_{sc} which are easily evaluated if the high frequency dielectric constant (ϵ_r) is known.

In interpreting their results in terms of the P-F effect many workers have noted that plots of $\ln\sigma$ versus $F^{1/2}$ give values for the slope that vary between β_{pf}/kT and $\beta_{pf}/2kT$, depending on the energy levels and distribution of donors, traps and acceptors [24,26,28], which do not agree with the theoretical values. This implies that there may be several slopes in $\ln\sigma$ versus $F^{1/2}$ plots and that even from the best fit curve the value of ϵ_r so determined is unlikely to be close to the value expected. This has led to several modifications to the P-F model. Jonscher [25] and Hartke [29] have proposed

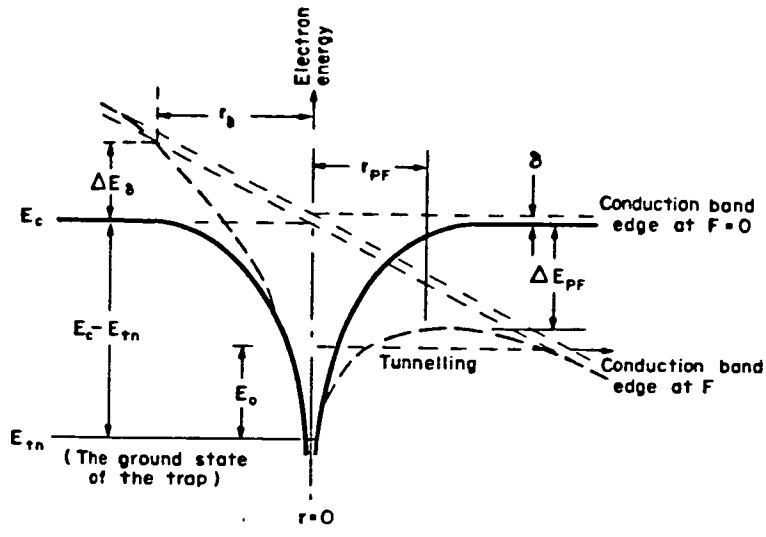

Fig 2.5 Schematic diagram illustrating the Poole-Frenkel effect.

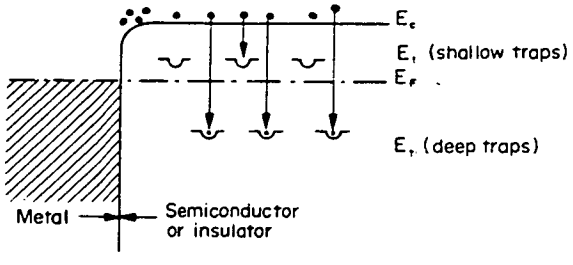

Fig 2.6 Energy level diagram for an electron injecting ohmic contact to a semiconductor or insulator with shallow and deep electron traps.

three-dimensional treatments which give a field and temperature dependent conductivity that is slightly different from the original P-F relation while Ieda et al [30] have developed a three dimensional model which follows a simple ohms law at low fields and approaches the P-F function at high fields. Their results were shown to be consistent with measurements by Hartmann [20], on SiO_x films.

Hill [27], on the other hand has argued that normalisation between the field and temperature, $F^{1/2}T^{-1}$, can be used to examine whether the conduction is due to the P-F detrapping process. His plots of J versus $F^{1/2}T^{-1}$ at high fields fit well with the results on SiO_x films obtained by Servini and Jonscher [31] and Klein and Lisak [32].

Choi, DeLima and Owen have recently looked more closely at the one dimensional P-F effect and have attended to the problem of the variation in the slopes of $\log\sigma$ versus $E^{1/2}$ plots. A copy of their paper is attached at the end of this thesis, in Appendix IV.

In conclusion, much of the argument over the P-F constant may be ascribed to misinterpretation of the mechanism of conduction.

2.5 SPACE CHARGE LIMITED CONDUCTION

In this section the phenomenon of space charge limited conduction (SCLC), specifically the subject of one carrier SCL currents, is examined with particular reference to the pioneering work of Rose and Lampert [33,35].

It was Rose [33], Smith [34] and Lampert [35] who were the first to recognise the spectroscopic character and potential of SCL analysis, in low-conductivity materials. Their basic contributions have shown that the concentration and energy levels of imperfections can in principle be obtained from the non-linear current-voltage characteristics. Although there are many aspects of SCL current flow which have received detailed reviews [36,37] we shall follow the work of Rose and Lampert with particular emphasis on two cases of the effect of trapping in the forbidden gap.

All discussions in the remainder of this chapter will in general, unless otherwise stated, be limited to *electron motion*.

2.5.1 Historical Background

The possibility of space charge injection into an insulator from an injecting contact was first considered by Mott and Gurney [38]. In their treatment, electrons were taken to be injected from a metal electrode into the conduction band of a trap free insulator where they remained free to move. The current was controlled therefore not by the injecting electrode but by the bulk of the insulator. The practical applicability of this model was somewhat limited since in most solids traps command a dominant role. This limitation was foreseen by Rose [33] who extended the simple theory of space charge injection to take into account the effect of traps. Lampert [35], took this a step further in forming a concise theory to describe all the features of the steady state SCL current-voltage (I-V) characteristics for an insulator having a single discrete trapping level.

Since the pioneering work of Rose and Lampert [33,35], the steady state SCL current-voltage technique has emerged as a very useful tool for purposes of investigating localised state distributions in both insulators and semiconductors. The theory has received wide use in the study of near perfect crystals(i.e.trap free) such as CdS [39,40] as well as structurally disordered materials like amorphous selenium films [41]. In organic crystals however, and some amorphous materials, more than one type of carrier trap distribution is apparent and models having an assumed distribution of trapping states have been developed. Typical models include (i)traps confined in discrete energy levels in the forbidden gap [42,43], and (ii)traps with a quasi-continuous distribution of energy levels either of gaussian or exponential form [44,45].

2.5.2 Introduction

Space charge limited conduction occurs when the contacting electrode injects either electrons into the conduction band or holes into the valence band of an insulator such that the rate of injection is higher than the rate of recombination. When such a contact emits more electrons per second than the material can accept or transport, the remainder forms a negative space charge which then creates a field to reduce the rate of electron emission.

As discussed originally by Rose and Lampert [33,35], one of the primary requirements for the injection of charge into a semiconductor or insulator is that at least one of the electrodes must be ohmic. This type of contact was dealt with in significant detail in section(2.2.3).

Carrier injection into a solid is generally classified as either single injection or double injection. Single injection is due mainly to one type of carrier either electrons or holes and in the following sections consideration will only be given to the subject of steady state d.c. one-dimensional single carrier injection of electrons with the assumptions outlined below.

(1) *The energy band model remains valid in the treatment of injected carriers.*

(2) *A perfect electron injecting contact is present-i.e. ohmic contact.*

(3) *The mobility of the free electrons is unaffected by the electric field or the presence of traps.*

(4) *Maxwell-Boltzmann statistics remain valid for the free electron while the trapped electron is described by Fermi- Dirac statistics.*

(5) *The electric field is large enough to neglect the component due to diffusion and thermal carriers.*

(6) *High field effects such as the Poole-Frenkel effect, impact ionisation or field dependent mobility are ignored.*

Consider first the situation of a trap free solid.

2.5.3 Trap Free Solid - Ideal Case.

The general current continuity equation may be expressed as

$$J=(n_o e+\rho)\mu E \tag{2.9}$$

where n_o is the density of thermal free carriers, ρ and E are the space charge density and field and μ is the electron mobility.

The electric field follows the Poisson relationship

$$\partial E(x)/\partial X=\rho(x)/\epsilon \tag{2.10}$$

and the potential in the system is given by

$$V_x = \int_0^x E(x)dx \tag{2.11}$$

Ignoring the effect of thermally generated carriers viz $n_o = 0$ in eqn.(2.9).

$$\rho=J/\mu E$$

Substituting for ρ in eqn.(2.10) gives

$$dE/dX = J/\mu\epsilon E \tag{2.12}$$

Using the virtual cathode approximation that the field is zero at the injecting electrode gives

$$J = \frac{9\mu\epsilon V^2}{8X^3} \tag{2.13}$$

This relationship is the well-known Mott-Gurney relationship[38] and is often referred to as the *square law* for *trap-free* SCL currents.

At low fields the J-V characteristic follows ohm's law as long as the density of thermally generated carriers n_o, is predominant. The departure from ohm's law and the onset of SCL conduction occurs when the carrier transit time is approximately equal to the dielectric relaxation time ; this transition is not abrupt but is a gradual change.

As there exist no perfect crystals, traps created by imperfections are always present and often interact with injected carriers to control the flow of current and determine the J-V characteristics. There are two cases of interest which arise from such effects namely, trapping due to *shallow traps* and that due to *deep traps*.

The probability that an electron is captured by a trap is expressed in terms of Fermi-Dirac statistics as

$$F(E) = \frac{1}{1 + g \exp\left[\frac{(E-E_f)}{kT}\right]} \tag{2.14}$$

The shallow traps are those which are located above the Fermi level [Fig.(2.6)] and in this case $F(E) << 1$ when $(E_t - E_f) > kT$ which implies that most of the traps are empty. If however, E_t is located below E_f then the traps are referred to as deep traps [Fig.(2.6)] and $F(E) \to 1$ when $(E_f - E_t) > kT$ which means most of the traps are filled.

In order to understand fully each of these cases it is necessary first to consider the situation of traps in single discrete energy levels. In general, the distribution function for the trap density as a function of energy level E, above the edge of the *valence band* and distance x from the injecting contact can be written as

$$h(E,x) = N_t(E)\, S(x) \tag{2.15}$$

Where $N_t(E)$ and $S(x)$ represent the energy and spatial distribution function of traps, respectively.

For the case of a single discrete energy level the distribution function can be represented as

$$h(E,x) = N_t\,\delta(E-E_t)\,S(x) \tag{2.16}$$

where N_t is the density of traps, E_t is the trap energy level *above the edge of the valence band* and $\delta(E-E_t)$ is the Dirac delta function.

The density of trapped electrons is then given by

$$n_t(x) = \int_{E_1}^{E_2} \frac{N_t\,\delta(E-E_t)\,S(x)\,dE}{1+\,g\exp\left[\dfrac{(E-E_f)}{kT}\right]} \tag{2.17}$$

$$\simeq \frac{N_t\,S(x)}{1+\left[\dfrac{N_t\,\Theta_n}{n(x)}\right]} \tag{2.18}$$

where

$$\Theta_n = \frac{N_c}{N_t}\,g_n \exp\left(\frac{-E_t}{kT}\right) \tag{2.19}$$

and represents the ratio of free carrier density to total carrier (free + trapped) density.

$$\Theta_n = \frac{n}{[n+n_t]} \tag{2.20}$$

It can be seen for the trap free case, $n_t=0$ therefore, $\Theta_n=1$. In the presence of traps, Θ_n is always less than 1 and can be as small as 10^{-7} [33]. The degeneracy factor g, will from now on be taken to equal unity.

Substitution of eqn.(2.18) into a general Poisson relationship of the form

$$\frac{dF(x)}{dX} = \frac{e}{\epsilon}\left[n(x)+\,n_t(x)\right] \tag{2.21}$$

yields

$$\frac{dF(x)}{dX} = \frac{e}{\epsilon}\left\{n(x) + \left[\frac{N_t\,S(x)}{1+\dfrac{N_t\Theta_n}{n(x)}}\right]\right\} \tag{2.22}$$

An analytic solution of the above equation is not possible but by assuming E_t *to be a shallow trap level* (i.e.E_t is above E_f) a current-voltage relationship represented by

$$J = \frac{9}{8} \epsilon \mu \Theta_n \frac{V^2}{L^3} \tag{2.23}$$

is obtained and the onset of the transition from ohmic to SCL conduction occurs when the applied voltage reaches

$$V_\Omega = \frac{8}{9} \frac{e n_o L^2}{\Theta_n \epsilon} \tag{2.24}$$

This equation predicts that

(1) *The voltage for the transition* V_Ω, *rises with increasing density of thermally generated free carriers* n_o *and*

(2) *The greater the concentration of traps, the higher is the value of* V_Ω *for the transition.*

As the applied voltage is increased the density of free carriers resulting from injection may increase to a value such that the quasi-fermi level moves up above the shallow electron-trapping level and at this point most traps are filled. This is termed the trap-filled limit(TFL) and is defined as the voltage at which the fermi level passes through the electron trapping level, E_t. The TFL is the condition for the transition from the trapped J-V characteristics to the trap-free J-V characteristic. After all the traps are filled, any carriers injected thereafter are free to move in the conduction band of the sample so that at the threshold voltage, V_{TFL}, the current rapidly jumps from its low trap-limited value to a high trap-free SCL current.

In thermal equilibrium and in the absence of an applied voltage the density of trapped electrons is

$$n_{t_o} = \int_{E_u}^{E_l} \frac{N_t \, \delta(E - E_t) \, dE}{1 + \exp\left[\frac{(E - E_{fo})}{kT}\right]} \tag{2.25}$$

$$= \frac{N_t}{1 + \exp\left[\frac{-(E_{fo} - E_t)}{kT}\right]} \tag{2.26}$$

and the density of unfilled traps is

$$N_t - n_{t_o} = \frac{N_t}{1 + \exp\left[\frac{(E_{fo} - E_t)}{kT}\right]} \tag{2.27}$$

Two cases may now be distinguished.

2.5.4 Shallow Traps

When $E_{fo}<E_t$ eqn.(2.27) can be approximated to

$$N_t - n_{t_o} \simeq N_t \tag{2.28}$$

On the assumption that $N_t>>n$ and that the applied voltage reaches V_{TFL} when all the traps are filled, then

$$\frac{dF_{TFL}}{dX} = \frac{eN_t}{\epsilon}$$

which gives

$$V_{TFL} = \frac{eN_tL^2}{2\epsilon} \tag{2.29}$$

and for cases in which Θ_n is not too small V_{TFL} *is greater than* V_Ω. Figure(2.7) shows schematically the variation of a log J versus log V plot for a solid with shallow traps.

2.5.5 Deep Traps

In this case $E_{fo}>E_t$ and eqn.(2.27) can be written as

$$N_t - n_{t_o} \simeq N_t \exp\left[\frac{(E_t - E_{fo})}{kT}\right] \tag{2.30}$$

Following the same procedure as before

$$V_{TFL} = \frac{e\,(N_t - n_{t_o})\,L^2}{2\epsilon} \tag{2.31}$$

Now, since $E_{fo}>E_t$, all injected carriers will first be used to fill the traps and at V_{TFL} all traps will be filled so that V_{TFL} can also be thought of as the voltage for the transition from ohmic to SCL conduction i.e. V_Ω.

The difference between this case and that of the shallow traps is that the transition is from the ohmic to the trap-free SCL current because all the traps have been filled. Figure(2.8) shows a schematic log J versus log V plot for this situation. The triangle in this plot is often referred to as the *Lampert triangle*, after Lampert [35].

In good single-crystal materials, the trap energy levels are often discrete while in amorphous materials, they tend to be distributed in energy. These differences have been ascribed to variations in the bond angles in amorphous materials, due to the intrinsic disorder.

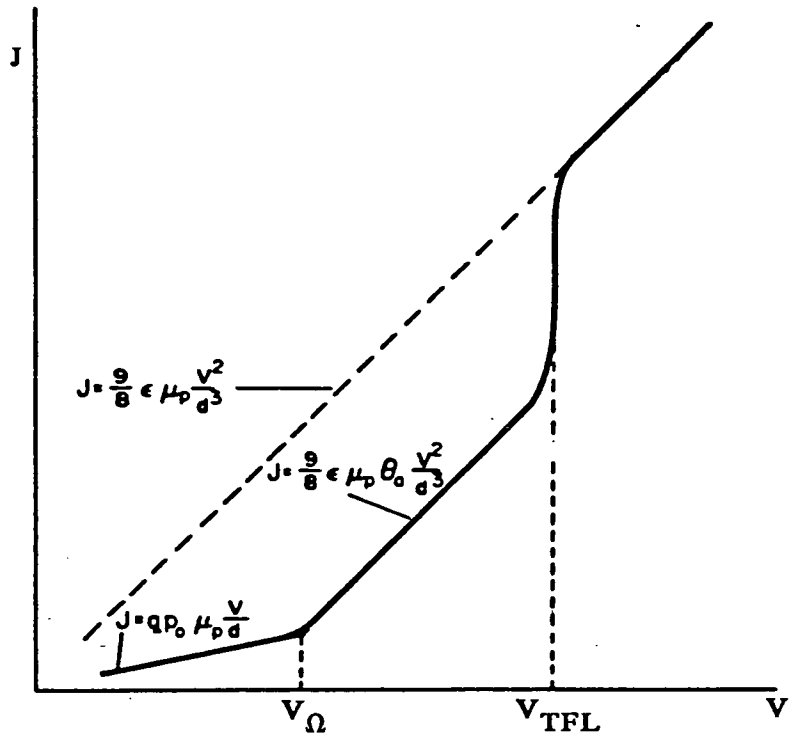

Fig 2.7 LogJ - LogV characteristic for a solid containing shallow traps confined in a trapping level $E_t(E_{fo}<E_t)$ [6].

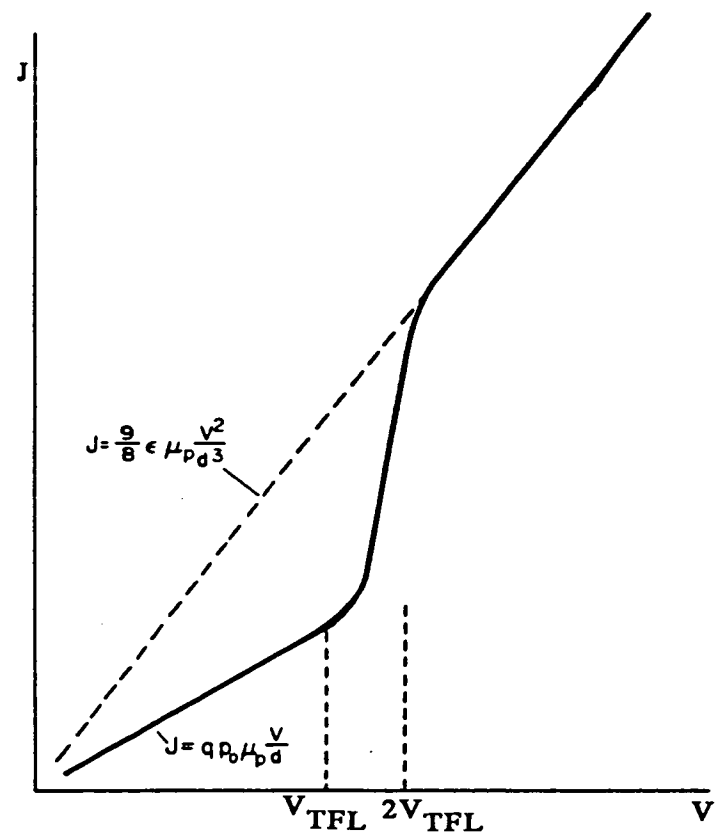

Fig 2.8 LogJ - LogV characteristic for a solid containing deep traps confined in a trapping level $E_t(E_{fo}>E_t)$ [6].

As indicated earlier, several trap distributions have been postulated but consideration will only be given to the uniform distribution, first investigated by Rose [33].

2.5.6 Traps Distributed Uniformly in Energy

An insulator in which the traps are distributed uniformly in energy is shown in Fig.(2.9) and the current-voltage relationship in terms of physical parameters may be represented as

$$J = 2n_o e \mu \frac{V}{L} \exp\left[\frac{2\epsilon V}{N_t kTeL^2}\right] \tag{2.32}$$

What is important in eqn.(2.32) is that as a result of the distribution of traps in energy, the SCLC now varies exponentially with voltage compared to the square law dependence in the trap-free and shallow trap models.

2.5.7 Thickness Scaling Rule

Evidence for SCL conduction can be obtained from thickness-scaling experiments. The general scaling rule [40] for one-carrier SCL conduction in any material with an arbitrary trap distribution can be expressed in the form

$$\frac{J}{L} = f\left(\frac{V}{L^2}\right) \tag{2.33}$$

This equation is universally valid provided the carrier diffusion is ignored.

2.6 IMPURITY HOPPING CONDUCTION

An electron occupying an isolated donor level in an insulator containing impurities has a wavefunction which is localised around the impurity and an energy which is generally slightly below the conduction band minimum. Due to a slight overlap of the wavefunction of an electron of one donor with neighbouring donors, a conduction process is possible in which the electron moves between centres, without activation into extended states. This is termed impurity or hopping conduction and a necessary condition is the presence of both donors and acceptors.

Because of the low mobility of an electron in an impurity level at normal temperatures, impurity conduction is often masked if there are many electrons in the

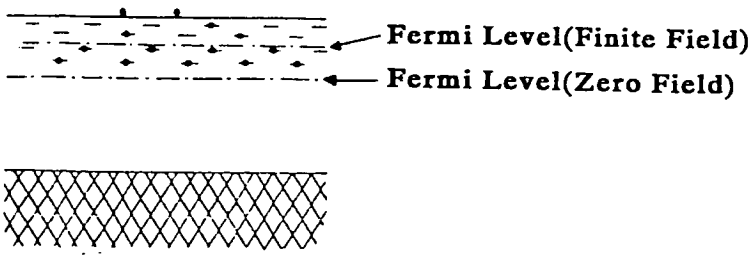

Fig 2.9 Insulator having a distribution of traps in energy and showing the shift due to an injected charge [33].

conduction band. An insulator however, has a very low density of thermally generated free carriers in the conduction band and consequently impurity conduction is more likely to be observed in this type of material.

Jonscher and Hill [46] have shown that the major contribution to conductivity at low temperatures and in the presence of a large density of such impurities is due primarily to hopping through these states which results in the well known $T^{-1/4}$ law of conductivity [47].

2.7 IONIC CONDUCTION

Mobile ionic charge in a-SiO_2 arises normally due to the presence of ionised alkali metal atoms the most important of which are sodium and potassium. These ions are metallic and therefore positively charged. Of all mobile ionic charge sodium is of greatest concern because of its rapid transport in SiO_2 and its natural abundance in the environment. Not all the sodium incorporated in the oxide is mobile however, some of it is chemically bound in the SiO_2 lattice and thus remains electrically inactive [48,49]. For equal concentrations, lithium is the most mobile alkali metal ion in SiO_2 followed by sodium and then potassium. Despite its rapid transport in SiO_2 lithium is not an important contaminant because of its scarcity in the environment and the electrical activity of potassium is thought to be at least an order of magnitude less than that for sodium.

These ions, on entering the oxide commonly reside at the metal-SiO_2 interface or at the Si-SiO_2 interface where they may have drifted under the influence of an applied electric field. From photoemission experiments, Williams [50] was able to locate the position of drifted sodium ions to be between 10-100Å from either interface but Di Maria [51] later modified this to 50Å.

Drift occurs because sodium ions are mobile in SiO_2 at relatively low temperatures. The number of ions which drift in SiO_2 is governed by emission from the interface where the sodium is initially present. In order to drift across the oxide the ions must first overcome any interfacial energy barriers.

In a study of bias-temperature measurements, Hofstein [52] showed that the drift of sodium ions from the silicon to the metal was more rapid than that from the metal to silicon and Stagg [53], on the basis of simple assumptions of constant drift velocity and negligible influence of the ionic charges themselves on the field, was able to show that measurements of transit time in dry oxides indicated an activated bulk mobility of

the form,

$$\mu = \mu_o \exp(- E_A/kT) \tag{2.34}$$

For sodium, this gives a value for E_A of 0.66eV and a mobility of about $4\times10^{-12}cm^2(Vsec)^{-1}$ at room temperature while E_A is about 1.1eV for potassium [53,54].

At temperatures below 390^oC the sodium ions may be cycled back and forth between the silicon and metal electrodes because they do not exchange charge with either electrode nor do they discharge even though they accumulate to within tunnelling distances of the electrodes [51,55]. This inability to discharge along with the relatively high mobility of sodium ions in SiO_2, (e.g. an applied field of 10^5Vcm^{-1} will cause Na^+ ions to drift across a sample 1μm thick, in 250sec.) causes gross instabilities in silicon devices as experienced by for example, Khang and Atalla [56] when they first demonstrated the MOS field effect transistor. It was however, Kerr et al [57] who showed that the instabilities were actually caused by ionic drift in the oxide under the influence of an electric field and Snow et al [58] finally identified the species as sodium ions.

The most direct and sensitive methods of determining the presence of mobile ionic charge are (i)the C-V method, and (ii) the triangular voltage sweep method. The validity of these techniques have been discussed in great detail by Nicollian and Brews [59].

2.8 CONCLUSIONS

In this chapter the subject of conduction mechanisms and electrode effects have in general been presented as separate issues. In a real material one or possibly more of these phenomena can occur at the same time. The occurrence jointly of one or more of these effects is very much dependent on the material in question, the conditions under which the experimentation is carried out and the reproducibility of the material.

In the chapters which follow, the ideas developed here are called upon in an attempt to interpret the results of this investigation and relate them to the results and interpretations, of other workers.

2.9 REFERENCES

(1) J.J. O'Dwyer, J. Appl. Phys. 40, 3887 (1969).

(2) N.F. Mott, Phil. Mag. 24, 911 (1971).

(3) J.G. Simmons, J. Phys. Chem. Solid. 32, 1987 (1971).

(4) J.G. Simmons, J. Phys. Chem. Solid. 32, 2581 (1971).

(5) A.K. Jonscher, "A.C. conductivity and high field effects", in Electronics and structural properties of amorphous semiconductors (eds. P.G. Le Comber and J. Mort), Academic Press, 329 (1973).

(6) K.C. Kao and W. Hwang, in "Electrical Transport in Solids" (Int. series in the science of the solid state) Pergamon, (1981).

(7) J.G. Simmons, Appl. Phys. Lett. 6, 54 (1965).

(8) J.G. Simmons, Phys. Rev. Lett. 15, 967 (1965).

(9) P.R. Emptage and W. Tantraporn, Phys. Rev. Lett. 8, 267 (1962).

(10) J. Frenkel, Phys. Rev. 36, 1604 (1930).

(11) R. Stratton, J. Phys. Chem. Solids. 23, 1177 (1962).

(12) E.L. Murphy and R.H. Good, Phys. Rev. 102, 1464 (1956).

(13) J.G. Simmons, J. Appl. Phys. 34, 238 (1963).

(14) J.G. Simmons, J. Appl. Phys. 34, 1793 (1963).

(15) J.G. Simmons, J. Appl. Phys. 35, 2655 (1964).

(16) McColl and Mead, Trans. Met. Soc. AIME, 233, 502 (1965).

(17) J. Schewchun, A. Waxman and G. Warfield, Solid-State Electron. 10, 1665 (1967).

(18) W.E. Dahlke and S.M. Sze, Solid-State Electron. 10, 865 (1967).

(19) J.G. Simmons, Phys. Rev. 166, 912 (1968).

(20) T.E. Hartman, J.C. Blair and R. Bauer, J. Appl. Phys. 37, 2468 (1966).

(21) M. Stuart, Phys. Stat. Sol. 23, 595 (1967).

(22) J. Frenkel, Phys. Rev. 54, 647 (1938).

(23) C.A. Mead, Phys. Rev. 128, 2088 (1962).

(24) J.G. Simmons, Phys. Rev. 155, 657 (1967).

(25) A.K. Jonscher, Thin Solid Films, 1, 213 (1967).

(26) J.R. Yeargen and H.L. Taylor, J. Appl. Phys. 39, 5600 (1968).

(27) R.M. Hill, Phil. Mag. 23, 59 (1971).

(28) P. Mark and T.E. Hartmann, J. Appl. Phys. 39, 2163 (1968).

(29) J.L. Hartke, J. Appl. Phys. 39, 4871 (1968).

(30) M. Idea, G. Sawa and S. Kato, J. Appl. Phys. 42, 3737 (1971).

(31) A. Servini and A.K. Jonscher, Thin Solid Films, 3, 341 (1969).

(32) N. Klein and Z. Lisak, Proc. IEEE 54, 979 (1966).

(33) A. Rose, Phys. Rev. 97, 1538 (1955).

(34) R.W. Smith, Phys. Rev. 97, 1525 (1955).

(35) M.A. Lampert, Phys. Rev. 103, 1648 (1956).

(36) M.A. Lampert, Rept. Progr. Phys. 27, 328 (1964).

(37) R.H. Tredgold, "Space charge conduction in solids", Elsevier London, (1966).

(38) N.F. Mott and R.W. Gurney, "Electronic Processes in Ionic Crystals", (Oxford: Clarendon Press, 2nd edition) p.168-173, (1950).

(39) R.W. Smith and A. Rose, Phys. Rev. 97, 1531 (1955).

(40) M.A. Lampert and P. Mark, "Current injection in solids" Academic Press, (1970).

(41) A. Touraine, C. Vautier and D. Carles, Thin Solid Films. 9, 229 (1972).

(42) M. Schadt and D.F. Williams, J. Chem. Phys. 50, 4364 (1969).

(43) D.C. Hoestercy and G.M. Letson, J. Phys. Chem. Solid. 24, 1609 (1963).

(44) A. Sussman, J. Appl. Phys. 38, 2738 (1967).

(45) P. Mark and W. Helfrich, J. Appl. Phys. 33, 205 (1962).

(46) A.K. Jonscher and R.M. Hill, Physics of Thin Films. 8, 169 (1975).

(47) See Reference 46 and references therein.

(48) E. Kooi and M.V. Whelan, Appl. Phys. Lett. 9, 314 (1966).

(49) H.G. Carlson, G.A. Brown, C.R. Fuller and J. Osborne, Phys. Fail. Electron. 4, 390 (1966).

(50) R. Williams, J. Appl. Phys. 37, 1491 (1966).

(51) D.J. Di Maria, J. Appl. Phys. 48, 5149 (1977).

(52) S.R. Hofstein, IEEE Transact. Electron. Devices, ED-14, 794 (1967).

(53) J.P. Stagg, Appl. Phys. Letts. 31, 532 (1977).

(54) R.J. Kriegler, 12^{th} Annual Proc. Reliability Phys. pp250-258 (1974).

(55) N.J. Chou, J. Electrochem. Soc. 118, 601 (1971).

(56) D. Khang and M.M. Atalla, "Silicon-Silicon dioxide field induced surface devices", paper presented at IRE-AIEE Solid State Device Research Conf. Carnegie Inst. of Techn. Pittsburgh, Pa. (1960).

(57) D.R. Kerr, J.S. Logan, P.J. Burkhardt and W.A. Pliskin, IBM. J. Res. Dev 8, 376 (1964).

(58) E.H. Snow, A.S. Grove, B.E. Deal and C.T. Sah, J. Appl. Phys. 36, 1664 (1965).

(59) E.H. Nicollian and J.R. Brews, "MOS Physics and Technology", (Wiley and sons, Inc.) (1982).

CHAPTER 3

THE FORMATION OF THIN FILMS OF SILICON DIOXIDE AND THEIR APPLICATION IN DEVICES.

3.1 INTRODUCTION

As a result of the various applications of insulators for passivation and protection of large scale integrated devices(LSI), several methods of dielectric deposition have evolved [1].

It is the objective of this chapter to focus on the deposition processes of those dielectric films which form an integral part of any completed device and which play an important role in its operation. These include both *active* films such as the channel dielectric in MOS devices and *passive* films such as encapsulants. The properties of these films are of great interest in determining the electrical characteristics of devices since they are required to have high breakdown strengths, high resistivities and reasonable chemical inertness. Attention is focussed on three of the most commonly used techniques of producing dielectric films of SiO_2 namely,(1) thermal oxidation, (2) chemical vapour deposition(CVD) and (3) the technique of particular interest to this work, r.f. sputtering.

It may also be noted that the choice of technique is dictated by the properties of the film desired, temperature limitations of the substrate, uniformity of the film, its compatibility with preceding and subsequent processing steps and finally but not least, the cost of production.

3.2 THERMAL OXIDATION

The oxidation of single crystal silicon (Si) has perhaps been the most intensively investigated topic over the last 30 years, and there is a very large literature on the subject [2-5].

Thermal oxides are prepared by the high temperature oxidation of Si in ambients of dry oxygen, wet oxygen or steam [2,6]. The fundamental chemical reaction which determines the production of SiO_2 may be expressed as

$$Si\ (solid) + O_2 \rightleftharpoons SiO_2 \tag{3.1}$$

in the case of oxidation in pure oxygen, and as

$$Si\ (solid) + 2H_2O \rightleftharpoons SiO_2 + 2H_2 \tag{3.2}$$

for oxidation in water vapour.

These oxidation reactions take place in three consecutive steps, all of which are influenced by external conditions; (1) transport of the oxidising species from the ambient to the surface of the solid; (2) transport across any oxide layer present† toward the

† At room temperature there is always present on the silicon surface, a thin natural layer of oxide.

reaction site; (3) reaction with the Si at the Si-SiO_2 interface to form a new layer of SiO_2.

Numerous attempts have been made at modelling the oxidation process but with little success, particularly in the lower temperature regimes (<500°C) where most expressions have been arrived at empirically [7]. It is at elevated temperatures(>700°C) where modelling has had greater success and our present understanding of the oxidation kinetics rest primarily on the work of Ligenza and Spitzer [8], Deal and Grove [9] and Pliskin [10]. It was Deal and Grove [9] who in 1965 formulated a simple linear-parabolic kinetic theory which allowed for the first time the possibility of determining physical parameters. The good fit of their model to existing data is shown in Fig.(3.1). The details of their theoretical formulation can be found in reference (11) but the general relationship for the thermal oxidation of Si is given by

$$X_o^2 + AX_o = B(t+\tau) \tag{3.3}$$

where $A = 2\,D\,(K_s^{-1} + h^{-1})$ cm.

$B = 2\,D\,C^*N_1^{-1}$ $cm^2/sec.$

$$\tau = \frac{(X_i^2 + AX_i)}{B}$$

and D - is the diffusion coefficient of the oxidant in SiO_2.

K_s - is the reaction rate constant at the Si-SiO_2 interface (cm/sec).

h - is the gas phase transport coefficient (cm/sec).

C^* - is the solubility of the oxidising species in SiO_2.

N_1 - is the number of oxidant molecules per unit volume of SiO_2.

X_i - is the initial oxide thickness-at time t = 0.

Solving the quadratic equation for X_o as a function of time t, gives

$$X_o = \frac{A}{2}\left\{\left[1 + \frac{4B(t+\tau)}{A^2}\right]^{1/2} - 1\right\} \tag{3.4}$$

There are two limiting cases for the above equation;

(i) For short times and thin oxides, when $(t+\tau)<<A^2/4B$

By expanding eqn.(3.4) to its first order term and rearranging, gives

$$X_o \simeq B(t+\tau)/A \tag{3.5}$$

This represents the *linear* oxidation regime and B/A is the *linear rate* constant. In this regime the oxidation rate is controlled by the concentration of oxidant at the silicon surface and the rapidity with which the oxidation reaction can proceed i.e. the availability of Si-Si bonds.

(ii) For long oxidation times and thick oxides, when $t>>A^2/4B$ and $t>>\tau$.

The fraction in the brackets of eqn.(3.4) is now much greater than unity so the equation reduces to

$$X_o^2 \simeq Bt \tag{3.6}$$

and represents the *parabolic* regime where B is the *parabolic rate constant*. In this case, the rate of oxidation is limited by the availability of oxidant at the Si-SiO_2 interface which in turn is controlled by its diffusion through the oxide.

Despite the success of this model there still remain doubts regarding the overall mechanism as evidenced by the large variations in reported values of B(~50%) and B/A(~300%) [12].

Examination of eqn.(3.3) reveals that all the effects which occur at the Si-SiO_2 interface are described by only one parameter, the reaction rate, K_s which is process-dependent itself. It depends on crystal orientation [10,13,14], sodium concentration [15], substrate doping [10,16] and the amount of water vapour present [17,18]. Moreover, the identification of the oxidising species and details of the reaction still remain a matter of contention. Among the prevailing schools of thought on the nature of the diffusing species are:

(1) *That it is a negatively charged oxygen ion [9,19,20].*

(2) *That it is a neutral oxygen molecule [21,22].*

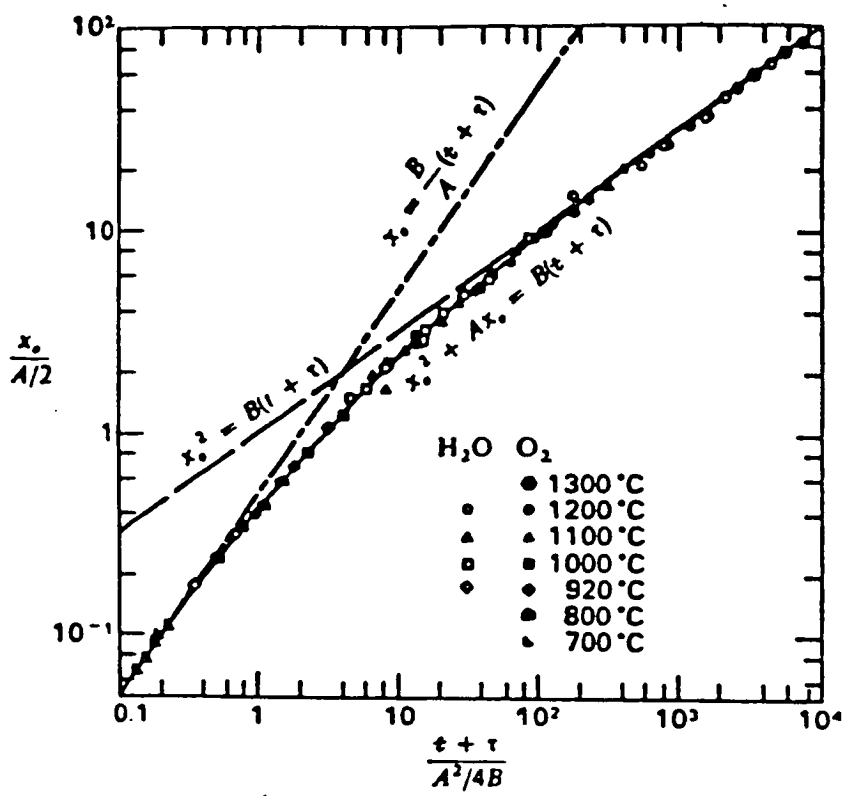

Fig 3.1 General relationship for thermal oxidation of silicon. The solid line represents the general relationship and its fit to experimental data. The dotted lines, its two limiting cases [11].

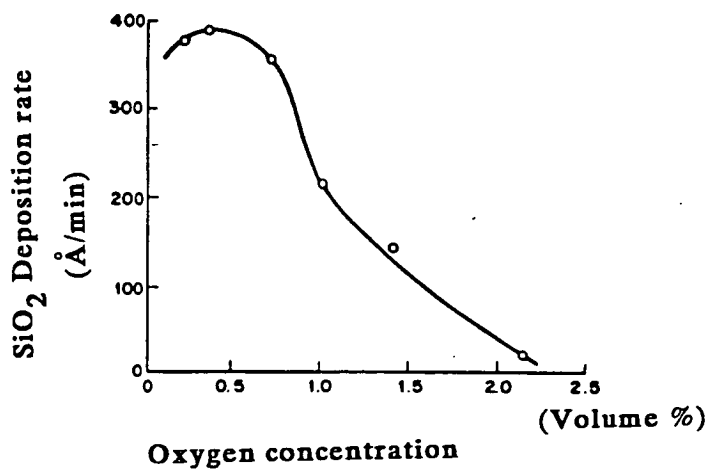

Fig 3.2 Effect of oxygen concentration on SiO_2 deposition rate. Silane concentration was 0.0845% in nitrogen carrier gas. Total flow rate was 7.1 l/min and temperature was 350°C [23].

In the case of thin oxides,($\leq$300Å) the model is moderately successful in describing the growth kinetics in H_2O/O_2 ambients but fails in mapping the growth kinetics in dry oxygen atmospheres [23].

3.2.1 The Effect of Chlorine in the Oxidation of Silicon

The addition of small amounts of a chlorine(Cl)-containing compound usually in the form of HCl, is known to increase the oxidation rate and significantly alter the growth kinetics [24-26]. Chlorine is often added to the oxidation ambient in order to grow an oxide that has a minimum sodium ion concentration, a reduced interface trap density and an increased dielectric breakdown strength [27-29].

While the physical mechanisms of HCl/O_2 oxidations are not fully understood it has been postulated that Cl atoms are incorporated into the oxide and at the interface in the the form of Si-O-Cl bonding assemblies, in which Cl takes the place of an oxygen atom [25,30-32], while the increase in growth rates have been attributed to the formation of H_2O and Cl_2 via the reaction

$$2HCl + 1/2O_2 \rightleftharpoons H_2O + Cl_2 \qquad (3.7)$$

The superior dielectric reliability of SiO_2 layers grown in Cl environments has allowed much thinner layers to be used in the semiconductor industry and at the same time allowed for faster processing.

3.3 CHEMICAL VAPOUR DEPOSITION

Chemical vapour deposition is one of the most widely used methods of preparing dielectric films for purposes of masking, electrical insulation between multilayer metallisations and the growth of single-crystal silicon on silicon substrates, commonly referred to as *epitaxial silicon*.

A very comprehensive set of reviews on CVD and its variations may be found in references [33-35] none of which will be treated here, apart from the basic ideas of CVD. The attraction of using CVD rests mainly on the following three reasons.

(1) *Its flexibility, which allows a wide range of films with varying chemical composition to be deposited on any material including silicon.*

(2) *The deposition rates are high which allows thicker films to be grown in times shorter than that required by thermal oxidation.*

(3) *The growth rates remain constant with time.*

In CVD, the desired substrates are placed on a heated support whose temperature is maintained either by a furnace or by r.f. induction heating. A gas mixture composed of the appropriate constituents is directed over the heated substrates and a chemical reaction ensues.

It was Goldsmith and Kern [36] who first showed that films of SiO_2 could be deposited by using silane, a gas which ignites spontaneously in air, an inert diluent such as nitrogen in order to control the reaction and a suitable oxidant such as O_2, N_2O or CO_2. Using this technique they revealed the useful deposition temperature for SiO_2 to be between 250-500°C, and the basic reaction to proceed as,

$$SiH_4(gas) + O_2(gas) \rightleftharpoons SiO_2(solid) + H_2O(gas) \qquad (3.8)$$

According to Nicollian and Brews [23] the deposition rate is a function of the concentration of silane, oxygen and temperature. Their results indicate that the deposition rate is nearly linearly dependent on the concentration of silane. The effect of oxygen on the deposition rate however, follows the curve in Fig.(3.2) where it can be seen that for concentrations of oxygen above 0.5% there is a decrease in the deposition rate. This is thought to be due to the increased deposition of SiO_2 on the walls of the chamber rather than on the substrate.

3.4 RF SPUTTERING OF SiO_2 FILMS

3.4.1 Historical Background

The sputtering of insulators was first attempted in 1955 by Wehner [37,38] and later the success of preparing insulating films by rf sputtering was reported by Anderson et al [39]. The process was eventually developed into a practical technique for the deposition of insulating films by Davidse and Maissel [40,41]. Since then, the growth of rf sputtering has been rapid and the subject of much attention. Although there have been several reviews on sputtering mechanisms [42,43] in general only a small fraction of these have concentrated on the sputtering of dielectrics. In this section attention is focussed on the basic parameters which influence film properties. No attempt is made however, to compare results directly because the rf sputtering process has many

variables. Emphasis will therefore be placed on the totality of events occurring at the target, in the gas discharge and at the substrate, which directly affect the properties of a film.

3.4.2 RF Sputtering Equipment

A typical rf sputtering system is shown in Fig.(3.3), it consists of a target which is subjected to ion bombardment in a glow discharge. Grounded shielding is located around the backing electrode in order to prevent the plasma and the electrode from coming into contact with one another. This contact, if it occurred, can lead to sputtering of the backing electrode, a lowering of the deposition rate and an unstable plasma condition. Both the backing electrode and grounded shielding are water cooled. The substrate holder is mounted on a platform below and argon fills the space between.

In the application of rf sputtering to the deposition of films such as SiO_2, the potential of the substrate has a strong influence on the properties of a growing film [43,44]. One technique for creating the desired potential is by coupling a portion of the rf signal to the substrate holder in the same way as it is applied to the target. This results in a negative bias on the substrate and is termed bias sputtering.

3.4.3 Target Processes

The sputtering process of *conducting materials* is known to depend on the transfer of momentum from the bombarding ion to the ejected particle [42] and it is thought likely that similar processes prevail in the case of insulating materials.

In order to sputter a material, rf power is applied to the top electrode and this sets up a plasma made up of positive argon ions. Due to their relatively high mobility the electrons which are liberated as a result of the ionisation are swept out of the plasma. These electrons are subsequently attracted towards the target during one half-cycle of the field where they remain during the other half. This rectifying behaviour gives rise to a negative potential at the target, to which the positive argon ions are drawn, resulting in the emission of secondary electrons which are then accelerated towards the substrate. Among a number of other species which are generated, positive target ions are also produced. However, the probability that a positive target ion will escape the negative field at the target surface is thought to be much less than 0.01 [45,46]. According to Benninghoven [47] this fraction is larger for compounds than for

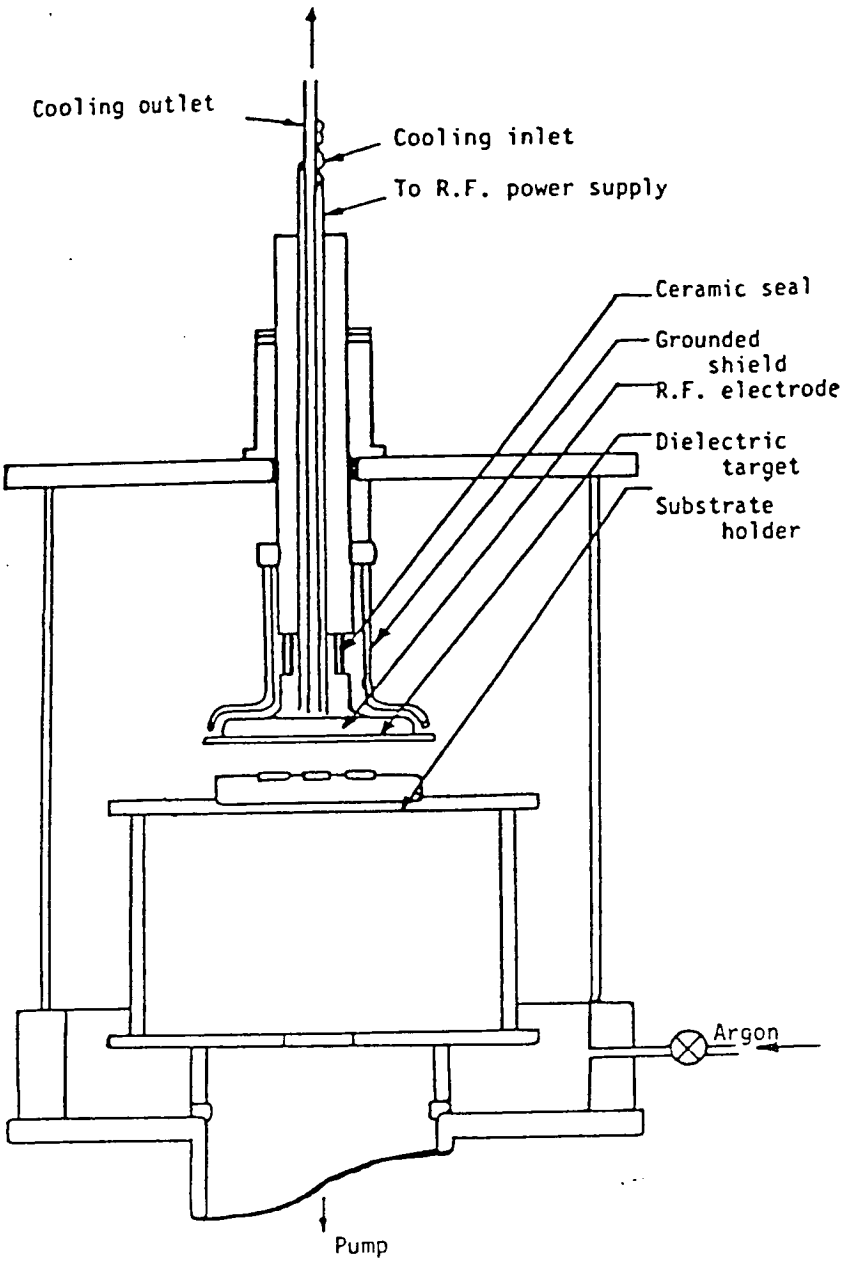

Fig 3.3 The rf sputtering system. Essential features of an rf sputtering arrangement [42].

monoatomic targets. The reason for this is that the primary bombarding ions tend to breakdown compounds into both positive and negative ions which are then sputtered.

A significant proportion of the energy of the primary bombarding ions is dissipated in the target as heat. Estimates put this as high as 75-90% [48,49]. Added to this is the heat generated due to the dissipation of rf power in the target. Target heating can easily cause sublimation of volatile species and bulk diffusion which alter the target surface composition. It also gives rise to grain growth and as the size of the grains increase wider grain boundaries are formed which tend to oxidise and trap impurities. These impurities are eventually sputtered and can have a profound effect on the composition of the deposited film as well as the sputtering rate [43].

Jackson [42] has indicated that in general the sputtering yield (i.e. the number of target atoms emitted per bombarding ion) is proportional to ion energies in the range 0-10KeV and varies linearly in the range 100-1000eV. The sputtering yield is also influenced by the angle of incidence and it increases for increasing angles of, 40^{o} to 80^{o} from the normal. On the basis of Tsui's [50] work on SiO_2 it is clear that at low power densities (approximately 25 KWm^{-2}) the sputtering rate is linearly proportional to the power density. Earlier work by Jones and co-workers [51] has shown that the sputtering rate is also affected by the addition of small traces of oxygen in the sputtering environment. In fact, the addition of oxygen in the range of a fraction of a percent to a few percent reduces the sputtering rate of SiO_2 in 10^{-3} torr Argon by nearly 50%. This dependence of the sputtering rate on the partial pressure of added oxygen has been attributed to changes in the impingement rate of gaseous oxygen and to the chemical absorption of oxygen onto the surface, resulting in a lowering of the sputtering rate of silicon atoms.

On arrival at the substrate any energy that the atoms from the target may possess, after collisions with the sputtering gas atoms, is released in the form of heat. Associated with this impingement of atoms upon the substrate are three phenomena.

(1) *Re-emission of the deposited material.*

(2) *Heating of the substrate and film.*

(3) *Radiation damage to the substrate and film.*

In the following sections each of these processes are examined in more detail.

3.4.4 Re-emission

According to Jones et al [52], one of the main parameters which has a direct influence on the rate of accumulation of a film is the re-emission coefficient. It is usually defined as the fraction of impinging particles which are re-emitted from the surface of a growing film. Through its influence on the rate of accumulation, any variation in the re-emission coefficient affects both the chemical purity and quality of a film. Fig.(3.4) shows the average dielectric breakdown strength of an SiO_2 film vs the re-emission coefficient. Jones has distinguished three factors which have an influence on the re-emission mechanism of sputtered SiO_2.

(1) *When high negative d.c. potentials exist on a deposit surface, re-emission results from sputtering caused by positive ions drawn out of the rf glow discharge. Such potentials can exist with deposited silicon dioxide because it is an insulator exposed to a high energy flux from the discharge.*

(2) *High energy neutral atoms or molecules that arrive at the surface also contribute to re-emission. The re-emission may be due to re-sputtering or the inability of the deposit to absorb high kinetic energy particles.*

(3) *Finally, there is also operative a residual mechanism which gives rise to a re-emission coefficient even when there is no potential on the film or substrate.*

Through the first comprehensive work on re-emission phenomena, Maissel and Co-workers [53] showed that a high re-emission coefficient is essential if good quality films are desired. In their experiments, chemical tests of film quality (P† etch rate) revealed a minimum number of defects when the re-emission ratio was greater than 0.55. The low defect density was thought to be due to the re-sputtering of what would otherwise have been trapped molecules in *non-ideal* positions.

To summarise, the re-emission coefficient is influenced by several parameters and is known to decrease for increases in the gas pressure, input power, and target to substrate spacing, while it increases for increases in substrate temperature [52].

† is a selective etch consisting of 15 parts Hydrofluoric acid (49%), 10 parts Nitric acid (70%) and 300 parts water.

3.4.5 Substrate Heating

The temperature that a substrate may reach under electron bombardment is directly related to its thermal characteristics. In fact, from the early work on substrate heating, Jackson and Putner [54] have measured levels of up to 2.5KWm^{-2} for an rf power input of 1.25KW to a silica target.

Pliskin et al [55], in an attempt to understand the influence of substrate heating upon film properties, noted that SiO_2 films deposited at 450°C were far closer to the properties of thermally grown SiO_2 films than were films deposited at 100°C. On the other hand, Davidse and Maissel [40] showed that the deposition rate decreases as the substrate temperature is increased. This reduction in deposition rate however, was shown to be beneficial in terms of the dielectric properties of SiO_2. Fig.(3.5) is a plot of the dielectric properties of SiO_2 vs deposition rate as obtained by Vossen et al [56]. For deposition rates above 200Å min^{-1} the film properties degrade rapidly. Thus, the heating of a substrate whether intrinsic or otherwise can result in reduced deposition rates, structural re-ordering of the film, a reduction in the sticking coefficient and changes in stoichiometry [40,56].

3.4.6 Radiation Damage

In addition to sputtered neutral species from which films are grown, both secondary electrons and negative ions are also accelerated towards the substrate. Depending on factors such as target material, system geometry and discharge conditions some of these particles retain a substantial fraction of their original energy and can represent a source of radiation damage. Substrates and growing films are also subjected to UV and X-ray radiation from the target and glow discharge. This bombardment can either be beneficial or harmful depending on the substrate and film desired. The limited use that rf sputtered films have received, (i.e. passivating films) is undoubtedly related to effects such as bombardment and radiation damage. They cannot be entirely eliminated but can be significantly reduced by for example, annealing in an inert ambient at elevated temperatures [43,57]. The damage can also be reduced by the use of magnetron sputtering, in which the low-voltage, high-current discharge is confined to the target surface by crossed electric and magnetic fields [58]. Magnetron sources are known in many forms but for purposes of dielectric deposition the two most common ones are *Sputter Gun [59]* and the *planar magnetron [60]*.

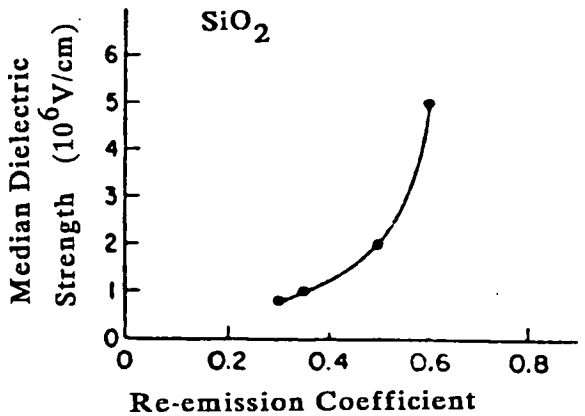

Fig 3.4 Median dielectric breakdown strength of SiO_2 films versus re-emission coefficient [43].

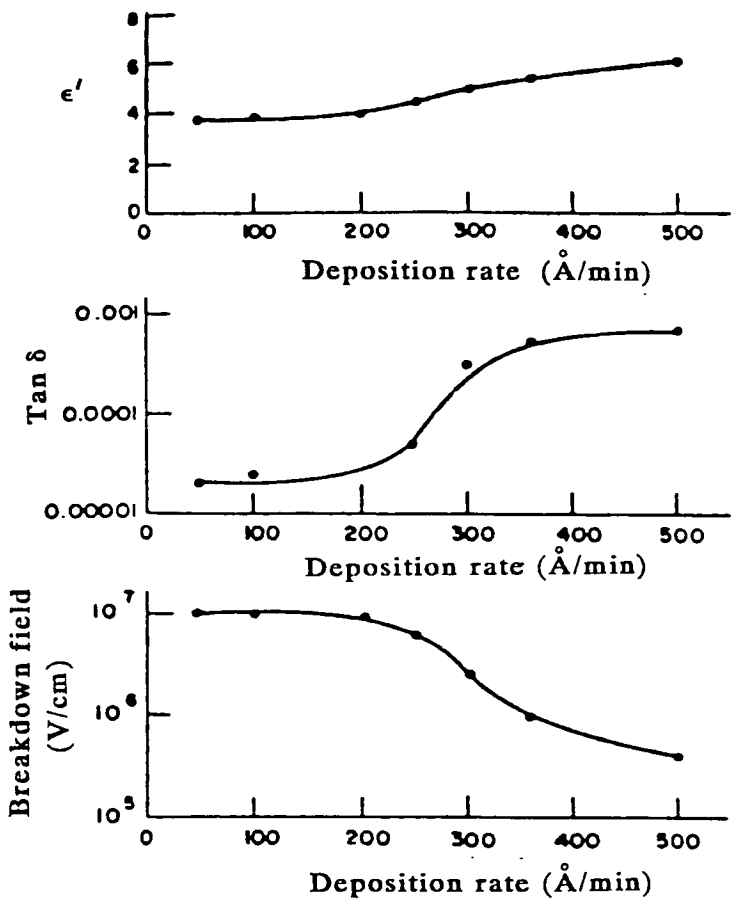

Fig 3.5 Dielectric properties of SiO_2 versus deposition rate. (Top:relative dielectric constant at 1KHz. center: dissipation factor at 1KHz. Bottom: dc breakdown field). Depositions were at temperatures of 150°C and high re-sputtering conditions [56].

3.5 ROLE OF SiO_2 IN SOLID STATE DEVICES

3.5.1 Dielectric Passivation

The electrical activity of a silicon device surface can be greatly reduced by forming a thin insulating layer on top of the semiconductor surface. This is termed *passivation* and provides protection of the surface from contamination which in turn enhances the performance, stability and reliability of the device.

Passivation coatings are categorised as primary if they are directly in contact with the silicon and as secondary when separated from the silicon by a dielectric layer.

The need for primary passivation coatings is to provide good dielectric properties, controlled immobile charge density and device stability. In fact, the most successfully passivated semiconductor is silicon with a thermally grown SiO_2 layer. Although thermal oxides are used as passivating layers in the *planar* process for forming transistors and integrated circuits(ICs) its most frequent use is as a channel dielectric in MOS devices [23,61,62].

With ICs and small-signal planar transistors a secondary passivation coating is applied over the primary passivation and metallisation [63]. Secondary passivation layers are usually oxide, glass or nitride films and their main function is to provide physical, mechanical and electrochemical protection to the metallisation and underlying structure. Secondary passivation coatings on silicon are commonly obtained by either r.f.sputtering or chemical vapour deposition (CVD). The main feature of sputtering which makes it attractive for dielectric film deposition is that it allows deposition on relatively low- temperature substrates and produces good coverage of topography.

Although CVD is used more often than r.f.sputtering for the deposition of SiO_2 layers neither CVD nor sputtered films are thought to be equivalent to those prepared by thermal oxidation unless annealed at high temperatures. It is for these reasons that both r.f.sputtered and vapour-deposited films are unsuitable for use as channel dielectrics in MOS devices. Their main use is in the form of dielectric encapsulants and ion barriers in transistors and ICs.

The resistance of dielectric films to absorption and adsorption of moisture are important aspects of passivating films and have been examined in great detail by several authors [64-66]. Moisture is an important factor because the surface conductivity of passivating materials increases by several orders of magnitude with increase in relative humidity. The result is that increased device stability is often achieved by specialised construction features which make the device less surface sensitive or, as has

been done in recent years, an increase in the use of phosphosilicate glass [67,68]. It is useful because of its ability to getter alkali ions and is particularly advantageous for MOS devices which are generally more surface sensitive compared to digital bipolar ICs.

In the following sections examples are given of some of the uses of SiO_2 for device purposes both in terms of its use as an insulator and as an active current carrying medium.

3.5.2 Charge Transport and Storage

There exist many MIS charge storage devices [69,72] in which the insulator has an active current carrying and/or charge storage role. Two such non-volatile memory devices which have received relatively greater success are the Al-Si_3N_4-SiO_2-Si (MNOS) and, Floating Gate Avalanche MOS (FAMOS) structures which rely on the storage of charge in; (1)traps at the interface of a multilayer insulator gate structure, as in the MNOS device or, (2)a thin conducting or semiconducting layer sandwiched between insulators as in the FAMOS device.

3.5.3 MNOS Memory

The memory potential of the MNOS structure was recognised by Pao et al [70] not long after the first investigations by Doo et al [71] of the potential of using Si_3N_4 as a fabrication tool.

The schematic diagram of an MNOS device is shown in Fig.(3.6). It is a dual-dielectric structure constructed of a thin (20-25Å) SiO_2 layer and a thicker (200-500Å) layer of Si_3N_4. Its operation is based on the storage of charge at the nitride-oxide interface after it has been transferred through the dielectric. This transfer of charge takes place by either of two mechanisms; the first is avalanche injection at the Si-SiO_2 interface and the second is due to tunnelling through the forbidden energy gap of the thin oxide.

The important parameter from the point of view of device applications is the growth and quality of the thin SiO_2 layer. The fabrication of such a thin layer in a reproducible manner using conventional thermal oxidation techniques is extremely difficult to control and is one of the main reasons for the limited use it has received.

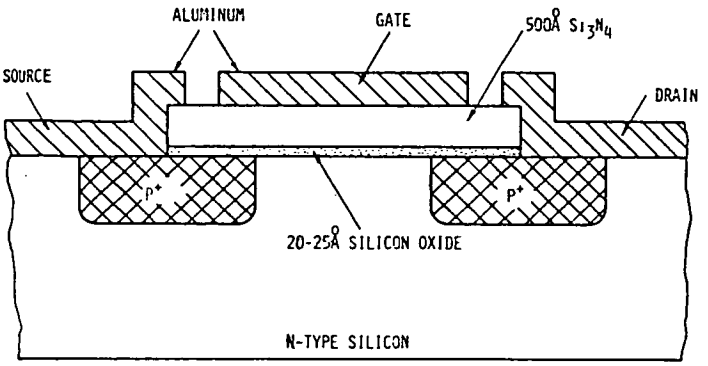

Fig 3.6 A cross-sectional view of an MNOS transistor.

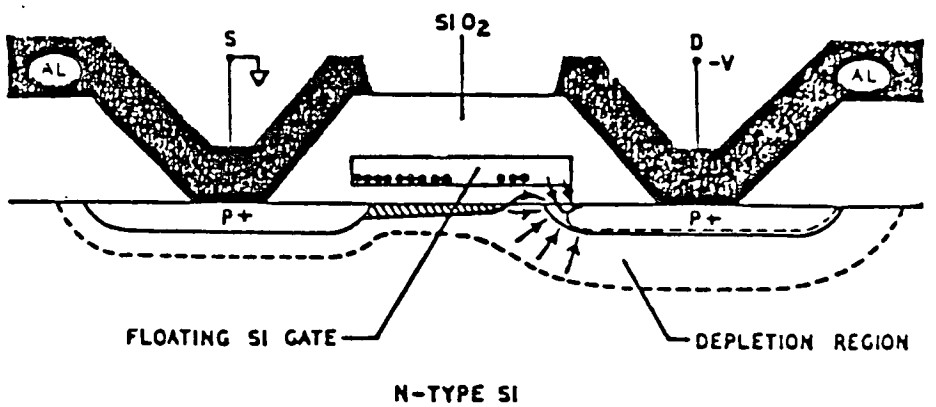

Fig 3.7 A cross-sectional view of an FAMOS device under bias.

3.5.4 FAMOS Memory Cell

The cross-sectional view of a FAMOS device is shown in Fig.(3.7). It is constructed from a p-channel silicon gate MOS insulated gate field effect device in which no electrical contact is made to the silicon gate.

The floating gate is formed by the deposition of degenerately doped n-type polysilicon over 0.1μm of thermal oxide and is isolated from the top surface by 1μm of vapour deposited oxide [72].

The memory behaviour of the cell depends on the avalanche injection of electrons into the floating gate. This is achieved by the application of an increasing negative voltage on the drain which eventually induces a surface depletion region of the drain near the SiO_2 interface. At this point some of the high energy electrons generated in the depletion region acquire sufficient energy to surmount the Si-SiO_2 energy barrier and be swept by the electric field in the SiO_2 toward the floating gate. Once the applied voltage is removed no discharge path is available for the accumulated electrons because the gate is surrounded by thermal SiO_2. The stored charge may however be removed by exposure of the device to U.V. light.

3.6 REFERENCES

(1) J.A. Amick, G.L. Schnable and J.L. Vossen, J. Vac. Sci. Technol. 14, 1053 (1977).

(2) M.M. Atalla, E. Tannenbaum and E.J. Scheibner, Bell System Tech. J. 38, 749 (1959).

(3) A.G. Revesz and K.H. Zaininger, RCA Rev. 29, 22 (1968).

(4) E.H. Nicollian, J. Vac. Technol. 8, S39 (1971).

(5) B.E. Deal, J. Electrochem. Soc. 121, 198C (1974).

(6) H.F. Wolf, in "Semiconductors"., (Wiley-interscience NY.) p.342-62 (1971).

(7) N. Cabrera and N.F. Mott, Rep. Prog. Phys. 12, 163 (1948/49).

(8) J.R. Ligenza and W.G. Spitzer, J. Phys. Chem. Solid. 14, 131 (1960).

(9) B.E. Deal and A.S. Grove, J. Appl. Phys. 36, 3770 (1965).

(10) W.A. Pliskin, IBM J. Res. Dev. 10, 198 (1966).

(11) A.S. Grove, "Physics and Technology of Semiconductor Devices". (Wiley) p.23 (1967).

(12) E.A. Irene and Y.H. Van der Meulen, J. Electrochem. Soc. 123, 1380 (1976).

(13) W.G. Spitzer and J.R. Ligenza, Phys. Chem. Solid. 17, 196 (1961).

(14) J.R. Ligenza, J. Phys. Chem. 65, 2011 (1961).

(15) A.G. Revesz and R.J. Evans, J. Phys. Chem. Solid. 30, 551 (1969).

(16) B.E. Deal and M. Sklar, J. Electrochem. Soc. 112, 430 (1965).

(17) P.J. Burkhardt and L.V. Gregor, Transt. Metall. Soc. AIME, 236, 299 (1966).

(18) E.A. Irene, J. Electrochem. Soc. 121, 1613 (1974).

(19) J.E. Thomas and D.R. Young, IBM J. Res. Dev. 8, 368 (1964).

(20) A.G. Revesz, IEEE Trans. Elect. Dev. 12, 97 (1965).

(21) Y. Nishi, Jap. J. Appl. Phys. 5, 333 (1966).

(22) R. Brucker, J. Non-Cryst. Solid. 5, 177 (1971).

(23) E.H. Nicollian and J.R. Brews, "MOS Physics and Technology" (Wiley) 675 (1982).

(24) R.J. Kriegler, Y.C. Cheng and D.R. Colton, J. Electrochem. Soc. 119, 388 (1972).

(25) Y.J. Van der Meulen and J.G. Cahill, J. Electronic Material. 3, 371 (1974).

(26) R.E. Tressler, J. Stach and D.M. Metz, J. Electrochem. Soc. 124, 607 (1977).

(27) R.J. Kriegler, Appl. Phys. Lett. 20, 449 (1972).

(28) R.J. Kriegler, Thin Solid Film. 13, 11 (1972).

(29) Y.J. van der Meulen, C.M. Osburn and J.F. Ziegler, J. Electrochem. Soc. 122, 284 (1975).

(30) K. Hirabayashi and J. Iwamura, J. Electrochem. Soc: 120, 1595 (1973).

(31) B.E. Deal, D.W. Hess, J.D. Plummer and C.P. Ho, J. Electrochem. Soc. 125, 340 (1978).

(32) B.E. Deal, A. Hurrle and M.J. Schulz, J. Electrochem. Soc. 125, 2024 (1978).

(33) J.A. Amick and W. Kern, Symposium on chemical vapour deposition, 2nd International conference.,(Electrochem. Soc. Princeton), 551 (1970).

(34) R.S. Rosler, Solid State Technol. 20, 63 (1977).

(35) See Reference No.1 and references therein.

(36) N. Goldsmith and W. Kern, RCA Rev. 28, 153 (1967).

(37) G.K. Wehner, Electronics and Electron Phys. VII, 253 (1955).

(38) G.K. Wehner, Adv. Electron. and Electron Phys. 7, 239 (1955).

(39) G.S. Anderson, W.N. Mayer and G.K. Wehner, J. Appl. Phys. 33, 2991 (1962).

(40) P.D. Davidse and L.I. Maissel, Proc. 3rd Int. Conf. on Vac. Techn. 2, 651 (1965).

(41) P.D. Davidse and L.I. Maissel, J. Appl. Phys. 37, 574 (1966).

(42) G.N. Jackson, Thin Solid Films, 5, 209 (1970).

(43) J.L. Vossen, J. Vac. Sci. Technol. 8, 512 (1971).

(44) J.S. Logan, IBM. J. Res. Develop. 14, 172 (1970).

(45) R.E. Honig, J. Appl. Phys. 29, 549 (1958).

(46) R.E. Honig, Proc. Conf. Ionization Phenomena Gases 5th Munchen., 1, 106 (1961).

(47) A.A. Benninghoven, Z. Physik. 220, 159 (1969).

(48) G.K. Wehner and G.S. Anderson, in Handbook of thin film Technology, eds. by L.I. Maissel and R. Glang. (McGraw-Hill, New York), pp.3-1 (1970).

(49) L.I. Maissel, in Ref 48, pp.4-1.

(50) R.T.C. Tsui, SCP and Solid State Technol. p.33, Dec (1967).

(51) R.E. Jones, H.F. Winters and L.I. Maissel, J. Vac. Sci. Technol. 5, 84 (1968).

(52) R.E. Jones, C.L. Standley and L.I. Maissel, J. Appl. Phys. 38, 4656 (1967).

(53) L.I. Maissel, R.E. Jones and C.L. Standley, IBM. J. Res. Develop. 14, 176 (1970).

(54) G.N. Jackson and T.I. Putner, Proc. 4th Intern. Vac. Congr. Manchester, 565 (1968).

(55) W.A. Pliskin, P.D. Davidse, H.S. Lehman and L.I. Maissel, IBM. J. Res. Develop. 11, 461 (1967).

(56) J.L. Vossen and J.J. O'Neill, RCA. Rev. 29, 149 (1968).

(57) D.V. McCaughan and V.T. Murphy, J. Appl. Phys. 44, 2008 (1973).

(58) F.M. Penning, Physica. 3, 873 (1936).

(59) P.J. Clarke, Solid State Technol. 19, 77 (1976).

(60) R.S. Nowicki, J. Vac. Sci. Technol. 14, 127 (1977).

(61) B.E. Deal, J. Electrochem. Soc. 121, 198C (1974).

(62) F.J. Feigl and S.R. Butler, in semiconductor silicon, ed. H.R. Huff and E. Sirtl (Electrochem. Soc. Princeton), 297 (1977).

(63) A.P. Gnadinger and W. Rosenweig, J. Electrochem. Soc. 121, 700 (1974).

(64) E. Arai and Y. Terunuma, J. Electrochem. Soc. 121, 676? (1974).

(65) W. Kern, RCA Rev. 32, 429 (1971).

(66) R. Castagne, P. Hesto and A. Vapaillo, Thin Solid Film. 17, 253 (1973).

(67) M.M. Schlacter, E.S. Schlegel, R.S. Keen, R.A. Lathlaen and G.L. Schnable, IEEE. Trans. Electron. Dev. ED-17, 1077 (1970).

(68) H. Sunami, Y. Itoh and K. Sato, J. Appl. Phys. 41, 5115 (1970).

(69) J.J. Chang, Proc. IEEE. 46, 1039 (1976).

(70) H.C. Pao and M. O'Connell, Appl. Phys. Lett. 12, 260 (1968).

(71) V.Y. Doo, IEEE. Trans. Electron. Devices. ED-13, 561 (1966).

(72) D. Frohman-Bentchkowsky, Solid-St. Electron. 17, 517 (1974).

CHAPTER 4

ELECTRONIC STRUCTURE AND TRANSPORT PROPERTIES OF PURE AND METAL-DOPED SILICON-DIOXIDE.

4.1 INTRODUCTION

The electrical and optical properties of pure and metal doped SiO_2 films are reviewed in this chapter and attention is drawn to aspects of what is generally accepted, from a chemical and physical point of view.

Defects in SiO_2 are examined and consideration is given only to those which are definitely known to exist. The chapter ends with some conclusions and thoughts on the present state of understanding of the effects of metal doping.

4.2 PURE SILICON DIOXIDE

4.2.1 Ideal Structure

Silicon dioxide can be grown either by the thermal oxidation or anodic oxidation of silicon, or by chemical vapour deposition(CVD). The feature common to both growth and deposition methods is that the silicon dioxide films are non-crystalline but from the standpoint of both interface and bulk properties, grown films are generally better, more reproducible and more widely used than deposited films. It is for this reason that the discussions which follow concentrate mainly on the properties of thermally grown silicon dioxide films.

The structure of all crystalline and non-crystalline polymorphs of silicon dioxide except shistovite are based on the tetrahedral configuration of four oxygen atoms to one silicon atom so that each oxygen bridges two silicon atoms. The various structural conformations of silicon dioxide arise as a result of the flexibility of the Si-O bond which is partly ionic and partly covalent and this leads to the possibility of a large spread in the Si-O-Si bond angles [1].

The main difference between the crystalline and an amorphous structure of SiO_2 is that the former possesses long range order while the latter does not. The amorphous structure of SiO_2 is also very open compared to the crystalline structure because only 43% of the space is occupied by SiO_2 molecules, making it relatively easy for a variety of electrically active impurities to enter and diffuse through it. This structural open-ness is emphasised when a comparison is made of the density of a-SiO_2, which is 2.2 compared to a value of 2.65, for crystalline quartz [1].

4.2.2 Electronic Structure of Amorphous-Silicon Dioxide

The general features of the electronic band structure of amorphous SiO_2 are thought to be similar to those of amorphous semiconductors i.e. mobility edges for electrons and holes, and a distribution of localised states extending into the forbidden gap [2]. A notable difference however is the drift mobility of electrons injected into the conduction band of SiO_2 is *unactivated* and comparatively large, $20-40cm^2(Vs)^{-1}$. This led Mott [3] to suggest that there is no mobility edge, or that the mobility edge of SiO_2 is very close to the conduction minimum- this is very different to the situation postulated for electrons in a-Si [4] or even holes in As_2Te_3 [5]. By contrast, the hole drift mobility in SiO_2 is very low (less than $10^{-5}cm^2(Vs)^{-1}$).

Early band structure calculations for the valence band suggested a narrow(3-4eV) non-bonding band formed from the oxygen lone-pair orbitals with a broader band below it due to the Si-O bonding orbitals [6] and this was later confirmed by X-ray photoelectron spectroscopy (XPS) [7]. Firm experimental evidence for the magnitude of the bandgap has not been forthcoming with estimates varying from 9-11eV [3].

4.2.3 Defects in Amorphous-Silicon Dioxide

Silicon dioxide is a wide bandgap insulator whose defects are similar to another class of materials, the chalcogenides. Like chalcogenides, the two-fold coordination of oxygen (O) in SiO_2 gives it an $p\pi$ upper valence band which makes it possible for valence-alternation pair defects to form [3] and as a wide-gap insulator, radiation can produce electron-hole pairs which result in atomic displacements rather than simple recombination. This means that both vacancies and interstitial-like species are possible defects in SiO_2[8].

Before proceeding, it is worth clarifying what is meant by defects in the context of this discussion. Defects, are conceived of as sites which produce states deep in the gap of the insulator, enabling the major disorders such as broken bonds and/or large bond length changes to be isolated from other types of perturbations which produce only band edge fluctuations.

At the present time there are thought to be four types of defects at or near the $Si-SiO_2$ interface which are responsible for interface traps [1]. Each of these is considered below.

The oxidation of Si can give rise to trivalent Si atoms, or Si in excess of the stoichiometric amount at the interface, due either to incomplete oxidation or the

generation of vacancies in the Si [1]. In this type of defect the Si atom shares three of its four valence electrons with neighbouring Si atoms whilst the fourth bond acts as a hole trap which becomes positively charged after hole capture and remains neutral when empty.

In a normal SiO_2 lattice, oxygen forms a bridge between two Si atoms. If one of the Si-O bonds is broken a *nonbridging oxygen* is formed and its unsatisfied valence bond then acts as an electron trap which becomes negatively charged upon electron capture but remains neutral when empty [8]. There are essentially three reasons for the presence of nonbridging oxygen or oxygen in excess of the stoichiometric amount near the Si-SiO_2 interface.

(1) *Excess oxygen associated with the oxidation may form nonbridging oxygen defects.*

(2) *The formation of this defect might relieve strain at the interface.*

(3) *There are water-related electron traps near the interface which may be related to the nonbridging oxygen defects.*

The third type of defect is an impurity atom. Strain at the interface creates a potential minimum for impurities, permitting the relatively open SiO_2 lattice to accommodate many such species [1].

The fourth type of defect is an oxide charge near the interface which induces an attractive coulombic potential well in the Si and there is evidence that sodium ions drifted to the Si-SiO_2 interface at low temperatures induce an interface trap band near the conduction band edge [9].

The creation and excitation of defects by irradiation in both amorphous and crystalline SiO_2 has been studied extensively by Griscom and several other authors [10,11].

Ionising radiation can free electrons from bonds directly, causing the bonds to break. Alternatively, electrons and holes produced optically or by radiation may themselves induce defect reactions if their energy is localised. The method of energy localisation is important and arises from extrinsic trapping at defects or intrinsic (self) trapping.

Extrinsic trapping occurs if a carrier is trapped by a state in the gap associated with a defect. For example, a Si-Si bond gives rise to a gap state. The trapping of a hole at this bond results in bond rupture and the creation of a neutral trivalent silicon and a positively charged trivalent silicon.

Electron spin resonance (ESR) has commonly been used to study defects in a-SiO_2 and three paramagnetic centres have consequently been identified; they are the non-bridging hole centre O_i^o, the peroxyl radical $-O-O^o$, and the E' centre shown in Fig.(4.1) [8]. The type of ESR centre depends on the water or hydrogen content of SiO_2 and in wet oxides the common oxygen defect is the non-bridging oxygen which has also been identified by Galeener et al [12] as the origin of a sharp line at 606cm^{-1} in their Raman studies of wet vitreous SiO_2. In dry SiO_2 the peroxyl radical is the common defect. The E' centre consists of a non-bridging oxygen and a trivalent Si atom formed when an Si-O bond is broken and this is the centre which has also commonly been associated with the 5.4eV optical absorption band [8].

Mott in 1977 [3], undertook a thorough survey of the evidence for and against the existence of all reported defects. Aided with the concept of charged and neutral dangling bond defects originally conceived by Street and Mott [13] for chalcogenides, he was able to locate the position of some of the above defects in the SiO_2 bandgap. For thorough accounts of Mott's, Greaves' and Lucovsky's ideas on these defects and their positions in the bandgap see references [3,14,15].

4.2.4 DC Conduction in Amorphous Silicon Dioxide

This review will not attempt to provide an exhaustive description of all the d.c. electrical measurements on SiO_2. That would be uninstructive, given that the impurities usually present are often unknown, making any discussion of the many investigations of electron traps meaningless. In fact the d.c. current-voltage behaviour of SiO_2 layers formed by the thermal oxidation of Si [16], the pyrolytic decomposition of $SiCl_4$ [17] and tetraethyoxysilane [18] has been extensively investigated. In general, the observed electrical conduction mechanisms in these films have been found to be bulk-limited by one of several mechanisms; tunnel hopping between isolated states in the forbidden gap [17]; the Poole-Frenkel effect [19]; space-charge limited currents [16] and ionic conduction [20]. Ionic conduction, often due to Na^+, has been detected in samples of high impurity content as have multiple conduction states and even switching [21]. Silicon-dioxide also exhibits electrode-limited conduction. Such mechanisms include Fowler-Nordheim tunnelling [22] and Schottky emission [23]. The important point to emerge from all these investigations is that the experimental results vary widely with the method of preparation and sample purity.

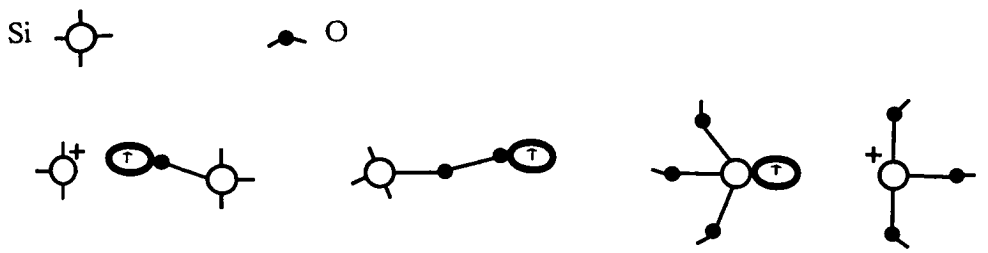

(a) (b) (c)

Non-bridging hole centre **Peroxyl Radical** **E′ centre**

Fig 4.1 Three paramagnetic centres: (a) non-bridging hole centre - associated with a proton; (b) peroxyl radical - a hole localised on the π orbital of the terminal oxygen and (c) E′ -centre - an oxygen vacancy [8].

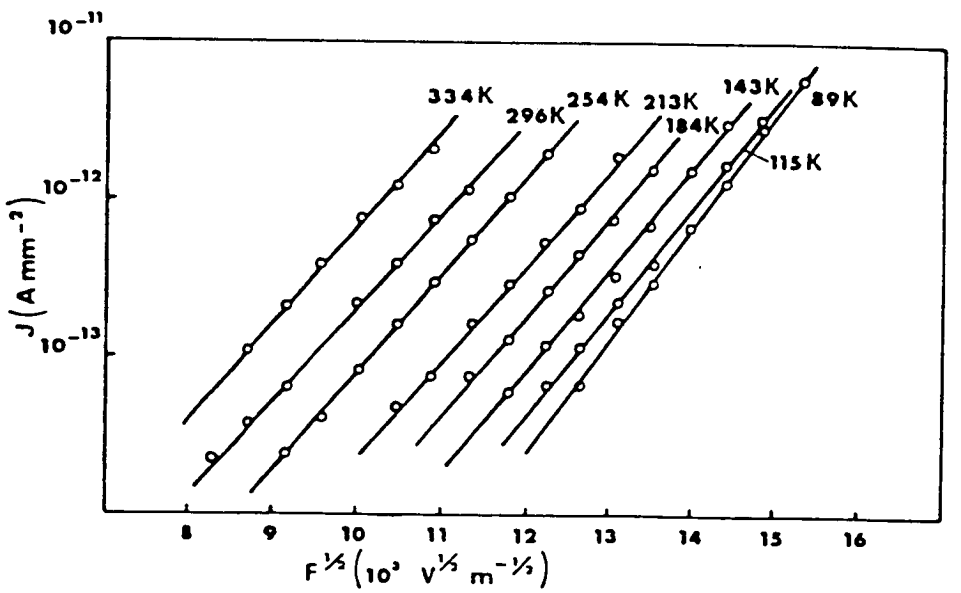

Fig 4.2 J versus $F^{1/2}$ characteristics at various temperatures (sample $P_{10}C_3$, of thickness 2100Å) [26].

Although there are several publications on rf sputtered films, these are often devoted to investigations of the influence of experimental conditions on thickness, density, structure and composition [24,25]. The only comprehensive set of electrical transport measurements that have been conducted on rf sputtered SiO_2 films were reported by Meaudre and Meaudre [26]. They have studied the d.c. current-voltage behaviour of Au-SiO_2-Au structures on silica substrates in a temperature range 77-370K, after annealing in vacuum at 573K for two days. Electron diffraction and infrared spectra were employed in order to establish the amorphous nature of the films. Helium-ion back-scattering analysis was also used to determined the film stoichiometry which varied between $SiO_{1.95}$ and $SiO_{2.03}$. Their results generally fitted well with plots of lnJ versus $F^{\frac{1}{2}}$, as seen in Fig(4.2), but mechanisms such as the P-F effect, hopping of carriers between localised states and hopping of carriers between coulombic centers failed to account for all of the important features of the data. Nevertheless, the current densities obtained by extrapolation of high-field data to zero field fitted well with plots of $T^{-1/4}$ and $T^{-2/5}$, Fig.(4.3). These particular type of relationships are commonly observed when the conductivity results from variable-range hopping of electrons and polarons respectively, at low fields. Indeed, Meaudre and Meaudre preferred to explain their data in terms of variable range hopping of carriers in percolation paths. Their reasoning, both from ac measurements and the non-linear dc behaviour, goes as follows. Mott [3] has located the negatively charged non-bridging oxygen ion, D^-, at 4.4eV below the SiO_2 conduction band, and a distortion energy W_p of 0.8eV has been associated with D^0 acceptors. The barrier height at the Au-SiO_2 contact is 4.1eV which means that the D^- level located at approximately the same energy below the SiO_2 conduction band constitutes a favourable position for dc conduction through the film. Meaudre and Meaudre have estimated a lattice distortion energy of approximately 0.7eV for the D^0 acceptors, therefore a possible conduction mechanism is hole-like polaron hopping in percolation paths between electrodes according to

$$D^0 + D^- \rightarrow D^- + D^0$$

This hopping behaviour is represented in Fig.(4.4).

What Meaudre and Meaudre have essentially shown is that electronic transport in rf sputtered films is controlled by non-bridging oxygen defects, D^-, D^+ and D^0, first proposed by Mott for a-SiO_2 at the Si-SiO_2 interface. The densities of these defects, since the films were irradiated during rf sputtering and then received only low temperature treatments, are thought to be large and more than, for example, thermally

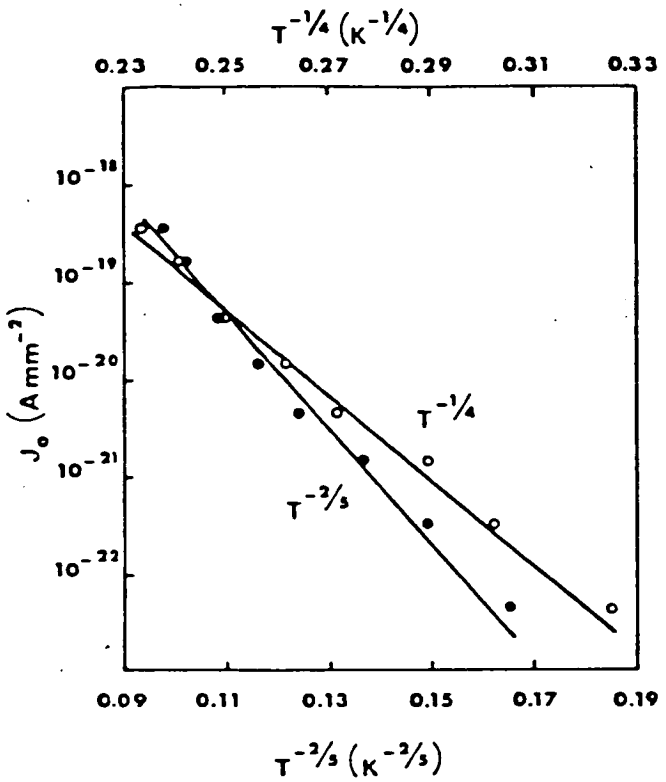

Fig 4.3 J_o vs $T^{-1/4}$ and $T^{-2/5}$. J_o is the current density obtained by extrapolation of the curves of Fig.(4.2) [26].

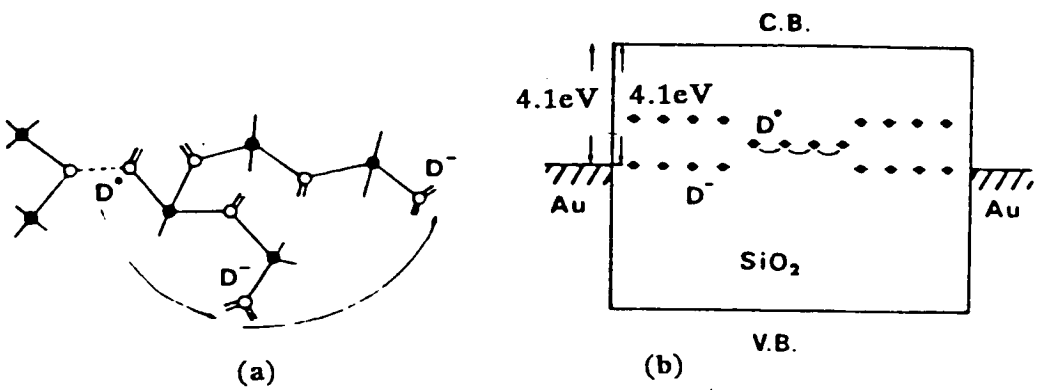

Fig 4.4 (a) Hole-like polaron hopping between D^- centers in percolation paths connecting the two electrodes according to $D^O + D^- \rightarrow D^- + D^O$. (a) Transport process; (b) energy levels [26].

grown SiO_2. According to Mott [3], this is to be expected but should be greatly reduced by annealing at much higher temperatures instead of the 573K used by Meaudre and Meaudre.

4.2.5 Electroforming

It has been well established that both thin and thick oxide films when sandwiched between a wide range of metal electrodes undergo an electroforming process before exhibiting voltage-controlled negative resistance, switching and memory effects and, occasionally, electron emission into vacuum and electroluminescence [27].

Before forming, samples subjected to high electric fields commonly display a log $I \propto V^{\frac{1}{2}}$ relationship, where I is the current through the sample and V the applied voltage [27]. Such behaviour has often been taken to indicate either Schottky or P-F conduction but as suggested in chapter 2 this interpretation has been the subject of much controversy [28].

Forming is initiated by the application of a voltage in excess of the forming voltage V_F and is an essentially permanent change in the conduction properties of the material. For silicon rich oxides, Verderber et al [29] have indicated a forming voltage of about 5V which remains independent of insulator thickness (for thickness <3000Å) and during forming the device currents increase by up to eight orders of magnitude, typically from 10^{-10}A to 10^{-2} at 1V.

A number of theories have been proposed to account for such behaviour. The theories of Simmons et al [30] and Hickmott [31,32] assume the presence of localised energy levels within the forbidden band of the insulator and conduction is taken to occur by tunnelling from one site to another. In the theory of Hickmott, the sites are present in the insulator after device fabrication and forming is the process by which these states are ionised. Verderber et al [29] suggest that the sites are metal ions injected into the insulator from the electrode to form positive centres between which tunnelling can occur. By utilising Rutherford Back Scattering, Dearnaley et al [33] were unable to detect gold(Au) ions in SiO_x with Au electrodes. This led them to subsequently suggest a polyfilamentary conduction model, where forming is the creation of conducting filaments which extend from the anode to the cathode. By assuming that conduction through each of the filaments is of an ohmic nature and that filaments rupture when the temperature of their weakest spot reaches a particular value, this model accounts for most of the observed effects. In particular, it takes into

account the localised nature of the conduction phenomena and the very long device memory of at least two years [34].

This filamentary model, which does not assume any specific band structure, has had considerable success in explaining various device properties and is applicable to many materials including, insulators, semi-conductors and polymer films [35].

4.2.6 Breakdown in Silicon Dioxide

Breakdown phenomena in SiO_2 have been categorised into three types:

(1) *High field, or intrinsic breakdown. This is often referred to as the breakdown of the network itself, due to bond-breaking.*

(2) *Medium field, or defect-related breakdown. This occurs before (1) above and is due to structural deformities, such as pinholes, microcracks or localised weakspots due to impurities, for example.*

(3) *Wearout. This is sometimes considered to be defect related but may occur at low and high fields and occurs only after prolonged electrical stressing.*

Dielectric breakdown often occurs at weak spots. Weak spots are features which either lower the injection barrier, enhance the field or lower the dielectric strength. Dislocations, stacking faults, traps and contaminations are all capable of influencing locally the dielectric strength of a device.

In thin-film capacitors, breakdown has been described by Klein [36] to be a multistage event consisting of (1) an initiating process followed by (2) instability and current runaway (3) voltage collapse and discharge of the electrostatic energy stored in the specimen, in a filament. Klein has also distinguished between two types of dielectric breakdown. These are electric(single-hole, self-healing, non-shorting) breakdown which is the result of electron avalanche inside the insulator causing a number of holes to appear in the material, and thermal breakdown which occurs when the power dissipation in the sample exceeds the rate at which heat can be conducted away without catastrophic temperature increases.

For capacitors having thin counter electrodes ($<1000\text{Å}$) non-shorting breakdown may occur. In this case, the highly localised currents and temperatures evaporate the electrode material around the breakdown channel, isolating the damaged area from the remaining device area. In addition to the previously mentioned events two more steps

are required for the completion of such breakdown namely (5) quenching of the hot breakdown channel and (6) recovery via a series-resistor-sample-capacitor time constant. At a certain voltage V_B, according to Klein, the breakdown rate becomes so large that complete device destruction occurs as a result of multiple single-hole breakdown and temperatures of 3000-4000K have been recorded and correlated with the electrostatic energy stored in the specimen. The process which finally destroys the device depends on the magnitude of V_B and the voltage for thermal breakdown. Whichever of the two processes occurs at the lower voltage is identified as the maximum-voltage breakdown.

Studies of non-shorting breakdown have also been conducted by Yang et al [37] as a function of crystallographic orientation in silicon. They found interesting star-shaped patterns of destruction due to asymmetry in the transport properties of charge carriers along <100> planes. Similar breakdown using nanosecond pulse techniques have been observed by Shatzkes et al [38]. They claimed however, that their low-voltage state was a true high-conductivity state of SiO_2, sustained by impact ionisation and injection from the electrodes.

The effect of sodium on breakdown has been extensively investigated since sodium is such a common impurity in MOS devices [39]. Raider et al [40] introduced sodium in their samples by NaCl evaporation and observed that breakdown occurred at lower voltages as the concentration of sodium increased.

Various theories have been proposed to explain breakdown phenomena and O'Dwyer [41] has summarised early treatments. Theories which treat a finite insulating layer and consider charge injection at the electrode-insulator interface have been examined by Forlani and Minnaja [42] and O'Dwyer [41]. Forlani et al assume that destruction is caused by avalanching electrons where the breakdown field is the field at which irreversible changes occur in the insulator. In O'Dwyer's treatment the breakdown is determined by the onset of current instability due to space-charge accumulation near the injecting contact.

Most of these models are compromises and this situation is partly related to the fact that techniques to determine densities and breakdown rates at defects are not unambiguous nor has the difference between wear-out-induced and defect-related or intrinsic breakdowns been clearly demonstrated. A particular problem has been the inability to distinguish between defect types i.e. defects with different breakdown rates.

Finally, in not one of the published works on this topic has the sample history been accounted for.

4.3 METAL DOPED SILICON DIOXIDE

4.3.1 Introduction

Ion implantation is a convenient method of incorporating impurities into the SiO_2 lattice but it creates many trapping centres in the oxide due the damage caused by ions of high energy traversing the film. If the oxide is annealed after implantation, typically at 1000°C in an inert ambient such as nitrogen(N_2), most of the traps due to damage are annihilated and trapping due to sites related to the implanted species may then be studied.

Once incorporated into the oxide, impurities may be accommodated at two types of sites depending on their nature and the method of introduction. Some impurities are found to enter substitutionally, in which case they replace either silicon or oxygen atoms, while other impurities can enter the oxide either at defect sites or act as network modifiers in which case they are present as interstitials.

The incorporation of impurity centres and the presence of structural defects may be associated with the creation of new localised energy levels in the forbidden gap of the oxide which can then result in a change in the properties of the oxide. Ion implanted Al, As, P,and Au, have been studied in this manner and some of this work is reviewed in what follows.

4.3.2 Ion Implanted Aluminium (Al)

In their study of SiO_2 films implanted with Al, Young et al [43] and DiMaria et al [44] have suggested that Al related traps have electron capture cross sections in the range 10^{-15} to $10^{-18}cm^2$ and trap densities which are proportional to the implantation energy for a fixed number of implanted ions. This was surprising, since the films they examined were annealed at 1050°C for 30 min. in N_2 and most implantation damage is expected to be annealed out at these temperatures. Young et al concluded, nevertheless, that the observed trapping *must* be due to implantation damage and they further suggested that the implantation process generated vacancies which made it possible for the Al to enter the SiO_2 structure substitutionally and subsequently act as trapping centers. As the implantation energy increases the number of vacancies increases and thus the number of substitutional Al atoms also increases. The trap densities were also found to be proportional to the number of ions for a given ion energy. In their work, an ion fluence of 10^{13} ions/cm^2 gave rise to a trap density

which varied between 10^{12}-10^{13}/cm^2, depending on the ion energy. Once trapped, electrons could not be detrapped by light with energy less than 6eV.

The results of Harari et al [45] for Al implanted into 1000Å of SiO_2 in the form of MOS capacitors indicate an increase in the conductivity for Al doses of 10^{14} ions/cm^2. The conductivity was found to be dependent on the sign of the gate voltage, being a few orders of magnitude higher for a positive bias. Figure(4.5) shows the temperature dependence of the conductivity between 300 and 80K. The conductivity in the unannealed samples followed a thermally activated process which did not depend on the ion species. The fact that the conductivity showed the same temperature dependence for Al^+ and Na^+ implantations suggests that the increase in conductivity did not arise as a result of lattice modifications involving the chemistry of the implanted species but that it was a result of the lattice displacement damage caused by the implantation process. For specimens that had been annealed for 30 min. at 500°C in dry nitrogen, the Al^+ implanted samples were restored to their insulating state. Harari et al noticed that although the annealing process restored the highly insulating condition of the implanted oxide it did not return the oxide to the unimplanted condition as far as its residual trap density was concerned. Using photodepopulation [46] measurements they were able to show that after implantation and annealing, electron traps were present in the oxide but no such traps were detected in the unimplanted samples. The effect of annealing may therefore be conceived of as the removal of displacement damage caused by the implantation and/or the incorporation of the implanted ions into the lattice.

4.3.3 Ion Implanted Phosphorus (P)

Haack [47] has discussed the enhanced conductivity and change in the electronic conduction mechanism due to the implantation of phosphorus into SiO_2. Thermally oxidised SiO_2 on silicon was implanted with several implants of different doses and energies in order to obtain a constant profile of impurity density (10^{21}cm^{-3}) across the oxide layer. The implantation altered the conduction mechanism from Fowler-Nordheim tunnelling in the unimplanted samples to a modified P-F type of mechanism, which accounted not only for the effect of barrier lowering due to an applied electric field but also that due to screening of the donor level and to overlapping potential wells. Haack has tentatively suggested that the effect of implantation is to

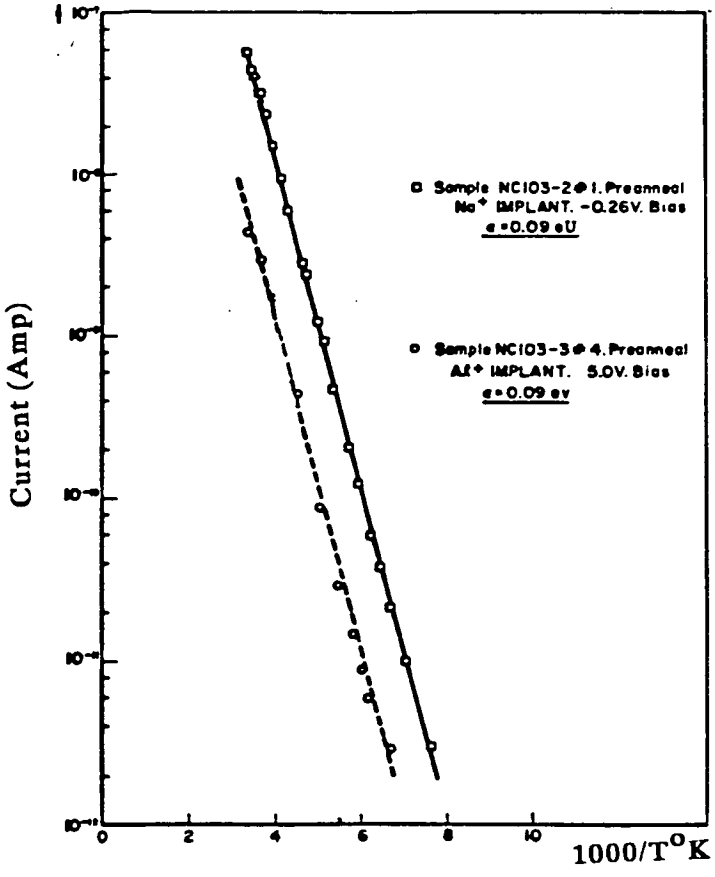

Fig 4.5 Temperature dependence of the post-implantation dark current [45].

Na^+ implant [] Preanneal E = 0.09eV.

Al^+ implant o Preanneal E = 0.09eV.

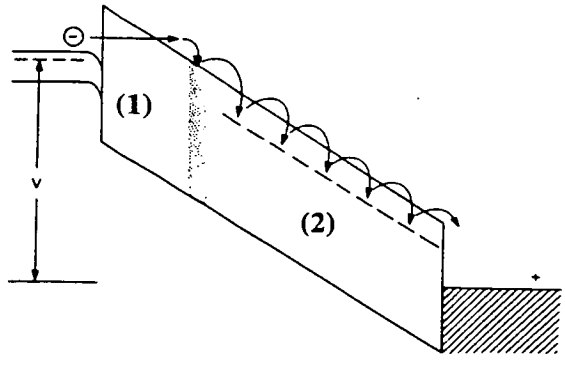

Fig 4.6 Energy band diagram of an ion-implanted MOS structure right after a positive voltage is applied to the metal electrode [51].

(1) *introduce network displacements resulting in localised states which are neutral when empty and charged when occupied and*

(2) *introduce donor states which are neutral when occupied and positively charged when empty.*

Using his modified P-F relationships, the density of electron traps due to displacement damage created during implantation were shown to decrease with annealing temperature from $N_t = 6 \times 10^{19}$ cm^{-3} in the unannealed state to $N_t = 7 \times 10^{18} cm^{-3}$ after annealing for 30 min. at 850°C. It must be noted however, that his modification of the P-F model was unable to account for the temperature dependence of the slope in the P-F plots.

Le Goascoz et al [48] have also measured the electrical conduction in samples implanted with phosphorus at levels $\geq 10^{20}$ ions/cm^2. The current was found to depend exponentially on the voltage and of the form $I = I_o \exp(\alpha V)$, where the variation in α was correlated with increases in the ion implanted dose. Annealing of the samples at 500°C for 15 min. had a considerable effect on the I-V characteristics, in particular on the value of α, which approached its initial value found in unimplanted samples.

DiMaria et al [49] have indicated that both P and arsenic(As) are very similar in their trapping-detrapping properties except for their capture cross sections (smaller for P) and sensitivity to annealing. Unlike Al, the trap densities are not a function of the implantation energy but remain proportional to the ion fluence. According to DeKeersmaecker et al [50] the implanted P does not occupy silicon sites as it does in the case when P is diffused in. Using a simple tight-binding model for substitutional impurities in SiO_2, based on the bond-orbital description of the bulk material, they were able to show that P(and As) are most likely to enter substitutionally at oxygen sites. This was confirmed by photoionisation experiments in which a threshold was observed at approximately 4eV which was consistent with a theoretical prediction of 3.7eV for substitutional P at an oxygen site. The authors acknowledged the fact that although their results suggest the traps are due to P at O sites, it was not prudent to exclude other possibilities.

4.3.4 Ion Implanted Gold (Au)

Chen et al [51] have examined carrier transport and charge storage effects in thermally grown films of SiO_2 implanted with Au ions. After annealing at 400°C, the mechanism of conduction in the region of oxide through which the ions were implanted was transformed from Fowler-Nordheim tunnelling to a bulk Poole-Frenkel mechanism. This was attributed to the creation of deep trapping centres at about 1.2eV below the SiO_2 conduction band. The band diagram, immediatedly after a positive voltage is applied to the metal electrode, is shown in Fig.(4.6). Electrons after tunnelling from the silicon into the oxide are trapped by the trapping centres located at the boundary of regions (1) and (2). The remaining electrons are then transported via the P-F mechanism to the adjacent metal electrode. According to the authors, the different transport mechanisms in the ion-implanted part of the oxide together with the ion-induced trapping centres are conducive to the storage of charge in the oxide. The difference between the flatband voltage of the implanted sample and that of a control sample serves as a measure of the effects associated with the ion-implantation. The flatband shift in Fig.(4.7) increases with increasing ion dose. This indicates that the damage caused by implantation increases the density of trapping centres at the Si-SiO_2 interface and in the oxide.

4.4 CONCLUSIONS

Although post implantation annealing temperatures in excess of 1000°C have been employed in some of the studies mentioned in this chapter, it is by no means certain that all the effects due to implantation damage were removed. In the work of Young et al [43] on Al related traps it was surprising to note that even after annealing at 1050°C for 30min. in N_2, the density of traps remained proportional to the implantation energy. In spite of the fact that DiMaria et al [44] were able to show, with the aid of photocurrent-voltage measurements, that the centroid of electrons trapped in the SiO_2 layer as a result of Al implantation was essentially the same as that of the implanted Al, as determined by secondary ion mass spectrometry, the exact nature of these traps in relation to the implanted atoms remains unresolved.

Finally, a matter which merits closer attention is that concerning the induced density of traps as a result of ion implantation. Both As and P are in the fifth column of the periodic table and it is to be expected that their trapping/detrapping properties will be very similar although the atomic mass of P is nearly half that of As. In contrast

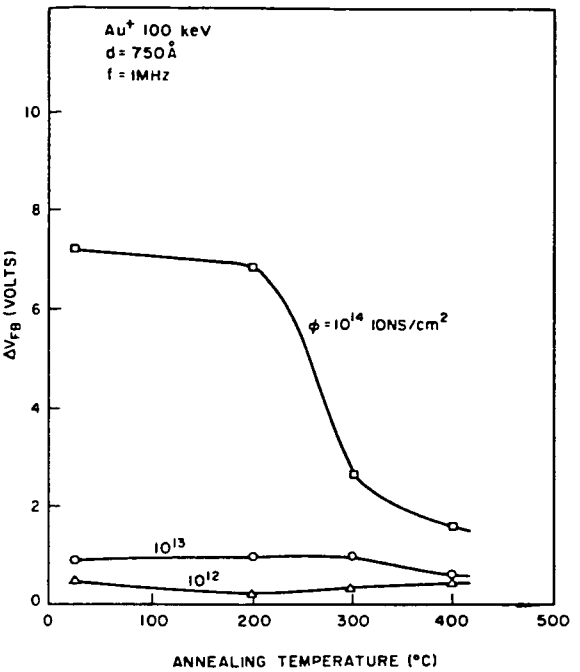

Fig 4.7 Measured flat-band voltage shifts vs annealing temperature for MOS structures with 750Å oxide layer. The Au^+ ion energy is 100KeV with doses of 10^{12},$10^{13}$and 10^{14} ions/cm^2 [51].

Authors	Element	Concentration of Implanted Element		Trap Density		Technique Used in Determining Trap Density
		ions/cm^2	ions/cm^3	ions/cm^2	ions/cm^3	
DiMaria et al [44] and Young et al [43]	Al	10^{13}	–	10^{12}-10^{13}	–	Photocurrent-Voltage and C-V.
Haack [47]	P	Equivalent to 10^{14}	10^{21}	Equivalent to 10^{12}-10^{13}	10^{18}-10^{19}	Modified Poole-Frenkel

Table 4.1 Comparison of Aluminium and Phosphorus trap densities in SiO_2.

to this, Al is in the third column of the periodic table and its properties are expected to be greatly different from those of either P or As although its atomic mass is very nearly the same as that of P. Table(4.1) summarises the data concerning the density of traps due to implantation of Al and P as obtained by DiMaria et al [44], Young et al [43] and Haack [47]. The third and fourth columns indicate the density of implanted Al and P respectively. Although the density of P was given as 10^{21}ions/cm^3 it is converted into ions/cm^2 and is shown in column three.

DiMaria et al and Young et al used the photocurrent-voltage technique in order to determine the residual trap density after annealing, whilst Haack utilised his modified P-F formulation. In columns five and six, the calculated trap densities are shown and once again in the case of Al, it is represented in terms of traps/cm^2 while in the case of P it is in terms of traps/cm^3 although its equivalent value in terms of traps/cm^2 is noted in column five.

The residual trap densities for both Al and P are *identical*. This is surprising because the implanted doses are very different and the properties of Al, which is in the third column of the periodic table, are expected to be much different from those of P. This suggests that the residual trap density for P and Al, after high temperature annealing, is not influenced much by the particular implanted element nor the dose, for ion doses $\geq 10^{13}$/cm^2. It would therefore be reasonable to suggest that although the residual trap density is not a function of the implanted element it is perhaps a property of the flexible SiO_2 network though it must be remembered that in neither case is the dose close enough to the saturation threshold of SiO_2.

4.5 REFERENCES

(1) E.H. Nicollian and J.R. Brews, "MOS Physics and Technology".,(Wiley) p665 (1982).

(2) N.F. Mott and E.A. Davis, "Electronic processes in non-crystalline materials"., (Oxford: Clarendon Press), p465, (1979).

(3) N.F. Mott, Advances in Physics., 26, 363 (1977).

(4) P.G. Le Comber, A. Madan and W.E. Spear, J. Non-Cryst. Solid., 11, 219 (1972).

(5) P. Nagels, R. Callaerts, and M. Denayer, "Amorphous and liquid semiconductors"., eds. J. Stuke and W. Brenig (London: Taylor and Francis Ltd), p869, (1974).

(6) S.T. Pantelides and W.A. Harrison, Phys. Rev. B., 13, 2667 (1976).

(7) B. Fischer, R.A. Pollak, T.H. Di Stefano ad W.D. Goodman, Phys. Rev. B., 15, 3193 (1977).

(8) J. Robertson, Phil. Mag. B., 52, 3, 371 (1985).

(9) A. Hartstein and A.B. Fowler, Phys. Rev. Lett., 34, 1435 (1975).

(10) D.L. Griscom, 'The Physics of SiO_2 and its Interfaces"., eds. S.T. Pantelides (Pergamon), p.232 (1978).

(11) M. Stapelbroek and D.L. Griscom, ibid. 263 (1978).

(12) F.L. Galeener, J.C. Mikkelsen and N.M. Johnson, ibid. p.284

(13) R.A. Street and N.F. Mott, Phys. Rev. Lett. 35, 1293 (1975).

(14) G.N. Greaves, same as reference no. 10, p.268.

(15) G. Lucovsky, Phil. Mag. B. 41, 459 (1980).

(16) R.W. Brander, D.R. Lamb and P.C. Rundle, Br. J. Appl. Phys. 18, 23 (1967).

(17) H. Krause and R. Grunler, Phys. Status Solidi A. 42, 149 (1977).

(18) L.I. Popova, B.Z. Antov and P.K. Vitanov, Thin Solid Films. 38, 247 (1976).

(19) D.E. Carlson, J. Appl. Phys. 47, 2754 (1976).

(20) J.F. Verwey, Inst. Phys. Conf. Ser. No. 50 : Chapter 1, 62 (1980).

(21) D.R. Lamb and P.C. Rundle, Brit. J. Appl. Phys., 18, 29 (1967).

(22) M. Lenzlinger and E.H. Snow, J. Appl. Phys. 40, 278 (1969).

(23) J. Bonnet and L. Lassabatere, Thin Solid Films. 22, 177 (1974).

(24) J.L. Vossen, J. Vac. Sci. Technol. 8, 5, S12 (1971).

(25) W.A. Pliskin, J. Vac. Sci. Technol. 14, 5, 1064 (1977).

(26) M. Meaudre and R. Meaudre, J. Non-Cryst. Solid. 68, 281 (1984).

(27) R.G. Gould and C.A. Hogarth, Int. J. Electron. 37, 2, 157 (1974).

(28) A.K. Jonscher, Thin Solid Film. 1, 213 (1967).

(29) R.R. Verderber, J.G. Simmons and B. Eales, Phil. Mag. 16, 1049 (1967).

(30) J.G. Simmons and R.R. Verderber, Proc. R.Soc., A301, 77 (1967).

(31) T.W. Hickmott, J. Appl. Phys. 33, 2669 (1962).

(32) T.W. Hickmott, J. Appl. Phys. 35, 2679 (1964).

(33) G. Dearnaley, D.V. Morgan and A.M. Stoneham, J. Non-Cryst. Solid. 4, 593 (1970).

(34) G. Dearnaley, Rep. Prog. Phys., 33, 1129 (1970).

(35) K.C. Kao ad H. Hwang, "Electrical Transport in Solids"., Int. Series in Science of Sol-St. Vol 14 (Pergamon) (1981).

(36) N. Klein, Thin Solid Film., 7, 149 (1971).

(37) P.Y. Yang, W.C. Johnson and M.A. Lampert, 13th Annual Proc. Reliability Phys. (IEEE, N.Y.) p10 (1975).

(38) M. Shatzkes, M. Av-Ron and R.M. Anderson, J. Appl. Phys., 45, 2065 (1974).

(39) C.M. Osburn and M. Raider, J. Electrochem. Soc., 120, 1369 (1973).

(40) S.I. Raider, Appl. Phys. Letts., 23, 34 (1973).

(41) J.J. O'Dwyer, J. Appl. Phys., 40, 3887 (1969).

(42) F. Forlani and N. Minnaja, J. Vac. Sci. Technol., 6, 518 (1969).

(43) D.R. Young, D.J. DiMaria, W.R. Hunter and C.M. Serrano, IBM J. Res. Develop., 22, 3, 285 (1978).

(44) D.J. DiMaria, D.R. Young, W.R. Hunter and C.M. Serrano, IBM J. Res. Develop., 22, 3, 289 (1978).

(45) E. Harari and B.S.H. Royce, IEEE Trans. on Nuc. Sci., N5-20, 6, 288 (1973).

(46) F.J. Feigl, S.R. Butler, D.J. DiMaria and V.J. Kapoor, in 'Thermal and Photostimulated Currents in Insulators. ed: D.J. Smyth, The Electrochem Soc. p.118 (1976).

(47) D. Haack, "Int Conf. on Amorphous and liquid Semiconductors"., ed: W.E. Spear p.673 (1977).

(48) V. Le Goascoz, J. Borel and G. Rigaux, C.E.N-G., N.T. LETI/ME, 773 (1971).

(49) D.J. DiMaria, "The Phys.of SiO_2 and its Interfaces", Proc. Int. Topical Conf. ed: S.T. Pantelides p.160 (1978).

(50) R.F. DeKeersmaecker, D.J. DiMaria and S.T. Pantelides, ibid p.189.

(51) L.I. Chen, K.A. Pickar and S.M. Sze, Solid-St. Electron., 15, 979 (1972).

CHAPTER 5

EXPERIMENTAL TECHNIQUES.

5.1 INTRODUCTION

This chapter gives a brief account of the principles of the main experimental techniques used in the present work. Where appropriate, more information is given in Chapter 6 which is concerned with the details of sample characterisation, and with the analysis and comparison of the results obtained from various techniques.

The metal-insulator-semiconductor(MOS) structures used in this work were fabricated on polished n-type silicon (phosphorus doped) of <100> orientation and resistivity, 0.6 - 1.4 Ωcm. Before deposition of the films the silicon wafers were cleaned following the schedule in Appendix I.

5.2 RF SPUTTERING OF OXIDE FILMS

Films were prepared by the sputtering of a high-purity silicon-dioxide target supplied by the Materials Research Corporation (MRC) in an MRC model 8620, 3-target sputtering chamber. The chamber was itself made of stainless steel and evacuated with a turbomolecular pump backed by a rotary pump.

The target, whose metal electrode was water cooled, was located 7.5cm above the sample platform under which was another water cooled electrode capable of being biased with a fraction of the applied rf potential, and of being heated up to 400^{o}C.

The external power supply was capable of delivering up to 1200W into a 50Ω load at 13.56MHz and its output was fed into the electrodes of the chamber via a matching network which served the dual function of matching the input impedance of the plasma to the output impedance of the supply in order to minimise reflection, and dividing the potential between the upper and lower electrodes.

The plasma was struck by introducing high-purity argon through an adjustable needle valve, and maintained at a constant pressure by balancing the pumping rate. The details of the sputtering conditions are given in Chapter 6, section (6.1).

5.3 INCORPORATION OF METAL IMPURITY

5.3.1 Introduction

Metal impurities were introduced into the oxide either by ion-implantation or, by co-sputtering the metal with silicon-dioxide.

5.3.2 Doping by RF Sputtering

Transition metal impurities, in particular vanadium, were incorporated into the films by co-sputtering with the silicon-dioxide. This was facilitated by attaching rectangular pieces of the appropriate metal to the SiO_2 target with adhesive. The concentration of the metal in the films was varied by altering the number of metal pieces attached to the target.

5.3.3 Doping by Ion-Implantation

Controlled doses of the appropriate metal were introduced into the oxide films by ion-implantation.

An ion-implanter consists basically of a mass spectrometer to separate unwanted ions from the beam, an accelerator, focussing and deflection system and an ion source. The ion source may be produced either by evaporating solid material into a plasma or by introducing gaseous material directly. The ion dose and energy with which the ions reach the target can be controlled by counting the ions as they pass a detector and by changing the voltage along the acceleration chamber, respectively [1,2].

All the implantations described in this work were carried out at AERE Harwell.

5.4 ANNEALING AND METALLISATION

After sputtering, the samples were subjected to heat-treatment in nitrogen ambients for up to 30 minutes at temperatures ranging from 200 - 900°C. A Centronics furnace with an electrically heated quartz tube, 7.5cm in diameter, capable of temperatures up to 1200°C, was used for this purpose. After annealing, (for details see Appendix II) the metal-oxide-silicon structures were completed by evaporating metal top contacts. Aluminium and gold top electrodes with areas varying from 2×10^{-3} to 3.5×10^{-2} cm^2 were deposited by evaporation from sodium free tungsten filaments through a shadow mask. Evaporations were carried out in a Nanotech evaporator in a vacuum of less than 10^{-6} *torr*. In the case of MOS capacitors, back ohmic contacts were made by evaporating nichrome and in all instances the samples were heated to 200°C before evaporation, in an attempt to improve adhesivity. In some cases, the top electrodes were defined by photolithography, the details of which are contained in Appendix II.

5.5 FILM THICKNESS MEASUREMENTS

5.5.1 Talysurf

Thickness of the sputtered films were measured with a mechanical stylus instrument (Taylor Hobson Talysurf 4). Films were sputtered onto pieces of silicon in the usual manner but with one half of the silicon slice covered with a straight edged mask. This permitted a suitably defined step for the mechanical stylus to profile.

Since the full scale sensitivity on the most sensitive range was 500nm, this method was useful as a first estimate of the film thickness.

5.5.2 Ellipsometry

Measurement of film thicknesses on silicon using ellipsometry is more common than the method outlined above. In this technique, measurement is based on the change in polarisation of a beam of plane polarised light on reflection by the oxidised surface.

An incident beam of visible light is plane polarised to have the plane of oscillation of its electric field vector inclined at 45^{o} to the plane of incidence. The ellipsicity of the reflected beam is characterised by the phase difference and amplitude ratio between the two components of electric field vector measured in and normal to the plane of incidence. Thickness and the index of refraction are then extracted from a measurement of the phase difference and the amplitude ratio of the reflected beam compared to the incident beam. This method, unlike the Talysurf, is non-destructive.

5.6 FILM ANALYSIS

5.6.1 Rutherford Backscattering

The detection of ions, neutral particles, electrons or photons emitted from a surface as a result of ion bombardment allows information on the nature of the surface to be obtained [1]. Light ions such as hydrogen and helium at energies ranging from 0.75MeV to 3MeV are considerably more penetrating than many other probes used in surface analysis [2], such as, electrons and heavy ions. This permits compositional information on the material under examination to be obtained beneath the surface to depths of a few microns. For many applications Rutherford backscattering is chosen because it probes the near surface region (0.1 - 1μm). These depths are too great for

surface analysis techniques to be of any value yet the dimensions are too small for standard bulk chemical analysis methods to be applicable [3].

Helium ions are used in preference to hydrogen for backscattering analysis because their greater mass allows superior depth and mass resolution [3]. Because the helium nucleus has no bound excited states and a very high binding energy, the backscattered spectra are not contaminated by the products of inelastic scattering and other nuclear reactions. Depth resolution may nevertheless be improved by the use of heavier ions such as carbon and oxygen but these produce considerably more damage in both targets and detectors and the eventual depth probed is much less.

Rutherford backscattering is commonly used in the investigation of surface oxides and the degree of radiation damage is generally small which makes it an ideal tool for the characterisation of thin layers, non-destructively, in terms of thickness and stoichiometry.

In the present work, RBS was used for exactly this purpose and additionally, to establish the amount of transition metal impurity in the films under investigation. All the RBS spectra presented in this thesis were run at AERE Harwell under the guidance of Drs. Dearnaley and Saint. The raw data was subsequently converted into thickness, stoichiometry and impurity concentration by the author.

5.6.2 Electron Spin Resonance

Electron spin resonance (ESR) spectroscopy or electron paramagnetic resonance (EPR) spectroscopy, as it is frequently known, is a very common investigative tool in chemical analysis. Numerous texts detailing the principles of this technique exist [4] but in what follows, only a simplified exposition of the rudiments are presented.

An electron, as a result of its spin angular momentum, possesses a spin magnetic moment which in the presence of an applied magnetic field, may split into two orientations, $m_s = \pm$ ½. The energy separation of the two spin states is given by

$$\Delta E = E_{1/2} - E_{-1/2} = 2\mu_b B$$

and shown schematically in Fig.(5.1).

If on the other hand a solid is irradiated at a fixed frequency ν the unpaired electron spins of the sample are found to resonate with the surrounding radiation when the magnetic field is adjusted such that

$$h\nu = gB_e H$$

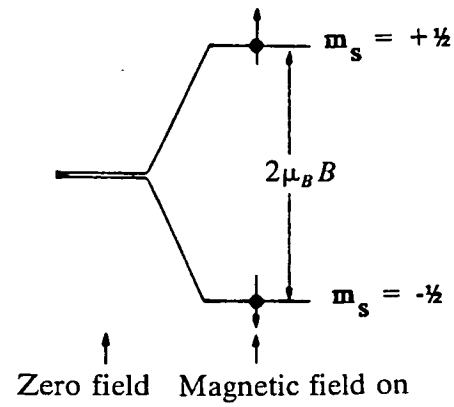

Fig 5.1 Electron spin energy levels in a magnetic field.

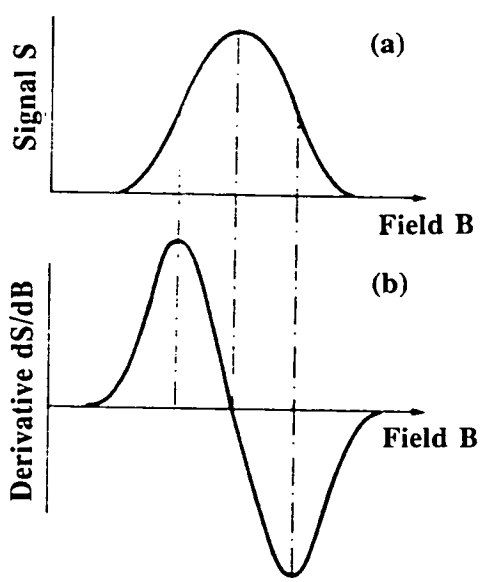

Fig 5.2 An absorption curve and its derivative.

When this condition is satisfied the spins absorb the energy strongly and this can be monitored by noting the absorption as a function of the magnetic field. A typical example is shown in Fig.(5.2) where the absorption is recorded as a first derivative. Magnetic fields of the order 0.1-1.0T are commonly employed and the radiation is in the X-band of microwaves.

Electron spin resonance of paramagnetic compounds is useful in many ways and in principle it may be observed in any system which has unpaired electrons. Two common uses of ESR are as a tool for fingerprinting because many radicals have own distinct g value and hyperfine splitting, and as a method of determining the number and orientation of groups coupling with the unpaired electron. For many radicals g lies between 1.9 and 2.1 whilst the value of g for a free electron is 2.0023.

All the ESR measurements reported in this work were carried out in the department of Chemistry, University of Edinburgh using a BRUKER ER 200D-SRC ESR machine. Measurements were conducted at room temperature and at liquid nitrogen temperatures.

5.6.3 Auger Electron Analysis

In Auger Electron Spectroscopy (AES), an incident photon or particle of sufficient energy is used to excite a core electron into a vacant state above the Fermi level. The atom containing the core vacancy then readjusts itself to fill the vacancy. Energy is conserved in the process which means that each downward transition of an electron is accompanied by the emission of an X-ray photon or, more frequently, an Auger electron [5].

This technique, is very useful for providing information concerning the composition, thickness and uniformity of a film.

The process of events following ionisation of a core level may be understood in terms of the diagram in the centre of Fig.(5.3). Consider for example, the K level as being ionised by an incident electron whose energy E_p is greater than the binding energy of the electron in level K. After the creation of a hole in this level the atom relaxes by filling the hole via a transition from an outer level, such as L_1. As a result of this transition the energy difference ($E_K - E_{L_1}$) becomes available as excess kinetic energy, and can be given to another electron either in the same level or in a more shallow level, whereupon a second electron is ejected. This process is termed Auger emission. The Auger transition depicted in Fig.(5.3), is termed the $KL_1L_{2,3}$

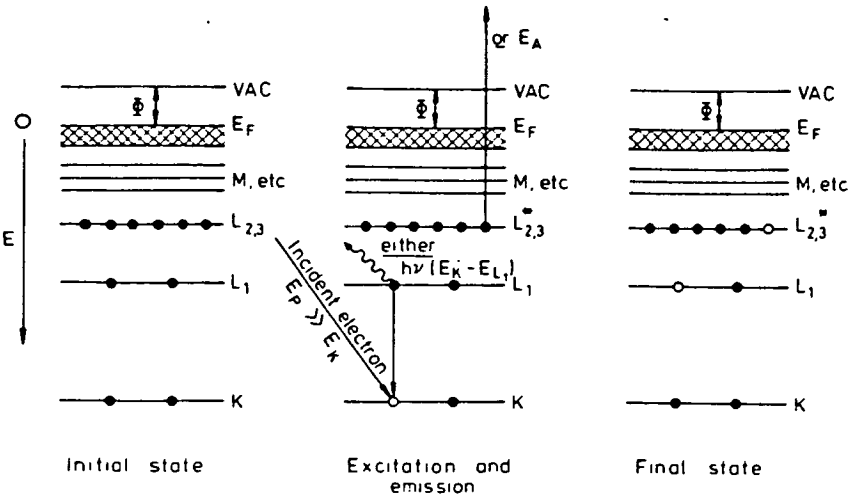

Fig 5.3 Schematic diagram of the process of Auger emission in a solid. The ground state of the system is shown at the left. In the centre an incident electron of energy E_p has created a hole in the core level K by ionisation. The hole in the K shell is filled by an electron from L_1, releasing an amount of energy $(E_k - E_{L1})$, which can appear as a photon of energy $h\nu = (E_k - E_{L1})$ or can be given up to another electron. In this example the other electron is in the $L_{2,3}$ shell, and it is then ejected with energy $(E_k - E_{L1} - E^*_{L2,3})$; $E^*_{L2,3}$ is starred because it is the binding energy not of $L_{2,3}$ in its ground state, but in the presence of a hole in L_1. The doubly ionised final state is shown on the right [6].

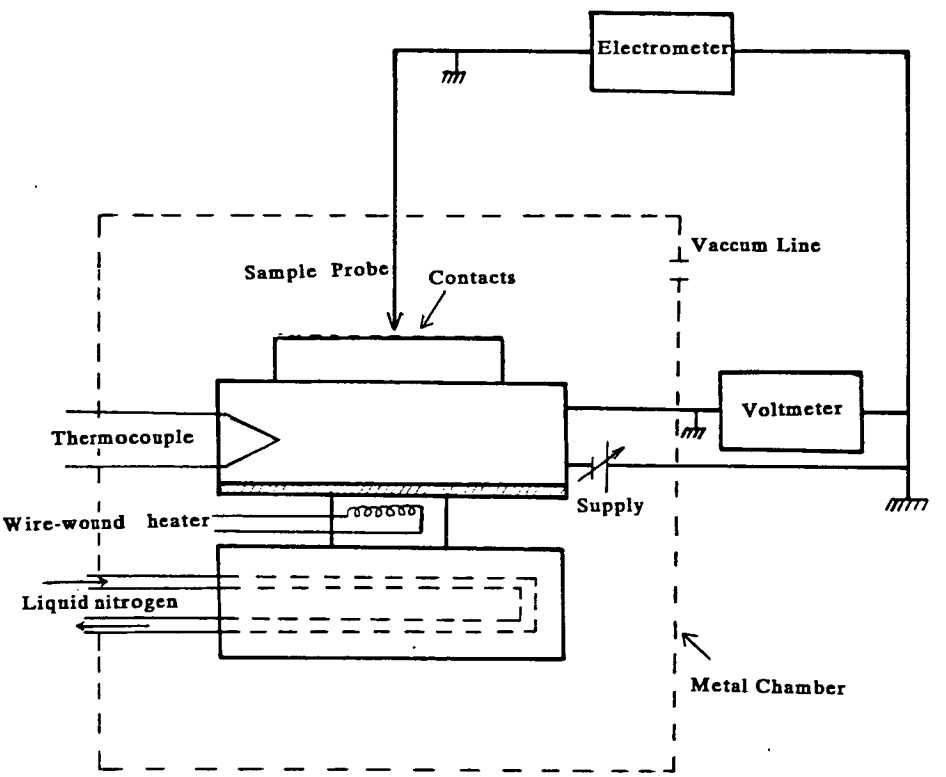

Fig 5.4 Experimental set-up used for D.C. conductivity measurements.

transition and the energy of the ejected Auger electron is given as

$$E_{KL_1L_{2,3}} = E_K - E_{L_1} - E^*_{L_{2,3}} \quad (5.1)$$

$E^*_{L_{2,3}}$ is starred because it is the binding energy of the $L_{2,3}$ level in the presence of a hole in level L_1, and is therefore different from $E_{L_{2,3}}$.

The important point to note is that the Auger energy as expressed in eqn.(5.1) is a function only of atomic levels, so that for each element in the periodic table there is a unique set of Auger energies, there being no two elements with the same set of atomic binding energies. Thus, the analysis of Auger energies immediately leads to elemental identification.

All the Auger measurements described in this work were carried out by Dr. C. Baker of the BP Research Centre, Sunbury, on-Thames.

5.6.4 Infrared Transmission

Infrared absorption spectra were measured using a Perkin-Elmer IR spectrophotometer (Model 598). This was a dual beam instrument in which a bare silicon wafer, the same as that used for film deposition, was always placed in the reference chamber in order to eliminate silicon lattice absorption bands.

5.6.5 DC Conductivity

DC conductivity **(I-V vs T)** measurements were carried out in the set-up shown schematically in Fig.(5.4). A Keithley 610C electrometer capable of measuring currents as low as 10^{-15}A was used as an ammeter. The electrometer was employed in its fast mode so that the voltage drop across the instrument was negligibly small compared to that across the sample, for all values of currents envisaged. Samples to be measured were placed on top of a copper support to which a thermocouple (copper-constantan) was attached, allowing the sample temperature to be monitored and contact to the metal electrodes was provided by a spring loaded gold probe. Beneath the copper support a heater was attached, permitting the sample temperature to be varied. The whole assembly was enclosed in a shielded chamber which allowed measurements to be made in the dark and in vacuum at pressures better than 10^{-2}torr.

5.6.6 Capacitance-Voltage Measurements

Capacitance-voltage(C-V) measurements were performed using an Hewlett-Packard 4280A C meter/C-V instrument. A block diagram of the measuring set-up used is shown in Fig.(5.5). The sample was housed in a unit similar to that used in the dc conductivity case which enabled measurements to be conducted as a function of temperature. The capacitance meter was a fixed frequency instrument with a dc bias range of +42 to -42 V. For measurement purposes the bias was applied to the upper electrode of the samples via a spring loaded probe and contact to the other side was via the copper platform. Both capacitance-voltage and conductance-voltage (G-V) measurements could be performed by controlling via the computer, the sweep rate, the voltage intervals and the voltage range.

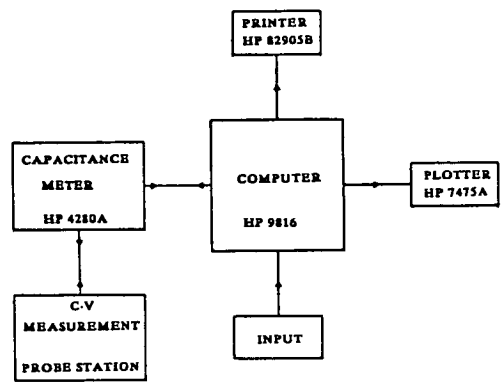

Fig 5.5 Block diagram illustrating the set-up used for C-V measurements.

5.7 REFERENCES

(1) P.E. Gise and R. Blanchard, Fairchild Corporation: "Semiconductor and Integrated circuit fabrication techniques". (virginia:Reston Publishing Co.) (1979).

(2) E. Walter, Springer Series in Electrophysics, vol 10, springer-verlag 1982.

(3) W.K. Chu, J.W. Mayer and M.A. Nicolet, "Backscattering Spectrometry" (Academic Press N.Y.). (1978).

(4) B.B. Goodman and J.B. Raynor, "Advances in inorganic chemistry and radiochemistry". (Ed: H.J. Emelevs and A.G. Sharpe) Vol 13, 135 (1970).

(5) R.L. Park, Phys. Today., 28, 52 (1975).

CHAPTER 6

PREPARATION AND CHARACTERISATION OF RF SPUTTERED SILICON-DIOXIDE FILMS.

6.1 RF SPUTTERING CONDITIONS

This chapter presents a detailed account of the preparation and characterisation of the *undoped* rf sputtered SiO_2 films, including comparisons with thermally grown SiO_2 and other relevant work. Information on the compositional analysis of the V-doped SiO_2 films used in the present study is given in chapter 7 and the experimental data on the electrical properties is discussed in chapter 8.

Although there has been considerable progress in the rf sputtering of SiO_2 layers, interest in this preparation technique generally declined after the great success in reducing interface states at the Si-SiO_2 interface by techniques such as the thermal oxidation of silicon. Amongst the considerable literature on rf sputtered SiO_2 little can be found on the electrical characteristics of MOS structures fabricated in this manner, yet to prepare good-quality SiO_2 layers it is essential to optimise several properties of the MOS system. These include the dc insulating characteristics of the oxide, the ac frequency dispersion associated with the quality of the film and the oxide-silicon interface and the electronic properties of the SiO_2-Si interface which are themselves determined by the interfacial region and its chemistry. Some of these properties may be controlled by optimising the substrate temperature, gas pressure, sputtering voltage and the preparation of the substrate surface.

For instance when selecting an optimum deposition temperature several considerations must be taken into account. The highest quality SiO_2 layers can, as suggested in the work of Vossen and O'Neill [1], be obtained by depositing at high temperatures. In the present work it was felt unwise to use temperatures greater than 200°C since the diffusion of the transition element through the oxide during fabrication could present major problems.

Factors of this nature imply that there must be a compromise in the deposition parameters and so the film preparation conditions were arrived at largely as a result of an experimental process of trial and error, in which the most favourable conditions were chosen after producing a variety of samples using a range of different values of r.f. voltage, power and argon pressure in an attempt at optimising the refractive index, lateral uniformity (see section 6.1.4) and capacitance-voltage characteristics.

6.1.1 Plasma Conditions

The energy and fluence of Ar ions responsible for sputtering were found to be functions of the rf power, voltage and gas pressure which were varied between 120-180W, 500-1.5kV and 1 to 40m torr respectively. The result of varying the rf voltage and Ar pressure was not examined methodically but the deposition rate was observed to increase as either of the above parameters were increased independently, while all other variables were held constant.

6.1.2 Substrate Bias

The matching network was capable of supplying a maximum of 400V peak to peak and the use of a substrate bias during sputtering resulted in a significantly lower deposition rate at all upper-electrode potentials, suggesting that some re-emission of incident particles was taking place. Although the matching network was capable of supplying 400V peak to peak to the platform the deposition rate reduced to zero at platform voltages of 300V for all upper-electrode potentials and the range of conditions for which uniform and relatively repeatable films were produced was so narrow that the specific effects of varying different conditions were not evaluated.

6.1.3 Substrate Temperature

Control of substrate temperature up to 350°C was available on the heated platform but heat and rf bias could not be applied simultaneously.

6.1.4 Film Preparation

Reproducible and repeatable films and MOS capacitors with good C-V characteristics, refractive indices close to 1.46 and film thickness variations of about 4 percent over 5.1cm in diameter, could be produced under the following conditions.

Prior to deposition, the chamber was evacuated to 5×10^{-6} torr. Argon was then introduced into the chamber at a pressure of 6−10m torr and with the shutter closed the six inch target was sputter cleaned for 15 minutes. The shutter is then opened and the deposition process is allowed to continue. On removal of the shutter the impedance of the glow discharge changes and some re-adjustments and retuning of the rf power source and matching network is necessary. The sputtering conditions after such

adjustments were typically

RF power = 180 ± 10W
Ar pressure = 6 to 10 mtorr
RF voltage = 1200 ± 50 V

This permitted films varying in thickness from 0.02 - 2.2μm to be prepared at growth rates as indicated in Figure (6.1). Two growth curves are represented in this diagram, one for pure SiO_2, the other for vanadium co-sputtered with SiO_2 at vanadium concentrations of 9 atomic percent (see chapter 5, section 5.2 and 5.3). In both instances the growth rates remain constant with time. The co-sputtered films are deposited at an average rate of 24Å/min which is slightly higher than the 22Å/min found for the pure SiO_2 films. Films with concentrations of less than 9% vanadium were deposited at rates of between 22-24Å/min but these are not shown in the diagram since they remained within the experimental error.

6.2 CHARACTERISATION OF SPUTTERED FILMS

The deposited films were characterised using standard physico-chemical and electrical methods which have already been well established and developed specifically for the analysis of thin film dielectrics [2].

Methods commonly used can be divided into two groups, mainly electrical and spectroscopic and the basic principles involved are explained in chapter 5. The electrical methods include capacitance-voltage measurements at 1MHz, sheet resistivity and dc conductivity.

Infrared spectroscopy (IR) is used extensively for compositional and structural analysis of deposited silicon dioxide whilst Rutherford back scattering and Auger electron spectroscopy have often been used to determine the composition of deposited dielectric films. Measurements of surface conductivity, stress and index of refraction of various dielectrics have also been reported and there are comprehensive reviews on the methods of characterising localised structural defects [3,4].

The techniques used in characterising films in the present work consisted of the following measurements

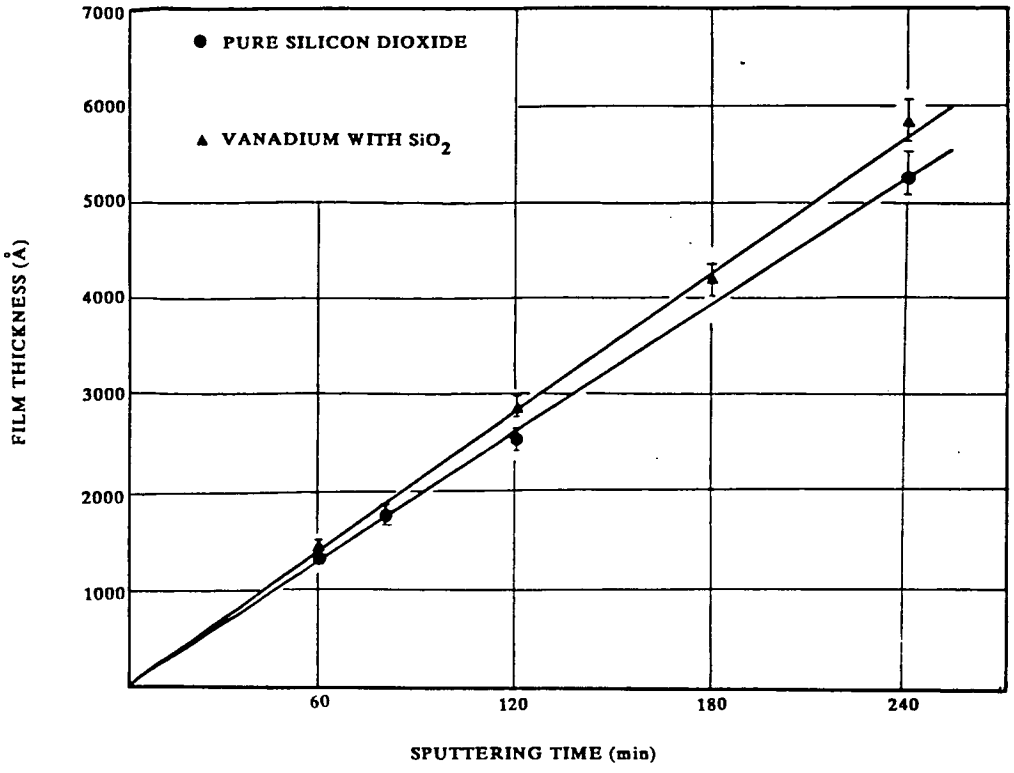

Fig 6.1 Plot of film growth with time, obtained under conditions indicated in the text. ● refers to pure SiO_2 and ▲ refers to vanadium with SiO_2 at 9 atomic % vanadium.

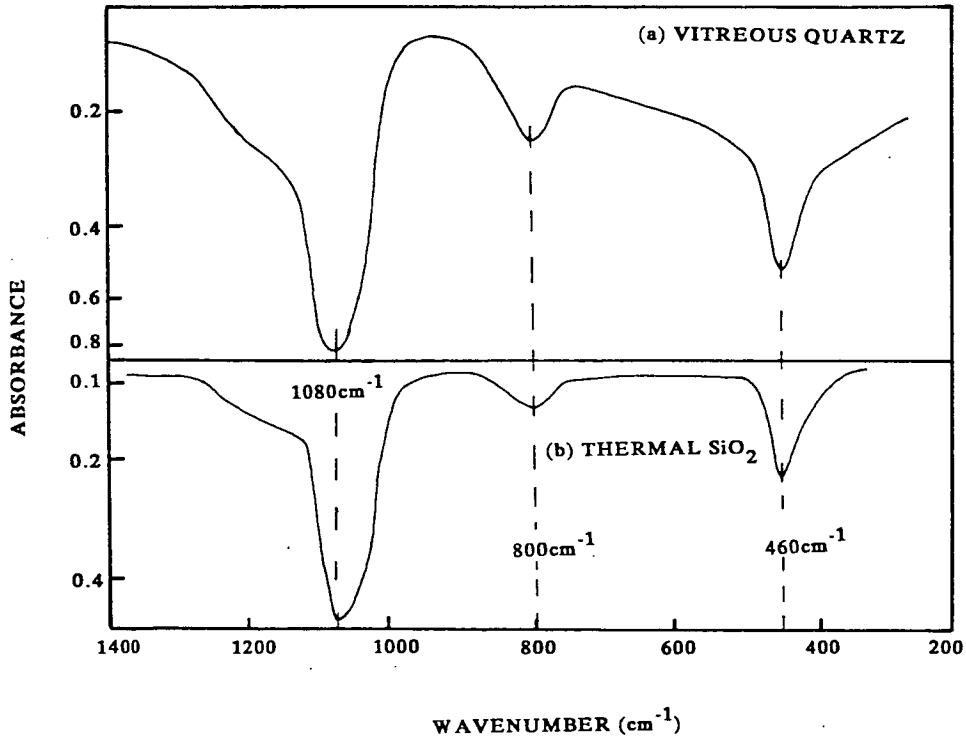

Fig 6.2 The Infrared spectra of (a) Vitreous and (b) Thermal SiO_2 [3].

(1) *Infrared Spectroscopy*

(2) *Film Density*

(3) *Rutherford Backscattering*

(4) *Auger Electron Spectroscopy*

(5) *Capacitance-Voltage*

and comparing these with the properties of thermal oxides. The superior chemical and physical properties of thermally grown SiO_2, which are little affected by moisture or moderate heat treatments, has allowed it to serve as a standard by which one can compare SiO_2 films deposited by other techniques, since in general the other deposition techniques lead to films which are more porous or less dense.

6.2.1 Infrared Spectroscopy

Transitions in the IR are associated with vibrational changes within bonds (or groups of bonds) and different bonds have different vibrational frequencies the presence of which can be detected by identifying the characteristic frequency as an absorption band in the IR spectrum. At ordinary temperatures all bonds are in a constant state of vibration, each bond having its characteristic stretching and bending frequency, and being capable of absorbing light of that wavelength.

In the case of thermally grown SiO_2 three absorption bands have been identified in the regions of 1100, 800 and 460cm^{-1}. The highest frequencies ($\simeq$1100cm^{-1}) involving the largest force constants are associated with the Si-O bond stretching; the progressively weaker vibrations at 800cm^{-1} and 460cm^{-1} are considered to be bending and rocking movements.

The strongest absorption band of SiO_2 films is the Si-O stretching vibration at $\simeq$1080cm^{-1} shown in Fig.(6.2), which is also very similar to that of fused silica. The exact position of this band is dependent on the method of film preparation and it is well known that both its position and width are influenced strongly by the bonding character, stoichiometry [4], density and the presence of foreign elements. Its position is also dependent upon the film thickness. As the thickness increases the position of the Si-O stretching vibration (measured in cm^{-1}) increases asymptotically to a limit of $\simeq$1080cm^{-1}. Sato [5] has measured this thickness limit and found it to lie between 0.4$-$0.5μm. This dependence on thickness has commonly been attributed to a very thin silicon-enriched layer at the Si-SiO_2 interface, the effect of which decreases as the

film thickness increases. Indeed, Ritter [6] has used the position of this band minimum to determine the oxygen content of SiO_x films, knowing that the absorption of deposited SiO layers is located at $1000cm^{-1}$ and extrapolating through an absorption near $1045cm^{-1}$ thought to be due to Si_2O_3 to obtain the relationship between (O) and (ν_{min}) shown in Fig.(6.3). This suggests that in addition to bond strain and lower density it is also necessary to consider non-stoichiometry induced by oxygen deficiency.

In order to compare rf sputtered films with thermally grown SiO_2 films, comparable thicknesses were used and the transmission spectra of an as-prepared film, that of a film heat treated in N_2 at 900°C for 30mins., and a thermally grown SiO_2 film is shown in Fig.(6.4).

Both the fundamental Si-O stretching vibration ($\simeq 1100cm^{-1}$) and the Si-O-Si bond rocking mode (at $460cm^{-1}$) in the as-prepared film are shifted towards lower frequencies by $10cm^{-1}$, compared to the thermally grown SiO_2 film. This shift to lower frequencies has often been attributed to oxygen deficiency in which the band is thought to move to $\simeq 1040cm^{-1}$ for Si_2O_3 and to $1000cm^{-1}$ (see Fig.6.3) for SiO.

Upon heating in N_2 at temperatures above 700°C, the spectrum of the sputtered film becomes essentially indistinguishable from that of the thermally grown film.

The behaviour of the two absorption bands with heat treatment were further examined using the definitions outlined in Fig.(6.5), so that the measured widths were defined as the full width at half minimum. The half widths of the $1100cm^{-1}$ and the $460cm^{-1}$ band in the as-sputtered film are considerably broader than that of the thermally grown SiO_2 film, the values of which are shown in Table (6.1) for comparison. On heating above 700°C, the half widths decrease and approach those of the thermal film. These changes in the width of the $1100cm^{-1}$ and the $460cm^{-1}$ band are shown in Fig.(6.6) and Fig.(6.7), respectively and are represented as a function of heating time in nitrogen at 900°C.

6.2.2 Film Density

The density of the sputtered films were determined from the oxide thickness and weight which were measured by an ellipsometer and a Sartorius (7474) microbalance, respectively. Accurate measurement of film thickness is essential to determine the density and it is for this reason that the film thickness was measured at six different points on the sample and then averaged. The data points marked as dots in Fig.(6.8) were calculated using these average values of thickness. The accuracy of this method is

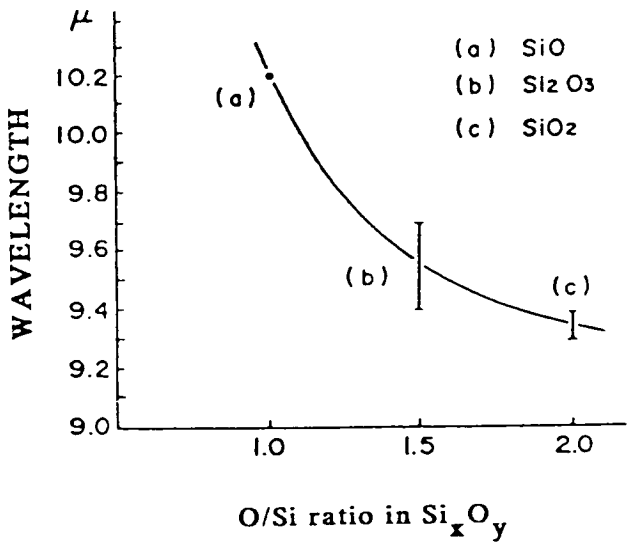

Fig 6.3 Relation between wavelength of absorption maximum and O/Si ratio in Si_xO_y for oxide thicknesses of 0.45μm [5].

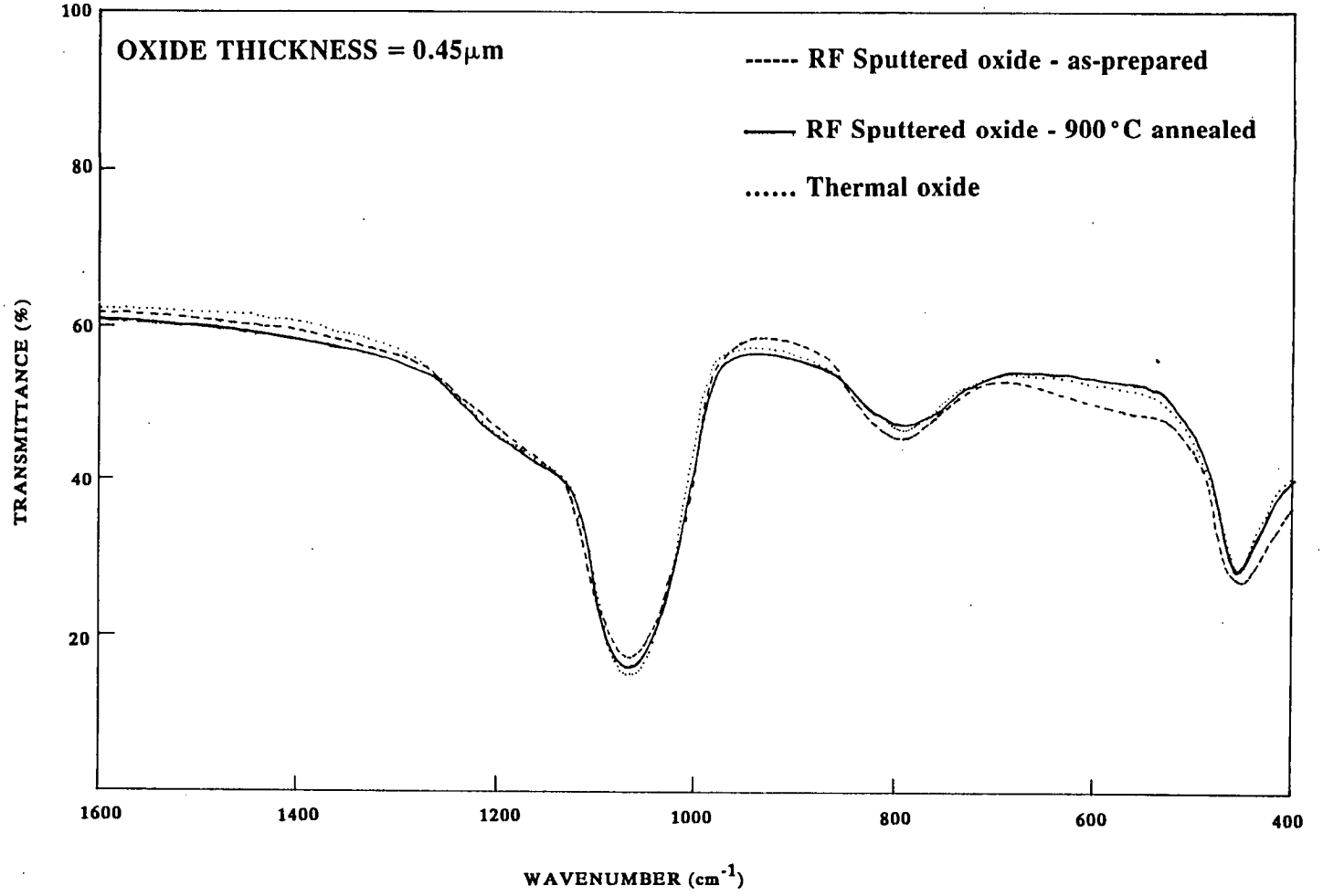

Fig 6.4 The infrared transmission spectra of an rf sputtered oxide in its as-prepared state and after annealing at 900°C in nitrogen. Also included in the diagram is the spectrum for an oxide thermally grown on silicon.

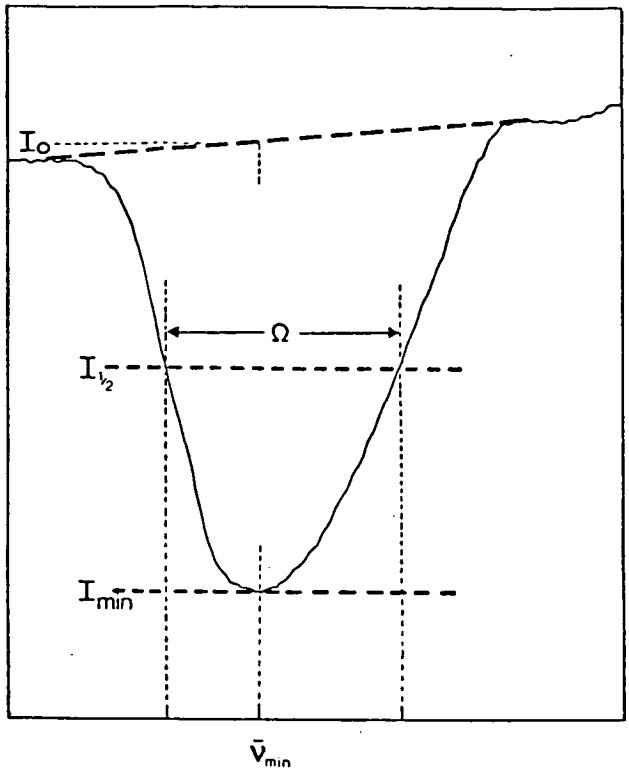

ν_{min} - is the position of the absorption minimum.

$I_{½} = \frac{[I_o - I_{min}]}{2}$ - half minimum.

and Ω - is the full width at half minimum.

Fig 6.5 Definitions of the parameters measured to examine the position and widths of the $1100cm^{-1}$ and the $460cm^{-1}$ absorption bands.

Sample	Halfwidth of Fundamental Si-O Absorption Band (cm^{-1}).
RF sputtered as-prepared	100
900°C Anneal for 30min. in N_2	89
Thermal Oxide	81

Table 6.1 Comparison of the halfwidths of the fundamental Si-O absorption band for rf sputtered and thermally grown SiO_2 films ($\simeq 0.45\mu m$).

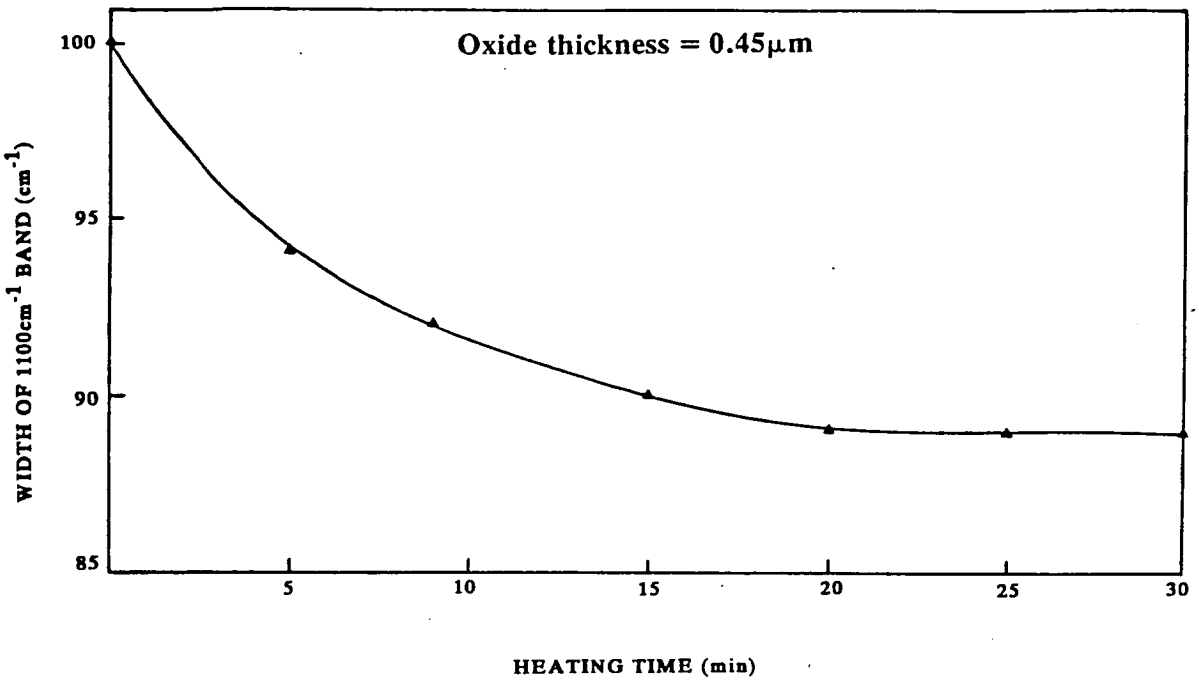

Fig 6.6 Dependence of the half-width of the $1100cm^{-1}$ band on heating time, at 900°C in nitrogen.

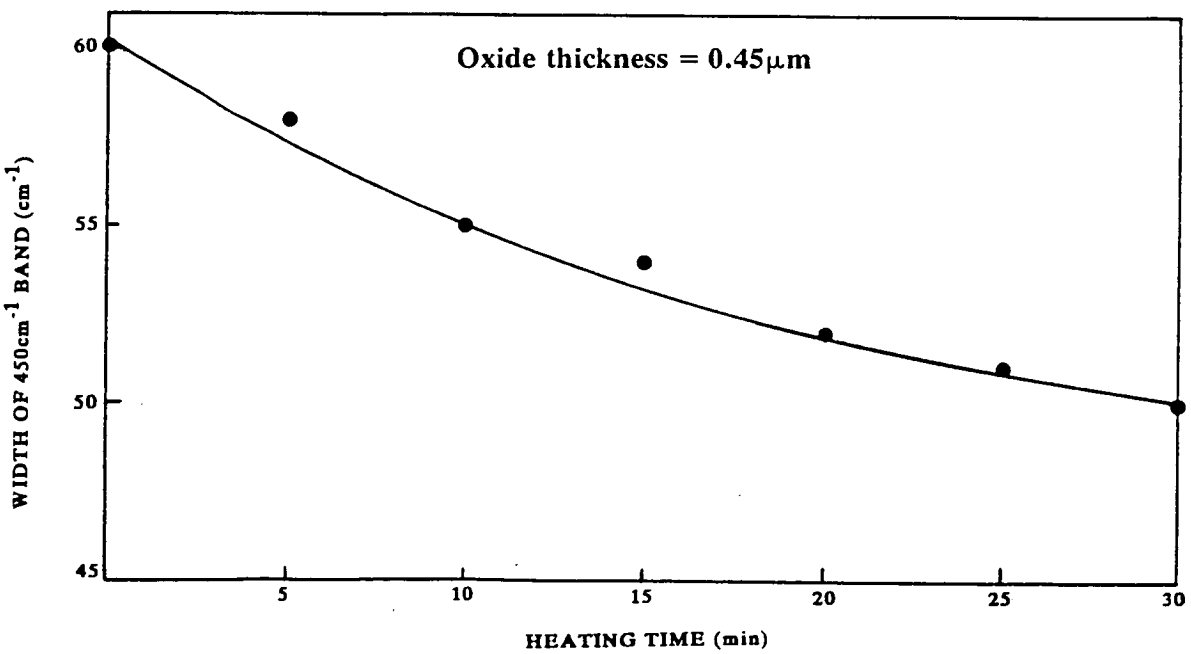

Fig 6.7 Dependence of the half-width of the $450cm^{-1}$ band on heating time, at 900°C in nitrogen.

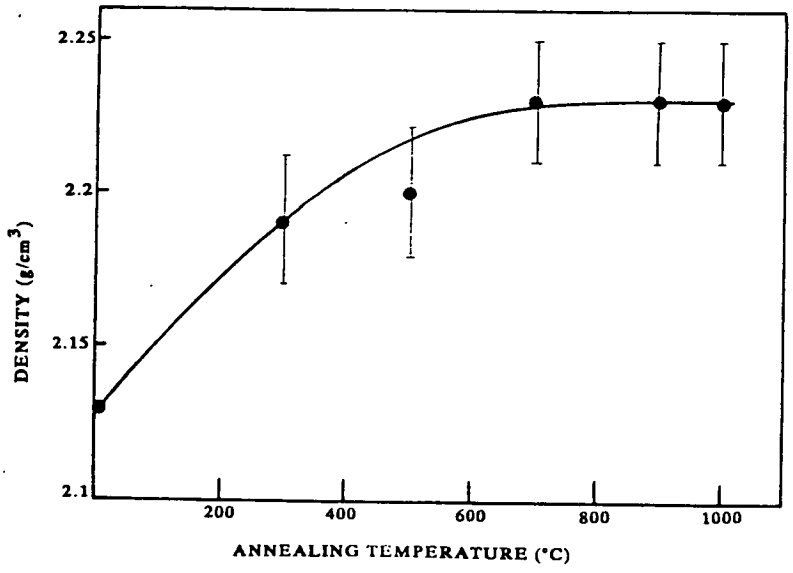

Fig 6.8 Variation in the density of the rf sputtered film as a result of heat treatment at various temperatures in nitrogen.

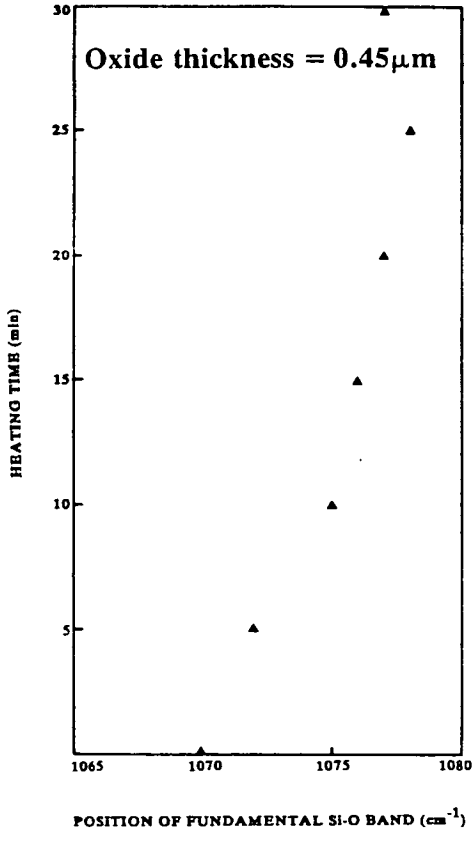

Fig 6.9 Shift of the fundamental Si-O absorption band as a function of heating time, at 900°C in nitrogen.

illustrated by considering the displayed error bars. These are thought to be the maximum possible variations and were arrived at by considering the oxide thickness measurements furthest away from the mean value which was found to be of the order of $\pm 1\%$. At the same time the microbalance was accurate to within 0.01mg.

The density at room temperature of the as-sputtered film was 2.13 ± 0.02 g/cm^3. This is smaller than the value of 2.22g/cm^3 for thermally grown SiO_2 reported by Nagasima [7]. Heat treating the films in N_2 at different temperatures however increases the density of the film until at temperatures above 700°C the density saturates at a value close to that for thermal SiO_2.

In the present investigation, the shift of the position of the band at 1100cm^{-1} towards lower frequencies, compared with the situation in thermally grown oxides as well as the broadening of the 1100cm^{-1} band in the as-sputtered films, may be attributed to a slight oxygen deficiency in addition to some bond strain leading to a decrease in film density. The oxygen deficiency can be understood in terms of the plot in Fig.(6.9). The as-sputtered film shows the fundamental Si-O absorption at 1070cm^{-1} which shifts asymptotically towards 1076cm^{-1} upon annealing. Translation of this data onto the curve in Fig.(6.3), and this can be done since the film thicknesses are the same, indicates a value for the stoichiometry (x) of 1.9 for the as-sputtered film. This does indeed reveal a slight oxygen deficiency which then undergoes a significant improvement to a value of 1.96 after heat treatment at 900°C in nitrogen.

After heating, both the IR absorption bands near 1100cm^{-1} and 460cm^{-1} which are due to the Si-O stretching and Si-O-Si bending vibrations respectively, are shifted to higher frequencies. Pliskin [4] has observed that the shift of the band near 1100cm^{-1} is also accompanied by an increase in density. In fact, both before and after heat treatment the weight of the films used in the present work did not change within the experimental error but the heat treated films were thinner by about 5% and this loss in thickness is the most likely cause of the increase in density.

In the absence of electron-diffraction data, it is useful to make comparisons of the present results with those of other workers [4,7].

Nagasima [7], in his examination of silicon dioxide prepared by oxidation of silane, noticed a shift of the absorption band at 1100cm^{-1} towards higher frequencies upon annealing but suggested that it is not necessarily congruous with the contraction of the Si-O bond length. In fact, by assuming that the amplitudes of thermal vibration of atoms are the same for the as-deposited and heat treated films he was able to show that the deviations of atomic distances from their mean values were larger for the as-

deposited film than the heat treated film and it is these variations which are responsible for the differences in the widths of the angle distributions of Si-O-Si bonds in as-prepared and heat treated films.

Following this line of reasoning and with reference to Figs.(6.6) and (6.7), the change in width of the 1100cm^{-1} band as a result of heating is small ($\simeq$11%) in comparison to the change in width of the 460cm^{-1} band ($\simeq$17%). Since a change in the distribution of the Si-O-Si bond angle is known to alter the vibrational frequency of a lattice, irrespective of whether the lattice is periodic or not, although of course the sensitivity of individual modes to changes in the bond angle will vary, it is probable that the observed shift to higher frequencies and narrowing of the 460cm^{-1} band upon heating, is also due to the contraction of the width of the angular distribution of the Si-O-Si bond. This effect could quite conceivably be related to the increased density upon annealing or, as suggested by Pliskin [4], the observed increase in density may be a consequence of the increased polymerisation of isolated SiO_4 tetrahedra.

6.2.3 Rutherford Backscattering

In addition to IR measurements, Rutherford backscattering was also used to characterise the films for their over-all stoichiometry. The general principles of this technique may be found in reference [8]. The depth composition analysis was carried out with a 2MeV $^4He^+$ ion beam and an over-all energy resolution of 13KeV.

Films were deposited on silicon substrates and the absolute amount/cm^2 of the elements were determined using a calibrated Bi in silicon standard. A typical backscattering spectrum from a layer produced by rf sputtering in Argon is shown in Fig.(6.10) and the elemental composition of three films, as-prepared, 500°C annealed and 900°C annealed in N_2 for 30 mins. is given in Table (6.2) and (6.3). Table (6.3) also indicates the stoichiometry for each sample relative to Si. The O/Si content through each layer appears to be fairly constant. A notable difference in the results of this measurement and the IR measurement is that even after annealing at 900°C in N_2 the RBS measurement suggests that the films are more significantly rich in silicon.

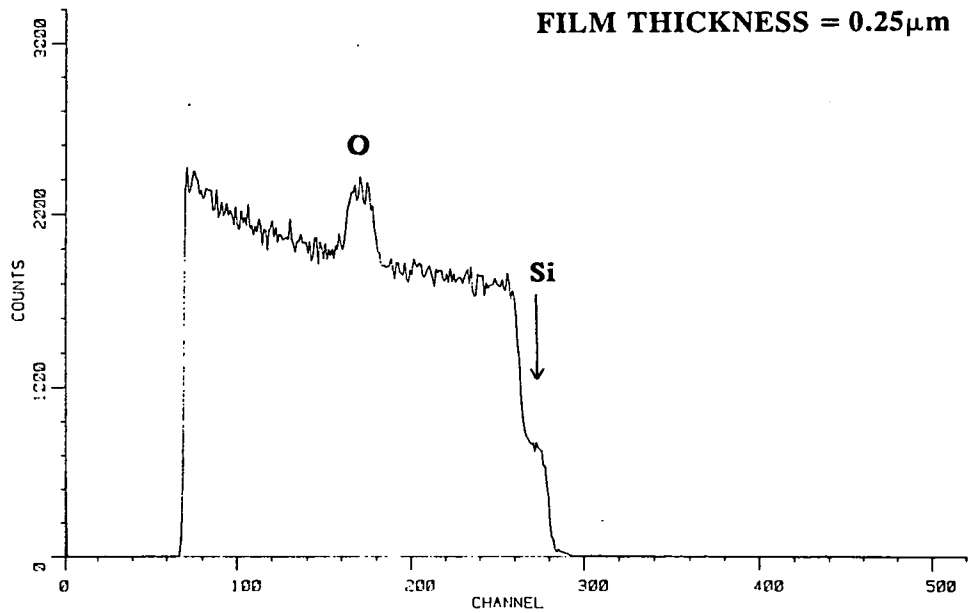

Fig 6.10 A typical backscattering spectrum for an rf sputtered film on a silicon substrate.

Sample	Silicon	Oxygen
	$\times 10^{18}$ atoms/cm^2	
RF Sputtered		
as-prepared	0.382	0.662
500°C anneal	0.391	0.638
900°C anneal	0.378	0.656

Table 6.2 Elemental composition in units of 10^{18} atoms/cm^2.

Sample	Percentage Composition of Layers		Stoichiometry
	Silicon	Oxygen	
RF Sputtered			
as-prepared	**36.5**	**63.5**	$SiO_{1.73}$
500°C anneal	**38**	**62**	$SiO_{1.63}$
900°C anneal	**36.5**	**63.5**	$SiO_{1.73}$

Table 6.3 Percentage composition and stoichiometry of layers.

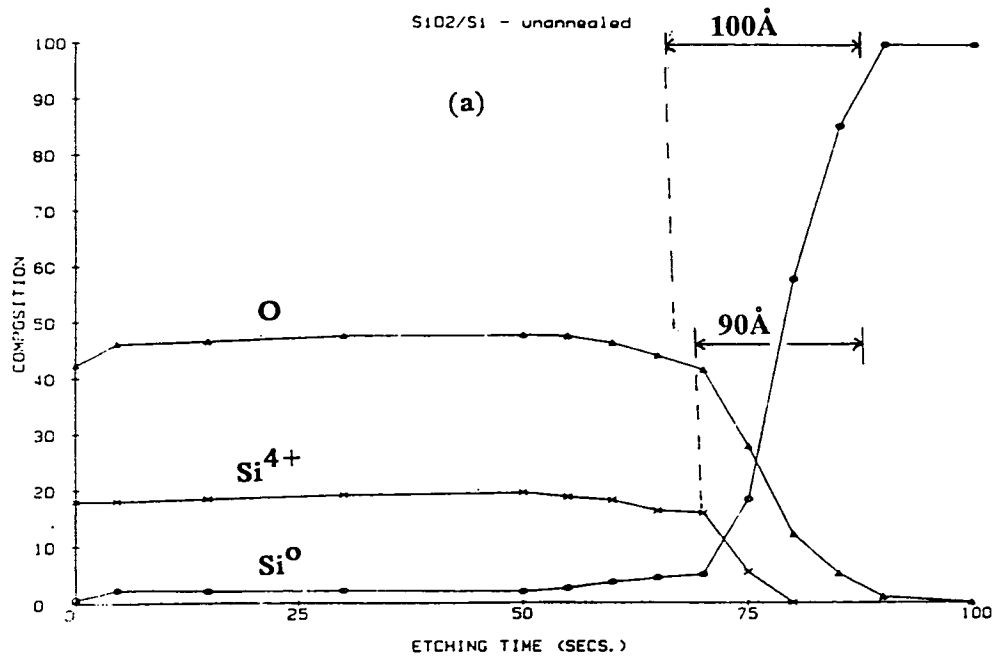

Fig 6.11(a) Chemical depth profile through 0.05μm of rf sputtered SiO_2 on silicon. The sample was unannealed. The widths of the transition regions are indicated in the figure.

6.2.4 Auger Electron Spectroscopy

The most common and best established application of Auger electron spectroscopy (AES) is in thin film analysis where an ion beam is used to sputter etch into a sample or layered structure while the composition of the immediate surface in the centre of the etched area is measured using AES. Chemical depth profiling is accomplished by automatically plotting the peak-to-peak heights of the Auger lines of the chemical elements in the sample as a function of the sputtering time. In silicon, the most pronounced low-energy Auger peak appears at 92eV and has its origin in the $L_{2,3}VV$ transition. It is usually monitored for purposes of identifying elemental silicon but when there is an overlap problem in the Si-92eV peak, it is common to monitor the high energy 1620eV peak, which has its origin in the $KL_{2,3}L_{2,3}$ transition. In the case of SiO_2, the most prominent low-energy peak occurs at 78eV and is usually monitored for purposes of its identification while oxygen is monitored for the O_{KLL} transition at 502eV.

In this work all the peak heights were normalised to the Si-92eV peak in silicon and knowing the sputtering rate of the material, the time scale could be converted to distance or depth, into the sample.

Figures 6.11(a), (b), and (c) exhibit features common to all oxides examined in this study. The data is for an oxide 0.05μm thick, sputtered at room temperature under the conditions discussed earlier in this chapter. In general, the composition and thickness of the oxide layers are very similar and the bulk of the oxide is homogeneous SiO_2 except the as-prepared film which appears to be slightly oxygen rich. If however (as is shown later) Si^o is added to Si^{4+}, the ratio O/Si_{total}, where $Si_{total}=Si^{4+} + Si^o$, is *two*, and the film can be considered as being stoichiometric.

After annealing the films at 500°C in an inert ambient such as N_2, the spectra are as shown in Fig.6.11(b). In this case, both the amount of four-fold coordinated silicon and oxygen has increased compared to the unannealed sample. It is evident therefore that after annealing at 500°C, the film takes up more oxygen and silicon. Although this may be true the important parameter as far as determining the stoichiometry is concerned, is the ratio O/Si_{total}, which is again found to be *two*. After annealing the sample at a higher temperature such as 900°C in N_2 for 30mins., the amount of oxygen reduces by a small fraction from its value at 500°C, as does the amount of four fold coordinated silicon but both the oxygen and Si^{4+} compositions are higher than in the as-prepared state and the film is again stoichiometric. The AES also seems to show the presence of elemental silicon Si^o at a low but fairly constant level across the

thickness of the films, as shown in Fig.6.11 (a), (b) and (c). As explained later, however, it is believed that this is an artifact caused by the sputter etching technique used to profile the films.

Prior to electron irradiation of the unannealed and the 500°C annealed sample (i.e. at time=0) there appears to be no "free" silicon present even though the IR and RBS measurements have shown these films to be slightly silicon rich. The reasons for this may be that since the samples were exposed to atmosphere before the measurements, they may have been oxidised to depths sufficient to screen off their bulk stoichiometry or, the amount of free silicon at the beginning of the measurement is well below the detection limit of the AES instrument. The latter reason appears to be more plausible especially when the results are considered in the context of the data in Fig.6.11(c). In this instance, even at time t=0, the amount of free silicon present is sufficient to be detected.

It must nevertheless be mentioned that before time t=0 all the samples showed traces of carbon and nitrogen on the surface which were removed during the first etch period and are not shown in the figures.

Detailed studies of the effects of electron-irradiation in the Auger analysis of SiO_2 by Thomas [9] and Johannessen et al [10] indicate that prolonged irradiation can have an adverse effect on the surface composition, the most pronounced effect being the dissociation of SiO_2 into elemental Si and oxygen. According to Thomas [9], continuous electron bombardment of the surface results in a new peak which is characteristic of elemental Si, and with time the Si-92eV peak increases in intensity while the SiO_2-78eV peak and the oxygen Auger peak decrease in intensity.

In the early stages of dissociation, the Si-92eV peak appears as only a shoulder on the high-energy side of the SiO_2-78eV peak but reaches an equilibrium value in a time which is dependent on the primary electron-beam current density, shown in Fig.(6.12).

In a similar manner, the profiles in Figs.6.11(a) and (b) indicate a linear increase in the Si-92eV peak during the early stages of dissociation, until they reach an equilibrium value after approximately 5sec. Though the time taken to reach equilibrium is different in the present samples compared to that reported by Thomas [9], it must be remembered that the sputtering rate used here was at least an order of magnitude higher.

Although the mechanism by which the dissociation and desorption observed in SiO_2 is not clearly understood, Thomas [9], using the laws of conservation of energy and momentum, has shown that it is unlikely to occur as a result of direct momentum

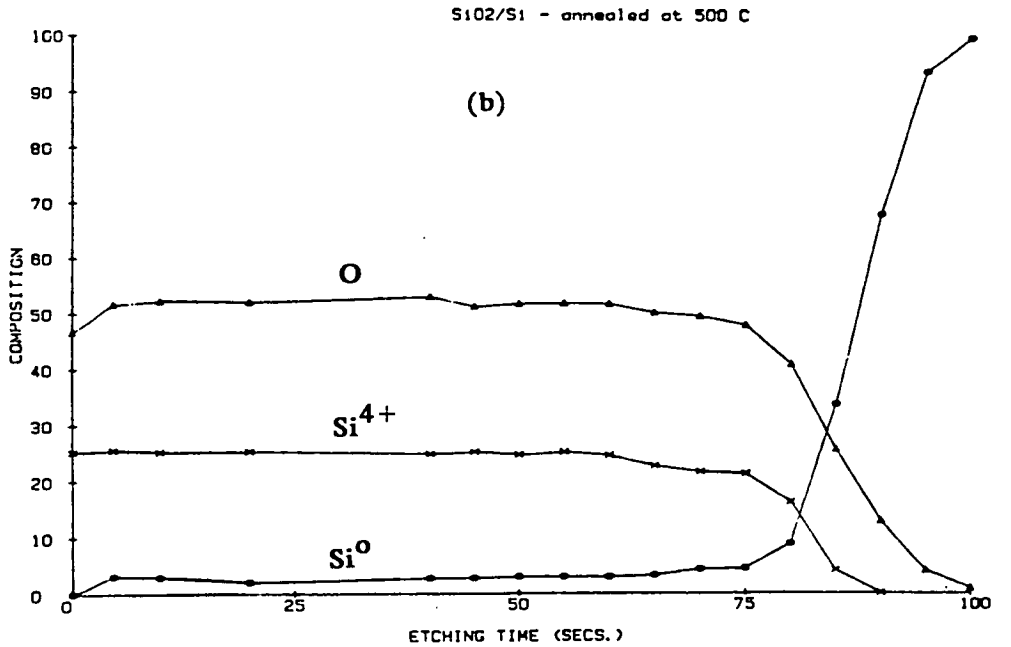

Fig 6.11(b) Chemical depth profile through 0.05μm of rf sputtered SiO_2 on silicon. The sample was annealed at 500°C in nitrogen for 30 min.

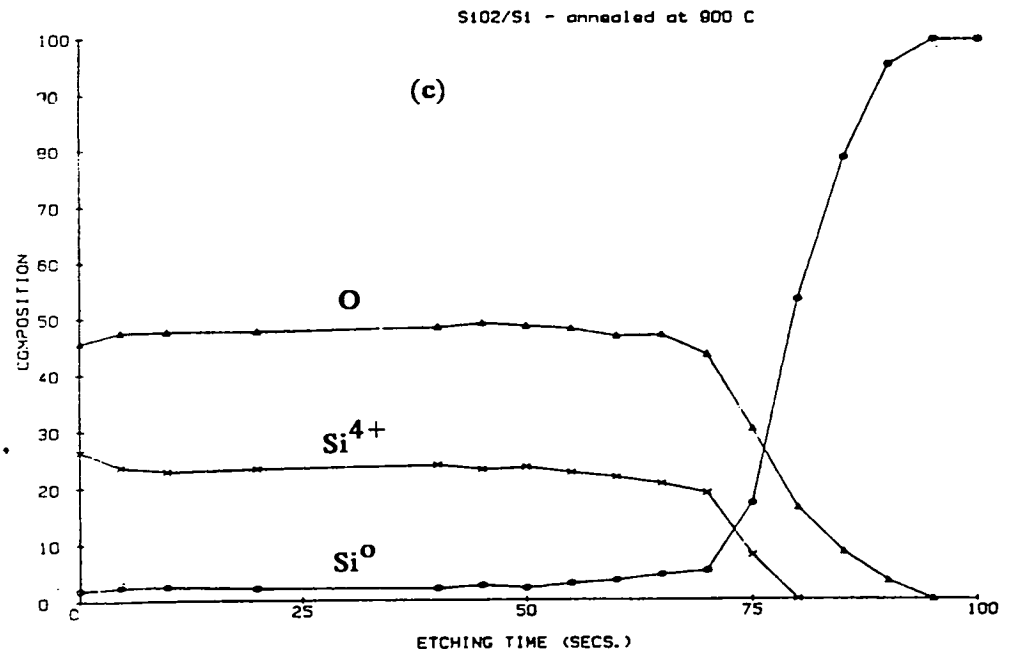

Fig 6.11(c) Chemical depth profile through 0.05μm of rf sputtered SiO_2 on silicon. The sample was annealed at 900°C in nitrogen for 30 min.

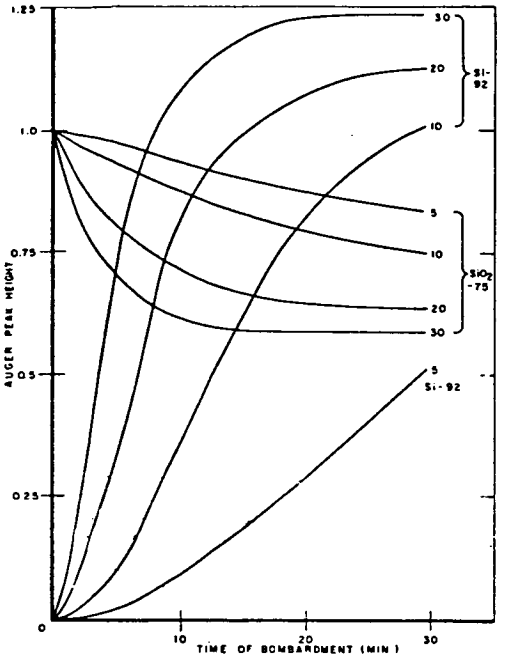

Fig 6.12 Variations in the Si-92eV and SiO_2-75eV peak heights with time of bombardment. The number beside each curve gives the primary electron current in μA [12].

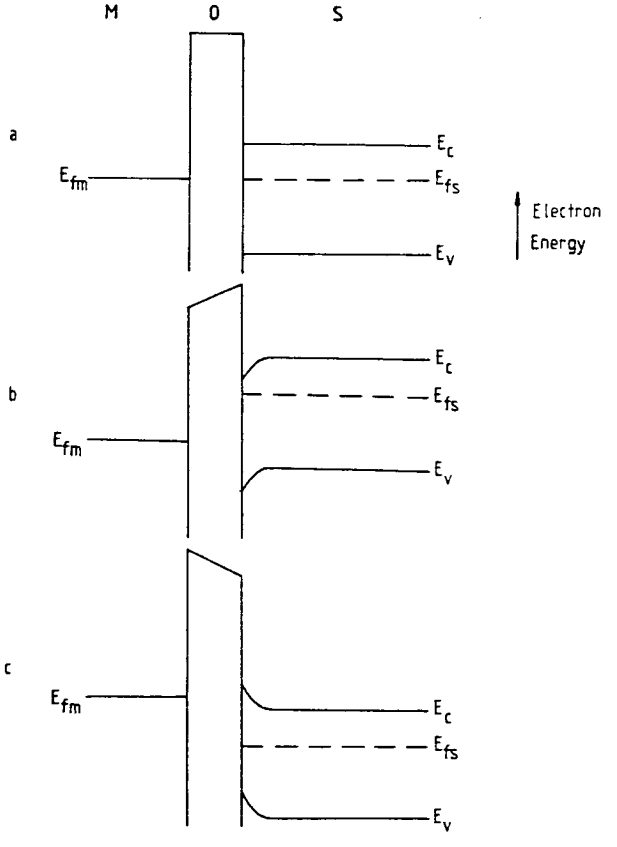

Fig 6.13 Energy band diagram for an ideal MOS capacitor with n-type Si.

(a) Zero applied potential (flat band).
(b) Negative potential to the Si substrate (Accumulation).
(c) Positive potential to the Si substrate (Depletion/inversion).

transfer from the bombarding electrons.

In all the reported investigations of dissociation and desorption in SiO_2, no estimates have been made of the localised temperature rise, yet it is not unreasonable to expect the beam-induced heating to supplement such reactions, and competing with the process of desorption there also exists the possibility of recombination of oxygen and silicon to form SiO_2, particularly at elevated temperatures.

What one therefore sees in an Auger spectrum is the net result of desorption and recombination and the observation of the Si Auger peak does not necessarily imply the presence of elemental Si but is a result of the damaging effect of the AES technique, and the final equilibrium state in the growth of the Si Auger peak is reached when the desorption and recombination rates are equal.

At the present time there does not exist any established method for the determination of interface widths from chemical depth profiles but a first order approximation has been attempted by extrapolating the steepest slopes as shown in Fig.6.11(a). Using this approach provides a closer view of the interface region which reveals that a change from Si-O bonding to Si-Si bonding takes place within an interface region of at most 90Å, while the oxygen atoms stay in the same state but decrease gradually to zero, over roughly 100Å. It must be stressed that these are rough calculations providing only an order of magnitude estimate and have not been extended to compare changes in the interface width with annealing. In order to perform a more accurate estimate of the interface width it is necessary to account for effects of 'broadening' by the ion distribution and the finite escape depth of the electrons. This exercise has nevertheless demonstrated that the chemical state of the silicon atoms at the interface change in an orderly fashion from a typical $Si\text{-}O_4$ tetrahedral coordination in the bulk of the oxide to $Si\text{-}Si_4$ tetrahedral coordination in the substrate.

6.2.5 High Frequency C-V Method

The heart of all MOS devices is the interface between Si and the oxide. In 1962, Lindner [11] developed and used the high frequency capacitance method in order to determine the interface trap capacitance. In this technique, capacitance is measured as a function of gate bias at a frequency high enough that the interface traps do not respond.

The energy band diagrams for an ideal n-type Si MOS structure under varying conditions of bias are depicted in Fig.(6.13). In the absence of any potential across the

device, the 'flat-band condition', illustrated in Fig.6.13(a) prevails. When a negative voltage is applied to the Si, band bending at the interface between the Si and the oxide occurs as shown in Fig.6.13(b), resulting in the accumulation of negative charge at the interface. Likewise, a positive potential to the Si results in a region on the Si side of the interface, depleted of majority carriers as depicted in Fig.6.13(c).

The induced charge in either the accumulated or depleted regions (Q_s) can be calculated as a function of the surface(interface) potential Ψ_s, and its derivative is then the small-signal capacitance of the Si surface, C_{si}.

where

$$C_{si} = \frac{\partial Q_s}{\partial \Psi_s} \tag{6.1}$$

Following the treatment of Lindner [11] and assuming that the small-signal frequency is too high for minority carriers to respond gives

$$C_{si} = \frac{\epsilon_{si}\lambda^{-\frac{1}{2}}(1 - e^{Y})}{\zeta(e^{Y} - 1 - Y)^{\frac{1}{2}}} \qquad \text{for } -Y-1 > e^{-Y}\lambda^2 \tag{6.2}$$

and

$$C_{si} = \frac{\epsilon_{si}\lambda^{-\frac{1}{2}}\zeta^{-1}(-y_1 - 1)^{\frac{1}{2}}}{-y_1 - e^{\frac{1}{2}}(Y - y_1)} \qquad \text{for } -Y-1 < e^{-Y}\lambda^2 \tag{6.3}$$

where

$$-y_1-1 = e^{y}\lambda^2 \tag{6.4}$$

ϵ_{si} = permittivity of silicon.

$\lambda = \frac{n_i}{n_B}$ silicon doping parameter

n_i = intrinsic carrier concentration

n_B = donor concentration

Y = surface potential; relative to bulk in kT units.

$\zeta = (\frac{2\epsilon_{si}}{\beta e n_i})^{\frac{1}{2}}$ Debye Length

$\beta = \frac{e}{kT}$

The calculations and derivations are outlined in detail in reference [11]. The total small signal capacitance of the MOS structure may then be represented as C_{si} in series with the oxide capacitance and is given by

$$C = \frac{C_{si}\, C_{ox}}{C_{si} + C_{ox}} \tag{6.5}$$

The resulting ideal capacitance-voltage (C-V) curve is shown in Fig.6.14(a).

A real MOS capacitor deviates from the ideal capacitor due the chemical structure of a real interface. At such an interface, there are always defects present and in this particular system these are oxide fixed charges and interface traps which contribute one or more energy levels within the Si bandgap. The effect of such charges is to cause distortions and changes in the shape of the high frequency C-V characteristic, as described below.

(1) *Due to excess silicon near the interface there is always a small positive charge present. This charge is termed fixed oxide charge and it creates a non-zero surface potential in the absence of an applied bias. The localised states of energies which such charge creates are outwith the Si bandgap so that they do not change their occupancy as the surface potential is varied but affect the C-V curve with a parallel shift along the voltage axis, as shown in Fig.6.14(b).*

(2) *In the absence of any surface states, band bending due to differences in the work-function of the metal and Si causes a parallel shift of the C-V curve without distortion along the voltage axis by an amount equivalent to the work-function difference, Fig.6.14(b).*

(3) *If interface states do not follow the ac signal but follow very slow changes in gate bias as the MOS capacitor is swept from accumulation to inversion then they contribute no capacitance to the high frequency C-V curve. These interface traps do however cause the C-V curve to stretch out along the voltage axis because interface trap occupancy must change in addition to a changing depletion layer charge. The smear-out of the C-V curve in the presence of a distribution of such states is illustrated in Fig.6.14(c).*

Knowing the doping level in the Si and the capacitance of the oxide, the density of interface states may be calculated from the voltage difference (ΔV) between the measured and ideal C-V curves, by subtracting the two curves at each value of C to give ΔV, where

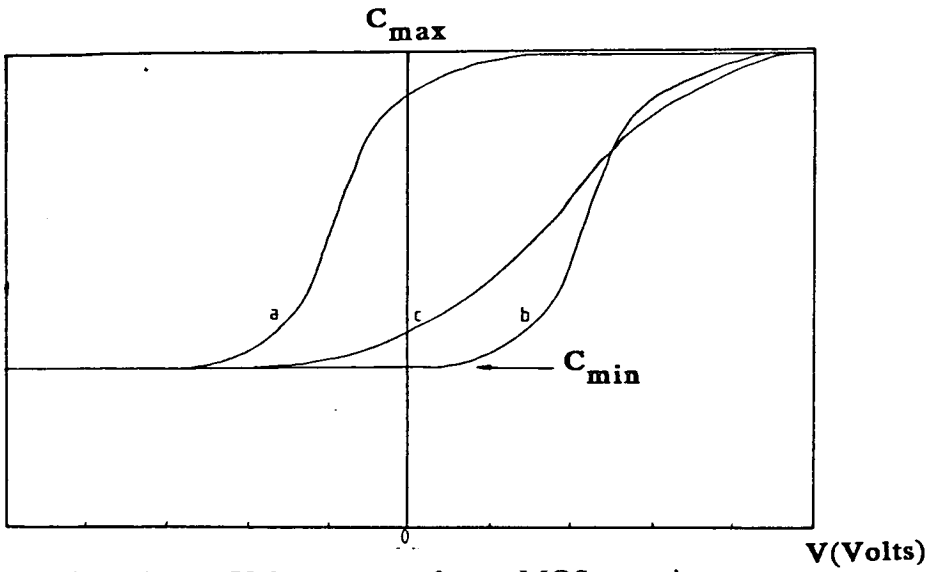

Fig 6.14 Capacitance-Voltage curves for an MOS capacitor.

(a) Ideal case.
(b) Shift of (a) due to fixed oxide charge and metal-Si work function difference.
(c) Effect on (a) due to interface states.

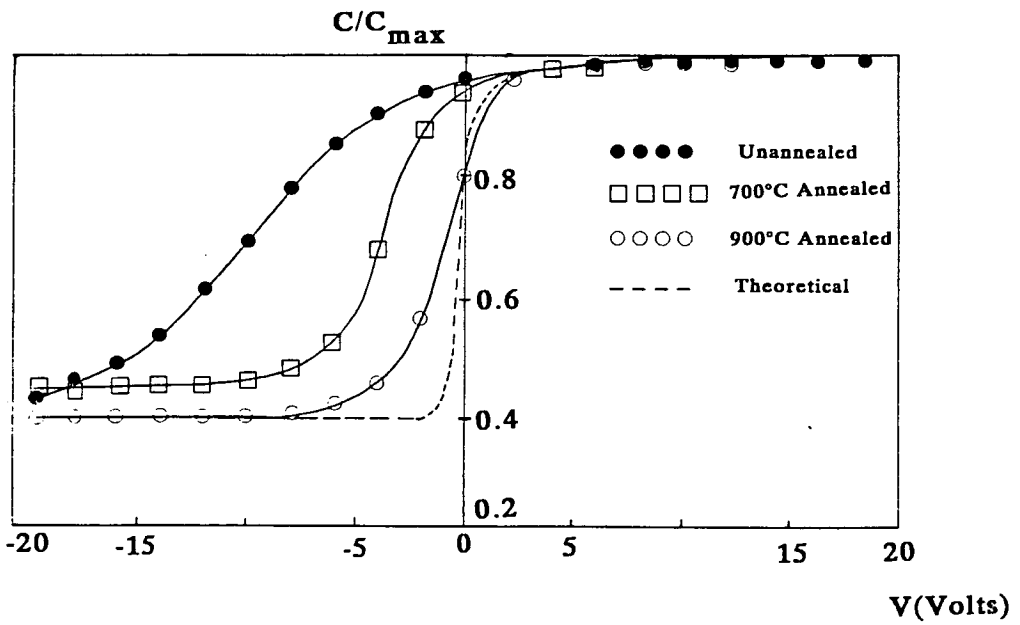

Fig 6.15 Normalised capacitance-voltage curves for samples annealed at different temperatures. Also plotted in this figure is the theoretically calculated curve, for comparison.

$$Q_{ss} = C_{ox} \times \Delta V \quad coul/cm^2 \tag{6.6}$$

Q_{SS} is the total surface charge and the density of surface states per unit energy N_{SS} is then obtained by graphical or numerical differentiation

$$N_{ss} = \frac{1}{q} \frac{\partial Q_{ss}}{\partial \psi_s} \quad cm^{-2}eV^{-1} \tag{6.7}$$

Interface traps and oxide fixed charge are sensitive to processing conditions. In particular, interface trap level and oxide fixed charge densities are affected by oxidation conditions, annealing and contaminants which must be controlled and minimised.

The early problems of device instabilities experienced by Khang et al [12] and discussed in Chapter 2 were basically due to high positive charge levels ($10^{12}-10^{13}cm^{-2}$) in the oxides. As technology improved and cleaner processing emerged, trapping instabilities have become more dominant with shifts in the C-V curve an order of magnitude lower than those observed by early workers. Today's clean technology results in charge levels of the order of 10^{10}-10^{11} charges/cm^2. In addition to information about the interface state density it is also possible to extract the high frequency dielectric constant (ϵ_{ox}) via the relationship

$$C_{ox} = \frac{\epsilon \epsilon_{ox} A}{d} \tag{6.8}$$

where C_{ox} is the capacitance in accumulation. For thermal oxides the value so calculated is given as 3.84 [2].

A typical set of C-V curves for an rf sputtered oxide, after annealing in N_2 at different temperatures is given in Fig.(6.15). Also represented in this figure, is the theoretically calculated curve for the ideal MOS capacitor. In the diagram, the oxide capacitance has been normalised with respect to the total capacitance. Using the method outlined previously the total density of interface states was calculated and seen to reduce from about 5×10^{12} charges/cm^2 in the as-prepared state to a value of about 10^{11} charges/cm^2, after annealing at 900°C and the high frequency dielectric constant, ϵ_{ox} was found to equal 3.78, which only differs by about 1.5% from its value for thermal oxides.

Although the C-V measurement has no spatial resolution it is clear that the net positive charge at the interface is considerably reduced as a result of heat treating the film at progressively higher temperatures, until at 900°C, the interface state density is comparable to that of thermally grown oxides [13].

Oxide Type	Density (g/cm^3)	Index of Refraction n_1 λ=546nm	Dielectric Strength 1MHz	Resistivity (Ωcm)
Bulk Silica Glass	2.2	1.462	3.8	10^{15}-10^{16}
THERMAL OXIDE				
Steam (97°C H_2O)	2.00-2.2	1.45-1.46	3.85	10^{15}-10^{17}
Open Tube High Pressure	2.3	1.48	—	—
Dry Oxygen	2.24-2.27	1.46-1.47	3.9	3×10^{15}-2×10^{16}
ANODIC OXIDE				
Electrolytic	1.8	1.32-1.49	—	—
Plasma	—	1.46-1.47	—	—
THIS WORK				
RF Sputtered 900°C Anneal in Nitrogen	**2.23±.02**	**1.45-1.46**	**3.78**	**10^{16}-10^{17}***

Table 6.4 Properties of SiO_2 prepared in various ways including this work.(*) see chapter 8.

6.3 CONCLUSIONS AND DISCUSSION

The results presented in this chapter have in general provided a consistent picture of the composition and properties of rf sputtered films. The only difference lies in the exact quantities measured by each technique. It is noticeable that the values of stoichiometry determined by RBS vary quite significantly from those suggested by the other two methods. Such variations can only be resolved when the differences in these techniques are considered in the light of their limitations.

Auger electron spectroscopy has the advantage of providing simultaneously information both about abundance of elemental species as well as their chemical state, yet dissociation and consequent compositional changes are a serious problem in Auger analysis if proper care is not taken in the choice of electron beam parameters. In contrast to this, the amount of radiation damage produced by the ion dose in RBS is small and unlike AES, which relies on sputter sectioning in order to profile to comparable depths, it is non-destructive. Rutherford backscattering however suffers from a fundamental ambiguity in that a count at a particular energy may be due to scattering from a lighter element near the surface or a heavier element at greater depth. This ambiguity can only be resolved with prior knowledge of the elements present. It is nevertheless worth noting that AES is also capable of identifying the presence of contaminants close to a surface ($\simeq 10\mathring{A}$), which is beyond the detectable limits of many conventional techniques.

In the light of these discussions, the films produced in this work can be considered as having the properties indicated in Table (6.4). Also summarised in this table are the properties of films obtained by other techniques, for comparison.

6.4 REFERENCES

(1) J.L. Vossen and J.J. O'Neill, Jr., RCA Rev. 29 149 (1968).

(2) E.H. Nicollian and J.R. Brews, "MOS Physics and Technology"., (Wiley) (1982).

(3) W.A. Pliskin, J. Vac. Sci. Technol., 14, 1064 (1977).

(4) W.A. Pliskin, in "Physical Measurement and Analysis of Thin films"., eds: E.M. Murt and W.G. Guldner. Progress in Analytical Chemistry vol 2 168 (1969).

(5) K. Sato. J. Electrochem. Soc., 117, 1065 (1970).

(6) E. Ritter. Opt. Acta., 9, 197 (1962).

(7) N. Nagasima, J. Appl. Phys., 43, 3378 (1972).

(8) W.K. Chu, J.W. Mayer and M.A. Nicolet, "Backscattering Spectrometry"., (Academic Press N.Y.). (1978).

(9) S. Thomas, J. Appl. Phys., 45, 161 (1974).

(10) J.S. Johannessen, W.E. Spicer and Y.E. Strausser, J. Appl. Phys., 47, 3028 (1976).

(11) R. Lindner, The Bell System Technical Jnl., XLI, 803 (1962).

(12) D. Khang and M.M. Atalla, "silicon-silicon dioxide field induced surface devices"., paper presented at IRE-AIEE Solid, State Device Research Conf. Carnegie Inst. of Techn. Pittsburgh, Pa. (1960).

(13) K.H. Zaininger and F.P. Heiman, Part 1, Sol. St. Technol., 49, (1970).

CHAPTER 7

STRUCTURAL CHARACTERISATION AND OPTICAL PROPERTIES OF VANADIUM-DOPED SILICON DIOXIDE.

7.1 RUTHERFORD BACKSCATTERING

Silicon dioxide films having different vanadium concentrations were also prepared by rf sputtering onto silicon substrates. The range of vanadium concentrations studied, their elemental compositions and stoichiometry is given in Table (7.1). Also displayed in this table is the data previously shown in chapter 6, Table (6.3), for an undoped SiO_2 film, for purposes of comparison.

A typical backscattering spectrum obtained for a V-SiO_2 film sputtered in argon and containing 9 atomic percent vanadium is shown in Fig.(7.1). In the cases where vanadium is co-sputtered with silicon dioxide its concentration throughout the layers appears to be constant which suggests that vanadium is being sputtered at a constant rate.

The variation in the percentage composition of silicon and oxygen in the films as a function of vanadium concentration is shown in Fig.(7.2) and Fig.(7.3), respectively. All the data in these diagrams correspond to measurements after annealing the samples in nitrogen at 900°C for 30mins.

As the amount of incorporated vanadium increases, for increasing concentrations up to 9 atomic percent, the amount of silicon decreases by 37% from its value in the undoped case. At the same time and over the same range of vanadium concentrations, the amount of oxygen increases by 7%. At first sight it would appear that vanadium displaces silicon in the oxide layer. This is not entirely true. Consider as an example the sample labelled (5) in Table (7.1). A reduction in the amount of silicon compared to its value in the undoped case by 13.5 atomic percent cannot all be accounted for by the introduction of 9 atomic percent vanadium. The decrease of silicon by this amount can however be explained by the increase in oxygen (compared to its value in the undoped case) of 4.5 atomic percent, such that the sum of the increase in oxygen and the added vanadium, is equal to the amount of reduction in silicon. This means that the relative decrease in the silicon arises as a result of an increase in the oxygen and the presence of vanadium.

7.2 INFRARED ABSORPTION

The infrared transmission spectra of a film 0.5μm thick and co-sputtered with 5 atomic percent of vanadium is shown in Fig.(7.4). Included in this diagram are the spectra of the film in its as-prepared state and after heat treatment at 700°C and 900°C for 30mins. each, in nitrogen. The features in all three cases are essentially the same as in

Sample No.	Sample	V%	Si%	O%	Stoichiometry
1	SiO_2	-	36.5	63.5	$SiO_{1.73}$
2	V-SiO_2	5	31	64	$SiO_{2.06}V_{0.16}$
3	V-SiO_2	6.5	28.5	65	$SiO_{2.28}V_{0.23}$
4	V-SiO_2	7	25.5	67.5	$SiO_{2.65}V_{0.27}$
5	V-SiO_2	9	23	68	$SiO_{2.95}V_{0.39}$

Table 7.1 The percentage composition and stoichiometry of both rf sputtered and vanadium co-sputtered oxides, after annealing at 900°C in nitrogen.

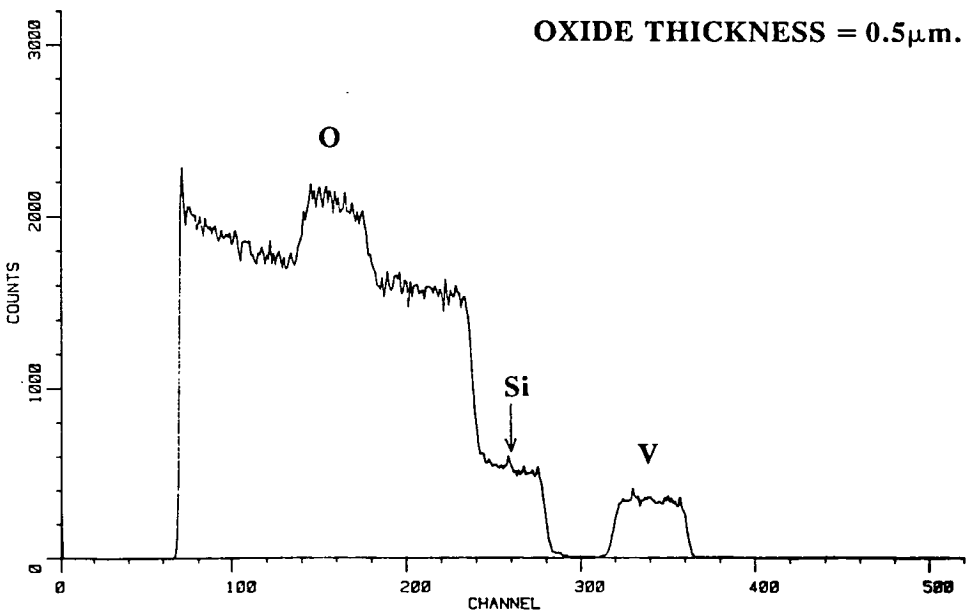

Fig 7.1 A typical backscattering spectrum for an SiO_2 film co-sputtered with 9 atomic percent vanadium. The sample was annealed at 900°C in nitrogen for 30mins.

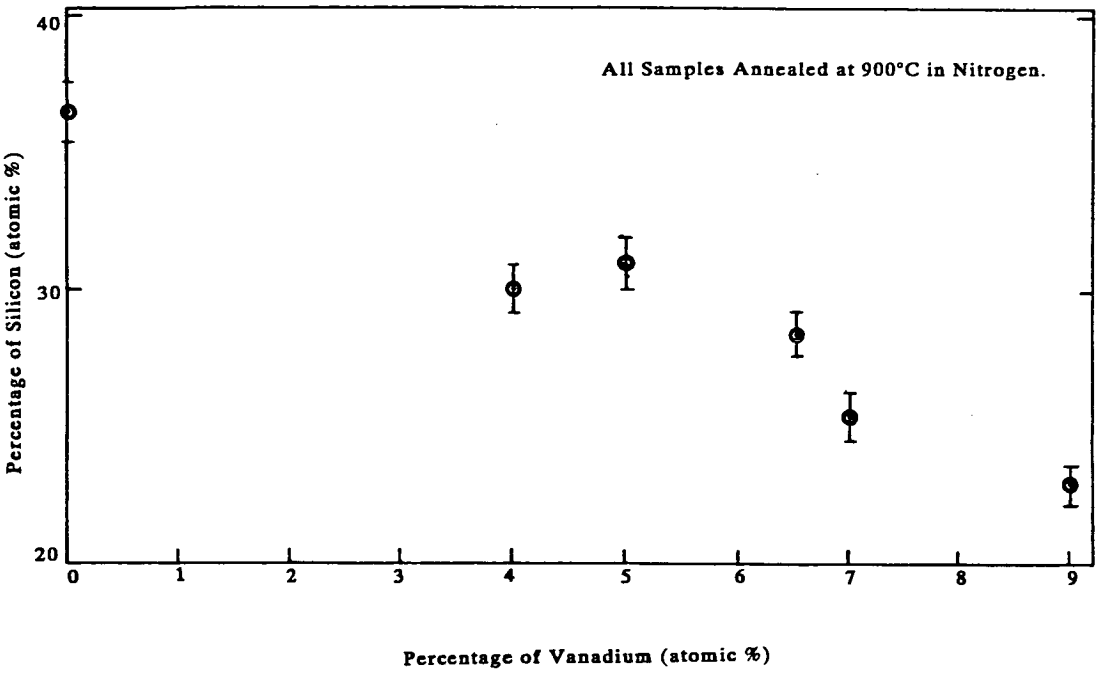

Fig 7.2 Variation in the percent composition of silicon as a function of incorporated vanadium (all samples were 0.4μm thick).

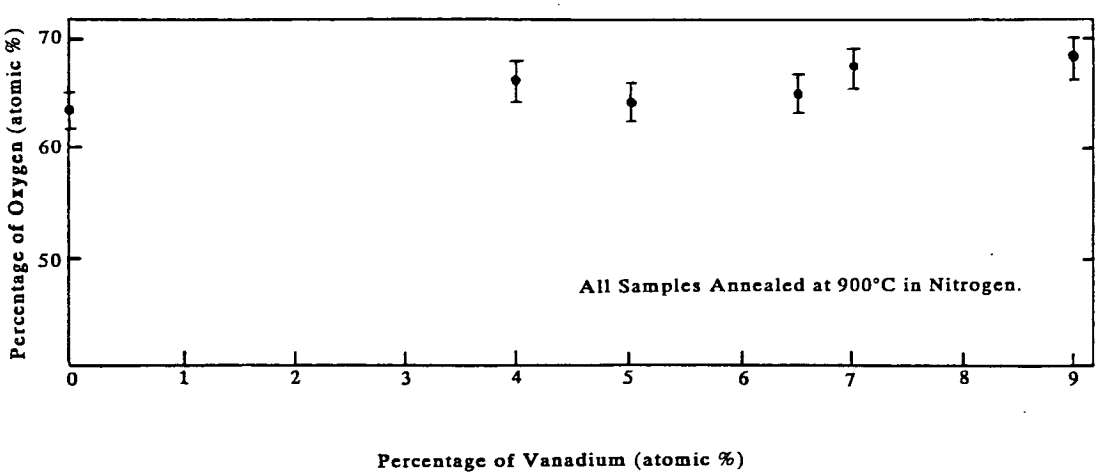

Fig 7.3 Variation in the percent composition of oxygen as a function of incorporated vanadium (all samples were 0.4μm thick).

the undoped SiO_2 films except that the absorption bands normally found at 1070 and 800 cm^{-1} in the as-prepared film are shifted to lower wavenumbers and broadened as a result of the incorporation of vanadium. The band at 450cm^{-1} however remains unchanged but a new band is present at 910cm^{-1}. Upon annealing at 700°C in nitrogen, the dominant Si-O band shifts to 1070cm^{-1}, the band at 795cm^{-1} to 800cm^{-1}, the 450cm^{-1} band remains as in its as-prepared state but the new band is now present at 920cm^{-1}. Further effects of annealing at 900°C in N_2 result in the fundamental Si-O band shifting to an even higher frequency of 1080cm^{-1}, the band at 800cm^{-1} remains fixed and the band at 450cm^{-1} moves to 455cm^{-1} while the new band shifts to 925cm^{-1}. The data for this sample and another containing 9 atomic percent of vanadium, are shown in Tables (7.2) and (7.3) respectively.

The position of the fundamental Si-O absorption band as a function of annealing time at 900°C has been plotted in Fig.(7.5), from the data in Table (7.2). This band which is present at 1060cm^{-1} in the as-prepared film is seen to shift relatively quickly towards 1080cm^{-1} upon annealing. Apart from the fact that it takes less than half the time to reach its final value in comparison to the undoped film (see chapter 6, Fig.(6.9)), the band also moves much closer to the value found for thermally grown oxides. In fact it shifts to exactly the same position as found in thermal oxides i.e. 1080cm^{-1}. This clearly suggests that annealing in N_2 can result in extra oxygen being incorporated into the films as well as the release of a substantial amount of bond strain - a subject which has been discussed in detail earlier in chapter 6, for the case of undoped oxides.

The data in Table (7.3) indicates that as the concentration of vanadium is increased the final position of the fundamental Si-O absorption is reached at lower anneal temperatures. In this particular instance, annealing at 700°C for 30mins. in N_2 is sufficient to cause the Si-O band to reach its final value of 1080cm^{-1}. Unlike the RBS data however, it is not possible to unambiguously relate the increase in vanadium concentration to an increase in oxygen up-take especially since the final position of the Si-O band is the same for all the vanadium concentrations studied.

The appearance of the new absorption band between 910-925cm^{-1} may be understood by making comparisons with the literature on crystalline and glassy vanadium pentoxide (V_2O_5) [1].

According to Rivoalen et al [2], the IR absorption spectra of amorphous and crystallised powders of vanadium pentoxide are essentially similar, showing the same number of bands, occurring at the same frequencies. The only difference is that the

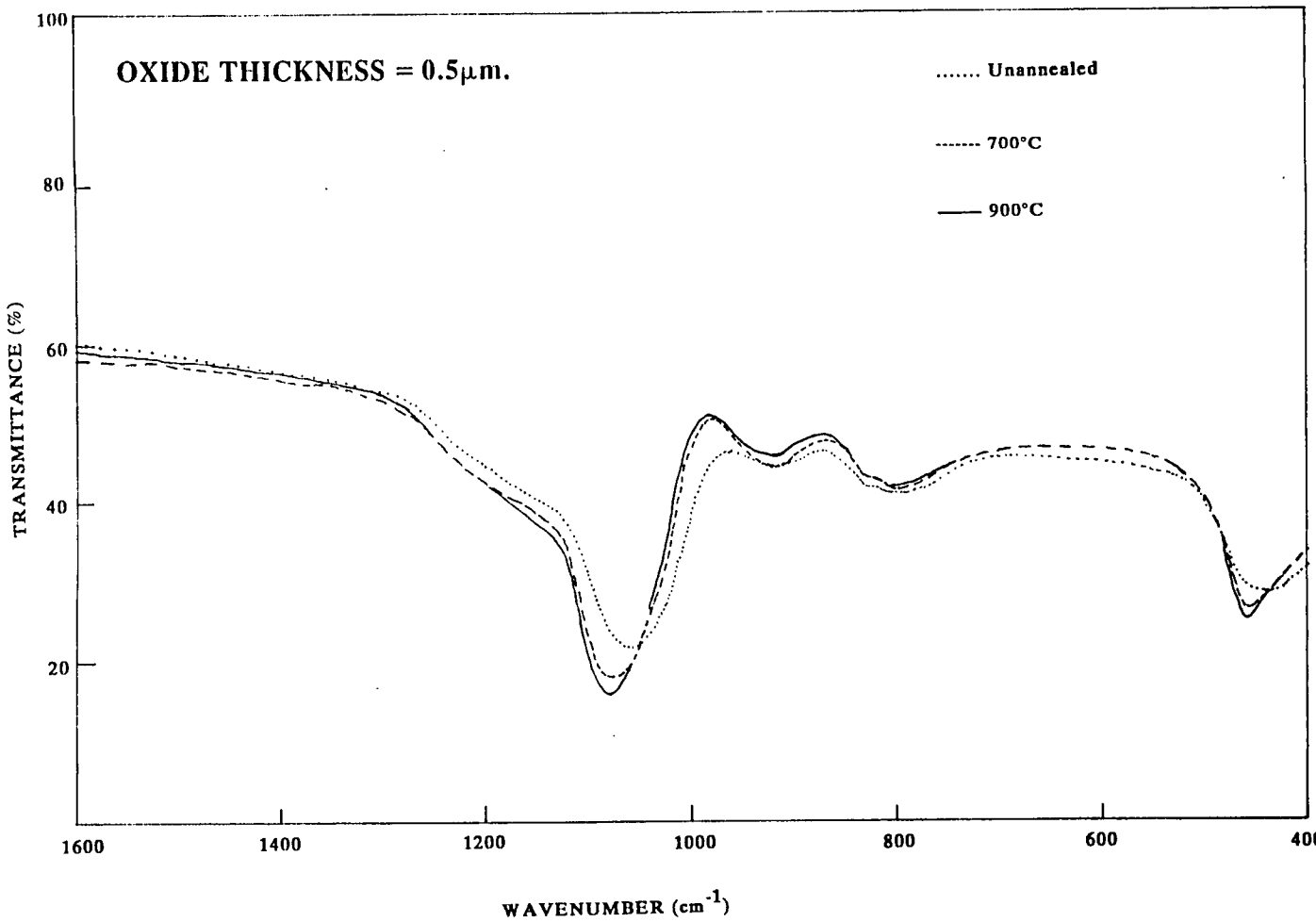

Fig 7.4 The Infrared transmission spectra of a film containing 5 atomic percent vanadium.

Annealing in Nitrogen		Si-O Stretching Absorption Bands (cm^{-1}).			V-O Stretching Band (cm^{-1}).
Temp(°C)	Time(min).				
as-prep	—	1060	795	450	910
700	30	1070	800	450	920
900	5	1075	795	455	920
900	10	1080	800	455	925
900	15	1080	800	455	925
900	20	1080	800	455	925
900	25	1080	800	455	925

Table 7.2 Position of all the infrared vibrational bands as a function of annealing time and temperature, for a film containing 5 atomic % vanadium.

Annealing in Nitrogen		Si-O Stretching Absorption Bands (cm^{-1}).			V-O Stretching Band (cm^{-1}).
Temp(°C)	Time(min).				
as-prep		1060	800	440	915
500	30	1060	800	445	915
700	30	1080	800	455	925
900	5	1080	800	455	925
900	25	1080	800	455	925

Table 7.3 Position of all the infrared vibrational bands as a function of annealing time and temperature, for a film containing 9 atomic % vanadium.

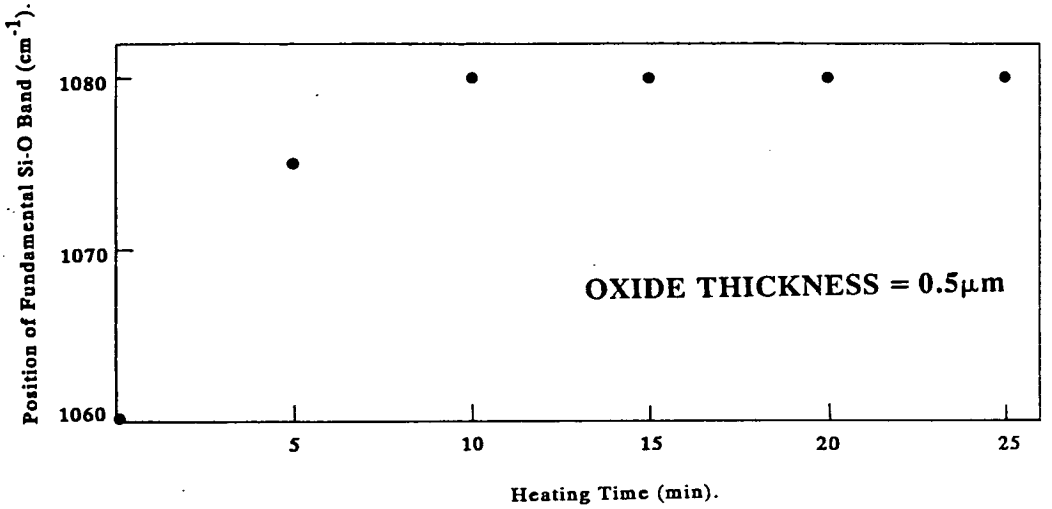

Fig 7.5 Shift of the fundamental Si-O absorption band as a function of annealing time at 900°C.

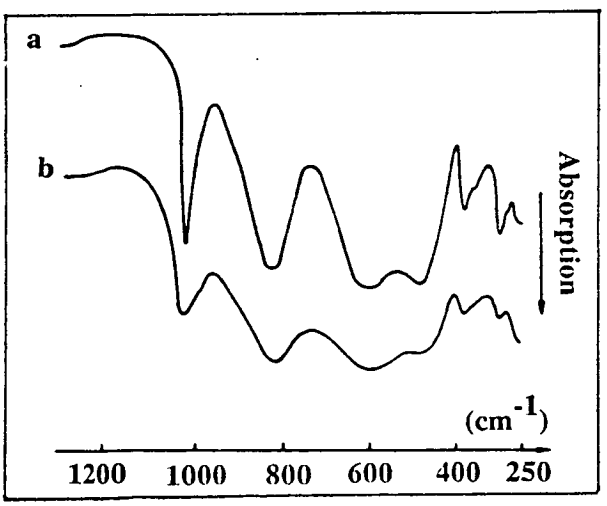

Fig 7.6 Infrared absorption spectra of vanadium pentoxide powders: (a) orthorhombic V_2O_5, (b) amorphous V_2O_5 [2].

line widths corresponding to the amorphous sample are larger and the spectrum poorly resolved. The results they obtained on crystallised and amorphous V_2O_5 are shown in Fig.(7.6). Although it is difficult to estimate accurately the position of the bands in this diagram, crystalline V_2O_5 is known to exhibit vibrational peaks at 280, 370, 480, 660, 800, 915, 1040, 1260 and 1275cm^{-1}. The peak at 1040cm^{-1} is the most pronounced and Dachille and Roy [3] have attributed it to the vanadium-oxygen (V-O) stretching frequency. In fact, in crystalline V_2O_5 the V^{5+} ion exists in sixfold coordination and Janakirama-Rao [4] recognised that as long as the coordination of a cation remains constant, the IR spectra of samples of a given compound are similar. So, when vanadium pentoxide in the glassy state and in the crystalline state give rise to similar absorption bands corresponding to that of the V-O vibration in crystalline V_2O_5, this indicates that the V^{5+} ions in the glassy state are also in sixfold coordination. Other workers [5] have noted, that for compounds in which vanadium ions have been totally ionised to V^{5+}, the V-O stretching frequency is in the range 1025-1005cm^{-1} but the presence of V^{4+} ions tends to reduce the V-O stretching frequency to the 1005-900cm^{-1} range.

From the data presented and by comparing the spectra with those obtained in this work, it is most likely that the effect noted here arises as a result of the vanadium being present in the oxide mostly as V^{5+} and the remainder as V^{4+}.

7.3 ELECTRON SPIN RESONANCE

Both pure silicon dioxide and vanadium co-sputtered films, 2.2μm in thickness were deposited onto pieces of fused silica. Before film deposition, the silica slices were cut into pieces, 2mm by 1.5cm, and three such pieces were used for each measurement. A standard consisting of pitch (strong)† was used to calibrate the position and magnitude of resonance lines. Since the calibration line overlapped the silicon dioxide resonance, spectra were run without the standard and <g> values for the samples were obtained by extrapolation between the line of the standard and the sample. The microwave power was kept low (2-10mW) so as to avoid saturation of the ESR lines and modulation fields were typically 1.0G. Measurements were carried out at 9.35GHz both at room temperature and at 77K and in the absence of any further irradiation. It must be emphasised that no irradiation of the films was performed after deposition. All the

† Standard used by the chemistry department.

paramagnetic centers measured in this work arose solely as a result of the low energy electron and X-ray flux associated with the sputtering process which is markedly different from the usual methods of creating defects in fused SiO_2 [6].

The ESR spectrum of the as-prepared pure SiO_2 film shown in Fig.(7.7) consists of an intense narrow line which is identified by its g value of 2.0007 as the E' center [7]. This center is associated with a hole trapped at an oxygen vacancy, i.e. with the electron in an unsaturated sp^3 orbital of a silicon atom [7]. Defects such as oxygen vacancies are thought to arise as a result of improper bonding and/or the breaking of strained Si-O bonds while additional oxygen vacancies are generated if the film is oxygen deficient.

The rf sputtering process can be conceived of as an intense low energy X-ray and electron flux which impinges on the substrate, creating electrons and holes which become trapped at sites of defect center precursors such as oxygen vacancies and non-bridging oxygens in the SiO_2 network. According to Koenig and Maissel [8], the maximum energy of the bombarding X-rays is in the range 2000-3000eV. X-rays with such energies can easily penetrate the depositing film but are not energetic enough to produce detectable radiation damage in thick fused SiO_2.

Annealing the samples in a nitrogen ambient caused the amplitude of the resonance to decrease, until after an anneal at 500°C it was no longer possible to resolve the ESR signal.

Radiation induced defect centers which arise as a result of rf sputtering have also been studied by Hickmott [6]. His examination centered around SiO_2 films prepared in pure argon but under *re-sputtering conditions*. He was able to resolve three lines, one due to the E' center and two due to the peroxy radical O_2^- [6], indicating that both oxygen vacancies and peroxy linkages were created during the deposition. The relative concentration of these centers (which were designated the HY resonance by Hickmott [6]) was found to depend on the stoichiometry of the film [9]. The broader peaks were attributed to a mixture of O_2^- and non-bridging oxygen hole centers [6]. In addition to these intrinsic defects, the ESR spectra contained broad weak absorptions in the as-sputtered films at about 75G on either side of the E' and O_2^- resonances, see Fig.7.8(b). Annealing the films reduced the E' center and peroxy centers [6,9] leaving a spectrum of three highly asymmetric absorptions which he designated as the HX resonances [6]. Although all the resonances decreased in intensity when annealed in oxygen or nitrogen, similar treatments in forming gas (20% H_2-80% N_2) actually increased the intensity of the three line structure at the expense of the E' and peroxy

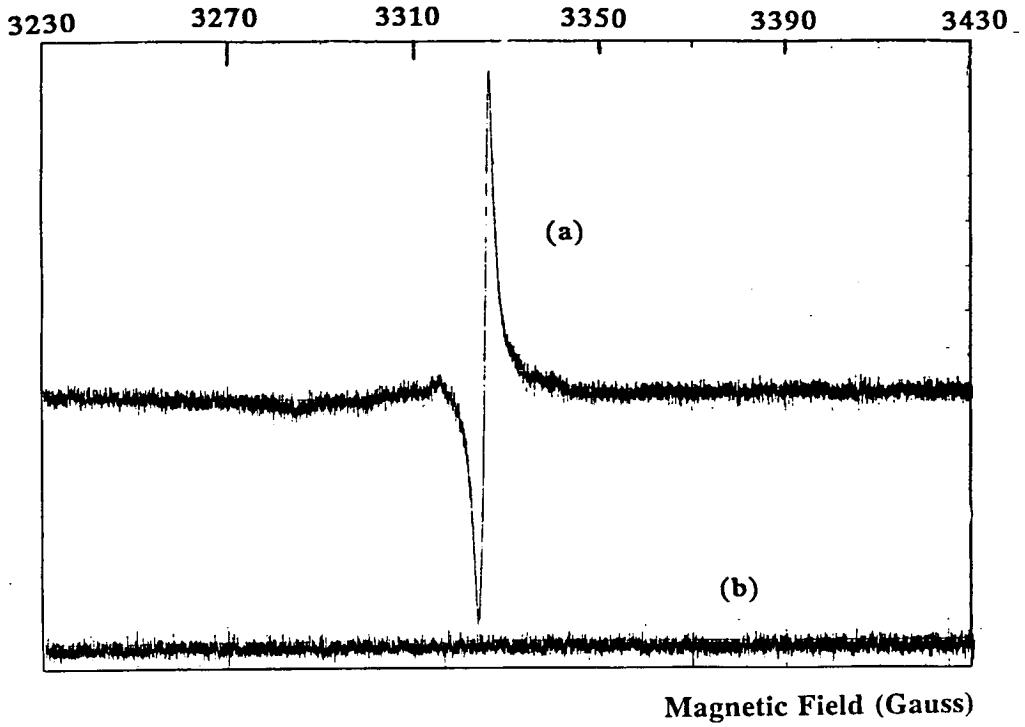

Fig 7.7 (a) The ESR spectrum of an as-prepared pure SiO_2 film at room temperature. (b) ESR spectrum of blank quartz which was used as the substrate. Conditions of measurements were: Gain=8×10^4, Power=10mW and Field Modulation=1.0G.

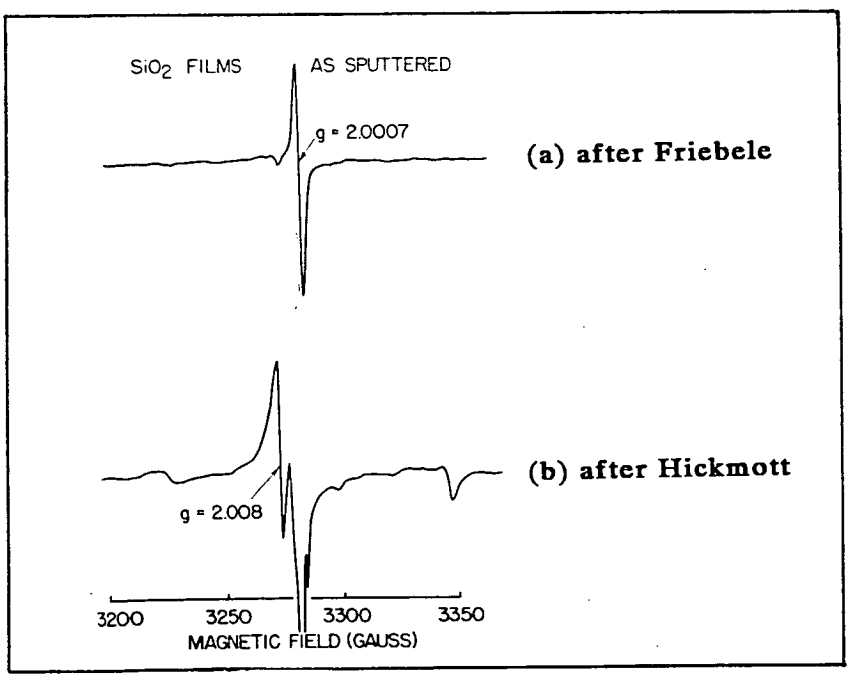

Fig 7.8 X-band ESR spectra of SiO_2 films sputtered in (a) Argon without re-sputtering [7] and (b) Argon with re-sputtering [6].

radical.

The ESR spectra of films prepared by rf sputtering in argon but *without re-sputtering* have been studied by Friebele et al [7]. As in this study, the HX resonances reported by Hickmott [6] were not evident, suggesting that they may well be related to the process of re-sputtering. In addition to the E' center they did however detect a weak absorption at lower fields which was tentatively ascribed to the peroxy radical [7], see Fig.7.8(a).

When vanadium is co-sputtered with silicon-dioxide the resulting ESR spectrum of an as-deposited film is shown in Fig.(7.9). Again, as in the case of the pure film the resonance is attributed to the E'-center. The first thing to notice is that the spectrum in Fig.(7.9) is drawn to the same scale as in Fig.(7.7) i.e. the gain is exactly the same - 8×10^4. Comparison of the two spectra clearly indicates that the incorporation of vanadium into the oxide causes a significant reduction in the intensity of the observed resonance, suggesting that the number of E' centers has been significantly reduced and as in the undoped films, annealing in nitrogen resulted in a decrease of the intensity of the signal until at temperatures of 400°C, it was no longer possible to resolve the resonance.

7.4 AUGER ELECTRON SPECTROSCOPY

The Auger spectra of V-doped (co-sputtered) silicon dioxide on silicon substrates are shown in Fig.7.10(a), (b) and (c). These spectra represent the results of films, 0.05μm thick and heat treated in nitrogen at different temperatures.

Although it was not possible in all three cases to identify the valence state of the vanadium because of the overlap with the large oxygen peaks, it is clear that the concentration and distribution of the impurity remains fixed throughout. A comparison of the spectra for the pure SiO_2 films i.e. Fig.6.11(a), (b) and (c) in chapter 6 and those of the V-SiO_2 films can be made via the diagram in Fig.(7.11). In this figure the average composition of the V-SiO_2 films has been plotted as a function of annealing temperature. Unlike the pure films discussed in the previous chapter, there is no evidence to suggest that Si^{4+} is reduced to Si^{o}.

The average oxygen content of pure SiO_2 films in the as-prepared state and after annealing at 500°C in N_2 for 30mins., is slightly less compared to the oxygen content of the V-SiO_2 films. At the same time the average Si^{4+} content in V-SiO_2 films has decreased. In both types of films, annealing at 900°C in N_2 results in a decrease of the

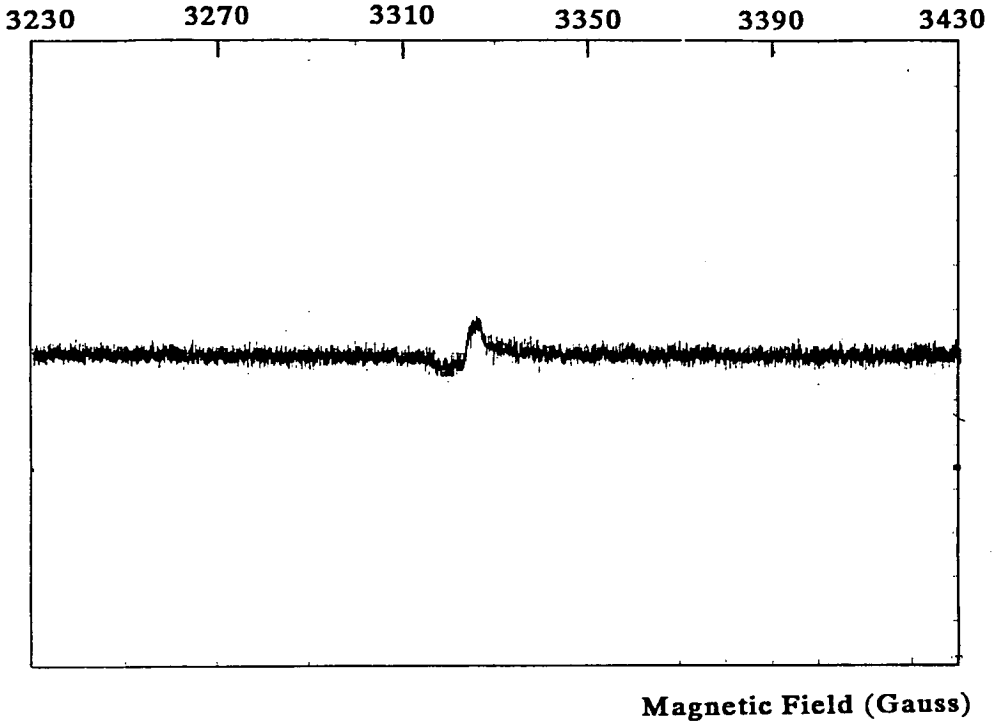

Fig 7.9 The ESR spectrum of an as-prepared vanadium co-sputtered film. Measurement was performed at room temperature under the same conditions as in Fig.(7.7).

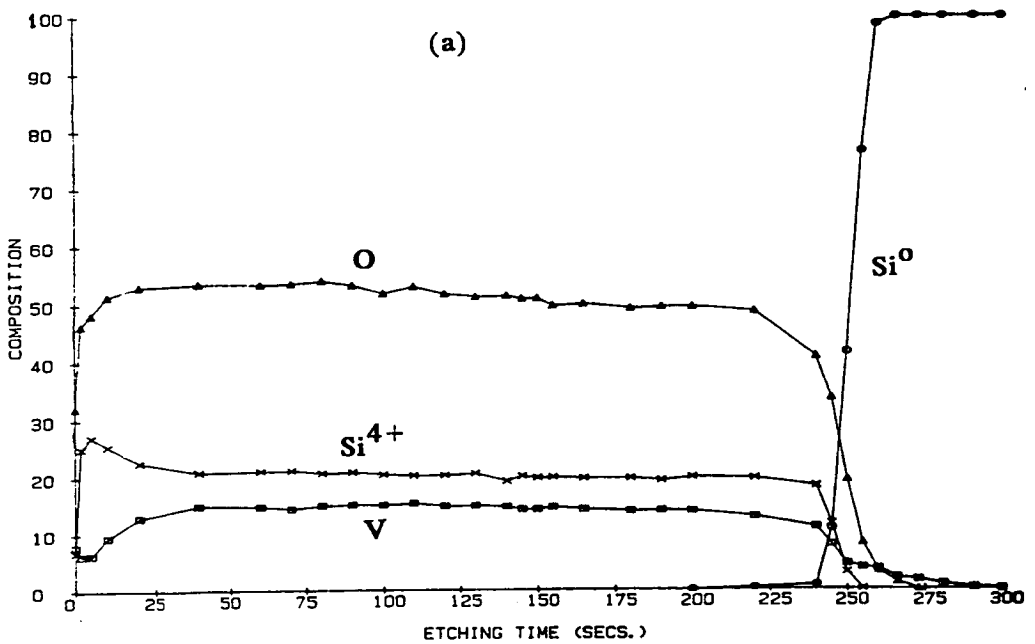

Fig 7.10(a) Chemical depth profile through 0.05μm of rf sputtered V-SiO_2 on silicon. The sample was un-annealed.

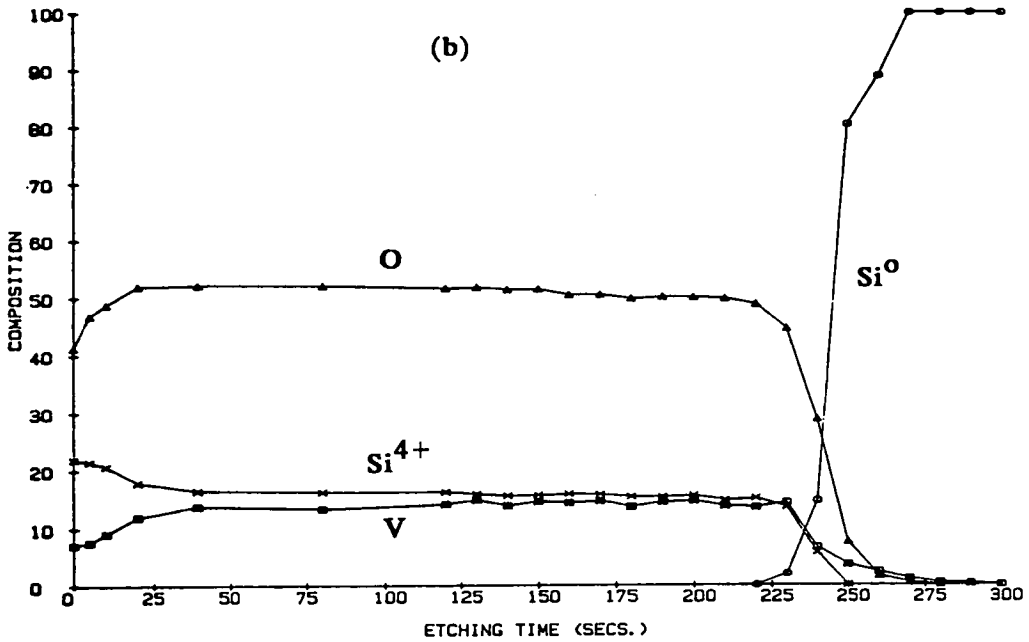

Fig 7.10(b) Chemical depth profile through 0.05μm of rf sputtered V-SiO_2 on silicon. The sample was annealed at 500°C in nitrogen for 30min.

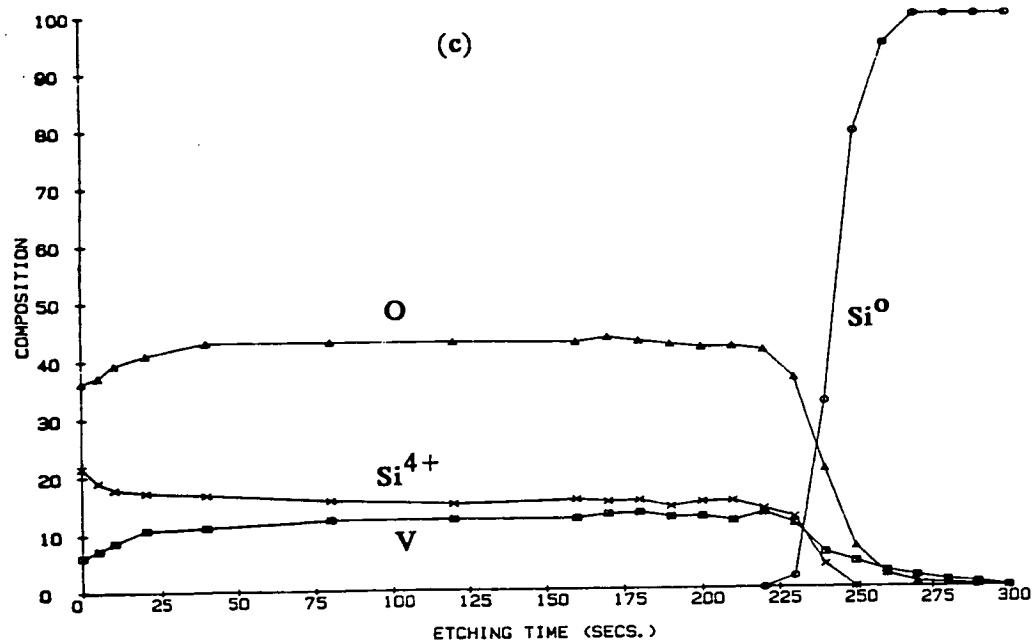

Fig 7.10(c) Chemical depth profile through 0.05μm of rf sputtered V-SiO_2 on silicon. The sample was annealed at 900°C in nitrogen for 30min.

oxygen level. This does not contradict the results presented thus far since at the same time, there is a more pronounced decrease in the Si^{4+} level in films containing vanadium (compare Fig.7.10(c) with Fig.6.11(c)). In fact the O/Si^{4+} ratio of the V-SiO_2 film annealed at 900°C in N_2 is at least ten percent higher than its corresponding value in the pure film. So, even if there is a reduction of the oxygen level, there must be a more significant decrease in the Si^{4+} level in order to maintain a larger O/Si^{4+} ratio in the V-SiO_2 film. This point is borne out in Fig.(7.2), where the amount of silicon is seen to reduce as a result of the addition of vanadium, particularly after annealing at 900°C in nitrogen.

At the interface between the V-SiO_2 film and the silicon substrate, the vanadium profile is seen to tail more so than the oxygen. This is either because the vanadium has been *knocked in* by the argon bombardment or because it has actually diffused into the silicon substrate.

In the as-prepared V-SiO_2 film and just before the vanadium profile reaches zero, the vanadium is most likely present as metal. This is apparent from the fact that the oxygen level has long before decreased to zero.

7.5 CONCLUSIONS AND DISCUSSION

The Auger spectra for the V-SiO_2 films indicate that in all three cases, i.e. as-prepared, 500°C and 900°C anneal, the O/Si^{4+} ratio is on average, at least 10% higher than in the case of the pure films. If as a first estimate it is assumed that the oxygen level does not change by very much across the two types of films and this is indeed seen to be the case in the RBS results of Fig.(7.3), then the only reason for the difference in the O/Si^{4+} ratios, between the pure and V-SiO_2 films, must be attributable to a decrease in the Si^{4+} level in films containing vanadium. This is clearly seen to be the case in both the Auger and RBS measurements of Fig.7.10(a), (b), and (c) [compare with Si^{4+} levels in Fig. 6.11(a), (b) and (c)) and Fig.(7.2)].

The lack of electron/ion beam reduction of Si^{4+} -> Si^{o} in films containing vanadium is presumably related to the stabilising presence of the metal. Knowing that both the pure and V-SiO_2 films are of the same thickness, the V-SiO_2 films appear to etch about three times slower than the pure films. This is again likely to be related to the fact that the V-SiO_2 films do not experience the reduction, Si^{4+} to Si^{o}, during the sputtering process.

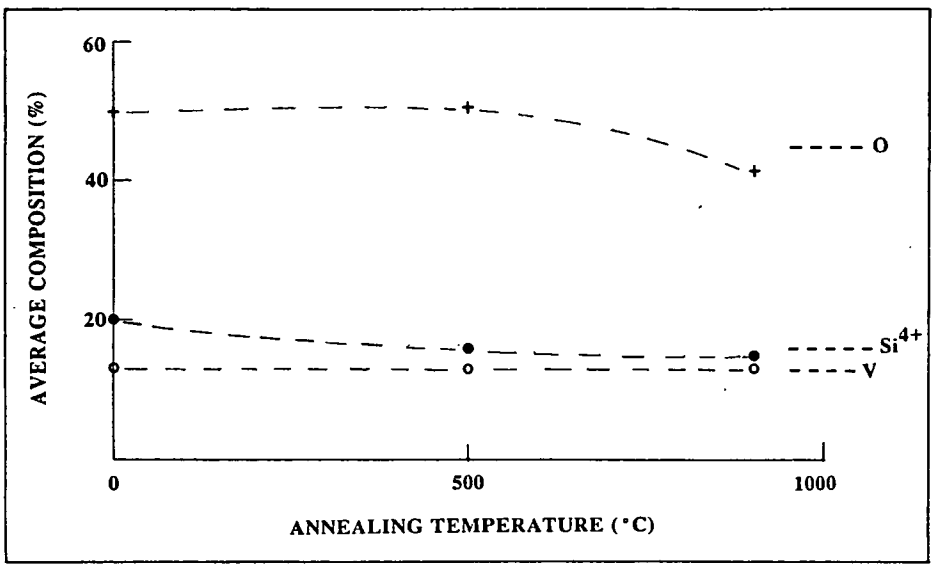

Fig 7.11 The average composition of a V-SiO_2 film (co-sputtered) as a function of annealing at different temperatures in nitrogen.

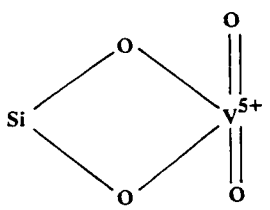

Fig 7.12 Suggested configuration of vanadium pentoxide in the SiO_2 network.

A comparison of the results obtained from IR and RBS measurements in general, indicate a reasonable degree of agreement. As far as both measurements are concerned, the addition of the metal to the films results in an increase in the level of oxygen (for films annealed at 900°C in N_2) in comparison to the films without the metal i.e. compare the final position of the Si-O band in Tables (7.2) and (7.3) with Fig.(6.9). It is however not possible to make comparisons of the RBS and IR data as functions of the impurity content for the sole reason that it is impossible to unambiguously relate the degree of shift of the fundamental Si-O absorption band, to either bond strain and/or oxygen deficiency. The relationship between the shift of the Si-O band, oxygen content and density has been discussed in great detail in chapter 6.

The information in Tables (7.2) and (7.3) represent data for two films of the same thickness but containing different amounts of vanadium i.e. 5 atomic percent and 9 atomic percent respectively. In both instances the final position of the fundamental Si-O band is $1080cm^{-1}$, however the RBS data suggests that the two films have a difference in oxygen level of approximately 4% (see Table (7.1)). It may be that the IR technique is not as sensitive as the RBS method in highlighting differences in oxygen content of the levels of concern here.

The IR spectra of V-SiO_2 films has revealed the presence of a new band which was associated with V_2O_5, in which some of the vanadium (V^{5+}) was considered to have been reduced to V^{4+}. The ESR signal of films containing vanadium however did not reveal any of the resonances commonly associated with the ESR spectrum of V^{4+}, even at 77K.

Rivoalen et al [2], in their study of amorphous vanadium pentoxide in which two percent of the vanadium ions were reduced to V^{4+}, have noted a strong ESR signal even at room temperature, which was attributed to the presence of the V^{4+} ion, but in V_2O_5 in which less than 2 percent of the vanadium ions were reduced to V^{4+}, no such signal was observable. If this is the situation and since the IR data in this study suggests that some V^{5+} ions may have been reduced to V^{4+}, it should then have been possible to identify the presence of the V^{4+} ion by ESR. This did not occur either because an insufficient amount of V^{5+} was reduced to V^{4+}, making it impossible to detect or, no V^{4+} was actually produced.

Recent X-ray Photoelectron Spectroscopy measurements on V-SiO_2 films, 2μm thick and in the as-prepared and 900°C annealed states, has revealed the presence of V_2O_5 in both cases. Therefore, if vanadium does enter the SiO_2 matrix and is present as V_2O_5, one possible configuration is that suggested in Fig.(7.12). This is the most

likely configuration because the vibrational mode of the alternative, V=O is known to occur at a higher wavenumber than that of O=V=O.

7.6 REFERENCES

(1) S.A. Kutolin, G.S. Botuinkova, O.M. Kotenko, R.N. Samoilova, and I.M. Dokuchaeva, Inorganic Materials., 10, 550 (1974); and references therein.

(2) L. Rivoalen, A. Revcoleuschi, J. Livage and R. Collongues, J. Non-Cryst. Solid., 21, 171 (1976).

(3) F. Dachille and R. Roy, J. Amer. Ceram. Soc., 42, 78 (1965).

(4) Janakirama-Rao, ibid., 49, 605 (1966).

(5) C.A. Hogarth and A.A. Hosseini, J. Mater, sci., 3, 359 (1984).

(6) T.W. Hickmott, J. Appl. Phys., 45, 1050 (1974).

(7) E.J. Friebele, D.L. Griscom and T.W. Hickmott, J. Non-Cryst. Solid., 71, 351 (1985).

(8) H.R. Koenig and L.I. Maissel, IBM J. REs. Develop., 14, 168 (1970).

(9) T.W. Hickmott and J.E. Baglin, J. Appl. Phys., 50, 317 (1979).

CHAPTER 8

ELECTRICAL PROPERTIES OF PURE AND VANADIUM DOPED SILICON-DIOXIDE FILMS.

8.1 INTRODUCTION

This chapter commences with a detailed analysis of the electrical transport properties of the rf sputtered pure SiO_2 films described previously. An extensive treatment was felt necessary, mainly because of the vast literature on pure SiO_2, allowing comparisons to be made between the results of this investigation and the observations of other workers. The effects on the electrical characteristics of the incorporation of vanadium are also examined. Although these measurements involved as much effort and were performed in the same detail as those of the pure films, to avoid repetition only typical examples of the results are presented.

8.2 UNDOPED RF-SPUTTERED SiO_2

Immediately after preparation, the current-voltage (I-V) characteristics of the MIS samples were asymmetric and an example is shown in Fig.(8.1). The top right-hand quadrant (i.e. with the n-type silicon negatively biased) is defined to be the forward direction and in the following sections all the results described on MIS structures correspond to measurements in that direction.

Before the d.c. measurements were conducted, the status of the sample (low- or high-conducting state) was checked by connecting it to a curve tracer (Phillips transistor curve tracer PM 6057). Most of the samples were found to be in a relatively unstable high-conducting state immediately after fabrication, including annealing at 900°C in nitrogen. Meaudre and Meaudre [1] and Meaudre et al [2] in their study of rf sputtered SiO_2 films have also observed a high-conducting state in the high-field region, which they attributed to an unstable state before the onset of breakdown of the oxide, and consequently confined their measurements to fields below this unstable region. As in the work of Meaudre and Meaudre [1], the low conducting state in this study was obtained by applying a relatively high potential across the sample (i.e. corresponding to a field in the range 10^5-$10^6 Vcm^{-1}$ on the assumption that the potential gradient across the sample is linear). At this stage the curve tracer was disconnected and I-V measurements were performed. After the I-V measurements were carried out in the low-conducting state, the sample was placed in the high conducting state by reconnecting the curve tracer, applying a high voltage (field$\simeq 5\times 10^6 Vcm^{-1}$) and using a suitable series resistor to control the current through the sample. Once the sample had been taken through the first cycle, both low- and high-conducting states were stable provided a critical field was not exceeded (e.g. $<10^6 Vcm^{-1}$).

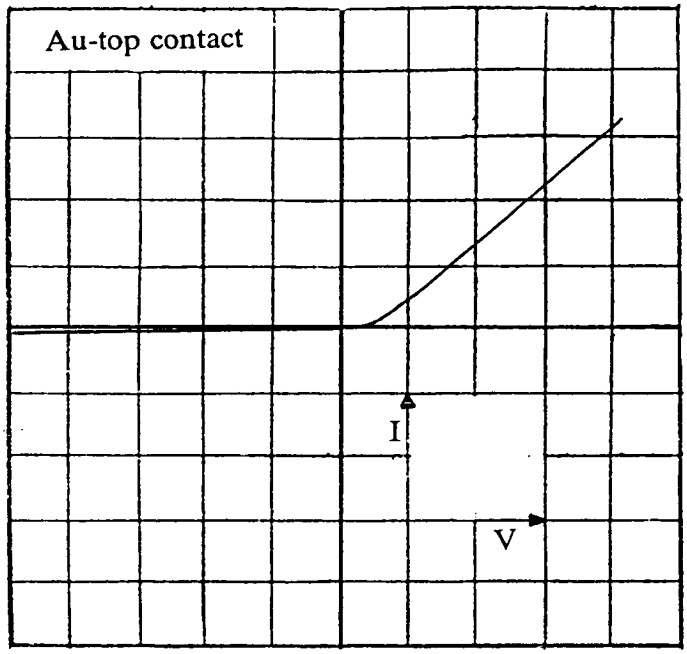

Fig 8.1 An oscilloscope trace of the current-voltage characteristics of a typical MIS structure. The right-hand top quadrant corresponds to the metal contact being biased positively. Vertical scale: 0.5mA per division. Horizontal scale: 0.5V per division.

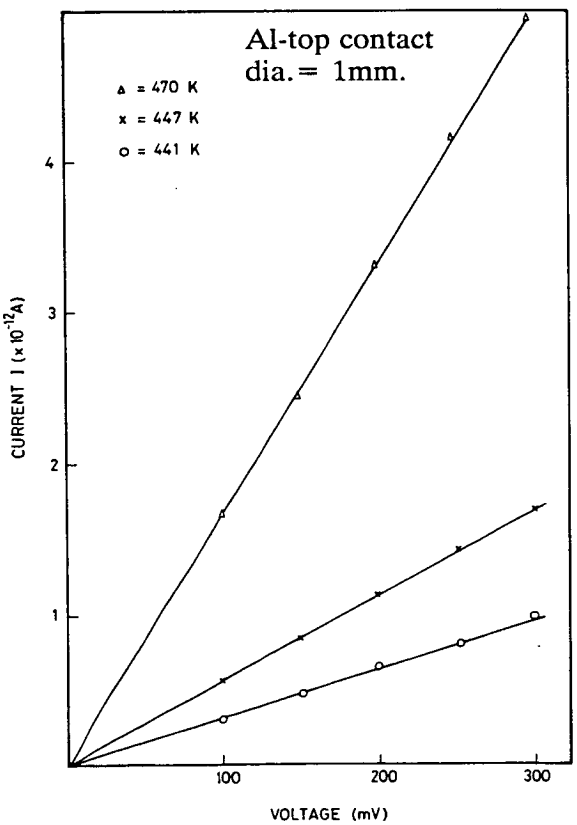

Fig 8.2 The low-field linear current-voltage characteristics in the low conducting state of an MIS structure. The sample thickness is 0.1μm; it was annealed at 1173K.

Detailed I-V measurements were made on the sample in both its low and high-conducting state.

8.2.1 Results

In common with previous work on amorphous SiO_2 thin films, it was observed that at high fields ($\simeq 5\times10^6 Vcm^{-1}$) there is an abrupt change in the electrical properties from a low-conducting state to a more highly-conducting state. Klein [3], Shatzkes et al [4], Verderber at al [5] and Meaudre and Meaudre [1] have also studied high-field conduction and breakdown processes in films of SiO_2 thermally grown on Si and in sputtered films. Klein [3] observed a high conducting state at high fields which he termed *self-healing breakdown*. Shatzkes et al [4] observed threshold switching in thermal oxides which they attributed to filamentary formation at high fields and Verderber et al [5] also reported similar effects in evaporated films of silicon monoxide. There are however significant differences in this work. The properties of the low- and high-conducting states are described and analysed in the following sections (also contained in reference [6], included in this thesis as Appendix IV).

8.2.2 Low-Conducting State

The I-V characteristics are linear (ohmic) at low voltages but become increasingly non-linear at higher voltages. Typical results in the ohmic region for an MIS sample with an oxide thickness of 0.1μm are shown in Fig.(8.2). Over the entire temperature range in which measurements were possible, and measurements were not possible in the case of pure SiO_2 below room temperature because of the very low currents, the conductivity in the ohmic region obeyed the relation

$$\sigma = \sigma_o \exp\left[\frac{-\Delta E}{kT}\right] \qquad (8.1)$$

so that plots of log σ vs 1/T gave good straight lines. The activation energy as determined from such a plot is 0.57eV and a typical set of experimental results is shown in Fig.(8.3).

The important consideration in the present context is the field dependence of current. When the high field measurements at different temperatures are plotted in the form of Log J versus V, as in Fig.(8.4), they provide a good fit to the data suggesting

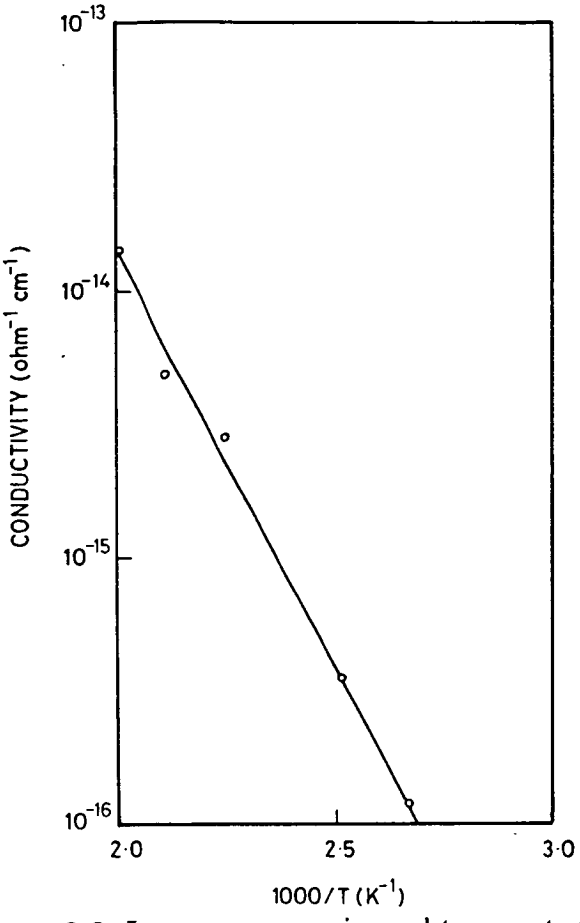

Fig 8.3 Log σ versus reciprocal temperature for the same sample described in Fig.(8.2).

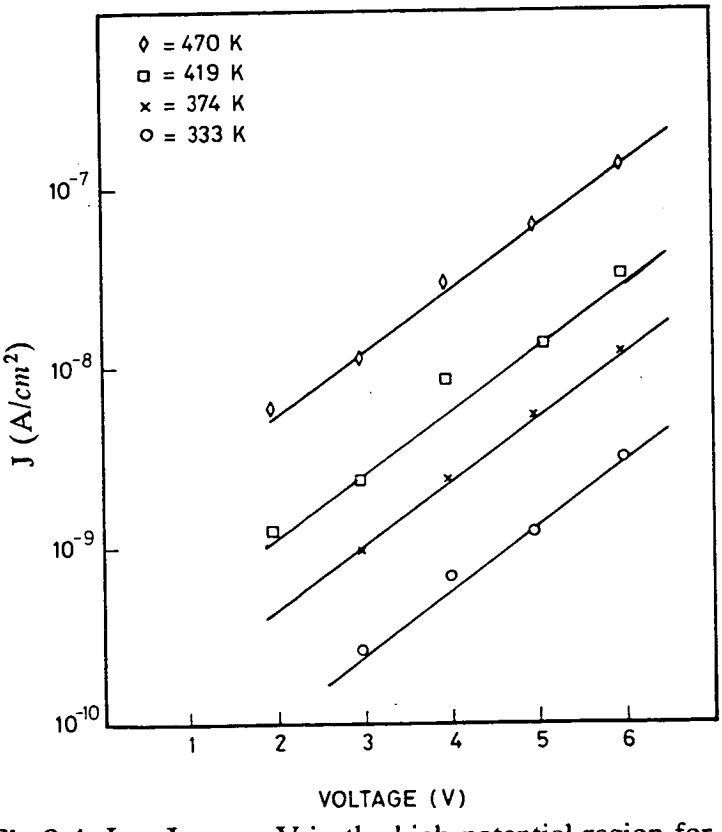

Fig 8.4 Log J versus V in the high-potential region for the sample shown in Fig.(8.2).

the possibility of single-carrier space-charge-limited current in a uniform distribution of traps, such that the current density relationship is given by [7].

$$J = 2en\mu(V/L)\exp(2\epsilon V/N_t kTeL^2) \qquad (8.2)$$

True evidence for space-charge injection however, is given by thickness-scaling measurements, discussed in chapter 2, section(2.5.7). If the scaling law, eqn.(2.33), is to be valid in the present situation then plots of J/L versus V/L^2 should superimpose. A typical set of such plots for three samples, two of which are near the extremes of thickness used in this study, are shown in Fig.(8.5) and it is obvious that the scaling rule does hold.

From eqn.(8.2) two parameters can be extracted, N_t and the $(n\mu)$ product, and in Fig.(8.6) values estimated from the data in Fig.(8.4) are plotted as a function of temperature. The calculated trap density is independent of temperature and is about $2\times10^{18}cm^{-3}eV^{-1}$ while the $(n\mu)$ product increases with temperature. The mobility probably does not vary much with temperature. Measurements of mobility by Hughes [8], shown in Fig.(8.7), indicate that it varies only very slightly with temperature and in fact, over the temperature range of concern, i.e. between the two dotted vertical lines in the diagram, the mobility varies from approximately 10 to $20cm^2(Vs)^{-1}$. It is therefore reasonable, bearing in mind the error in the measurement, to regard the mobility as essentially independent of temperature. This implies that the carrier concentration is temperature dependent and its corresponding activation energy obtained from Fig.(8.6), is 0.51eV.

In the non-ohmic region of conductance, no change in the current-voltage characteristics was observed for fields up to $\simeq7\times10^5$ Vcm^{-1} but the activation energy was found to depend on the applied potential and the results for the sample in Fig.(8.2) are plotted in Fig.(8.8). As the voltage is increased the activation energy is seen to decrease and extrapolates to the value of 0.57eV at low voltages, which is exactly the same value as derived from measurements in the ohmic region (see Fig.(8.3)).

8.2.3 High-Conducting State

Increasing the fields above 10^6Vcm^{-1} caused instabilities to occur until at fields of about $5\times10^6Vcm^{-1}$ there was a rapid transition to a stable higher-conducting state. During the transition to the high-conducting state the current through the device was limited by a series resistance (under typical experimental conditions, a series resistor of

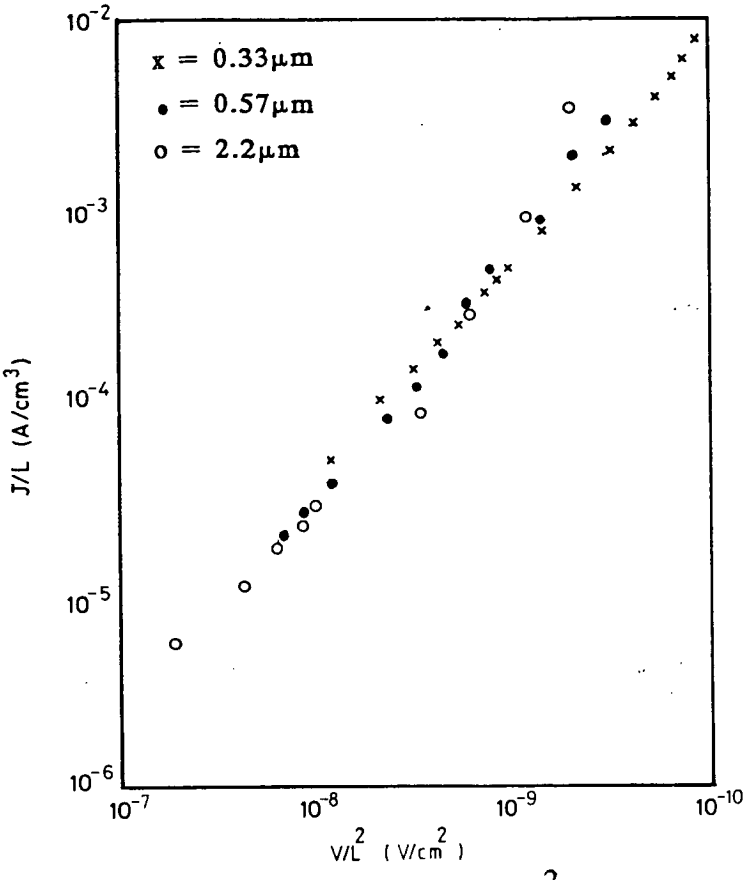

Fig 8.5 Typical results of J/L versus V/L^2 for rf sputtered films in the low-conducting state. Two of the three samples (L= 0.33μm and 2.2μm) are close to the extremes of the thickness range studied in the present work.

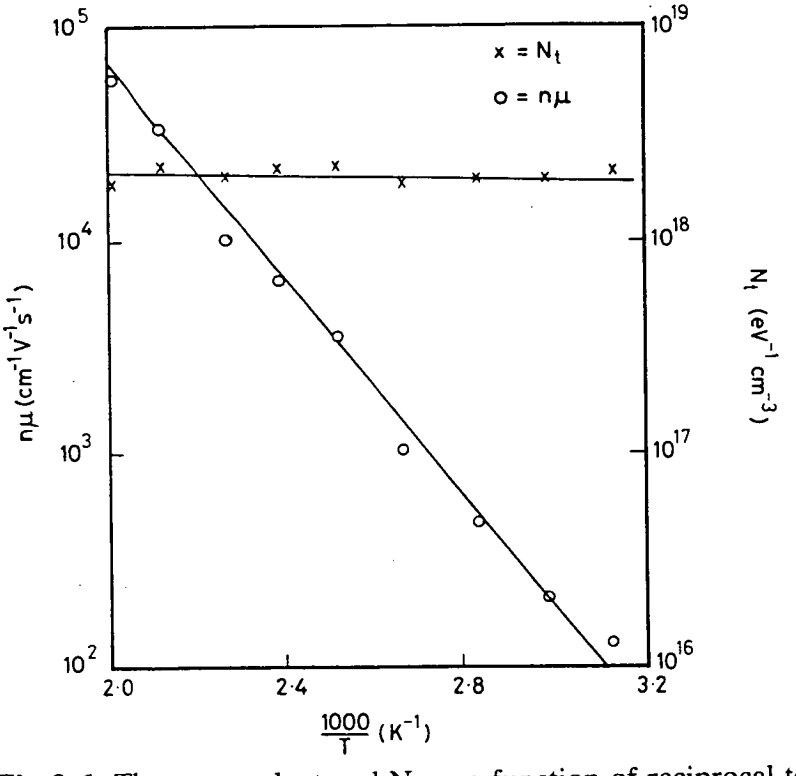

Fig 8.6 The nμ product and N_t as a function of reciprocal temperature in the low-conducting state.

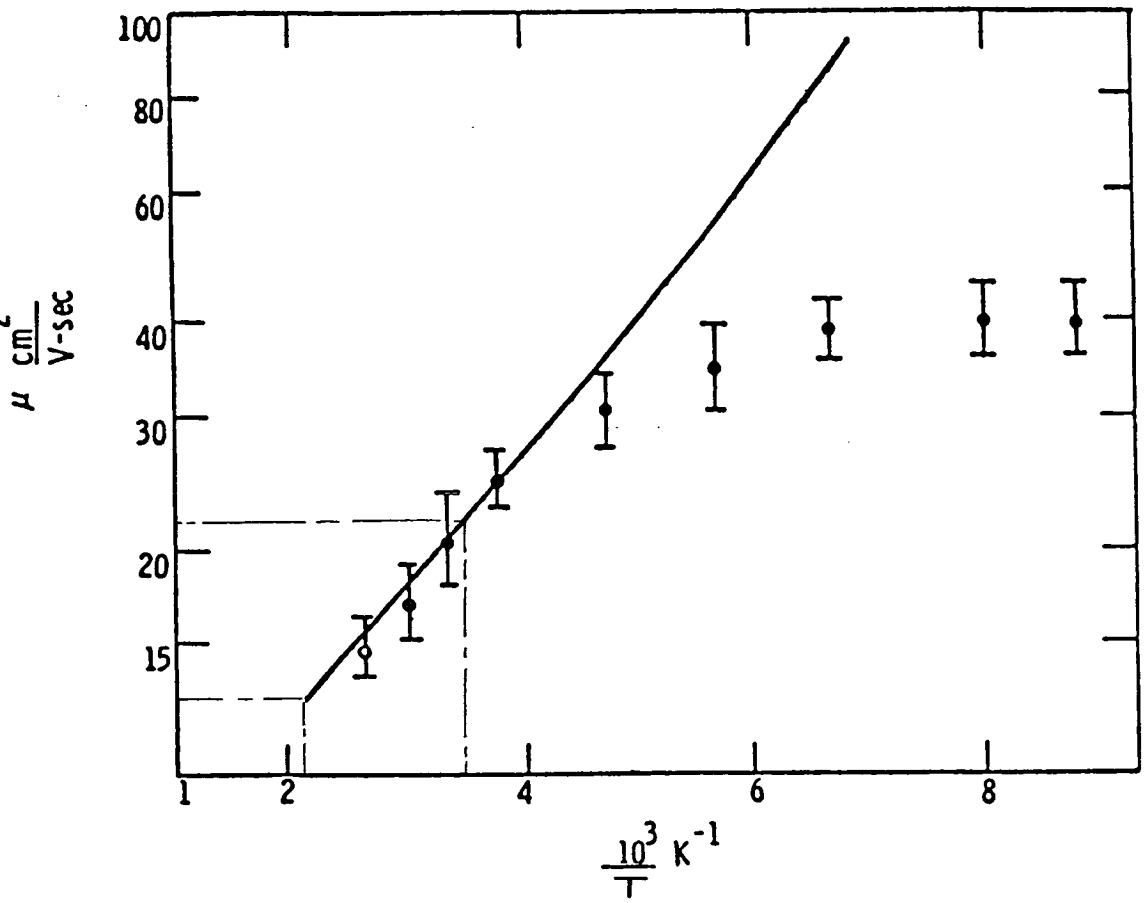

Fig 8.7 Temperature dependence of the electron drift mobility. The solid line is from the Thornber-Feynman theory of electron scattering from LO phonons [7].

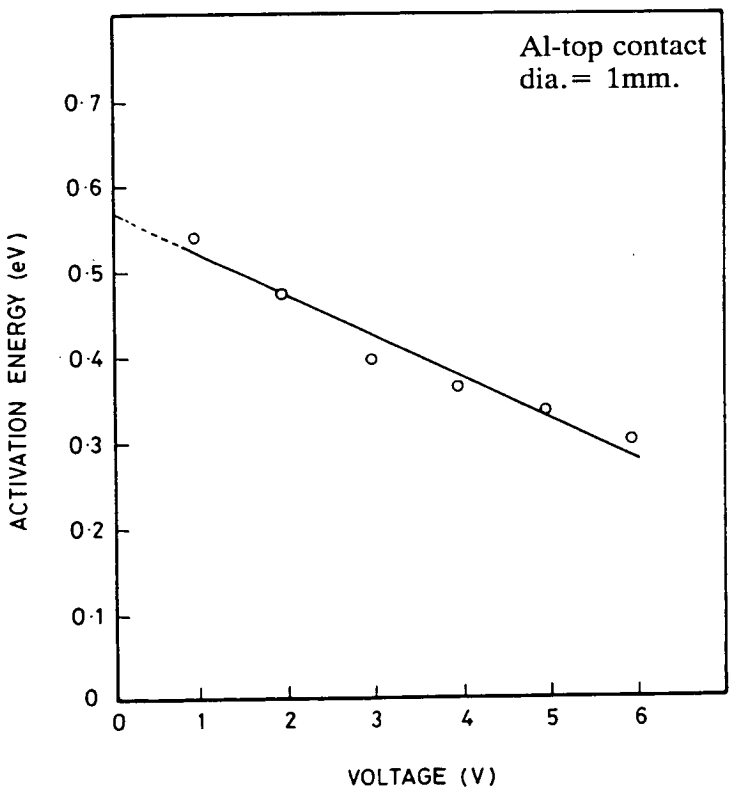

Fig 8.8 The voltage dependence of the activation energy of a typical sample in its low-conducting state. The extrapolated value of activation energy at zero voltage is 0.57eV.

10kΩ, limited the current levels to not more than 3-5mA) to avoid any destructive breakdown. The subject of breakdown has been dealt with in chapter 4, section (4.2.6).

Current-voltage measurements were then performed in exactly the same manner as in the low conducting state, and at least three regions of voltage with different I-V characteristics were evident. At low voltages, the current is ohmic and follows the usual activated form. This is illustrated in Fig.(8.9) for the same sample for which results are shown in Fig.(8.2). These results are plotted in the form of log σ versus 1/T in Fig.(8.10) and while there is a noticeable curvature at high temperatures, a good straight line is obtained over most of the temperature range, corresponding to an activation energy of 0.51eV. The ohmic region at low voltages is followed by a region in which the characteristics are of the form

$$J \propto V^n$$

with $n \simeq 2$ and at higher voltages there is an even higher power-law dependence.

The current-voltage behaviour in the non-ohmic region has been plotted in Fig.(8.11) as log J versus log V and over at least a significant range of voltage, the high-conducting state seems to follow the simple square-law dependence of single-carrier space-charge-limited current appropriate to either the trap-free case or to the situation where the current is controlled by shallow traps [8]. At higher voltages, there is a change to a higher power law and the point at which this change occurs is dependent on the temperature in a manner such that the voltage at which the change occurs decreases as the temperature is increased.

In the region of the characteristics of Fig.(8.11) where $n \simeq 2$, the situation when the current is controlled by shallow traps, can according to Lampert and Mark [7] be represented as

$$J = \frac{9}{8} \Theta \epsilon \mu \frac{V^2}{L^3} \qquad (8.3)$$

where Θ is the ratio of free carrier concentration to the total (free plus trapped) carrier density.

Den Boer in 1983 [9], developed a graphical method of analysis to calculate the density of states from an arbitrary J-V characteristic, with the following assumptions: (a) the injected charge is uniformly distributed in the sample, (b) the electric field is uniform in the film and (c) the trap distribution is continuous and only slowly varying with energy. Taking two points (J_1,V_1) and (J_2,V_2) on a logarithmic J-V curve, the

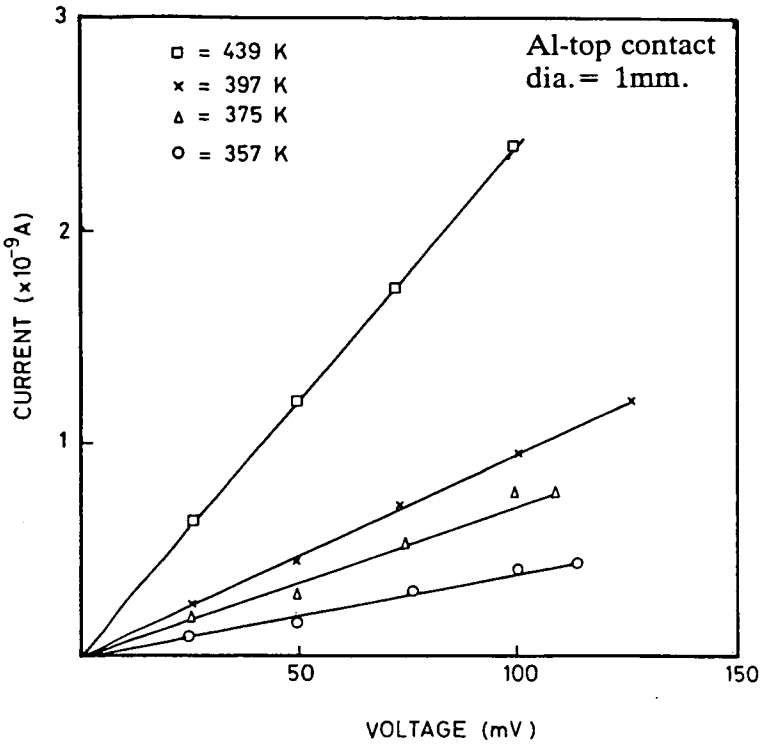

Fig 8.9 Low-field (ohmic) current-voltage characteristics of a sample in its high-conducting state (0.1μm thick).

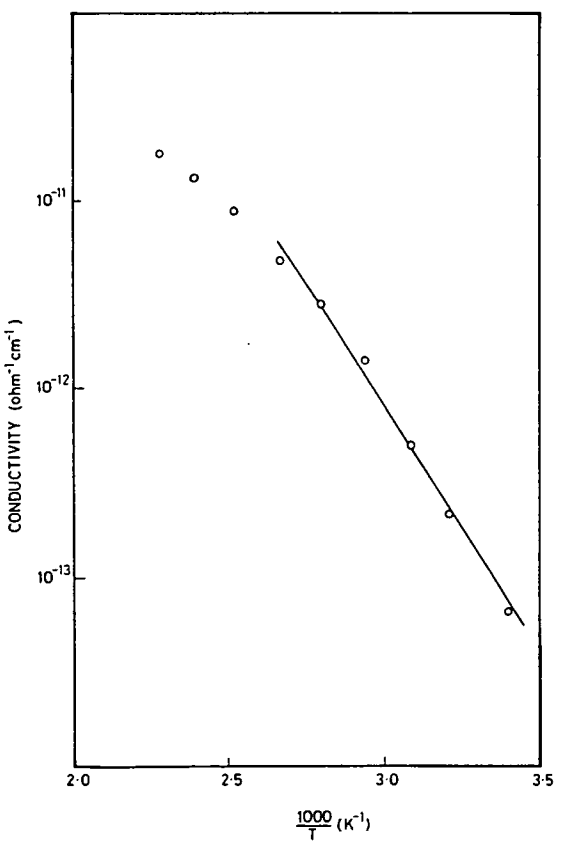

Fig 8.10 Log σ versus reciprocal temperature for a typical rf sputtered silicon dioxide film in its high-conducting state.

shift in the quasi-Fermi level ΔE for a voltage change (V_2-V_1), can be calculated and it is possible to show that

$$N_t = \chi \frac{\epsilon_o \epsilon_r (V_2 - V_1)}{eL^2 \Delta E} \qquad (8.4)$$

The details of the various steps in the analysis of the SCL J(V) characteristic in terms of this graphical method is given in Appendix III and on this basis N_t can be estimated directly from the J-V characteristic. The factor χ, lies between 1 and 2 and accounts for the non-uniformity of the internal space charge field.

In all the analysis in this work, a mean value of $\chi=1.5$ was chosen to obtain the trap density N_t and the results are shown in Fig.(8.12). Note that all the simplifications introduced in this analysis over-estimate N_t by a factor of not more than two.

The data in the $J \propto V^2$ region of the high-conducting state can also be fitted approximately to eqn.(8.2), (i.e. the case of SCLC in a uniform distribution of states, as applied to the low-conducting state) and it is worth noting that values of N_t so derived, are essentially the same as those in Fig.(8.12). It appears therefore that the estimation of the density of states is not very sensitive to the method of analysis and probably gives only an upper limit. The $(n\mu)$ product again calculated from eqn.(8.2), is also shown in Fig.(8.12), and as in Fig.(8.10), there is once more a tendency towards a curve of lower slope at high temperatures.

This data has been summarised in Table(8.1) where the values of N_t and $n\mu$ at room temperature are represented, ΔE_σ is the activation energy for dc conduction and ΔE_n the activation energy for carrier concentration obtained from the $\log(n\mu)$ versus 1/T plot, assuming that μ is independent of temperature. It is apparent that in the high-conducting state the magnitude of the $(n\mu)$ product has increased by about two orders of magnitude compared to the low-conducting state, while its temperature dependence has not changed. On the other hand, N_t has decreased by at least an order of magnitude in the high-conducting state and these relative changes in $(n\mu)$ and N_t are reflected in an increase of about four orders of magnitude in the current on going from a low-to a high-conducting state. The reduction of N_t suggests the possibility of a structural modification in the oxide but whatever the cause of the high-conducting state, it appears to be a bulk phenomenon since the current drawn in the high-conducting state scales proportionately with the area of the electrical contacts (i.e. the conductivity is constant) and some representative results of current as a function of area of the contacts are shown in Fig.(8.13). This result is significantly different to ostensibly similar observations by other workers [3,4,5], who have commonly attributed

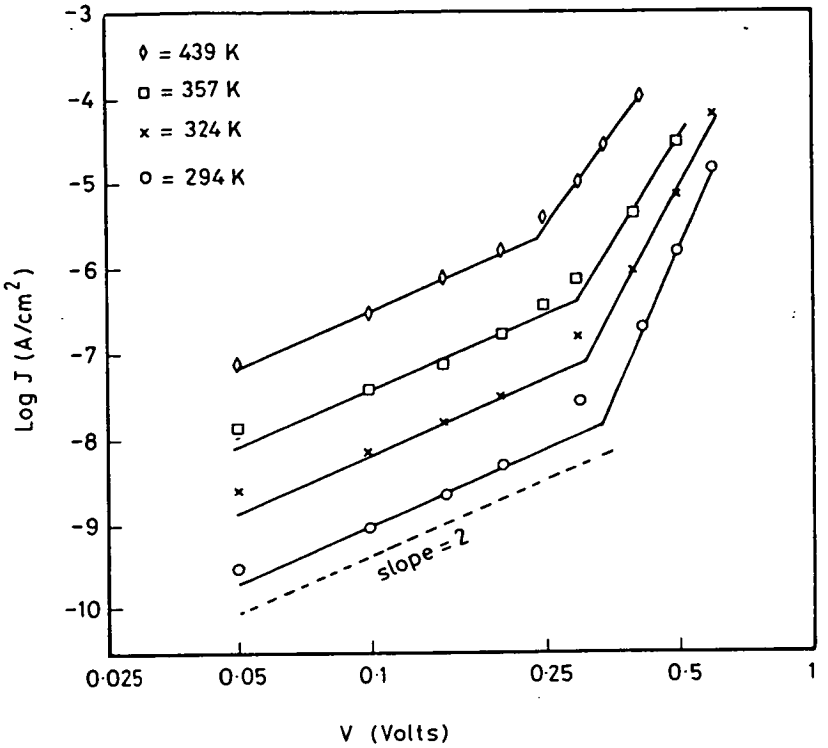

Fig 8.11 Log J versus Log V in the high-field region for the sample shown in Fig.(8.9). The dashed line has a slope of 2 (i.e.$J \propto V^2$).

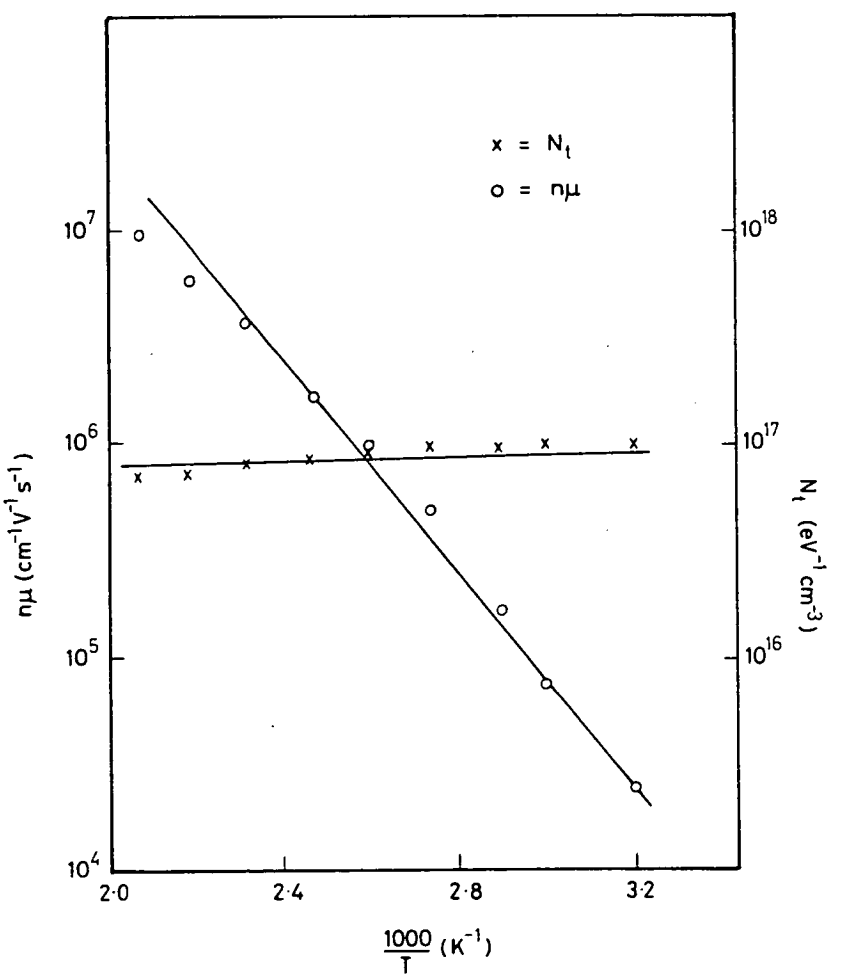

Fig 8.12 The nμ product and N_t as a function of reciprocal temperature in the high-conducting state.

Conducting state	N_t ($eV^{-1}cm^{-3}$)	$n\mu$ ($cm^{-1}V^{-1}s^{-1}$) (room temp.)	ΔE_σ (eV)	ΔE_n (eV)
Low	2×10^{18}	3×10^{2}	0·57	0·51
High	9×10^{16}	$2{\cdot}4 \times 10^{4}$	0·51	0·51

Table 8.1 Summary of the results of N_t, $n\mu$, ΔE_σ and ΔE_n at room temperature for samples described previously.

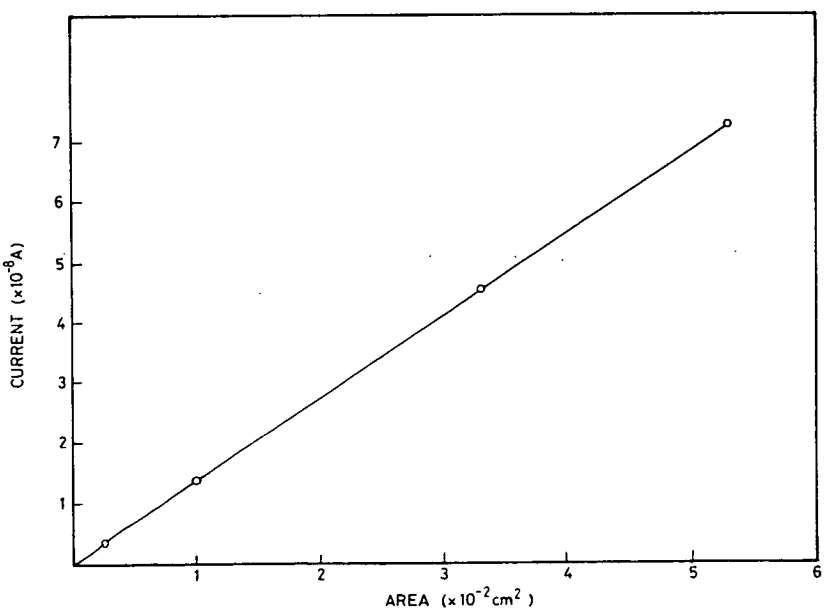

Fig 8.13 A plot of the current versus contact area of a sample in its high-conducting state.

their high-conducting state to the formation of conducting metallic or semi-metallic filaments. Even though the current in the high-conducting state in this work is three to four orders of magnitude greater than in the low-conducting state, the samples retain the characteristics of a uniform insulating or semi-insulating oxide.

All the analyses presented here have assumed that electrons are the mobile species and this is not inconsistent with what is known about the mobilities of electrons and holes in amorphous SiO_2. Indeed, Hughes [8] has shown that the electron mobility is surprisingly high - of the order of $30cm^2(Vs)^{-1}$ at room temperature and only slightly temperature dependent. For this reason, the considerable asymmetry in electron and hole mobilities ($\mu_{hole} \simeq 10^{-5} cm^2(Vs)^{-1}$ at room temperature) is consistent with the single-carrier SCLC being regarded as an electron current.

Although it is too early to speculate, especially in the absence of a.c. measurements, on whether the difference in activation energies in the low-conducting state, i.e. 0.51eV compared with the d.c. activation energy of 0.57eV, is experimentally significant and perhaps attributable to an activation energy for electron hopping, the simplest and obvious interpretation of these results is that the transition from a low- to a high-conducting state is caused by some possibly field induced structural modification in the bulk of the oxide which changes the density and distribution of traps. It is notable that the best fit to the J-V data in the low-conducting state is given by SCLC controlled by a uniform distribution of traps in a range of energy which includes the Fermi level, while for the high- conducting state SCLC controlled by shallow traps (i.e. traps above the Fermi level) seems appropriate.

8.3 VANADIUM DOPED SiO_2

In the sections which follow, the effects of the incorporation of vanadium on the electrical properties of the MIS system are examined. Although the addition of vanadium into the oxide causes a significant increase in the conductivity, the mechanism of conduction does not appear to alter from single carrier SCLC. For this reason, the information is dealt with in a less comprehensive manner with only a presentation of typical results. A list is provided in Table(8.2) of the samples studied, together with informa-

tion on their vanadium concentration and film thickness.

8.3.1 Low-Conducting State

As in the case of the pure films, immediately after fabrication and annealing at 900°C in nitrogen for 30mins., the samples were in a relatively unstable high-conducting state. The low-conducting state was obtained by applying potentials corresponding to fields of the order $10^5 Vcm^{-1}$. Once in the low conducting state, detailed current-voltage measurements were performed and typical results in the form of logJ versus logV, for a V-SiO_2 film, 0.29μm thick is shown in Fig.(8.14).

At low fields (i.e.$<3.5\times10^3 Vcm^{-1}$) the characteristics are linear and ohmic but become increasingly non-ohmic at higher voltages. Plots of logσ versus 1/T in the ohmic region gave good straight lines, corresponding to an activation energy of 0.35eV. The ohmic region at low voltages is followed by a region in which the J-V curves display a reasonably well defined transition to V^2 behaviour. Increasing the fields much above $10^5 Vcm^{-1}$ caused instabilities to occur until a rapid transition to a stable higher-conducting state took place.

8.3.2 High-Conducting State

Once in the high conducting state, current-voltage measurements were performed in exactly the same manner as in the low conducting state and four distinct regions of voltage with different I-V characteristics were observed. This is illustrated in Fig.(8.15) for the same sample for which results are shown in Fig.(8.14).

At low voltages, the current is again ohmic and plots of logσ versus 1/T gave good straight lines corresponding to an activation energy of 0.2eV. On increasing the voltage, at temperatures below about 440K, the ohmic region is followed by a region in which the characteristics are of the form

$$J \propto V^n$$

where $n \simeq 2$. At higher voltages an even higher power law is observed and the index n is about 5. This region is immediately followed by a region in which the index is again 2 i.e. $J \propto V^2$ and is termed the *trap-free* region.

The above result suggests un-equivocally that in samples containing vanadium, the trap-filled limit is easily achieved. The reason for this may lie in the fact that the

Sample Number	Sample Type	Atomic Percent Vanadium	Sample Thickness (Å)
1	V-Cosputtered	4	2900
2	" "	4	3250
3	" "	4	6700
4	" "	5	3100
5	" "	8	6000
6	" "	6.5	4500
7	V-Implanted	equiv. 1	3580

Table 8.2 Tabulated list of the samples studied together with information on their thickness and vanadium concentration.

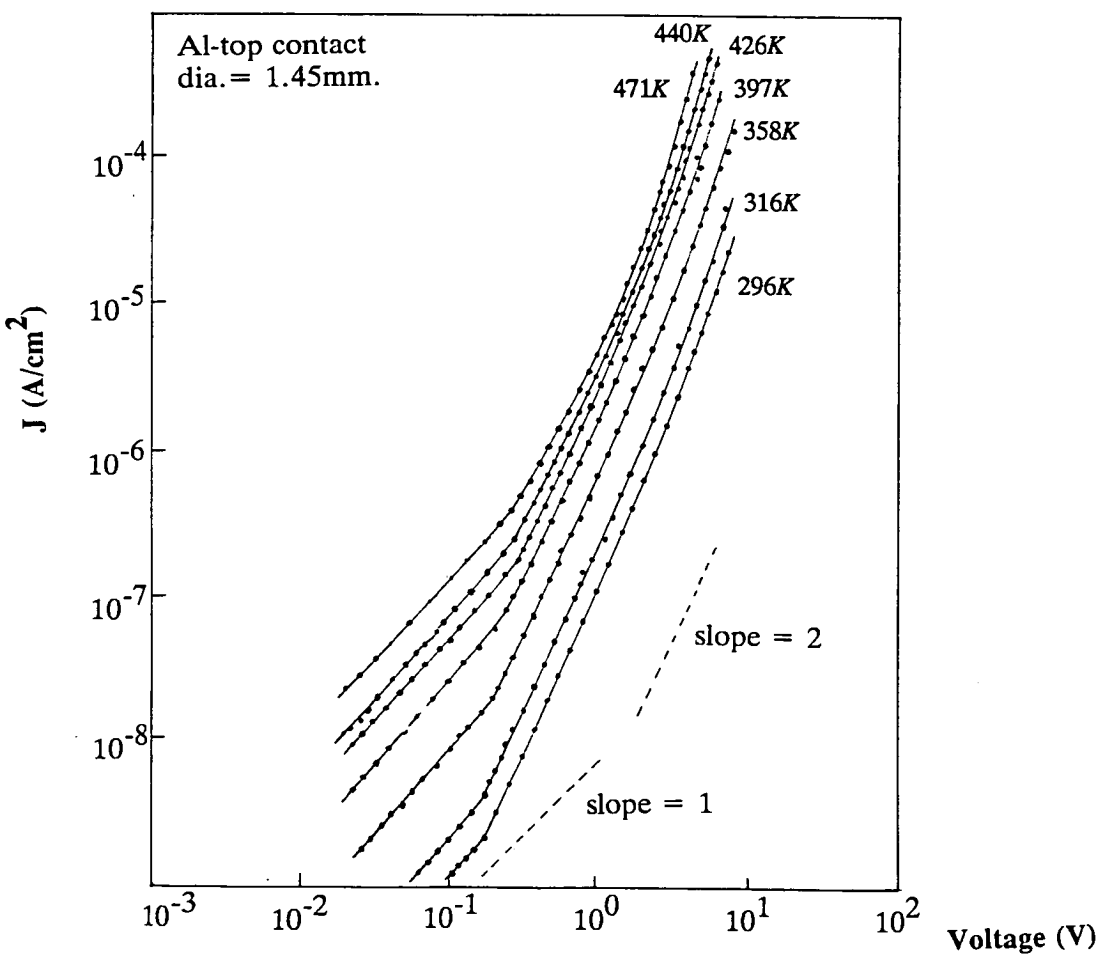

Fig 8.14 Log J versus Log V in the low conducting state of a V-SiO_2, MIS structure. The sample thickness is 0.29μm; it was annealed at 1173K.

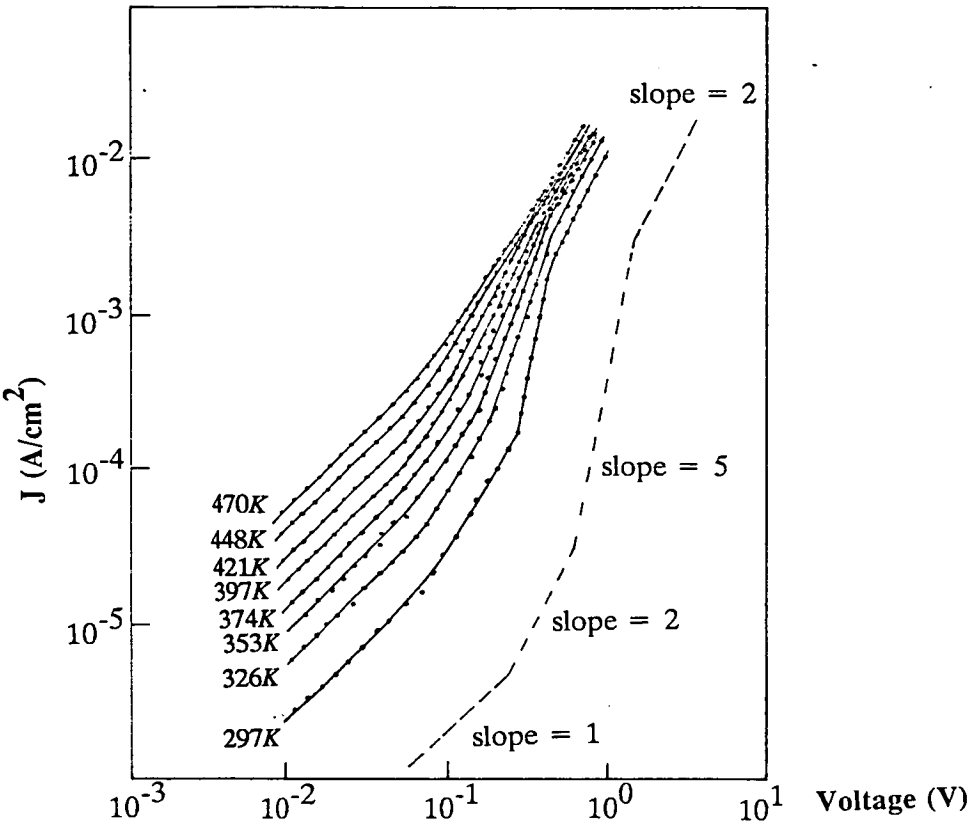

Fig 8.15 Log J versus Log V in the high-conducting state for the sample shown in Fig.(8.14).

Sample Number	Conducting state	N_t ($eV^{-1}cm^{-3}$)	$n\mu$ ($cm^{-1}V^{-1}s^{-1}$) (room temp.)	ΔE_σ (eV)
1	Low	9×10^{17}	2×10^{7}	0.35
	High	2×10^{16}	6×10^{9}	0.2
4	Low	8×10^{17}	3×10^{8}	0.32
	High	5×10^{16}	8×10^{9}	0.21
5	Low	7×10^{17}	3×10^{8}	0.35
	High	1×10^{16}	4×10^{10}	0.18
7	Low	1×10^{18}	5×10^{7}	0.33
	High	7×10^{16}	9×10^{8}	0.22
Pure SiO_2	Low	2×10^{18}	3×10^{2}	0.57
	High	9×10^{16}	2×10^{4}	0.51

Table 8.3 Summary of the results of N_t, $n\mu$ and ΔE_σ at room temperature for various samples including undoped SiO_2. All samples were annealed at 900°C in nitrogen for 30mins.

trap density in these samples is generally lower than in the undoped films. Following Den Boer's [9] step-by-step method of analysis, the trap densities were estimated and the corresponding results are summarised in Table(8.3), along with data on the activation energy and ($n\mu$) products, for some of the other samples. Also included in this table are the data for the undoped films, for comparison.

8.3.3 Capacitance-Voltage Measurements

The effect on the dielectric properties and charge storage capabilities of MOS structures, in which vanadium was co-sputtered with SiO_2, was examined using the high frequency (1MHz) capacitance-voltage technique. The resulting C-V curve for a film, 0.67μm thick is shown in Fig.(8.16). For the range of samples studied, estimates of the relative dielectric constant and fixed oxide charge density on the basis of the analysis presented in chapter 6, section(6.2.5), suggest values of 7.99-8.01 and 3×10^{10}-5×10^{10} charges/cm^2 , respectively.

The C-V technique was also used to determine the charge state of the MOS structures by using the flat band condition as a measure of the charge stored in the oxide. Though these measurements proved inconclusive, the results presented here are not inconsistent with what has been noted so far. From a device applications point, the increase in the relative dielectric constant from its value of 3.78 in the undoped case is significant and not unexpected, since vanadium is a relatively large polarisable ion. Secondly, interface charge in the oxide is known to affect the field at the silicon surface and hence the operating threshold of an MOS device. The observation that the fixed oxide charge reduces when vanadium is incorporated into the oxide is another useful property of the V-SiO_2 structure.

8.4 CONCLUSIONS AND DISCUSSION

D.C. conduction in thin films prepared by the rf sputtering of SiO_2 in an argon atmosphere is shown to be bulk controlled, by the process of single carrier space-charge-limited current. The introduction of vanadium into the oxides whether by co-sputtering of the metal or by ion-implantation, results in films with significantly higher conductivities and lower activation energies compared to the undoped material. The mechanism of conduction does not necessarily alter however and the single carrier space-charge-limited current found suitable in the case of the undoped films, also fits

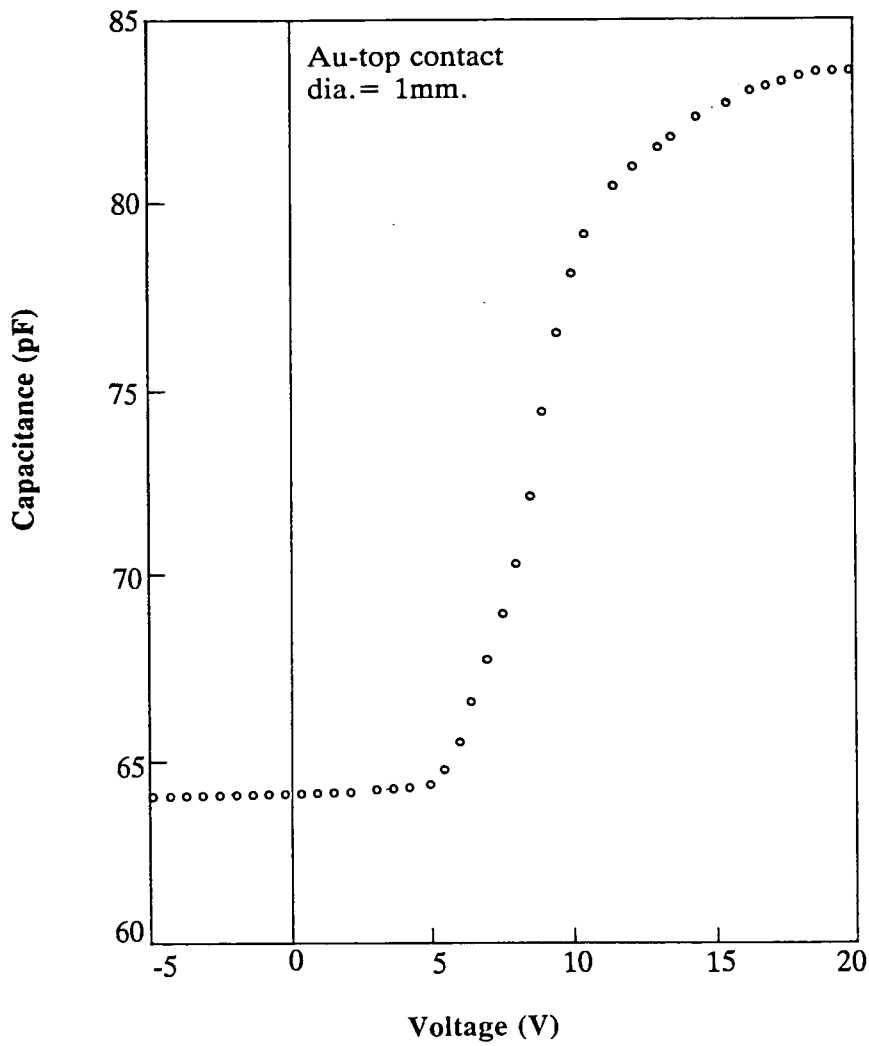

Fig 8.16 The capacitance-voltage curve for a V-SiO_2 film after annealing at 900°C in nitrogen for 30mins. (d≃ 0.67μm).

well with the results of the doped oxides.

Vanadium, also has the effect of increasing the high frequency dielectric constant and reducing the fixed oxide charge density- these results are very significant in terms of device applications, as is shown in the next chapter.

8.5 REFERENCES

(1) M. Meaudre and R. Meaudre, J. Non-Cryst. Solid., 46, 31 (1981); 68, 281 (1984).

(2) M.Meaudre, R. Meaudre and J.J. Hauser, J. Non-Cryst. Solid., 58, 145 (1983).

(3) N. Klein, IEEE. Trans. Electron Dev., 13, 788 (1966).

(4) M. Shatzkes, M. Av-Ron and R.M. Anderson, J. Appl. Phys., 45, 2065 (1974).

(5) R.R. Verderber, J.G. Simmons and B. Eales, Phil. Mag., 16, 1059 (1967).

(6) J.J. DeLima, K.V. Krishna and A.E. Owen, Phil. Mag., 53, 115 (1986).

(7) M.A. Lampert and P. Mark, "Current injection in solids", (NY: Academic Press) (1970).

(8) R.C. Hughes, Phys. Rev. Lett., 30, 1333 (1973).

(9) W. Den Boer, PhD. Thesis, Delft University, (1983).

CHAPTER 9

CONCLUSIONS AND RECOMMENDATIONS FOR FUTURE WORK.

9.1 SUMMARY OF RESULTS ON PURE AMORPHOUS-SiO_2 FILMS

(1) The rf sputtered amorphous SiO_2 films are in an unstable high-conducting state after the initial preparation and annealing but can be stabilised into a low-conducting state by the application of a large potential across the samples.

(2) In the low-conducting state and after careful annealing in nitrogen at 900°C the films possess properties such as density, refractive index and dielectric constant which closely resemble those of thermally grown SiO_2.

(3) The high conducting state is a property of the bulk material rather than due to metallic or semi-metallic filaments.

(4) The two states have different activation energies, i.e. 0.57eV in the low-conducting state and 0.51eV in the high-conducting state.

(5) The high field behaviour in both cases can be explained by single carrier space charge limited conduction and analysis on this basis yields lower values for the density of states in the high-conducting state compared to the low-conducting state.

(6) The validity of the SCLC interpretation was confirmed by thickness scaling measurements.

(7) Analysis on the basis of single carrier SCLC suggests that the transition from the low-to the high-conducting state is caused by a field (potential) induced change in the density and distribution of traps in the bulk of the oxide.

One of the more notable results to emerge is that the high conducting state is *also* a bulk-controlled property, in contrast to many previous reports of similar electrical instabilities in insulators such as SiO_2, where the transition to a state of high conductance has been associated with filamentary conduction or even some form of incipient breakdown.

9.2 SUMMARY OF RESULTS ON VANADIUM-SiO_2 FILMS

(1) RF co-sputtering is an extremely versatile technique for the incorporation, homogeneously, of any metal into silicon dioxide. This is accomplished very simply by attaching, with adhesive, the appropriate metal to the silicon dioxide target.

(2) Segregation of the metal impurity towards the silicon-silicon dioxide interface does not occur.

(3) Incorporation of vanadium into rf sputtered silicon dioxide substantially increases its conductance.

(4) The dc activation energy is reduced when vanadium is added to the oxide.

(5) The presence of the metal in the oxide does not appear to alter the mechanism of dc conduction from that found in the pure films.

(6) Calculations based on the SCLC mechanism, indicate that the presence of the metal causes a decrease in the density of traps.

(7) Incorporation of vanadium into the oxide results in a bleaching of the ESR signal and consequently a reduction in the number of E' centers.

(8) Results from capacitance-voltage measurements indicate that the presence of vanadium causes an increase in the high frequency dielectric constant and a reduction in the fixed oxide charge density.

(9) Finally, the metal is present in the silicon dioxide network as V_2O_5.

9.3 APPLICATIONS

There exist several MOS devices in which the insulator has an active current carrying and/or charge-storage role, such as the MNOS [1] and FAMOS [2] memory structures discussed earlier in chapter 3. In both cases, device operation is determined by the electronic properties of a very thin insulating layer whose thickness is in the range of a few tens of angstroms to about a hundred angstroms, so as to allow sufficient electrical current to pass by the process of quantum-mechanical tunnelling. In these types of application the electronic properties of the insulator are of critical importance. The growth of such thin layers is inherently difficult to control and reproduce and oxides on this scale of thickness tend to be non-uniform, have a large number of pinholes and are leaky.

As a direct result of the present study, it became apparent that a useful alternative is to modify the insulator by doping, so that the same function could be served by thicker and hence more reliable and reproducible insulating layers.

From the results and analysis presented thus far, it is clear that vanadium doped a-SiO_2 films have higher conductivities and lower activation energies compared to pure a-SiO_2 films, and some preliminary experiments on the possible applications of metal-

doped a-SiO_2 were therefore performed. To this end, FAMOS-type semiconductor memory test structures were fabricated in collaboration with Hughes Microelectronics Ltd, Glenrothes.

Test structures having the configuration illustrated schematically in Fig.(9.1) but without the sputtered oxide layer or the polysilicon floating gate were provided by Hughes and the normal thin 'tunnel' thermal oxides were replaced with thicker rf sputtered vanadium doped a-SiO_2 films.

Testing was carried out on a Hewlett Packard Semiconductor Parameter Analyser (4154A). Conditions were maintained and measurements were performed in accordance with the criteria adopted by Hughes for tests carried out on their own thin tunnel oxides. This meant that devices were tested for a current of 1μA and the voltage at which the required current (1μA) was reached, was noted. The current through the devices was controlled by the HP Parameter Analyser and current-voltage characteristics for a structure having 200Å of a sputtered vanadium doped layer are shown in Fig.(9.2). Shown in Fig.(9.3) is another I-V characteristic for an identical structure but with 80Å of a thermally grown pure SiO_2 film, for comparison. The structure with 80Å of thermal oxide, Fig.(9.3), passes a tunnelling current of 1μA at about 15V and most of these devices broke down after about 50 voltage sweeps. The structure with 200Å of vanadium doped SiO_2 gave the same current at between 2-5V which is much lower compared to the thin thermal oxide.

The I-V characteristic of the same V-doped oxide when left in a continuous ramping mode for 3 hours is shown in Fig.(9.4), which is only slightly different from the characteristic at the beginning of the test. It is clear therefore, that devices with thicker layers and containing a transition metal such as vanadium, give more reproducible I-V characteristics on cycling and at much reduced voltages. It is also worth pointing out that the doped oxides are not as prone to rapid degradations, as are the thin thermal oxides.

9.4 RECOMMENDATIONS FOR FUTURE WORK

If device technology of this sort is to be used with reliability and to be transferable from one oxide system to another, it is important to have basic information concerning the nature of the oxide modifications and in particular, to examine carefully the changes in the oxide charge storage capabilities. Other parameters of concern relate to the thermal stability of the induced oxide modification and their spatial distribution

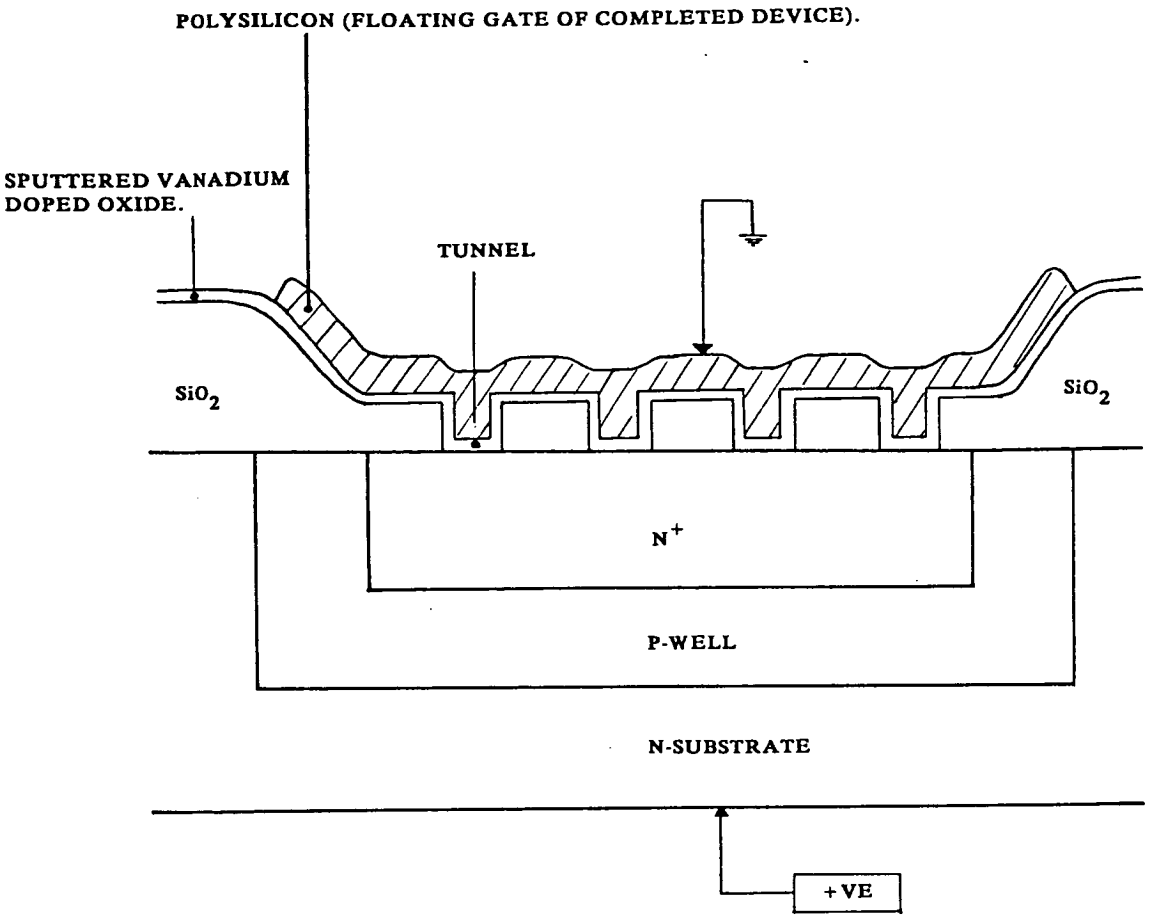

Fig 9.1 Schematic illustration of a typical test structure.

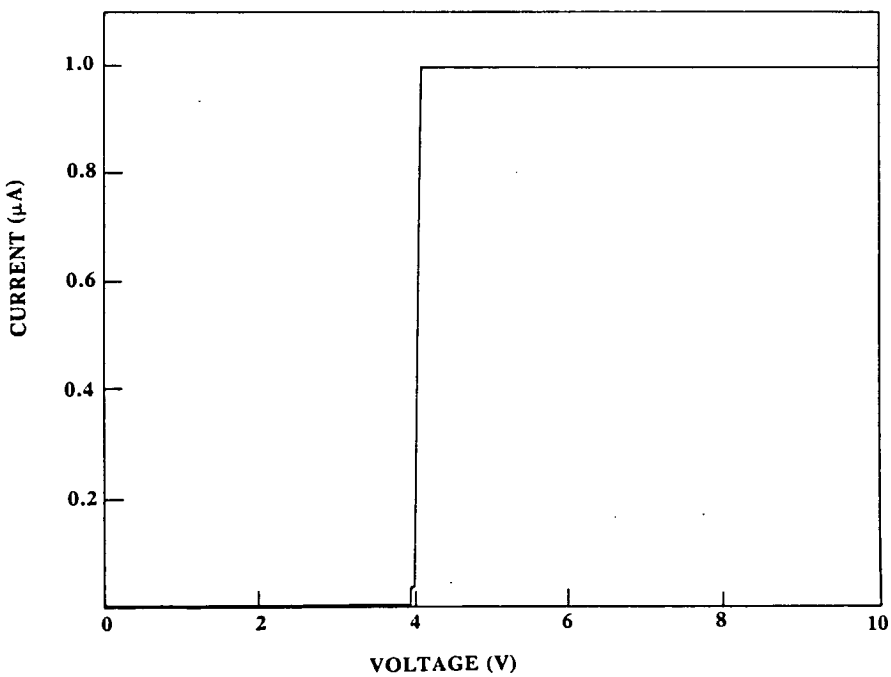

Fig 9.2 Current-voltage characteristic for a test structure containing 200Å of sputtered V-SiO_2. The measuring instrument compliance was set at 1μA.

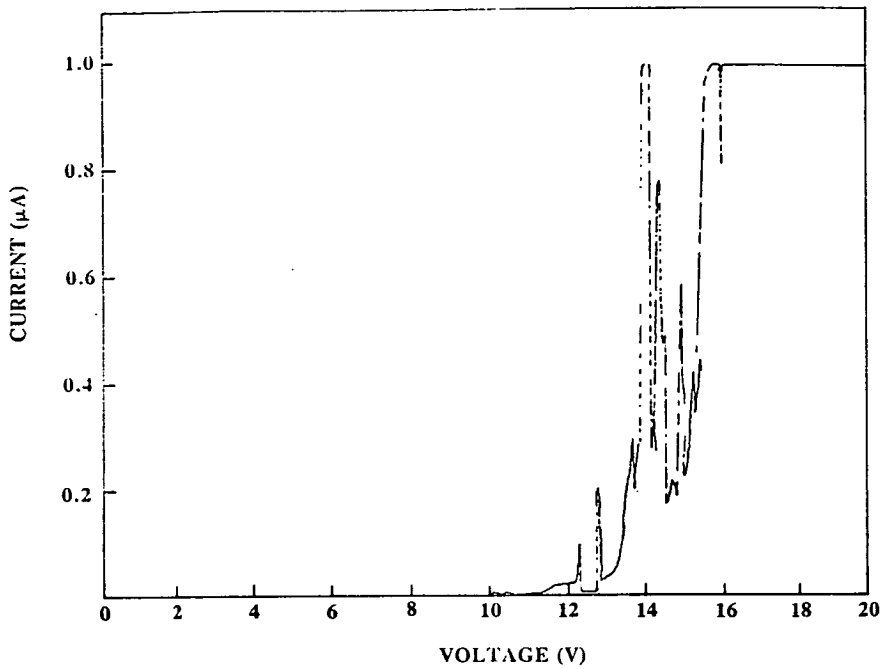

Fig 9.3 Current-voltage characteristic for a test structure containing 80Å of thermally grown SiO_2.

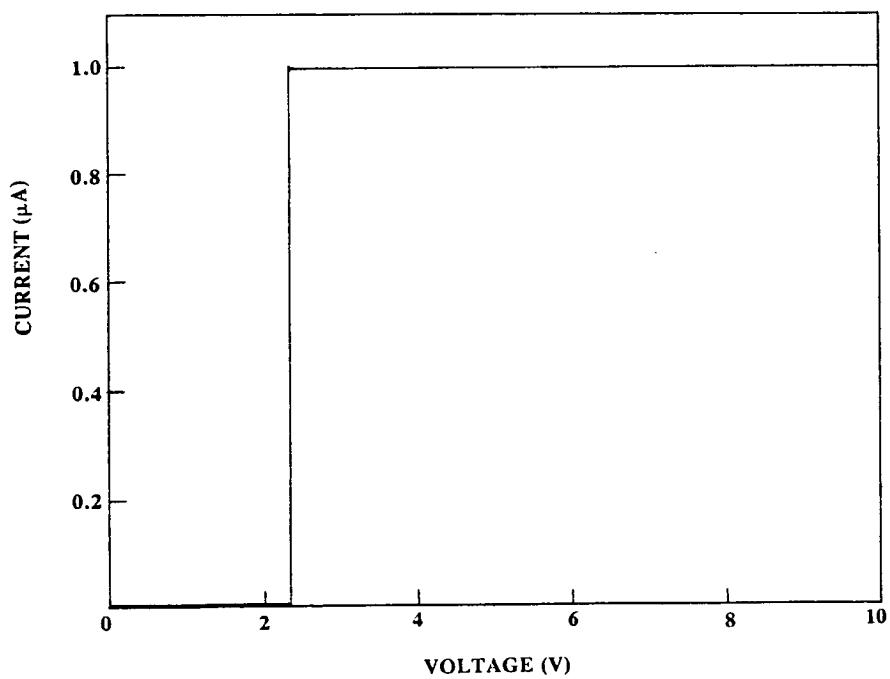

Fig 9.4 Current-voltage characteristic for the sample shown in Fig.(9.2) but after three hours of continuous ramping.

within the oxide. These types of investigations may be undertaken using standard techniques such as, photoinjection, photodepopulation and capacitance-voltage measurements.

As a first step, it would be useful to examine thoroughly the nature and magnitude of any built-in charge associated with the doped insulator for comparison with the positive charge normally associated with pure SiO_2. For this purpose the MOS configuration is a particularly convenient one since the capacitance of the semiconducting layer close to the insulator is very sensitive to the applied field and frequency. Measurements and comparison with control undoped samples, of the flat band voltage shifts as a function of vanadium concentration and of temperature, would be most informative.

On the question of the mechanisms of conduction, further information may be obtained by performing low temperature current-voltage and even a.c. measurements. This is particularly relevant in light of the infrared and ESR results.

Consider as an example, studies of conduction in transition-metal glasses which indicate that in the case of V_2O_5, the vanadium is present as a mixture of V^{4+} and V^{5+} ions and the influence on the electrical properties is a function of the ratio of oxidised to reduced species i.e. V^{4+}/V^{5+} [3,4]. Whether an equivalent situation prevails in the films of this work can only be tested by coupling the low temperature and a.c. measurements with ESR and IR measurements on films containing much higher concentrations of vanadium.

Finally, the methods of doping described in this work need not be restricted to only rf sputtering and/or ion implantation. It may in fact be possible to obtain greater control of the dopant by incorporating it during the thermal oxidation of silicon.

Elements such as vanadium and even titanium and chromium, have compounds which are volatile and decomposable at low temperatures. They are commercially available and so can readily be incorporated into oxides during thermal oxidation or even chemical-vapour-phase deposition. Doping by these techniques would cater for the possibility of varying the electronic properties of a dielectric film in a controlled way by varying the dopant concentration during growth. It would also make it relatively easy to build what would effectively be a dual-dielectric layer, by the sequential deposition of doped and undoped silicon dioxide.

9.5 REFERENCES

(1) E.C. Ross and J.T. Wallmark, RCA Rev. 30, 366 (1969).

(2) D. Frohman-Bentchkowsky, Sol. St. Electron. 17, 517 (1974).

(3) I.G. Austin and N.F. Mott, Adv. Phys. 18, 41 (1969).

(4) A.E. Owen, Contemp. Phys. 11, 227 (1970).

APPENDIX I

DETAILS OF WAFER CLEANSING PROCEDURE.

STEP A

In order to remove the native oxide which slowly forms on the surface of silicon as a result of exposure to air, all the wafers were first placed in a bath of

HF: 15cc
HNO_3: 10cc
H_2O: 300cc

for 30sec., rinsed in deionised water and blown dry with a jet of nitrogen. The rate of attack of SiO_2 was 200A/min.

STEP B

The wafers were then placed in boiling HNO_3 for 10mins., rinsed in deionised water and dried in nitrogen.

STEP C

Organic contaminants which are often found on the silicon surface were removed by placing the wafers for 10mins. in a hot bath of

NH_4OH: 10cc
H_2O_2: 10cc
H_2O: 50cc

This was followed by rinsing in deionised water and drying in nitrogen.

STEP D

The wafers were then placed for 5mins. in a hot bath of

HCl: 10cc
H_2O_2: 10cc
H_2O: 60cc

in order to render ineffective heavy metal complexes such as Cu, Au and Cr. The wafers were then washed in deionised water and dried in nitrogen.

STEP E

The wafers were finally cleaned in trichloroethylene to remove any greasy stains.

APPENDIX II

DEFINITION OF MOS CAPACITORS USING PHOTOLITHOGRAPHY.

After deposition of the appropriate film, Al was evaporated on top of the oxide as described in section (5.4). Photoresist was then spun onto both sides of the wafer and placed in an oven at 80^{o}C for 30mins. The top side of the wafer was exposed to UV light for 5sec. through a positive mask which consisted of dots of the appropriate diameter, developed in developer, rinsed and reloaded into an oven at 120^{o}C for a further 30mins.

The Al on the exposed surface and the remaining photoresist were removed with HCl and acetone, respectively. The wafers were finally rinsed in deionised water and blown dry in nitrogen.

APPENDIX III

THE DETERMINATION OF DENSITY OF TRAPS FROM SCL CURRENT-VOLTAGE CHARACTERISTICS.

In chapter 8 mention was made of the step-by-step method of analysis used by Den Boer to determine $N(\epsilon)$ from a log J versus log V characteristic. The principle of this method is shown schematically in Fig.(A1).

Consider points (J_1,V_1), (J_2,V_2), ... on a logarithmic J-V curve, occurring at intervals defined by a,b,... . As the applied voltage is increased from V_1 to V_2 the quasi-Fermi level moves towards ϵ_c by

$$(\Delta\epsilon_{fn})_a \simeq kT \ln\left(\frac{J_2/V_2}{J_1/V_1}\right) \qquad (A3.1)$$

and the charge per unit area injected in the interval **a** may be expressed in terms of the capacitance as

$$Q_a \simeq \chi \frac{\epsilon_o\epsilon_r}{L}(V_2 - V_1) \qquad (A3.2)$$

where ϵ_r is the relative permittivity and L is the sample thickness. The non-uniformity of the internal space-charge field is accounted for by the factor χ, which is thought to lie between 1 and 2. In all the analysis involving the step-by-step method a mean value of $\chi = 1.5$ was used. As most of the charge injected in the interval **a** will condense into localised states lying in the energy range $(\Delta\epsilon_{fn})_a$, Q_a can be related to the average density of states N_a by :

$$Q_a \simeq eL(\Delta\epsilon_{fn})_a N_a \qquad (A3.3)$$

Substitution of the above equation into eqn.(A3.2) gives for the first interval:

$$N_a \simeq \chi \frac{\epsilon_o\epsilon_r}{eL^2(\Delta\epsilon_{fn})_a}(V_2 - V_1) \qquad (A3.4)$$

As shown in Fig.(A1), $N(\epsilon)$ may be traced out by the repeated application of eqn.(A3.4) in a step-by-step process.

In the present work, N_t was calculated from eqn.(A3.4) using $\Delta\epsilon_{fn}$ steps of 0.01eV. Note also that with $\chi=1.5$ eqn.(A3.4) gives an average N_t with an uncertainity of $\pm 50\%$.

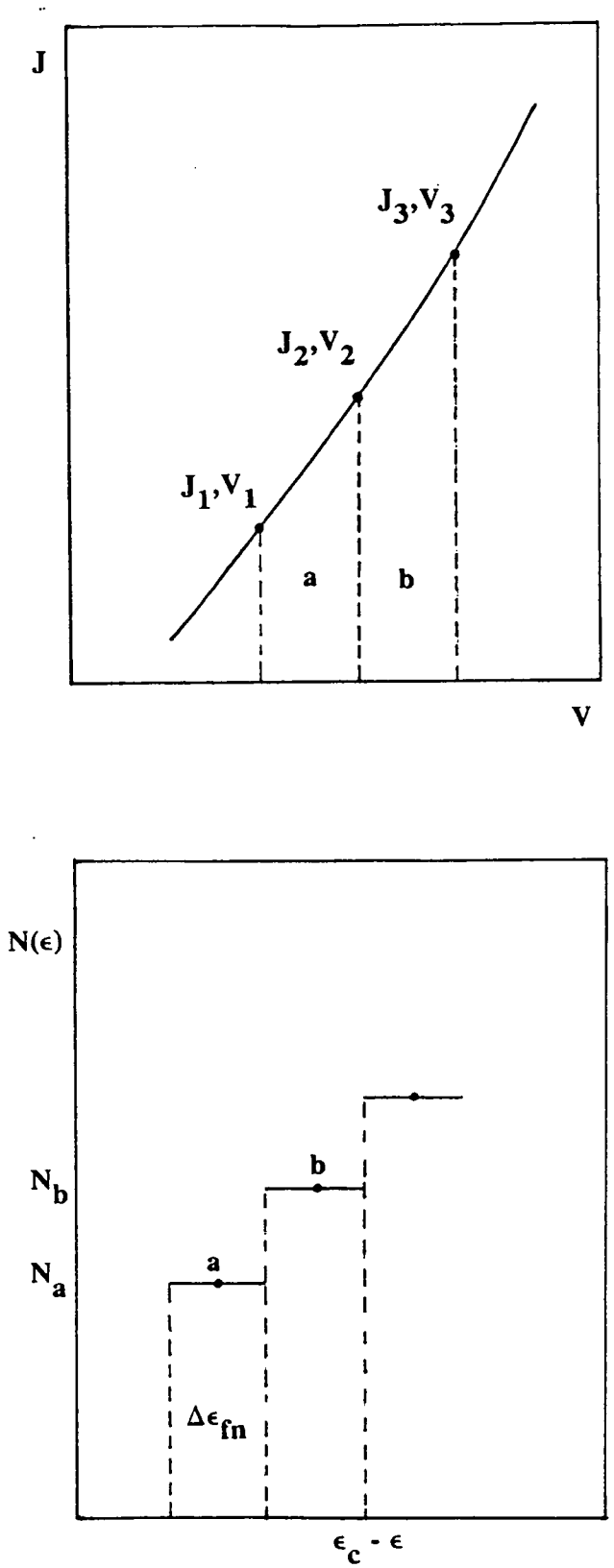

Fig A1 Schematic J-V and N(ϵ) diagrams illustrating the step-by-step method of analysis.

APPENDIX IV

PUBLISHED WORK.

- "A model for the variations in the field-dependent behaviour of the Poole-Frenkel effect", Phys. Stat. Sol (b)., 137, 345 (1986).

- "Electronic conduction and instabilities in thin films of amorphous silicon dioxide", Phil. Mag., 53, 115 (1986).

phys. stat. sol. (b) 137, 345 (1986)

Subject classification: 72.20; 71.55

Department of Electrical Engineering, University of Edinburgh[1])

A Model for the Variations in the Field-Dependent Behaviour of the Poole-Frenkel Effect

By

W. K. Choi, J. J. Delima, and A. E. Owen

The Poole-Frenkel effect is often observed in the field-dependent properties of amorphous materials. Experimentally, it is frequently found that the slopes of log σ versus $E^{1/2}$ plots differ from that predicted by the Poole-Frenkel equation and several theorems have been postulated to explain this discrepancy. Recently, Török used the concept of multiple ionisation to account for such discrepancies. In this paper some of the arguments presented by Török and others is examined in more detail, and the Poole-Frenkel effect is discussed for two limiting cases. The situation when the free carrier density (n) in the case of an n-type material containing both donor (N_d) and acceptor (N_a) impurities, is of the same order of magnitude as N_a where the two approximations are invalid, is more closely examined. It is shown that by assuming a field dependent value of n, a transition region situated between the two approximations is evident. It is also shown that by considering basic parameters such as temperature, and acceptor densities, a Poole-Frenkel plot is obtained which is very sensitive to variations in temperature and acceptor density.

L'effet de Poole-Frenkel est souvent observé dans les propriétés de matériaux amorphes dépendant du champ électrique. Du pont de vue expérimental, on trouve souvent que les gradients de log σ en fonction de $E^{1/2}$ sont différents de ce que donne l'equation de Poole-Frenkel et plusieurs théorèms ont été postulés pour expliquer cette différence. Dans cet article, nous examinous d'une façon plus détailleé quelques unes des idées présentées par Török et d'autres auteurs et nous discutions l'effect Poole-Frenkel dans deux cas particuliers. La situation où la densité des électrons libres dans le cas d'un type de matériaux contenant à la fois les impuretés du donneur (N_d) et de l'accepteur (N_a) est du mème ordre de grandeur que N_a où les deux approximations sont invalides, est examineé de plus près. Nous mettons en évidence que pour une valeur de n dépéndant du champ électrique, une région transitoire située entre les deux approximations est évidente. Il est aussi démontré qu'en considérant des paramètres de base tels que la température et les densités du l'accepteur, on obtient un diagramme de Poole-Frenkel qui est très sensible aux variations de température et de densité de l'accepteur.

1. Introduction

The Poole-Frenkel model of field enhanced emission of electrons from Coulombic donor-like centres (or holes from acceptor centres) is often invoked to explain the non-ohmic conduction frequently observed in many semiconductors [1] and insulators [2]. In its simplest one-dimensional form the Poole-Frenkel model predicts a field-dependent conductivity of the form

$$\sigma(E) = \sigma_0 \exp\left[\frac{\beta_{PF} E^{1/2}}{kT}\right], \tag{1}$$

where

$$\beta_{PF} = \left[\frac{e^3}{\pi \varepsilon_r \varepsilon_0}\right]^{1/2}, \qquad \sigma_0 = e\mu n_0 \exp\left[\frac{-\Delta E_d}{kT}\right],$$

[1]) King's Buildings, Edinburgh EH9 3JL, Scotland.

and ε_r is the high frequency relative dielectric constant, E the applied electric field, $\Delta E_d = E_c - E_d$, E_c is the conduction band level, and E_d is the donor level. It is well-known, however, that the slopes derived from experimental results rarely agree with the prediction of equation (1), and hence it is sometimes generalised as

$$\sigma(E) = \sigma_0 \exp\left[\frac{\beta_{PF} E^{1/2}}{rkT}\right], \tag{2}$$

where $1 \leqq r \leqq 2$, and r (i.e. the slope of $\log \sigma$ versus $E^{1/2}$ plots) may vary as a function of field and temperature.

Török has recently proposed a simple theory [3], involving the notion of multiple ionisation of Coulombic centres, to account for variations in r, as an alternative to earlier less physical models. In 1967, for example, Simmons considered a band model with (for electrons) neutral traps lying above the Fermi level and donor states lying below it, predicting a conductivity which is field dependent in a manner described by the contact-related Schottky effect [4] (i.e. $r = 1$ in equation (2)) but the current is bulk limited, as in the Poole-Frenkel effect. On the other hand, Yeargan and Taylor [2] pointed out that two limiting cases exist for an n-type material containing both donor (N_d) and acceptor (N_a) impurities and for $n < N_a \ll N_d$, r will be 1 while for $N_a < n \ll N_d$, r is equal to 2. They postulated that the experimental results could be better explained by supposing the existence of an intermediate case where $1 \leqq \leqq r \leqq 2$ and this supposition has been widely used [5, 6].

In this paper we examine in more detail some of the arguments presented by Török, and discuss the Poole-Frenkel effect for the above two limiting cases. The situation when the free carrier density is of the same order of magnitude as N_a, where the two approximations of Yeargan and Taylor [2] are invalid, is more closely examined. By resorting to basic band diagrams and introducing appropriate field-dependent parameters, we are able to describe Poole-Frenkel behaviour more completely. It is also shown that by considering parameters such as temperature and acceptor densities, we obtain a Poole-Frenkel plot which is very sensitive to variations in field, temperature, and acceptor density, as is often observed experimentally.

2. Theory. The Field Dependent Carrier Density Model

The concentration of conduction electrons for compensated semiconductors with $N_a < N_d$ may be written as follows [7]:

$$n = N_d - N_a - \frac{N_d}{1 + \frac{1}{2}\exp\left(\frac{-(\Delta E_d + E_F)}{kT}\right)} \tag{3}$$

and the Fermi level (E_F) can be determined from (3) as

$$E_F = -\Delta E_d - kT \ln\left[-2\left[1 + \frac{N_d}{n + N_a - N_d}\right]\right]. \tag{4}$$

The value of n may also be rewritten as [3, 7]

$$n = -\tfrac{1}{2}(N_a + N_c') + \tfrac{1}{2}[(N_a + N_c')^2 + 4N_c'(N_d - N_a)]^{1/2}, \tag{5}$$

where

$$N_c' = \frac{1}{2} N_c \exp\left(\frac{-\Delta E_d}{kT}\right)$$

and N_c is the effective density of states in the conduction band. The carrier concentration, n, for values of n such that $n < N_a \ll N_d$ can be approximated as follows [2, 3]:

$$n_1 = \frac{N_c'(N_d - N_a)}{N_a} = \frac{N_d - N_a}{2N_a} N_c \exp\left(\frac{-(\Delta E_d - \beta_{PF}E^{1/2})}{kT}\right) \tag{6}$$

so that

$$\sigma_1 = e\mu \frac{N_d - N_a}{2N_a} N_c \exp\left(\frac{-(\Delta E_d - \beta_{PF}E^{1/2})}{kT}\right). \tag{7}$$

The Poole-Frenkel plot with this approximation is shown in Fig. 1a. For the case where $N_a < n \ll N_d$, the value of n may be approximated by the following equation [2, 3]:

$$n_2 = (N_c'N_d)^{1/2} = \frac{1}{\sqrt{2}} (N_d N_c)^{1/2} \exp\left(\frac{-(\Delta E_d - \beta_{PF}E^{1/2})}{2kT}\right); \tag{8}$$

$$\sigma_2 = e\mu \frac{\sqrt{N_d N_c}}{\sqrt{2}} \exp\left(\frac{-(\Delta E_d - \beta_{PF}E^{1/2})}{2kT}\right). \tag{9}$$

In this case, the $\log \sigma$ versus $E^{1/2}$ plot is shown in Fig. 1b. In the region where $n = N_a$, neither of the above two approximations is valid. In order to fully understand this transition region, we have to revert to equation (3) for a full description of n. As we are considering field enhanced ionisation of donor centres, we note that the carriers generated as a result of the Poole-Frenkel effect are field dependent. We now introduce a field dependent term in the description of n, such that

$$n = N_d - N_a - \frac{N_d}{1 + \frac{1}{2} \exp\left(\frac{-(\Delta E_d - \beta_{PF}E^{1/2} + E_F)}{kT}\right)}, \tag{10}$$

where N_c' in equation (5) may now be represented as

$$N_c' = \frac{1}{2} N_c \exp\left(\frac{-(\Delta E_d - \beta_{PF}E^{1/2})}{kT}\right). \tag{11}$$

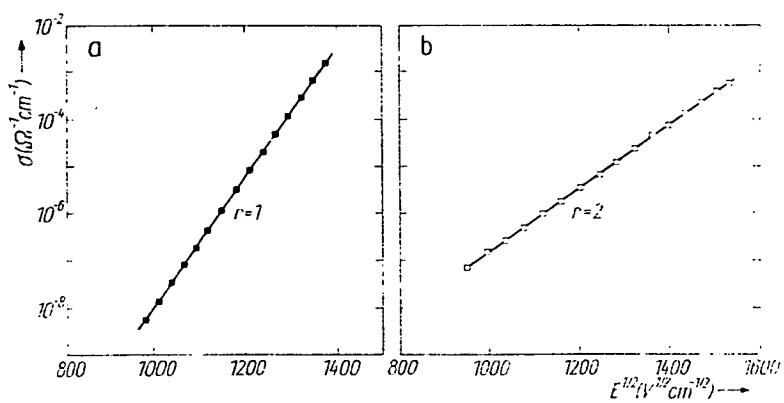

Fig. 1. $\log \sigma$ versus $E^{1/2}$ according to the approximations of a) (7) and b) (9). The parameters used are as follows: $\varepsilon_r = 7.5$, $T = 100$ K, $N_c = 10^{18}$ cm^{-3}, $N_d = 10^{15}$ cm^{-3}, $N_a = 10^{12}$ cm^{-3}, $\Delta E_d = 0.5$ eV, $\mu = 10$ cm^2 V^{-1} s^{-1}, sample thickness 2×10^{-5} cm

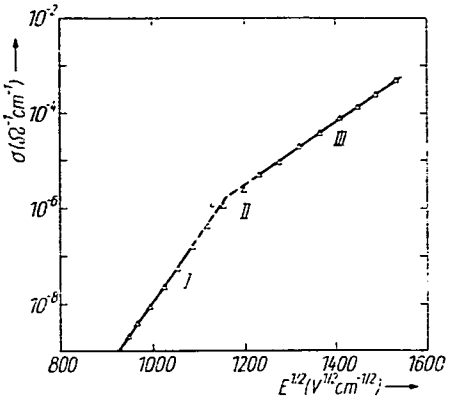

Fig. 2. $\log \sigma$ versus $E^{1/2}$ according to our modified field dependent carrier density model (see (10)), parameters as in Fig. 1

We obtain a complete description of the variation of conductivity versus applied field. Fig. 2 shows such a complete curve of the $\log \sigma$ versus $E^{1/2}$ plot.

3. Discussion

In the previous section we discussed the limitations of the two approximations of the Poole-Frenkel effect for an n-type semiconductor. If the field dependence of n, via equation (10), is taken into consideration, three regimes, marked I, II, and III in the $\log \sigma$ versus $E^{1/2}$ plot can be located (see Fig. 2). The approximation used in (7) fits exactly the region I, see Fig. 2. An equivalent situation is apparent when we compare the approximation of (9), i.e. $r = 2$, with region III in Fig. 2. The good fit of regions I and III with the straight lines obtained from the two approximations is not surprising since equations (7) and (9) are special cases of equation (10). If we now turn to the case when $n = N_a$, we observe a curve with a continuously decreasing slope in the Poole-Frenkel plot, as suggested by Tőrök [3].

Bearing in mind that the two approximations are a good fit to a general equation of the form $\sigma = e\mu n(E, T)$, it is interesting to examine the behaviour of n in these regions. For this purpose Fig. 3 shows a plot of n versus $E^{1/2}$. It is clear that at low fields where $n < N_a$, equation (7) provides a good description for the conductivity and the position of the Fermi level deduced from equation (4) is located below E_d. As the field is increased, the Fermi level moves closer to E_d, as shown in Fig. 4. A similar argument applies at high fields where $n > N_a$ and equation (9) is then a good approximation. In this case the Fermi level is located above E_d (see Fig. 4). The

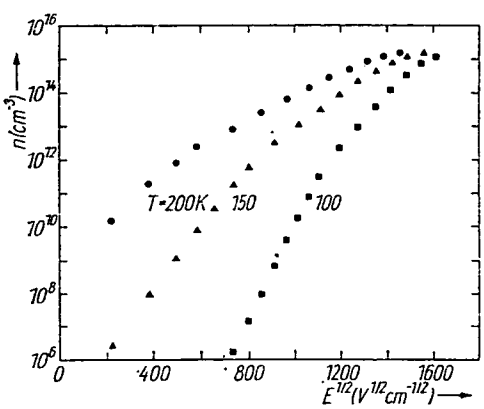

Fig. 3. Free carrier density (n) versus $E^{1/2}$, for different temperatures; parameters as before

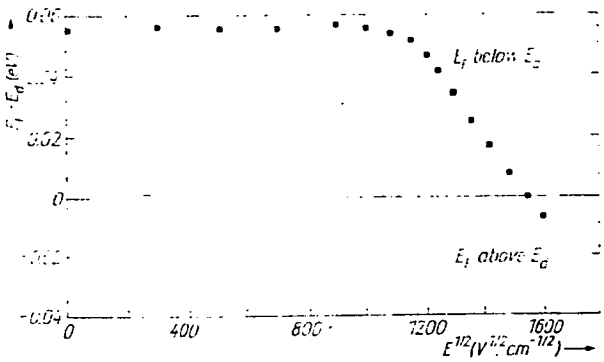

Fig. 4. Movement of the Fermi level with respect to the donor level, as a function of field; parameters as before

physical processes which give rise to the three distinct regions in Fig. 2 may be understood in terms of band diagrams, illustrated in Fig. 5. At low fields and low temperatures, where $n < N_a \ll N_d$, the situation may be represented as shown in Fig. 5a. At low temperatures some of the donor centres (N_d), will be partially ionised. As the field is increased, trapping and detrapping of carriers will occur via the donor level. The detrapping of carriers occurs as a result of the field enhanced emission of the donor centres whilst the trapping/retrapping process is a result of the originally ionised donor centres. This is associated with $r = 1$ in a $\log \sigma$ versus $E^{1/2}$ plot as shown in Fig. 1a since $(N_d - N_a) \approx N_d$ and $N_d > n$. At high fields where $N_a < n \ll N_d$, such that E_F lies above E_d (see Fig. 4), the situation may be represented as in Fig. 5b. In this case the trapping of carriers cannot occur to any extent since the donor level is located below the Fermi level and hence the donor states are essentially all filled and this condition is associated with $r = 2$ in a $\log \sigma$ versus $E^{1/2}$ plot (see Fig. 1b). The transition region, region II shown in Fig. 2, arises as a result of E_F traversing from below to above E_d. In doing so, the probability of a carrier being trapped continually decreases until E_F reaches the position described in Fig. 5b. If this description of the physical process is correct then for the case where $N_d = N_a$ one would expect $r = 1$ over the whole range of field in a $\log \sigma$ versus $E^{1/2}$ plot, since the Fermi level will remain pinned between the donor and acceptor levels. This situation is indeed shown to hold in our model. The result is shown in Fig. 6.

In all the calculations, the parameters selected are arbitrary and we have examined several cases with different values of N_a. The influence of N_a on the Poole-Frenkel plot is shown in Fig. 7, where a shift of regions I, II, and III occurs as a result of choosing $N_a = 5 \times 10^{13}$ cm^{-3}. In Fig. 8, we also show two more Poole-Frenkel plots for different temperatures. From these plots, it is seen that regions I and II are very sensitive to any variation of temperature, and this is further confirmed by the values of n, depicted in Fig. 3.

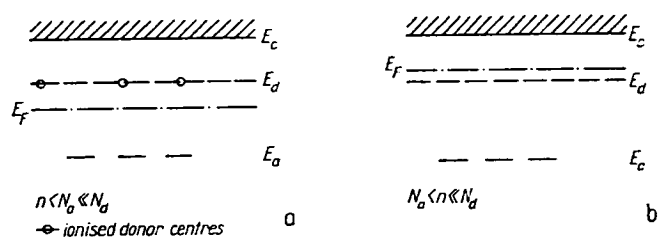

Fig. 5. Energy band diagrams of a) $n < N_a \ll N_d$ and b) $N_a < n \ll N_d$, parameters as before

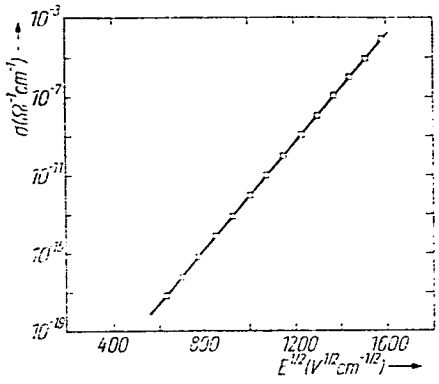

Fig. 6. $\log\sigma$ versus $E^{1/2}$ according to our modified field dependent carrier density model (see (10)): parameters as in Fig. 1 except $N_a = 9.5 \times 10^{14}$ cm^{-3}

In conclusion, from our calculations we have shown that in the Poole-Frenkel effect, for a specific donor and acceptor density, and temperature, the values of n can change from $n < N_a$ to $n > N_a$. We have also shown that the temperature and the values of N_a at which the measurements are carried out is very critical in arriving at the proper value of r. This is because as the temperature is increased, the regime before the transition region is not evident even at very low fields and the value of n remains the controlling factor. Finally we believe that our model of the simple one-dimensional Poole-Frenkel effect provides a physical basis for the variation in slope (i.e. of r in plots of $\log\sigma$ versus $E^{1/2}$) which is almost always observed, experimentally. Although we have considered in this paper the situation for an n-type material, the same arguments hold for a p-type material with the appropriate changes.

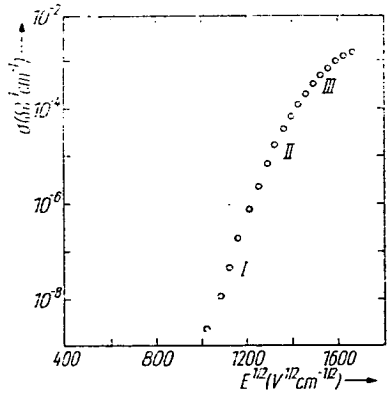

Fig. 7

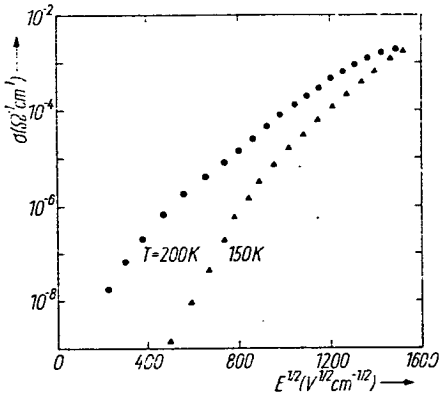

Fig. 8

Fig. 7. Influence of N_a ($= 5 \times 10^{13}$ cm^{-3}) in our $\log\sigma$ versus $E^{1/2}$ curve; parameters except N_a are the same as in Fig. 1

Fig. 8. Influence of temperature on the $\log\sigma$ versus $E^{1/2}$ curve; parameters except temperature are the same as in Fig. 1

Acknowledgements

The authors wish to express their sincere thanks to Drs. M. I. Török, S. Reynolds, and Prof. P. N. Butcher for many useful and illuminating discussions. One of us (WKC) is grateful to the University of Edinburgh for the provision of a Postgraduate Studentship and another (JJD) to the Science and Engineering Research Council for a Research Studentship.

References

[1] A. K. Jonscher, Thin Solid Films **1**, 213 (1967).
[2] J. R. Yeargan and H. L. Taylor, J. appl. Phys. **39**, 5600 (1968).
[3] M. I. Török, phys. stat. sol. (b) **126**, K97 (1984).
[4] J. G. Simmons, Phys. Rev. **155**, 657 (1967).
[5] G. A. N. Connell, D. L. Camphausen, and W. Paul, Phil. Mag. **26**, 541 (1972).
[6] L. Fritzsch and W. Bode, phys. stat. sol. (b) **58**, K49 (1973).
[7] R. A. Smith, Semiconductors. Cambridge University Press, 1959 (Chap. 4.3).

(Received April 16, 1986)

PHILOSOPHICAL MAGAZINE B, 1986, VOL. 53, NO. 2, 115–131

Electronic conduction and instabilities in thin films of amorphous silicon dioxide

By J. J. DELIMA, K. V. KRISHNA and A. E. OWEN

Department of Electrical Engineering, University of Edinburgh, King's Buildings, Edinburgh EH9 3JL, Scotland

[*Received 12 July 1984 and accepted 5 August 1985*]

ABSTRACT

The d.c. electrical properties of well annealed r.f. sputtered silicon dioxide films are reported. It has been observed that although these films have low- and high-conducting states similar to those previously reported for amorphous silicon dioxide, there are also very significant differences from previously observed data. The low- and high-conducting states have been characterized and it has been shown that both these states are stable bulk phenomena. The results are discussed in the light of previous reports and the conduction is tentatively interpreted in terms of single-carrier space-charge-limited current.

§ 1. INTRODUCTION

High-field conduction and breakdown processes in silicon dioxide are of great importance both fundamentally and technologically. They have been studied by many researchers (see, for example, Klein 1966, Lamb and Rundle 1967, Laverty 1971, Shatzkes, Av-Ron and Anderson 1974, Meaudre and Meaudre 1981, 1984, and Meaudre, Meaudre and Hauser 1983), both in films of SiO_2 thermally grown on silicon and in sputtered films. Klein (1966) observed a high conducting state at high fields which he termed as 'self-healing breakdown'. Shatzkes *et al.* (1974) observed threshold switching in thermal oxides which they attributed to filamentary formation at high fields. Meaudre and Meaudre (1981, 1984) and Meaudre *et al.* (1983) also observed a high-conducting state in the high-field region, but they attributed this to an unstable state before the onset of breakdown of the oxide, and they confined their measurements to fields below this unstable region. Verderber, Simmons and Eales (1967) also reported similar effects in evaporated films of silicon monoxide.

This paper reports measurements on d.c. conduction as a function of temperature and applied voltage in well annealed films of r.f.-sputtered amorphous silicon dioxide (SiO_2). In some respects the results are similar to the earlier ones mentioned above, particularly in that a transition was observed from a low- to a high-conducting state at a critical potential. Significant new features have emerged from the present work, however, which are probably related to differences in the methods of preparation and/or the circuit conditions used in the measurements. The results are compared with the previous work and the voltage-dependent conduction is tentatively interpreted in terms of single-carrier space-charge-limited conduction.

§ 2. EXPERIMENTAL

In all the experiments the oxide was grown by sputtering from a silicon dioxide target. An MRC r.f.-sputtering system (Model 8620, three target) was used for this

purpose. The high-purity silicon dioxide target was also supplied by MRC. The system was pumped below 10^{-6} Torr and baked for two hours before introducing high-purity argon into the chamber. The argon pressure was kept at 10^{-2} Torr and the inter-electrode distance was fixed at 10 cm. The r.f. power during the sputtering was 200 W and the voltage applied to the target was 1200 V. The target was pre-sputtered for about an hour before deposition of the experimental samples. The system was monitored for zero reflected power throughout deposition. The growth rate was about 20 Å min^{-1}.

Both metal–insulator–semiconductor (MIS) and metal–insulator–metal (MIM) structures were used in the present experiments. For MIS structures 0·6 Ω cm n-type Si wafers were used as substrates. The wafers were first cleaned in dilute HF solution to remove the native oxide. At this stage they were hydrophobic and were quickly rinsed in de-ionized water and methanol before being dried by blowing in nitrogen and loaded into the sputtering chamber. Aluminium was evaporated onto the oxide and the area of contact was defined by photolithography. MIM structures were made on tungsten sheets and the top electrode was sputtered tungsten (McCaughan and Murphy 1973). All samples (MIS and MIM) were normally annealed at 1173 K for half an hour in nitrogen before any measurements were made. Samples with thicknesses ranging from 0·1 μm to 2·2 μm were made. The thickness was measured by a Talysurf instrument and by an ellipsometer.

As a check on the quality of the r.f-sputtered amorphous SiO_2, its infrared spectrum was compared with that of SiO_2 grown by thermal oxidation of silicon (Pilskin, Davidse, Lehman and Maissel 1967). The two infrared spectra were similar in all respects and there was no evidence for -OH groups or water in the sputtered and well annealed SiO_2 films. Also, from the ellipsometer measurements the refractive index of the annealed r.f.-sputtered SiO_2 films was found to be 1·46, which is very close to that of thermally grown SiO_2 (i.e. 1·47). In addition, capacitance–voltage measurements at high frequency gave a value of 3·78 for the dielectric constant, again close to the value for thermal oxides (3·8).

The current–voltage (I–V) characteristics of the MIS samples were asymmetric and a typical example taken from an oscilloscope trace is shown in fig. 1. The top right-hand quadrant (i.e. with the n-type silicon negatively biased) is defined to be the forward direction and in the subsequent sections all the results described on MIS structures correspond to measurements in that direction. The MIM samples generally gave symmetric I–V characteristics, similar to those in the forward direction of the MIS structures, although sometimes slight asymmetries were observed which were presumably associated with the thermal asymmetry inherent in the MIM structures.

For all the electrical measurements the sample was contained in an evacuated chamber capable of covering the range 300–500 K. Before the d.c. measurements were conducted the status of the sample (low- or high-conducting state) was checked by connecting the sample to a curve tracer (Phillips transistor curve tracer PM 6507). Most of the samples were found to be in a relatively unstable high-conducting state immediately after completion of all the preparation steps, including annealing. The low-conducting state was obtained by applying a relatively high potential across the sample (i.e. corresponding to a 'field' in the range 10^5–10^6 V cm^{-1} on the assumption that the potential gradient across the sample is linear). At this stage the curve tracer was disconnected and I–V measurements were carried out. A Keithley electrometer (Model 610C) was used for measuring the small currents that were encountered. After the initial decay (i.e. over a period of two to three minutes at all temperatures) it was observed that

Fig. 1

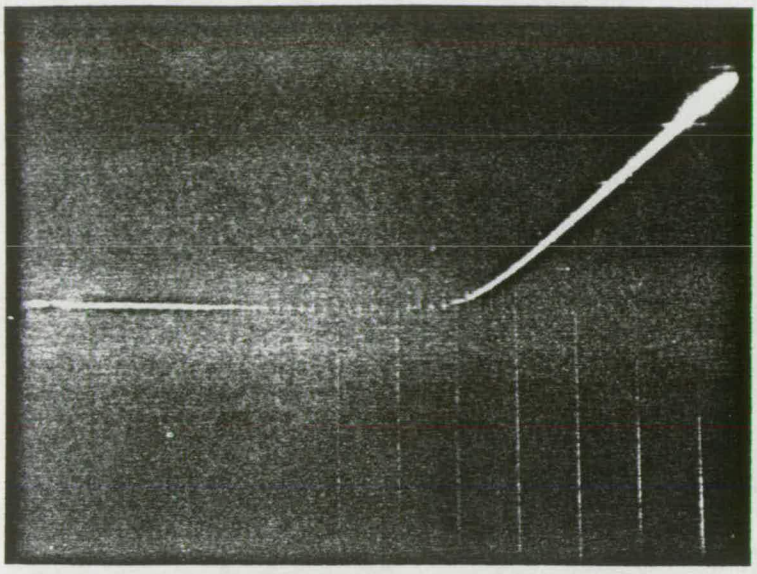

Oscilloscope trace of the I–V characteristics of a typical MIS structure. The right-hand top quadrant corresponds to the metal contact positively biased. Vertical scale: 0·5 mA per division. Horizontal scale: 0·5 V per division.

the current remains constant for periods of up to at least 24 hours, indicating electronic conduction and the absence of ionic polarization. After the I–V measurements were performed in the low-conducting state, the sample was put into the high-conducting state by reconnecting the curve tracer, applying a high voltage (field $\sim 5 \times 10^6$ V cm^{-1}) and using a suitable series resistor to control the current through the sample. Once the sample had been taken through the first cycle, both low- and high-conducting states were stable provided a critical field was not exceeded (see §§ 3.2 and 4.2). Detailed I–V measurements were then also made on the sample in its high-conducting state.

§ 3. Results

In common with previous work on amorphous SiO_2 thin films, it was observed that at high fields ($\sim 5 \times 10^6$ V cm^{-1}) there is an abrupt change in electrical properties from a low-conducting state to a more highly conducting state. There are however very significant differences in our work. The properties of the low- and high-conducting states are described and analysed in the following sections.

3.1. *Low-conducting state*

The current–voltage (I–V) characteristics are linear (ohmic) at low voltages but become increasingly non-linear at higher voltages. Typical results in the ohmic region for an MIS sample with an oxide thickness of about 0·1 μm are shown in fig. 2. (Note that, as mentioned in § 2, these and all other measurements described in the following were made in the forward direction.) In the ohmic region plots of $\log \sigma$ vs. $1/T$ gave good straight lines; an example from the data of fig. 2 is shown in fig. 3. The activation energy derived from fig. 3 is 0·57 eV.

The important consideration in the present context is the voltage or field dependence of current (or conductivity). The high-field (10^3–10^5 V cm^{-1}) data fit a $\log J$

Fig. 2

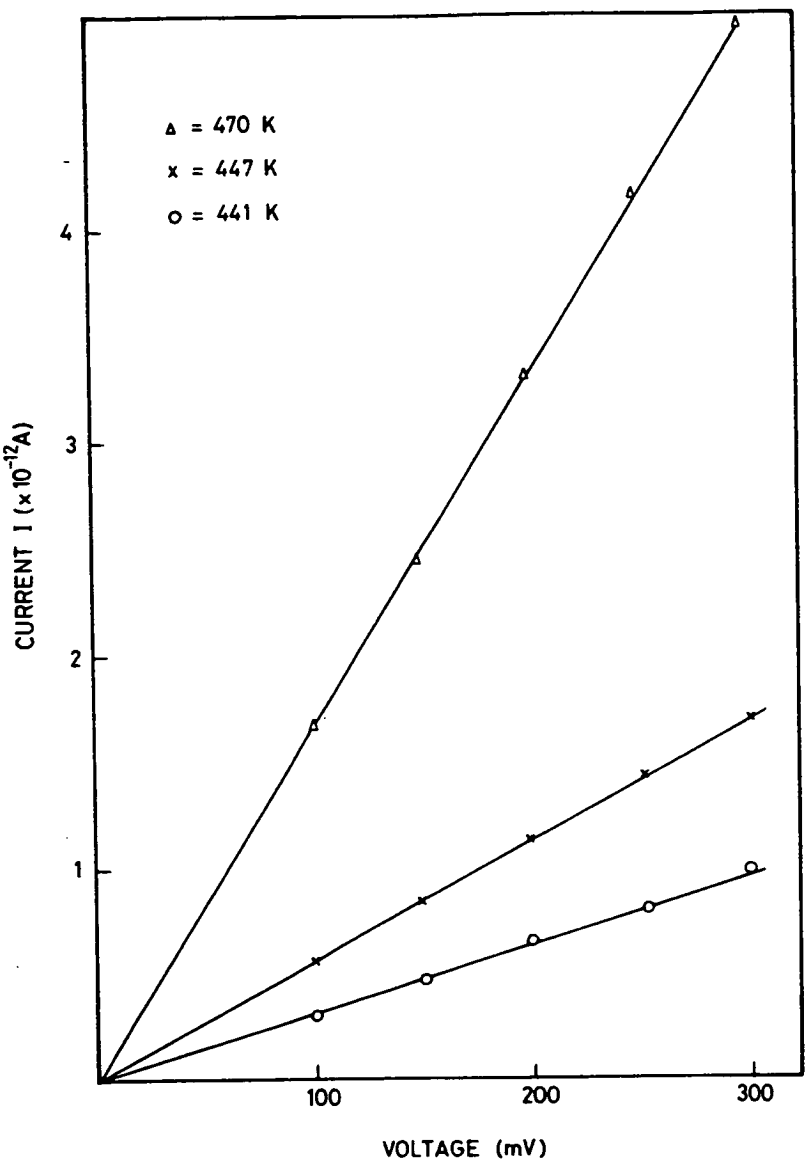

The low-field linear I–V characteristics in the low-conducting state of an MIS structure. The sample thickness is 0·1 μm; it was annealed at 1173 K.

versus $E^{1/2}$ plot (where J is the current density), giving good straight lines, indicating the possibility of Poole–Frenkel conduction. Analysis on this basis gives a reasonable value of 3·8 for the dielectric constant but a very low value (2×10^5 m^{-3}) for the donor concentration. It is worth noting that Meaudre and Meaudre (1981, 1984) made similar observations. They also considered their results in terms of the Poole–Frenkel effect and concluded that unacceptably low donor concentrations are obtained, but they did not derive a value for the dielectric constant. A significant difference between their results and our own is in the activation energy. They report a value of 0·28 eV compared to our value of 0·57 eV. It should be noted that although they also used r.f. sputtering,

Fig. 3

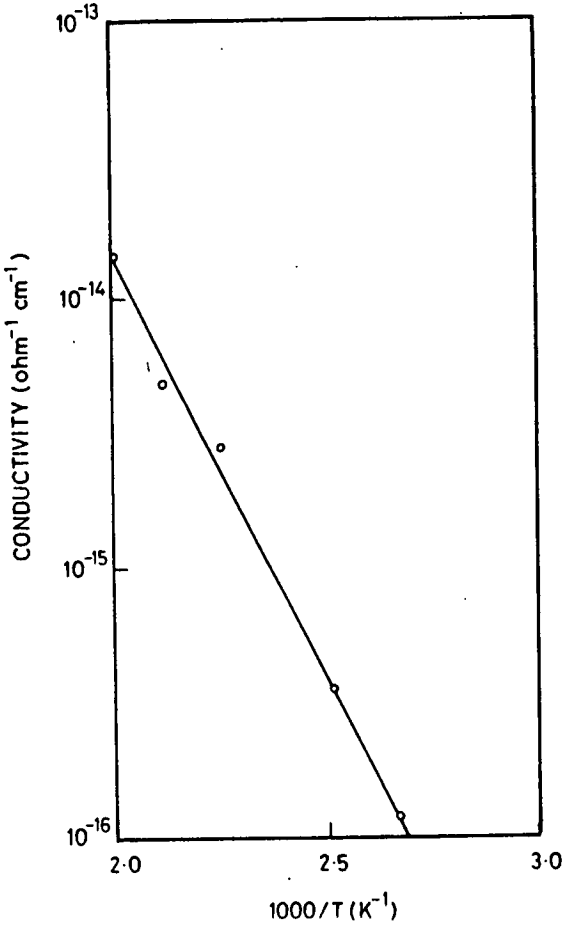

Log (conductivity) versus reciprocal temperature for the same sample described in fig. 2.

Fig. 4

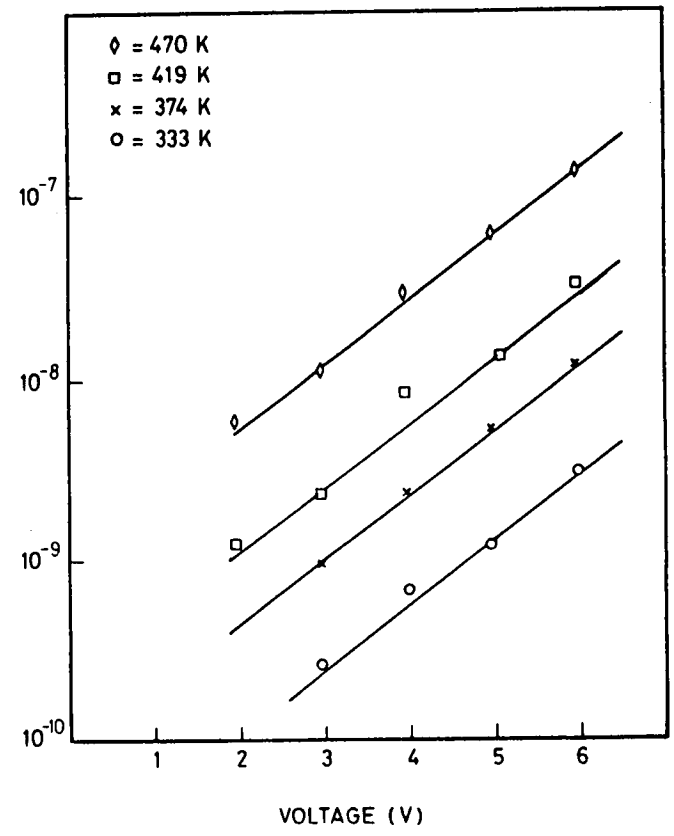

Log J versus V plot in the high-potential region for the same sample shown in fig. 2.

Fig. 5

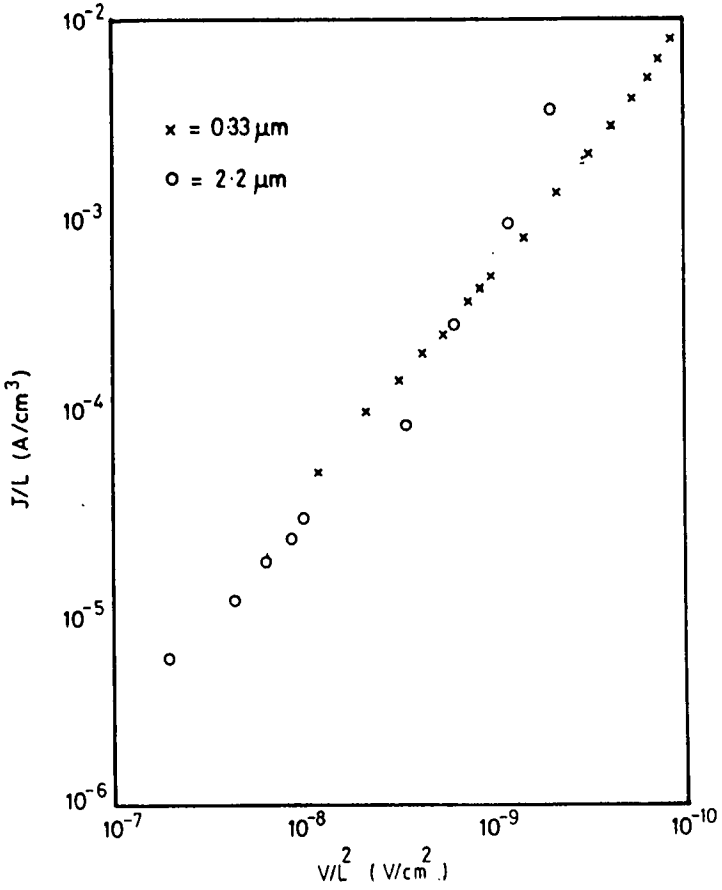

Typical results of J/L versus V/L^2 for r.f.-sputtered a-SiO_2 films in the low-conducting state (L is sample thickness). The two samples (thickness 0·33 μm and 2·2 μm) are close to the extremes of the thickness range studied in the present work.

Fig. 6

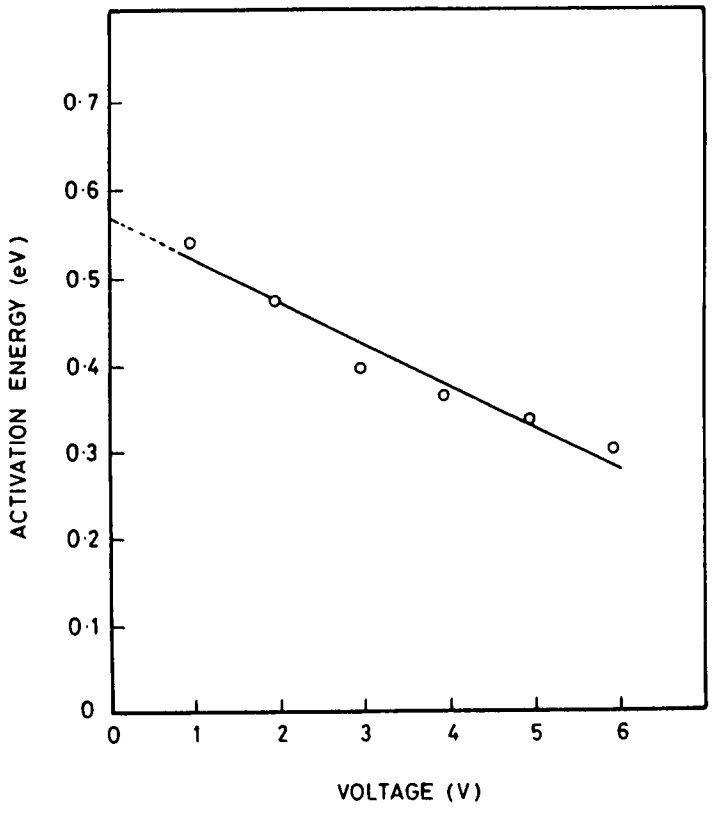

The voltage dependence of the activation energy of a typical sample in its low-conducting state. The extrapolated value of activation energy at zero voltage is 0·57 eV.

Fig. 7

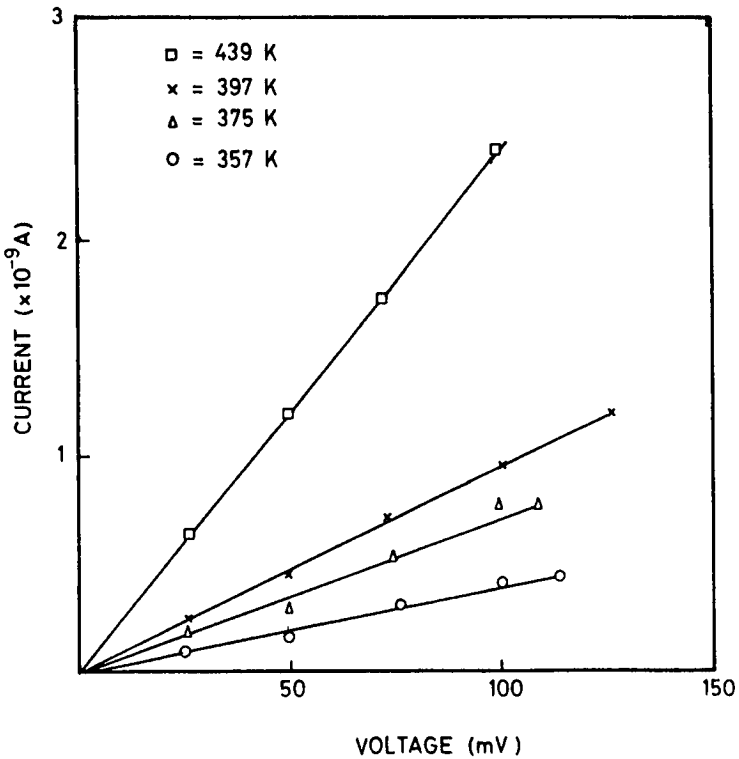

Low-field (ohmic) I–V characteristics of a sample in its high-conducting state (0·1 μm thick).

Fig. 8

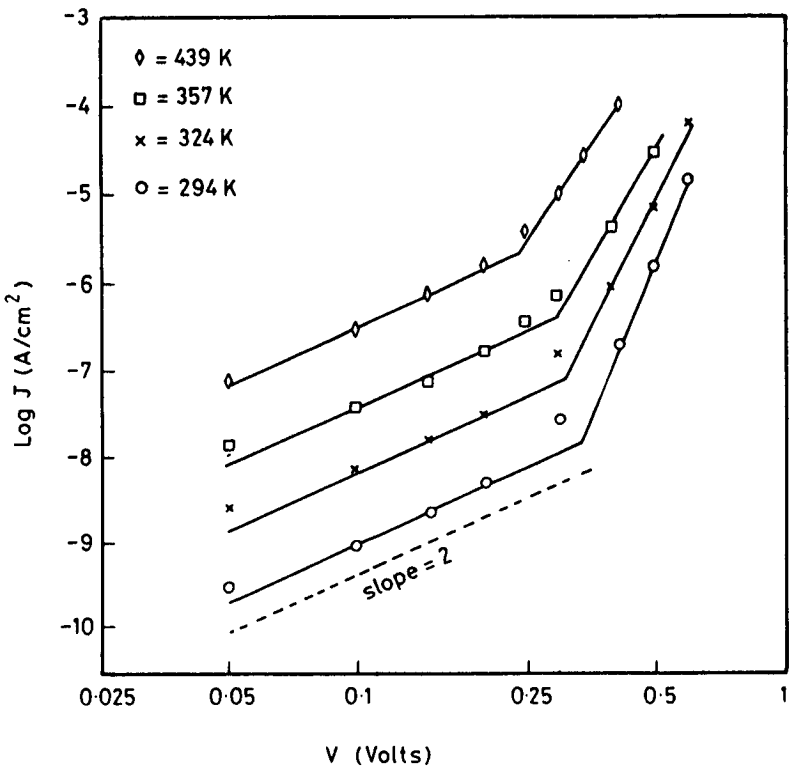

Log J versus log V plot in the high-field region for the sample shown in fig. 7. The dashed line has a slope of 2 (i.e. $J \propto V^2$).

Fig. 9

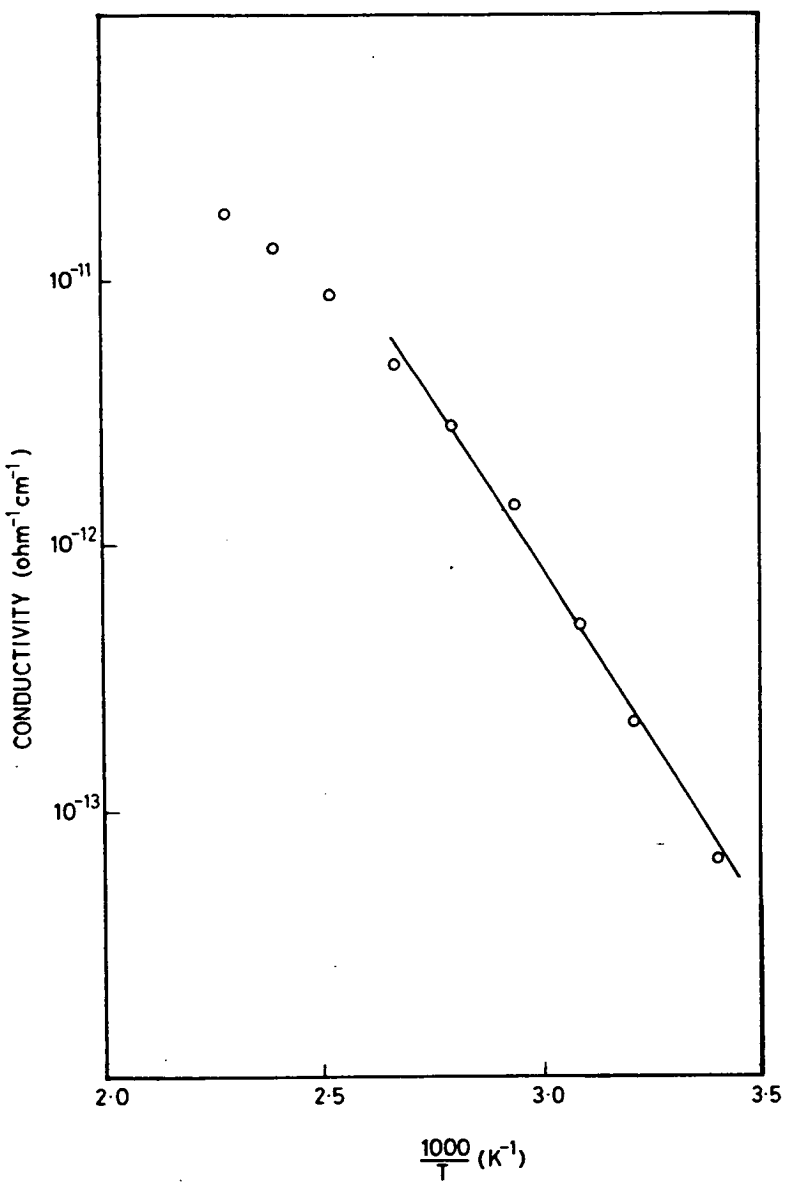

Log (conductivity) versus reciprocal temperature for a typical sputtered SiO_2 film in its high-conducting state.

Fig. 10

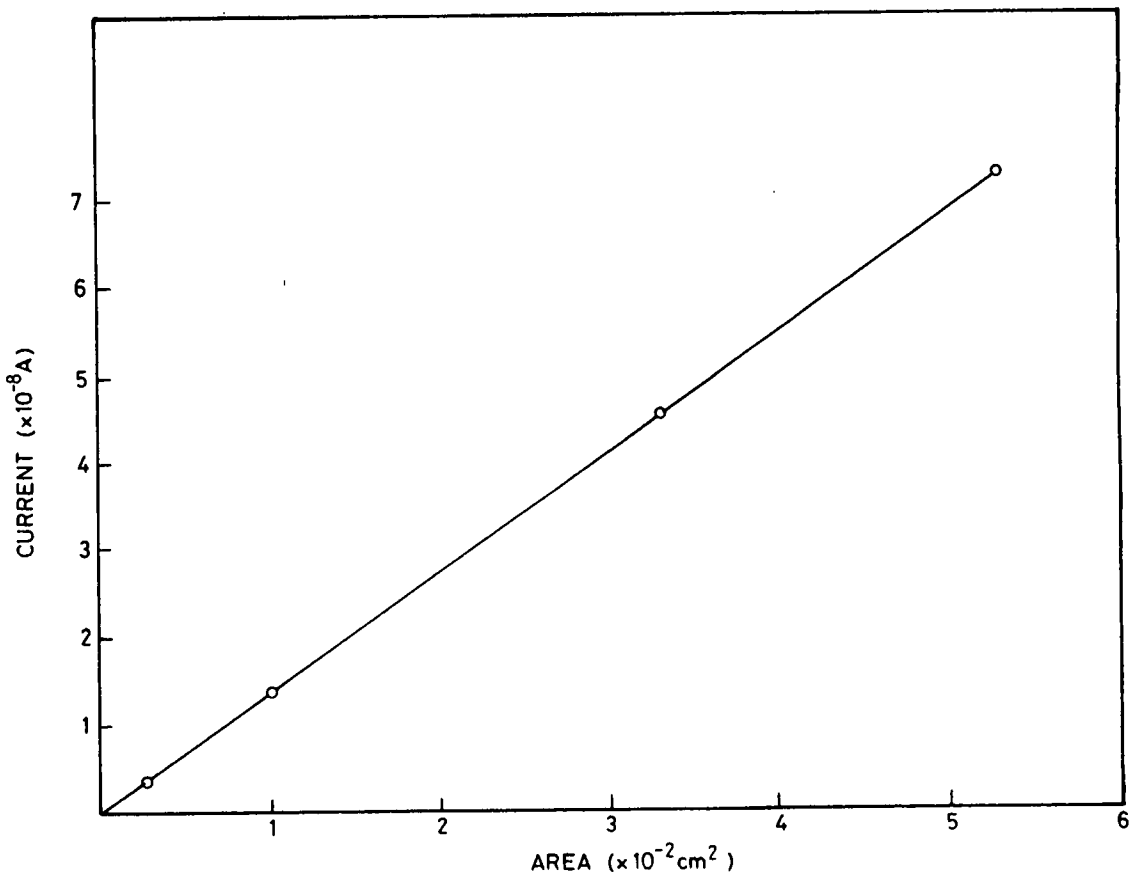

A plot of current versus contact area of a sample in its high-conducting state.

Fig. 11

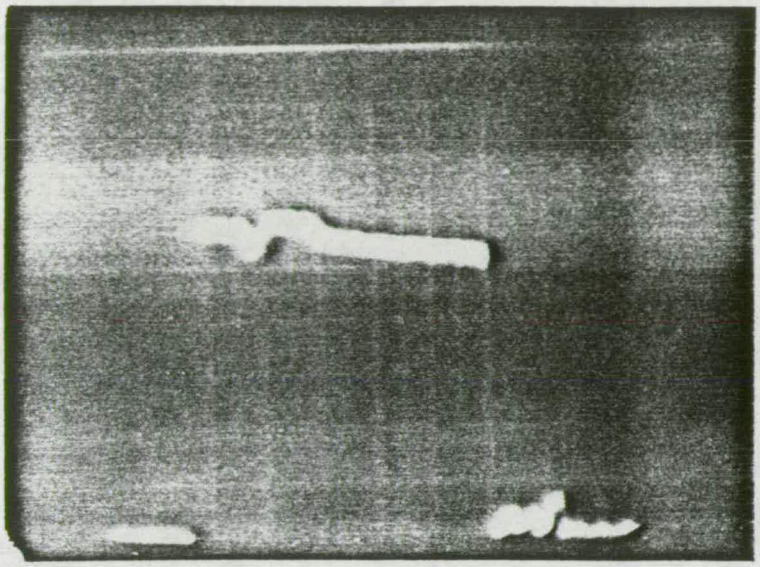

(*a*)

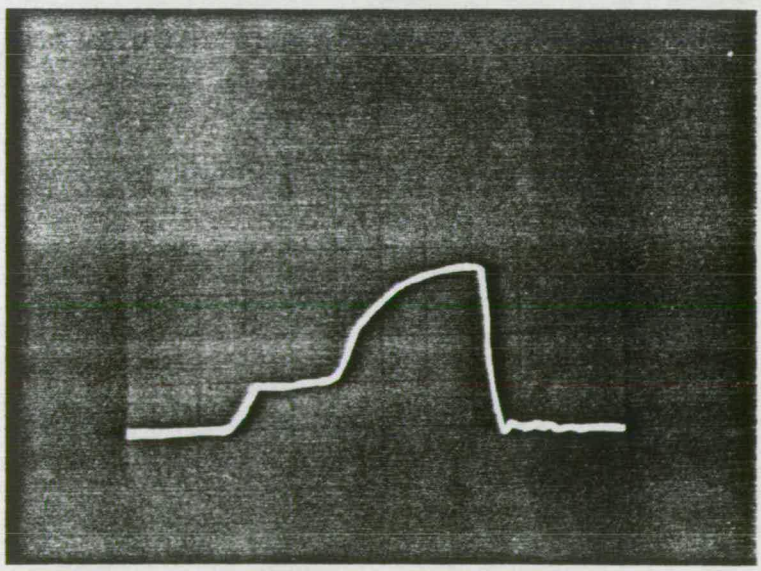

(*b*)

Oscilloscope traces of (*a*) voltage and (*b*) current, showing the transition from low- to high-conducting state in a sample of thickness 0·085 μm. In (*a*) the scale of the *Y*-axis is 5 V per division and of the *X*-axis is 50 ns per division. In (*b*) the current is measured as a voltage drop across a 220 Ω resistor. The scale of the *Y*-axis is 0·01 V per division and of the *X*-axis is 50 ns per division. Note that in (*b*) the sample current rises sharply from its low-conducting value after a delay of about 100 ns. A current-limiting resistor is also included in the measuring circuit (see text).

their silicon dioxide films and our own are different in preparation and annealing conditions. In particular they used a very much lower annealing temperature (573 K compared to our annealing temperature of 1173 K). It seems very likely that the different annealing treatment is responsible for the difference in activation energies, and for other important differences noted below. We have also made some observations on silicon dioxide films annealed at 573 K and observed lower activation energies. Moreover, on samples annealed at lower temperatures the current decays continuously over many days. Such behaviour is also reported in the literature (J. G. Doherty and W. D. Ryan, private communication).

The high-field data are plotted in fig. 4 in the form $\log J$ versus V. This gives a good fit to the data, suggesting the possibility of single-carrier space-charge-limited current in a uniform distribution of traps (Lampert and Mark 1970). Particularly strong evidence for space-charge effects is given by thickness-scaling experiments; typical results are shown in fig. 5 for two samples near the extremes of thickness used in the studies. It is evident that the space-charge scaling law holds. In the non-ohmic region of conductance the activation energy also depends on the applied potential; typical results, for the same sample, are plotted in fig. 6. The activation energy decreases with voltage and it extrapolates to the value of 0·57 eV derived from the measurements in the ohmic region (fig. 3).

The experimental results are discussed in more detail in § 4.

3.2. *High-conduction state*

At fields up to $\sim 5 \times 10^5$ V cm^{-1} no change in the slope of the current–voltage characteristics of the low-conducting state was observed (probably indicating that the trap-filled limit had not been reached). In all the samples studied, however, increasing the applied field caused an instability until, at fields of about 5×10^6 V cm^{-1}, there was a rapid transition to a stable higher-conducting state. Note from the experimental details that it is necessary to control the current at this stage to avoid permanent breakdown.

There are at least three regions of voltage in the high-conducting state with different current–voltage characteristics. At low voltages the current is ohmic and this is illustrated in fig. 7 for the same sample for which results are shown in fig. 2. This is followed by a region in which the characteristics are of the form

$$J \propto V^m,$$

with $m \sim 2{\cdot}0$, and the voltage at which the transition from ohmic to non-ohmic behaviour occurs is independent of temperature. At higher voltages there is an even higher power-law dependence; both of the higher-voltage (non-ohmic) regimes are shown in fig. 8. Over at least a significant range of voltage, however, the high-conducting state seems to follow the simple square-law dependence of single-carrier space-charge-limited current appropriate to either the trap-free case or to the situation in which current is controlled by shallow traps (Lampert and Mark 1970). Clearly there is a change to a higher power law (or some other I–V dependence) at voltages in the range 0·15–0·3 V, for the particular sample illustrated, depending on temperature (as temperature increases, the voltage at which the change in slope occurs decreases—see fig. 8).

It is important to note that during the transition to the high-conducting state the current through the device must be controlled by a suitable series resistance to avoid any destructive breakdown of the device. Note also from fig. 8 that the voltage

magnitudes are much lower and currents are about four orders of magnitude higher than in the lower-conducting state (fig. 4).

In the ohmic region of the high-conducting state (fig. 7), the current follows the usual activated form as a function of temperature. Typical results are plotted in the form of $\log\sigma$ versus $1/T$ in fig. 9. While there is a noticeable curvature at high temperatures, over most of the temperature range a good straight line is obtained with an activation energy of 0·51 eV. No significant and systematic voltage dependence of the activation energy in the non-ohmic region of the high-conducting state was observed (cf. fig. 6), but it must be noted that the range of voltages over which measurements were made in the high-conducting state was much less than in the low-conducting state (e.g. 0–1 V compared to 0–10 V). Once in the high-conducting state the sample is very stable and no change is observed in samples which were left in this state for up to four months. However the samples can be returned to the low-conducting state by applying a reverse bias (see § 2) of 1–10 V. Our experiments suggest that it is probably a current-controlled process. The results described above are fully representative of the general behaviour observed in all of the MIS and MIM structures studied in the present work.

It is particularly important to note that in the high-conducting state the current scales proportionately with the area of the electrical contacts (i.e. the conductivity is constant) and some representative results of current as a function of the area of the contacts are shown in fig. 10. Further experiments have not yet been made on the high/low instability but preliminary observations have shown that the samples can be cycled at least a hundred times through the low–high–low transitions without any degradation, provided the current through the device is suitably controlled. Moreover, preliminary pulse experiments have shown that the high–low and low–high transitions occur in times of a few hundred nanoseconds; a typical oscilloscope trace for the low-to-high transition is illustrated in fig. 11. Experiments on thermally grown oxides, while not so detailed and complete, also revealed transitions from low-to-high conducting states and vice versa.

§ 4. Discussion

4.1. *Low-conducting state*

The results shown in figs. 5 and 6 indicate that the J–V characteristics of amorphous silicon dioxide films are explicable in terms of single-carrier space-charge-limited conduction (SCLC) controlled by a uniform distribution of traps, i.e. by the current density–voltage (J–V) relationship (Lampert and Mark 1970):

$$J = 2en\mu(V/L)\exp(2\varepsilon V/N_t kTeL^2), \tag{1}$$

where e is the electronic charge, n the number of charge carriers, μ the mobility, V the applied voltage, L the thickness of the film, ε its dielectric constant, N_t the trap density, k Boltzmann's constant and T the absolute temperature. As already pointed out, the results of scaling experiments (fig. 5) provide strong evidence for this conclusion.

From eqn. (1) both the $(\eta\mu)$ product and N_t can be calculated, and in fig. 12 values estimated from the data in fig. 4 are plotted as a function of temperature. The trap density is about $2\times10^{18}\,\mathrm{cm}^{-3}\,\mathrm{eV}^{-1}$, and it is independent of temperature. The $(\eta\mu)$ product increases with temperature and, assuming that the mobility does not vary much (Hughes 1973), this implies that the carrier concentration is temperature dependent. The corresponding activation energy for the carrier concentration (n),

Fig. 12

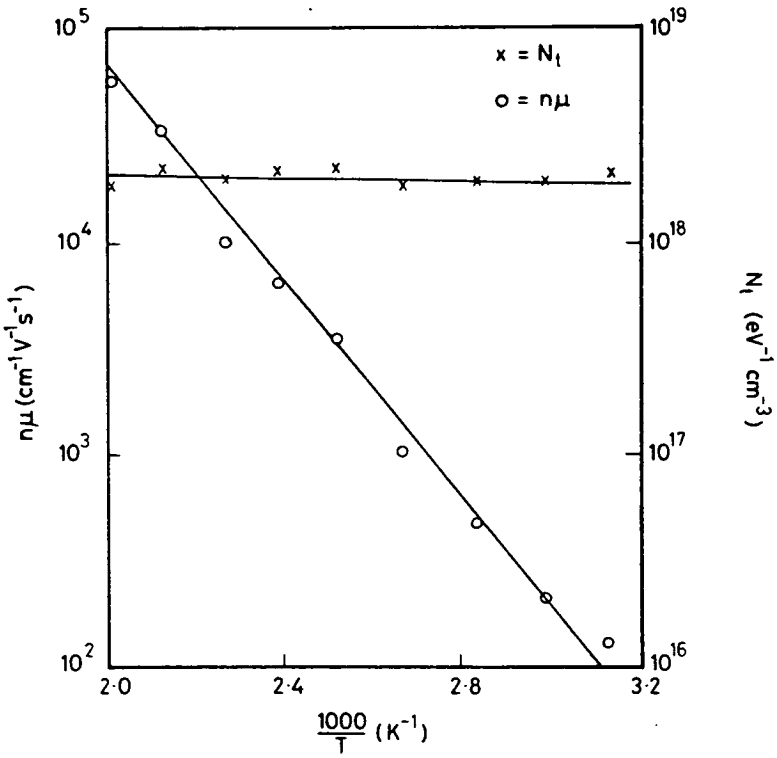

The $n\mu$ product and N_t as a function of temperature in the low-conducting state.

obtained from fig. 12 on the assumption that μ is independent of temperature, is 0·51 eV. It is assumed here that electrons are the mobile species and this is consistent with what is known about the mobilities of electrons and holes in amorphous SiO_2 (Hughes 1973). Indeed Hughes has shown that the electron mobility is surprisingly high ($30\,cm^2\,V^{-1}\,s^{-1}$ at room temperature) and only slightly dependent on temperature, but it is too early to speculate on whether the difference in activation energies (i.e. 0·51 eV compared with the d.c. activation energy of 0·57 eV) is experimentally significant and perhaps attributable to an activation energy for electron hopping.

By the same token, the considerable asymmetry in electron and hole mobilities is consistent with the single-carrier SCLC being regarded as an *electron* current. In the MIS samples the n-type silicon substrates must therefore be an injecting contact under the experimental conditions used here.

It should be noted in passing that according to Lampert and Mark (1970), SCLC controlled by an exponential distribution of traps provides a more accurate description of experimental results on amorphous materials than a uniform distribution. Den Boer (1983) has shown, however, that for an amorphous material with an activation energy of about 0·65 eV, analyses based on both uniform and exponential distributions give similar results for densities of states and hence the results are not significantly sensitive to different treatments.

4.2. *High-conducting state*

For fields up to 5×10^6 V cm^{-1} in the low-conducting state no instabilities were observed but, as previously noted (see § 3.2), increasing the field above 5×10^6 V cm^{-1} causes a transition to a high-conducting state. Similar behaviour has been reported in the literature, as already mentioned in the introduction, i.e. there is what appears to be a voltage-controlled transition from low- to high-conduction states and the high-conducting state is retained even after the potential is removed.

The important difference which must be emphasized in the present work is that, in the high-conducting state, the current is proportional to the area of the electrode contacts as illustrated in fig. 10 (the current is also proportional to area in the low-conducting state, of course). Also, in the low-field region of the high-conducting state a $\log\sigma$ versus $1/T$ plot gives a good straight line with a slope corresponding to an activation energy of 0·51 eV (e.g. fig. 9). In other words, whatever the cause of the high-conducting state in the present experiments, it appears to be a bulk phenomenon and the current is uniform across the device. This is a highly significant difference to superficially similar previous observations, which have commonly been attributed to the formation of a conducting metallic or semi-metallic filament. By contrast, in the present work, even though the current is three to four orders of magnitude greater than in the normal low-conducting state, the sample retains the characteristics of a uniform insulating or semi-insulating oxide. Thus, these observations are clear evidence that metallic or semi-metallic conducting filaments are not formed under the conditions described in this paper. Cycling experiments have shown that it is possible to take the sample through low–high–low conducting states at least one hundred times without any degradation in their characteristics. Also, the surface under the contacts was observed under a microscope and no damage was found in any of the samples examined.

As described in § 3.2 there is a substantial range of voltages in the high-conducting state (fig. 8) where the current has the characteristics of either trap-free space-charge-limited conduction (SCLC) or SCLC controlled by shallow traps. In the latter case the current density J is given by (Lampert and Mark 1970)

$$J = \tfrac{9}{8}\theta\varepsilon\mu V^2/L^3, \tag{2}$$

where θ is the ratio of free carrier concentration to the total (free plus trapped) carrier density.

Den Boer (1983) has developed a method of analysis to calculate the density of states from an arbitrary J–V characteristic, with the following assumptions: (*a*) the injected charge is uniformly distributed in the sample, (*b*) the electric field is uniform in the film and (*c*) the trap distribution is continuous and only slow varying with energy. These simplifications over-estimate N_t by a factor of not more than two.

Taking two points (J_1, V_1) and (J_2, V_2) on the measured J–V curve, the Fermi level shift ΔF for a voltage change ΔV can be calculated and it is possible to show (Den Boer 1983) that

$$N_t = 2\varepsilon\,\Delta V/eL^2\,\Delta F.$$

On this basis N_t can be estimated directly from the J–V characteristics by a graphical method.

The analysis has been applied to the present data to obtain the trap density N_t and the results are shown in fig. 13. The data in the $J \propto V^2$ region of the high-conducting state can also be fitted approximately to eqn. (1), (i.e. the case of SCLC in a uniform

Fig. 13

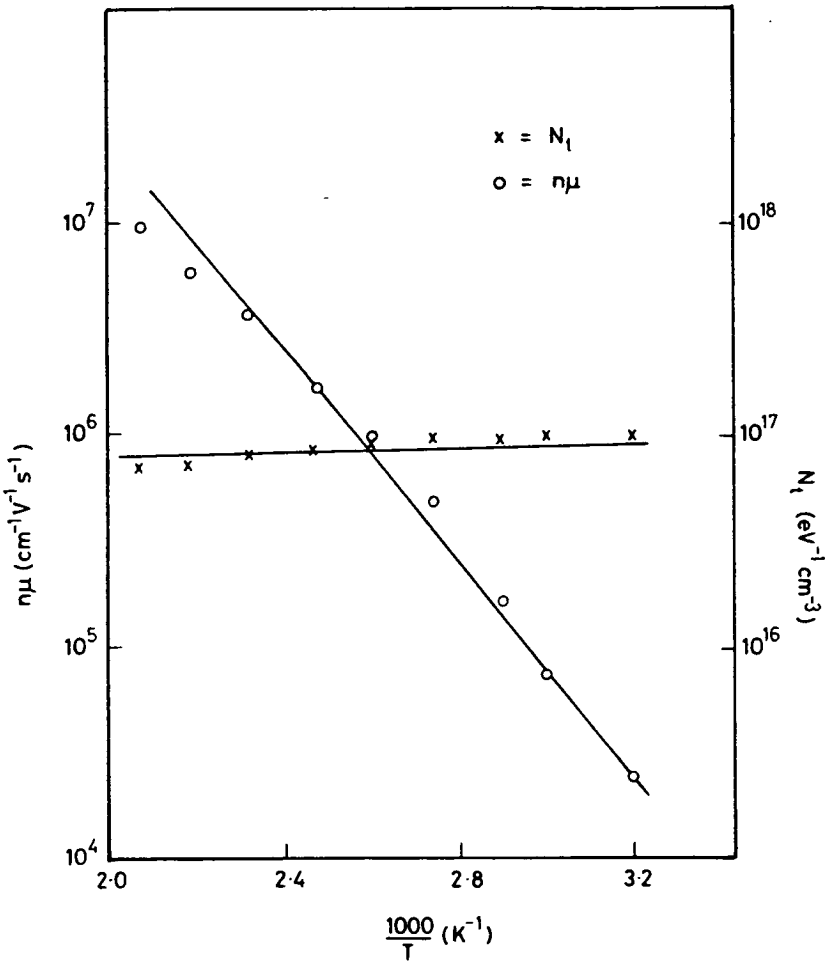

The $n\mu$ product and N_t as a function of temperature in the high-conducting state.

distribution of states, as applied to the low-conducting state). It is interesting to note that values of N_t so derived are essentially the same as those shown in fig. 13.

It appears therefore that the estimation of the density of states is not very sensitive to the method of analysis and probably gives only an upper limit. The $(\eta\mu)$ product, again calculated from eqn. (1), is also shown in fig. 13, and note that as in fig. 9 (for $\log\sigma$ versus $1/T$ in the high-conducting state) there is also a tendency towards a curve of lower slope at high temperatures.

The table summarizes the results for N_t and $(\eta\mu)$ at room temperature, ΔE_σ being the activation energy for d.c. conduction and ΔE_n the activation energy for carrier concentration obtained from the $\log(\eta\mu)$ versus $1/T$ plot, assuming that μ is independent of temperature. From this table and the appropriate figures it is apparent that in the high-conducting state the magnitude of the $(\eta\mu)$ product has *increased* by about two orders of magnitude compared to the low-conducting state, while its temperature dependence has not changed. On the other hand, N_t has *decreased* by two orders of magnitude in the high-conducting state and these relative changes in $(n\mu)$ and

Table

Conducting state	N_t ($eV^{-1}cm^{-3}$)	$n\mu$ ($cm^{-1}V^{-1}s^{-1}$) (room temp.)	ΔE_σ (eV)	ΔE_n (eV)
Low	2×10^{18}	3×10^{2}	0·57	0·51
High	9×10^{16}	$2{\cdot}4\times10^{4}$	0·51	0·51

N_t are reflected in the increase of four orders of magnitude in conductance on going from a low- to a high-conducting state. The reduction of N_t suggests the possibility of a structural modification in the bulk of the oxide. It is possible that because of the lower number of traps in the high-conducting state the trap-filled limit is reached at much lower voltages than in the low-conducting state, and this is consistent with the experimental observations (fig. 8).

The simplest and most obvious interpretation of these results is that the transition from low- to high-conducting states, or vice versa, is caused by some possibly field-induced structural modification in the bulk of the oxide which changes the density and distribution of traps. For example, it is notable that the best fit to the I–V data in the low-conducting state is given by SCLC controlled by a uniform distribution of traps (in a range of energy which includes the Fermi level) while for the high-conducting state SCLC controlled by shallow traps (i.e. traps above the Fermi level) seems more appropriate.

§ 5. Conclusions

The d.c. electrical properties of r.f.-sputtered and well annealed amorphous silicon dioxide films have been investigated as a function of temperature and applied voltage (field). Two distinctive conducting states have been observed and detailed investigations have been made in both the low- and high-conducting states. The following new features have emerged:

(1) The r.f.-sputtered amorphous silicon dioxide films, after the initial preparation and annealing, are in an unstable high-conducting state but they can be stabilized into the low-conducting state by applying a large potential across the samples.
(2) In the low-conducting state the films are essentially identical in electrical properties to good-quality silicon dioxide films grown by thermal oxidation of silicon.
(3) The films can be brought to a stable higher-conducting state by applying a high field across the sample, provided that the current through the sample is controlled by a suitable series resistance to avoid the destructive breakdown of the oxide.
(4) Experimental evidence shows that the high-conducting state is a property of the bulk material rather than due to metallic or semi-metallic filaments. It is also shown that both low- and high-conducting states are stable.
(5) Samples can be taken through the low–high–low conducting states at least one hundred times without any observable degradation or changes in properties, as long as the current through the device is suitably controlled.
(6) Preliminary results from pulse experiments indicate that the low–high and high–low transition takes place in the order of a few hundred nanoseconds.

(7) The two states have different activation energies, i.e. 0·57 eV in the low-conducting state and 0·51 eV in the high-conducting state.
(8) The observed high-field behaviour in both cases could be explained by single-carrier space-charge-limited conduction, and analysis on this basis yields lower values for the density of states in the high-conducting state compared to the low-conducting state.
(9) The experimental results must be interpreted with caution but the evidence is that the transition from the low- to the high-conducting state is caused by a field- (potential-) induced change in the density and distribution of traps in the bulk of the oxide.

ACKNOWLEDGMENTS

The authors wish to acknowledge financial assistance from the Science and Engineering Research Council. Thanks are also due to Mr A. M. Gundlach for technical help. One of the authors (JJD) would also like to express his thanks to Hughes Microelectronics Ltd. for a CASE studentship.

REFERENCES

DEN BOER, W., 1983, Ph.D. Thesis, Delft University.
HUGHES, R. C., 1973, *Phys. Rev. Lett.*, **30**, 1333.
KLEIN, N., 1966, *I.E.E.E. Trans. Electron Devices*, **13**, 788.
LAMB, D. R., and RUNDLE, P. C., 1967, *Br. J. appl. Phys.*, **18**, 29.
LAMPERT, M. A., and MARK, P., 1970, *Current Injection in Solids* (New York: Academic Press).
LAVERTY, S. J., 1971, *Int. J. Electron.*, **30**, 165.
MCCAUGHAN, V. D., and MURPHY, V. T., 1973, *J. appl. Phys.*, **44**, 2008.
MEAUDRE, M., and MEAUDRE, R., 1981, *J. non-crystalline Solids*, **46**, 31; 1984, *Ibid.*, **68**, 281.
MEAUDRE, M., MEAUDRE, R., and HAUSER, J. J., 1983, *J. non-crystalline Solids*, **58**, 145.
PILSKIN, W. A., DAVIDSE, P. D., LEHMAN, H. S., and MAISSEL, L. I., 1967, *IBM Jl Res. Dev.*, **11**, 461.
SHATZKES, M., AV-RON, M., and ANDERSON, R. M., 1974, *J. appl. Phys.*, **45**, 2065.
VERDERBER, R. R., SIMMONS, J. G., and EALES, B., 1967, *Phil. Mag.*, **16**, 1059.